ROMA TRE
UNIVERSITÀ DEGLI STUDI

Multimodal Imaging as a tool to study the neurovascular coupling in the spinal cord

Michela Fratini

Scuola Dottorale in Scienze Matematiche e Fisiche: Dottorato di Ricerca in Fisica XXVIII Ciclo

Program Coordinator

Prof. Roberto Raimondi

Tutor

Prof.ssa M.A. Ricci

Cotutor:

Prof. B. Maraviglia
Dr. F. Giove
Dr.ssa A. Cedola

To Anita and Marco

INDEX

INTRODUCTION

Functional Magnetic Resonance Imaging (fMRI) has become one of the most powerful tools in neuroscience research, with promising applications in clinical practice.

In particular, fMRI based on blood oxygenation level dependent (BOLD) contrast [1-5] has gained a primary role in the study of human brain, both for the characterization of regular brain activity and in clinical practice. Up to now, however, relatively few studies of the human spinal cord (SC) by functional imaging have been presented, starting from the work published in 1996 by Yoshizawa et al. [6], with a subsequent relevant contribution by Stroman et al. [7-16].

Recently, studies on the task-dependent modulation of the SC fMRI activations signal in response to innocuous and painful sensory stimuli or to motor tasks have been performed, and an hemodynamic response function (hrf) specific for the SC has been proposed [17]. It has been shown that there is a linear relationship between the applied force and the BOLD signal amplitude during isometric exercise [18], and that there is also a movement rate-dependent increase in spinal fMRI signals [19]. All these studies have shown that spinal BOLD fMRI has the potential for becoming a reliable and sensitive tool for studying the modulation of functional activity in the SC.

SC fMRI may be of immediate application in neuroradiology, in particular for the assessment and follow-up of spinal injuries, pain, and neurodegenerative diseases (e.g. multiple sclerosis), as well as in the development and evaluation of new therapies. Indeed, a non-invasive tool capable of monitoring the function, and thus complementing the available anatomical information, is a crucial need in these fields.

Preliminary studies of people with spinal cord injuries (SCI) and multiple sclerosis (MS) have demonstrated an altered activity in the SC, depending on the injury severity and on the advancement of the disease [7, 20-24].

Nonetheless, the application of fMRI to the SC remains confined to a few laboratories, mainly because of the vagaries of the activation patterns and of their characteristics [25-27]. In particular, the potential of SC fMRI is significantly impaired by the limited overall quality of the functional series, emerging in the form of geometrical distortions, signal losses, and poor contrast to noise ratio. These issues can be ascribed, at least in part, to a poor control of physiological noise. In a research environment, on an experiment-to-experiment basis, suitable solutions can be found by carefully

choosing the appropriate experimental procedures at the acquisition stage, and by properly treating the data at the post processing stage. However, SC fMRI is still far from defining the standardized protocols required for an everyday clinical use.

To further complicate matters, the exact features –and even the biophysical origins– of the functional response in the SC are still unclear. While for the brain the neurovascular coupling is clear and well characterized, for the SC this is not yet the case. The investigation of the characteristics of the SC functional signal, and in particular of its linear relationship with the underlying neural activity, is therefore crucial for the physiological characterization of the BOLD response, as well as for the analysis of fMRI time series (which is heavily based on the assumption of linearity). Recently, some promising advancements have been made in this field. On the one hand, it was observed by electrophysiological studies that there is a linear relationship between the neuronal activities of the SC and the muscular tensing. Moreover, Madi et al. [18] found the existence of a linear functional relationship between the neuronal activity and the BOLD fMRI signal. However, in spite of the increasing numbers of reports on spinal fMRI studies in the literature, we are still far from a clear and complete knowledge on the characteristics of the functional signal.

Within this context, in the present thesis we study and report the characterization of the functional response of the human SC to a multilevel motor task, designed to assess the linearity of the hemodynamic response as a function of the intensity of a graded task. In addition, we study the structure and distribution of the vascular network (VN) and of the neuronal network (NN), which together contribute to the BOLD fMRI signal, by means of high-resolution X-ray Phase Contrast Tomography (XrPCμT). One of the goals of this study is the definition of a suitable replacement for the vascular model currently used in fMRI, which was developed only for a specific real geometry of the VN (*i.e.*, for the rat brain [4]) and may not be applicable to the SC. Of course, the development of a more accurate vascular model would be of paramount importance for the application of SC fMRI to the clinical practice (for the treatment of SC injuries, pain and neurodegenerative diseases). In addition, a better understanding of the SC could be important for the investigation of neuronal metabolism and of neurodegenerative diseases in an environment that may be regarded as a simplified model of the brain.

The present thesis is organized in six Chapters.

In the first Chapter we briefly describe the current state-of-the-art of SC imaging, by reviewing current methodologies and applications. We also identify the greatest current needs, especially from a clinical point of view, that will drive forward future developments of SC imaging.

The second chapter deals with the main aspects of the SC and of its constituents, necessary for a better understanding of this thesis. The SC anatomy has implications for the development and applicability of spinal fMRI. As a matter of fact, the main difficulties facing researchers attempting to image the SC function can be easily traced back to the peculiarities of the SC anatomy. At the same time, the vascular anatomy of the SC is optimally organized for the generation of a strong and spatially specific BOLD effect. This can help in overcoming the numerous other difficulties that characterize SC fMRI.

In the third chapter, we discuss the essential physical concepts at the basis of Magnetic Resonance Imaging, and in particular of BOLD-based fMRI. In addition, we present a selection of recent results in SC fMRI.

The fourth chapter reports the experimental fMRI results obtained on the relationship between the intensity of the stimulation and the amplitude of the SC BOLD response in humans during a controlled motor task (graded isometric force) with the dominant hand. The results confirm the physiological origin of the response, and will be of great help in model-based SC fMRI inference.

The fifth chapter presents the results of our investigation of the vascular and neuronal network of the mouse SC by XrPCμT. The obtained results will be useful to develop an optimised BOLD fMRI signal model for the SC, on the basis of its real vascular geometry.

The sixth chapter discusses the progress made towards the definition of an optimised BOLD signal model for SC fMRI, and outlines the additional steps still required to fulfil this goal.

CHAPTER 1

SC BIOMEDICAL IMAGING: LIMITS AND FUTURE DEVELOPMENTS IN PRE-CLINICAL AND CLINICAL FIELD

Non-invasive imaging methods have become an essential tool for assessing the effects of damage or disease processes, with the potential to support the planning of surgical interventions and of other treatments, and to determine if treatments are effective. There are a number of approaches available, including magnetic resonance imaging (MRI), X-ray based imaging (Computer Tomography- CT), nuclear medicine (Positron Emission Tomography–PET), magnetoencephalography (MEG), and each have strengths and weaknesses in terms of what they can show, and what they cannot. These non-invasive approaches provide the only means of accessing the structure and function of the human spinal cord (SC). As a result, there is currently a great need for the development of these methods and of these techniques into pre-clinical and clinical use.

The potential outcomes of advancing these methods are great, enhancing our basic understanding of healthy human SC function, and influencing our ability to accurately diagnose and treat injury and disease, and predict outcomes. In order to support the need for developing of SC imaging methods and advancing the current technology, we report on the key aspects of SC imaging from basic research to clinical practice, while devoting most of our attention to SC functional MRI (fMRI).

In particular the objectives of this chapter are:

1) To describe the current state-of-the-art of SC imaging by reviewing current methodologies and applications;

2) To identify the current greatest challenges, both innate to SC imaging, and relative to hardware and software development;

3) To identify the greatest current needs, especially from a clinical point of view, that will drive forward future developments of SC imaging.

1.1 Introduction to non-invasive imaging methods in neuroscience: Historical overview

The impact of medical imaging on the field of neuroscience has been considerable. The advent of x-ray CT in the 1970's allowed clinicians to see features inside the heads of patients without the need for surgery. By making the small step of placing the source of radiation within the patient, x-ray CT became autoradiography, so that now not only structure but also blood flow and metabolism could be followed in a relatively non-invasive way. A big step forward was made by choosing to use a positron emitter as the radioisotope. Since a positron almost immediately annihilates with an electron, emitting two photons at 180 degrees to each other, much better localisation of the radioisotope within the scanner is obtained. Using labelled water, PET became the first technique to potentially allow researchers to produce maps of the mind, by measuring blood flow during the execution of simple cognitive tasks. Since local blood flow is intimately related to cortical activity, regions of high regional blood flow indicate the area in the cortex responsible for the task being performed.

At around the same time, another technique, which promised even better anatomical pictures of the brain, was being developed. MRI, based on the phenomenon of nuclear magnetic resonance [28], produces images of the human body with excellent soft tissue contrast, allowing neurologists to distinguish between grey and white matter, and brain defects such as tumours. Since MRI involves no ionising radiation, the risks to the subject are minimised. The development of contrast agents suitable for dynamic MRI studies, and improvements in the speed of imaging, opened up the possibility of using the technique for functional brain studies. In 1990 the first experiment using MRI to study brain function was performed, imaging the visual cortex whilst the subject was presented with a visual stimulus [2]. A contrast agent was used in this first study, but it was not much later when the first experiment was carried out using the blood as an endogenous contrast agent. The haemoglobin in the blood has different magnetic properties depending on whether it is oxygenated or not; these differences affect the signal recorded in the MR image. By imaging a subject at rest and whilst carrying out a specific task, it became possible to image brain function in a completely non-invasive way. The functional studies of the Central Nervous System (CNS), that have been produced over the past few years have started to make a big impact on the way neuroscience is approached. There are, however, still areas of the technique of fMRI that require refinement. The mechanisms behind the observed activation response are not well understood, and there are issues in regard to the way that the data from such experiments are analysed. However, the potential of fMRI, alongside that

of PET, means that the study of the human CNS has entered a new era, offering new insights into neurology, psychiatry and psychology.

1.1.1Non- invasive SC imaging methods

Non-invasive investigations of human SC function, and of the effects of SC injury (SCI) or disease, are significantly hampered by the inaccessibility of the SC. In order to supplement current methods for assessing residual function, pain, and quality of life factors after SCI or disease, sensitive methods are needed to reveal changes in neurological function and structure. Non-invasive imaging methods such as MRI, PET, and CT provide the only means for accessing the structure and function of the human SC. As a result, there is currently a great need for development of these methods. While progress is being made, only a relatively small number of research labs in the world are actively working on SC imaging methods, and these techniques have yet to be advanced into clinical use. The potential benefits of advancing these methods are tremendous, enhancing our basic understanding of healthy human SC function, and impacting our ability to accurately diagnose and treat injury and disease.

The greatest current challenges for SC imaging were identified as arising from the imaging environment itself, which is made difficult by the bone surrounding the spinal canal, by the physiological motion of the cord and of adjacent tissues, and by the small cross sectional dimensions of the SC, exacerbated by the metallic implants often present in injured patients. Challenges were also identified as a result of a lack of "critical mass" of researchers taking on the development of SC imaging, affecting both the rate of progress in the field, and the demand for equipment and software to manufacturers to produce the necessary tools.

In the following, we will define the current state-of-the-art of SC imaging. Only PET and MRI methods-fMRI and Diffusion Tensor Imaging (DTI) - are described in this chapter, with most of the attention on fMRI. In addition, we will describe the current applications (on SCI, on multiple sclerosis and on pain) of these techniques employed in clinical research, discuss the underlying theory and challenges, and present the evidence for the current and potential power of these methods. In particular, we will discuss all aspects of SC imaging from basic research to clinical practice.

1.2 Positron Emission Tomography: a general overview

PET produces images of the body by detecting the radiation emitted from radioactive substances. These substances are injected into the body and are usually tagged with a radioactive atom, such as Carbon-11, Fluorine-18, Oxygen-15, or Nitrogen-13, that has a short decay time. These radioactive

atoms are formed by bombarding normal chemicals with neutrons to create short-lived radioactive isotopes. PET detects the gamma rays given off at the site where a positron emitted from the radioactive substance collides with an electron in the tissue.

PET provides images of blood flow or other biochemical functions, depending on the type of molecule that is radioactively tagged. For example, PET can show images of glucose metabolism in the brain, or rapid changes in activity in various areas of the body. However, PET has high cost of installation and maintenance.

The choice of different injected tracers provides the potential for obtaining unique information regarding the injured SC. PET imaging has at least two distinct uses in the evaluation of traumatic SCI: assessment of the metabolic activity within remaining tissue and monitoring the degree of axonal connectivity. With regard to the first use, 18F-labeled fluorodeoxyglucose (FDG) has been used to monitor nervous system function in a range of preclinical and clinical studies. For example, traumatic brain injury reduces glucose utilization detected by FDG-PET, and a reduced uptake is associated with impaired outcome [29, 30]. This technique has also been applied to compressive and radiation myelopathies of the cervical SC [31-34] (Figure 1.1) as well as to one preclinical study of traumatic SC injury [35]. For cervical compressive myelopathies, some lesions show locally reduced glucose utilization while other cases show increased glucose uptake [32, 34].

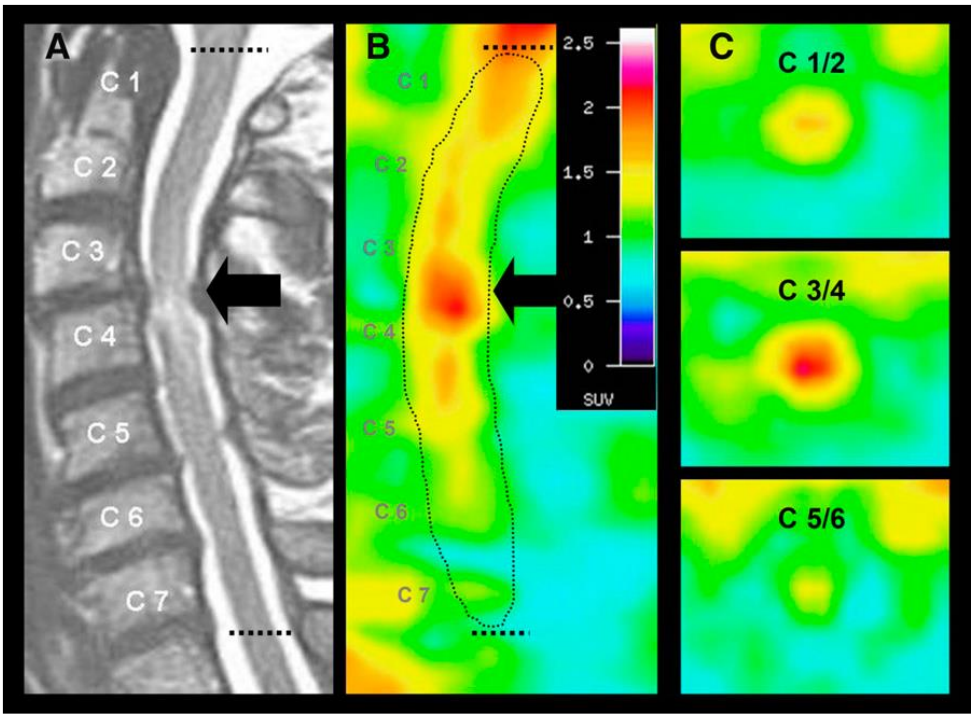

Figure 1.1: Patient with myelopathy. **(A)** Sagittal T2-weighted MRI scan shows stenosis with compression of cervical cord and intramedullary hyperintensity at level C3/C4 (arrow). **(B** and **C)** Corresponding sagittal **(B)** and transaxial **(C)** 18F-FDG PET slices demonstrate focally increased uptake at level of stenosis. Patient had good clinical recovery 6 month after decompression of stenosis [31].

There is a positive correlation between a pre-operatively elevated uptake and later improvement after de-compressive surgery in two studies [31, 34]. In one study, the PET data were uncorrelated with magnetic resonance (MR) images [34], providing a distinct means to predict positive outcome from surgery. A challenge for SC PET remains the spatial resolution. Even with high-resolution scanners and CT registration, the spatial resolution is one or more orders of magnitude worse than structural MRI. Regional distinctions between zones of the SC at one segmental level are not possible by PET imaging in axial projections.

There is growing clinical trial activity focused on therapeutic strategies intended to promote axonal growth, regeneration, sprouting and repair.

PET tracers with neurotransmitter specificity have the potential for tracking the degree of damage and repair for specific fiber tracts. Thus, PET ligands may function as biomarkers in the development of new repair strategies. The potential utility of this approach has been demonstrated in one preclinical study [36]. The raphe spinal system is the only serotonergic system in the SC; therefore, all presynaptic serotonin markers depend on the continuity of descending fibers. PET tracers, that bind to the presynaptic serotonin re-uptake sites (such as 11C-labeled 2-(2-(dimethylaminomethyl) phenylthio)-5-fluoromethylphenylamine (AFM)), have been developed [37-39]. In rats, the SC has a

clearly defined specific AFM uptake, which is lost caudal to a complete SC transection. With a moderate SC contusion, there is a partial loss of caudal AFM signal. Most critically, treatment with an axon regenerative therapy, namely Nogo receptor (NgR1-Fc) decoy protein, promotes an increase in caudal AFM signal after chronic SC contusion [36].

This increased signal is correlated with behavioural improvement and matches post-mortem histological evidence of serotonin fiber regrowth. In this case, a neurotransmitter-specific PET tracer is a radiological marker that highlights the extent of axonal connectivity across a lesion site and reports the degree of axonal repair with treatment. The use of tracers specific to presynaptic markers of different long tracts in the SC may extend the anatomical specificity of this technique. PET measurements of fiber regrowth do not require the presence of highly ordered fasciculated fiber tracts as DTI-MR measurements. This is critical because the majority of preclinical studies in which interventions promote some fiber regeneration show that new fiber growth is highly branched and irregular. Thus, PET may provide an imaging modality to detect regenerative growth in proof-of-concept clinical trials, Even though, the use of ionising radiation in PET (as opposed to MRI) remain an issue.

1.3 Specific Magnetic Resonance Imaging methods and applications

MRI may be the most widely used method for detecting pathology in the CNS because of the high tissue contrast and relatively high spatial resolution that it provides. MRI also provides several different methods for visualizing tissues and pathology in addition to detailed anatomical imaging, including diffusion-weighted imaging and functional imaging. However, every method has limitations and weaknesses, as detailed below. In particular, imaging of the SC presents inherent challenges that are common to all MR imaging applications. Specifically, these are 1) the spatially non-uniform (inhomogeneous) magnetic field environment when in an MRI system, 2) the small physical dimensions of the cord cross-section, 3) physiological motion. In addition, the application of fMRI to the SC requires specific modifications to the conventional brain methodology and conventional brain tools. Here, we discuss the key challenges and future developments for SC MRI methods (DTI and fMRI), with more attention to spinal fMRI.

1.3.1 Diffusion Tensor Imaging: state of the art, limitations, future developments

DTI is a MR technique capable of measuring the magnitude and direction of the diffusion of water molecules in various tissues, thereby providing information about the microstructural composition of tissues [40].

DTI developed from a technique known as diffusion-weighted imaging, which measures the attenuation of MR signals caused by diffusion [41]. DTI was formally introduced by Basser et al, [42] and subsequent improvements in this technique have led to the development of DTI as a tool to delineate white matter tracts in the brain. In particular, the indices calculated from diffusion MRI experiments -mean diffusivity (MD), axial and radial diffusivity, and fractional anisotropy (FA), which are able to document and quantify orientation changes of water molecules in otherwise normally appearing white matter, are sensitive to changes in microstructural integrity, demyelination, axonal loss, and inflammation. DTI of the SC in humans was initially inadequate because of the small area of the cord, of susceptibility artefacts and of cardiac and respiratory motion artefacts [43, 44]. Improvements in scanning protocols have allowed for obtaining usable diffusion images of the SC, so that this imaging technique can now be applied in healthy and diseased SC in humans in vivo [45]. In particular, in healthy subjects good contrast is observed between grey and white regions, with the highly anisotropic white matter showing much higher FA values than the central grey matter as reported in Figure 1.2. In addition, given the sensitivity and specificity of DTI to white matter integrity, this technique is sensitive to structural changes due to pathology [16, 24]. A groups of researchers has shown that DTI is able to detect cord damage in regions of the cord that appear normal on T2- weighted images [46, 47]. DTI has also proven to be sensitive to Wallerian degeneration through animal models of pericontusional traumatic axonal injury [48], demyelinating lesion [49] and dorsal root axotomy [50].

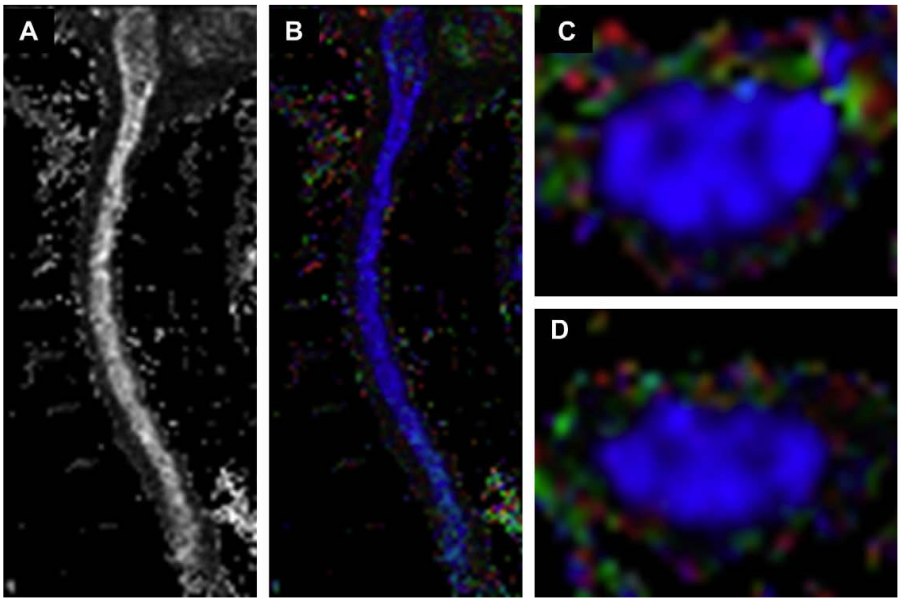

Figure 1.2: Sagittal (gray scale and color) (**A, B**) and axial (**C, D**) fractional anisotropy maps from a healthy volunteer obtained at 3 T. On the axial acquisitions, note the ability to resolve the grey and white matter (the grey matter has lower FA compared with the white matter). The axial acquisition allows for quantitation of DTI metrics, such as FA [51].

The specificity of diffusion measurements to white matter pathology has been studied in animal models of de/dysmyelination. This study suggests that axial diffusivity is more specific to axonal degeneration whereas radial diffusivity is more specific to demyelination [40, 48-50, 52-57]. Other studies however reported possible interactions between axial and radial diffusivities, thereby limiting the specificity of these measures [58-60]. One argument refers to the pathophysiology of axon degeneration, as this process is known to be associated with demyelination in several pathologies such as in Multiple Sclerosis (MS) [61] or in SCI [50, 62]. Another argument is related to the biophysical properties of DTI, in which several physical parameters can influence diffusion metrics including myelination, axonal density, axonal diameter, or orientation of fiber bundles, as well as changes in the tissue matrix surrounding the axons [60, 63, 64].

SC DTI therefore represents an important advancement in the field of neuroimaging, and its use is being expanded both for prognostication and for guiding therapy. Ultimately, it is always important to remember that the diffusion tensor is an imperfect model used to explain data and one must always look at the data and make sure that interpretations in terms of axonal loss and demyelination are well supported by the behavior of the underlying model [60].

In the following paragraphs, we provide a summary of the limitations and future developments of SC DTI.

1.3.1.a Limitations of DTI in the human SC

SC DTI in humans still has a number of limitations. Adequate spatial resolution remains a problem, and it is difficult to visualize the individual funiculi on diffusion-weighted images, particularly in the lower thoracic cord [65]. DTI of these segments is affected more by artefacts arising from cardiac and respiratory motion as well as cerebrospinal fluid (CSF) pulsation [51]. The use of faster imaging techniques such as parallel imaging and single shot echo-planar imaging, as well as the use of cardiac pulse-gating, have helped to reduce these artefacts. However, the scan acquisition time is still a limitation for patients with acute SCI, since these patients cannot withstand even 30 minutes of additional scanning time in the MRI suite. The signal to noise ratio in human SCI is sub-optimal in most studies and can lead to overestimation of anisotropy measures, particularly in low-anisotropic tissues such as the central grey matter [66]. The use of 3T MR scanners does improve the signal to noise ratio (SNR) [67], but is still not used universally. The use of DTI postoperatively is hampered significantly by the use of spinal instrumentation, which creates numerous artefacts. Additionally, standardized software to process tensor images is essential to make this a feasible option for routine clinical use.

1.3.1.b Future Developments and final considerations

DTI has given us a unique insight into the pathophysiology and microstructural alterations associated with SC disorders. DTI provides useful information about the direction of fibres and the diffusion anisotropy properties of neural tissue, complementing the information obtained by conventional MRI. DTI in the brain is being used to help diagnose various clinical conditions, but its exact application in spinal imaging is largely unexplored. While initial studies in rat models have primed this modality for human research, more data is required on the accuracy and reliability of DTI indices in defining cord pathology. DTI of the SC does show promise in certain neurosurgical conditions, such as traumatic SCI and intramedullary tumours. However, scanning protocols and image processing need to be refined and standardized. Once these challenges are overcome, we can expect the use of DTI in mainstream clinical practice, both to prognosticate as well as to monitor patients with SC disease. In particular, in the future DTI indices may help surgeons to determine their surgical approach. Correlation between quantitative diffusion measures, such as FA and apparent diffusive constant (ADC), and acute or chronic injuries of the SC may be useful to predict outcome and to monitor the response to treatment. Nevertheless, the clinical use of DTI calls for a careful understanding of acquisition and processing issues. The full potential of DTI will probably not be realized until it is integrated with other modalities to obtain a richer characterization of white matter, in a manner analogous to the combination of perfusion and diffusion imaging data used to demonstrate an

ischemic penumbra. Perhaps the most intriguing application is the integration of DTI-tractography [51] with functional imaging. The excellent correlation of BOLD functional MR data with DTI-tractography findings in motor and visual cortex may illustrate the future of structure- function investigations in the brain and SC.

1.3.2 Functional Magnetic Resonance: general information, applications, state of the art, future developments.

1.3.2.a General information about the fMRI contrasts

fMRI refers specifically to the imaging of neuronal function in the central nervous system (CNS). In fMRI the anatomical images are acquired quickly and repeatedly over time in order to detect changes corresponding to tasks or to sensory stimuli. In fact, during the acquisition a pattern of tasks or stimuli (called the "paradigm") is applied and tissue changes corresponding to the time-series of the neural response are captured. Image quality, both in terms of spatial resolution and of signal-to-noise ratio, is sacrificed to reduce the imaging time, thereby providing higher temporal resolution in the time-series data.

The fMR signal intensity changes arise from a sequence of related phenomena. A change in neural activity corresponds to a change in metabolic activity and oxygen consumption. An increase in metabolic activity triggers the release of vasoactive substances that cause local relaxation of pre-capillary smooth muscles, thereby increasing the local supply of oxygenated blood. The increase in oxygen supply exceeds the increase in demand, and so the local blood oxygenation level increases at sites of increased metabolism. In 1936, Drs. Pauling and Coryell had discovered that the magnetic properties of haemoglobin are different between the oxygenated and the de-oxygenated states [68]. This effect was observed in the form of dark veins in T_2^*-weighted MR images (T_2^*, T_2[1] are MR signal relaxation times) and triggered the development of MRI [2]. The local relaxation rate, $1/T_2^*$, is a function of the concentration of de-oxygenated haemoglobin [69, 70]. In order to detect the changes in blood oxygenation it is therefore necessary to acquire the time series of images with T_2^*-weighting, using a gradient echo imaging methods, and the echo time optimally set equal to the T_2^* of the tissues

[1] T_2 is the spin-spin relaxation time, while T_2^* is the spin-spin relaxation time composed of both the contributions from molecular interactions and inhomogeneities in the magnetic field. These relaxation times govern the return of the transverse magnetization to its equilibrium value (zero), and characterize the exponential decay of the NMR signal.

being investigated [70]. With this method, it is possible to observe relatively subtle changes in local blood oxygenation, and in the CNS, this is inferred to reflect changes in neural activity.

This is the "blood – oxygenation level dependent" or "BOLD" contrast that is most commonly used for fMRI [69, 70]. The BOLD contrast relies on the paramagnetic properties of deoxyhemoglobin that acts as endogenous contrast agent. Therefore, the increase of metabolism triggered by neuronal activity induces an enhancement of oxygen consumption and a subsequent increase of local blood flow and volume. The overcompensating increase of hemodynamic parameters produces an overall decrease of tissutal deoxyhemoglobin content and thus an increase of T_2^*; consequently, T_2^*-weighted images show an intensity increase in activated regions. Such an increase enables the localization of underlying neuronal activity. After its introduction in the early 1990s [2], BOLD-based functional imaging was widely utilized for non-invasive studies on human brain function. In recent years, similar approaches have been attempted for the study of the SC function [11, 14, 16, 24, 71, 72]; however, obtaining good functional images of SC still represents a technical and scientific challenge.

A second source of functional contrast has been hypothesized as active in the SC and brain fMRI, the so-called signal enhancement by extravascular water protons (SEEP) [8, 10, 73, 74] resulting from an increase in water content in active neural tissues [8, 75]. This mechanism is hypothesized to be related to neuronal swelling and /or glial cells shown to arise at sites of neuronal activity. Also, an increased blood flow to active tissues has been shown to be accompanied by increased intravascular pressure and by on increased production of extra-cellular fluid at sites of neuronal activity. The net effect is a local increase in water content near active neural tissues, causing a higher magnetic resonance signal intensity. Thus, spinal fMRI is generally able to detect neuronal activity in SC grey matter, which allows for the mapping of SC responses to sensory and motor stimulation.

Spinal fMRI reveals neuronal function indirectly by detecting changes in blood flow and blood oxygen levels occurring near metabolically active grey matter. Depending on the scanning parameters, the signal change arises in part from the BOLD contrast and in part from the SEEP contrast.

The application of fMRI to the SC is a logical extension of its use in the brain but has been slow to develop because of the many challenges posed by the application of this method to this specific anatomic region. SC fMRI requires specific modifications to the conventional brain fMRI methodology. Further work is required before the method is optimal for pre-clinical and clinical purposes. The following paragraphs briefly review the recent developments in SC fMRI and discuss the feasibility and potential applications of using SC fMRI in the clinic and pre-clinic field.

1.1.1.a State of the art of SC fMRI: general overview, limits and future perspectives

fMRI has become one of the most powerful tools for neuroscience research, and yet its use is limited to studies of the cortex, with relatively few exceptions [14, 19, 71, 76]. It has been demonstrated that important neuronal activity can be identified in the SC using spinal fMRI. Previous studies have shown that BOLD fMRI is feasible in the SC at both 1.5 T and 3 T, and the activation areas detected have good localization at the segmental level [11, 12, 18, 71]. In particular SC fMRI has been able to detect areas of activity in the cervical and lumbar regions with high sensitivity and reliability, in response to thermal, sensory, motor and painful stimuli [7, 19, 22].

Furthermore, spinal specificity for the stimulation of different dermatomes [9], and also the differentiation of motor and sensory areas were observed, and a large overlap was found. Even though substantial advances in knowledge have arisen from these studies, the poor reproducibility of the activation patterns and their characteristics – in terms of amplitude and location – have been invoked as significant concerns by several authors [25-27, 72, 77, 78]. In the clinical area, spinal fMRI has been applied to the study of injured SCs. The lumbar SC was imaged during noxious thermal stimulation of the L4 dermatome of complete and incomplete SC–injured volunteers [7, 13]. Signal intensity changes for the injured groups were of similar magnitude and had a similar time course pattern as those of the healthy group. However, the areas of activity in grey matter were altered. Spinal fMRI was also used to detect neuronal activity elicited by passive and active lower limb movement tasks in regions caudal to the injury site in volunteers with SCI [22]. Activity was detected in all volunteers regardless of the extent of injury. During both active and passive participation, activity was seen caudal to the injury site, although the number of active voxels detected with passive movement was less than with the active movement task. Therefore, spinal fMRI is able to detect a neuronal response in the SC caudal to the injury site during both active and passive lower limb movement tasks, and in response to a noxious stimulus, even when subjects could not feel the stimulus. Thus, spinal fMRI is useful for revealing areas of impaired and preserved activity in SC–injured patients. In addition, patients' studies provide further evidence of response sensitivity to pathological changes. Studies of people with SCI and MS have demonstrated altered activity in the SC depending on the state of their disease [7, 20-23]. However, obtaining BOLD images of the SC activation still remains a technical challenge. The main difficulties in spinal fMRI, like for the other MRI techniques, arise from the small size of the SC, from the presence of large movements due to cardiac pulsation and to respiration and from the presence of magnetic field inhomogeneities around inter-vertebral disks, [72, 77, 79] which induce significant susceptibility artefacts. In addition, SC motion and the flow of cerebrospinal fluids (CSF) are thought to further confound the analysis, and

therefore the interpretation of functional data [25]. Finally, the application of the fMRI to the SC requires specific modification to the conventional brain fMRI methodology, even if the theory of conventional brain fMRI is applied. However, if these challenges can be overcame, SC fMRI may be of immediate application in the clinical framework. Further the study of the SC could also be important because of the possibility to treat the SC as a simplified model of the brain, suitable for experiments aimed at investigating the neuronal metabolism and the neurodegenerative diseases. Finally, the study of the SC system may be of immediate and fruitful application in the treatment of SC injuries, pain and neurodegenerative disease (e.g. multiple sclerosis).

Recently, experiments based on the task-dependent modulation of the SC fMRI activations signal in response to innocuous and painful sensory stimuli or motor tasks have been done and an hemodynamic response function (hrf) specific for SC has been proposed [17]. It has been shown that there is a linear relationship between the applied force and the BOLD signal amplitude during isometric exercise [18], and that there is also a movement rate-dependent increase in spinal fMRI signals [19]. All these studies have shown that spinal BOLD fMRI is a reliable and sensitive tool for studying the modulation of functional activity in the SC.

Nonetheless, the exact features and even the biophysical origins of the functional response are still unclear. In the brain the neurovascular coupling is clear and well characterized, but for the SC this is not the case. Indeed, electrophysiological studies have shown that there is a linear relationship between the neuronal activities of the SC and muscular tensing [80]. In addition, Madi et al. [18] found the existence of a linear functional relationship between the neuronal activity and the BOLD fMRI signal as in the case of the brain, demonstrated by Logothetis et al. [5], but, nowadays there is not a direct demonstration on that relationship in the SC.

Within this context, in this thesis we study and report the characterization of the functional response of the human SC to a multilevel motor task, in order to assess the linearity of the haemodynamic response as a function of the intensity of a graded task. In addition, we study the structure and distribution of the vascular network (VN) and the neuronal network (NN), with high resolution X-ray techniques to refine the vascular model used in fMRI, which was developed only for a specific real geometry of the VN, (i.e. for the rat brain [4]) and may be not be applicable to the SC. As a consequence, the development of a more accurate vascular model would be of paramount importance for the application of fMRI of the SC to the clinical practice.

1.3.2.b Capabilities of human SC imaging applications:

In order to provide an overview of the current state of the art and of the capabilities of human SC imaging applications, we provide in the following a general overview of the SC fMRI techniques employed in the clinical research, focusing on the specific applications of SC imaging to SCI, pain and MS.

SC injury:

Improving the ability to assess tissue viability and to detect residual neuronal function in the SC, in order to identify and distinguish morphological and functional changes, is a key step to advancing our capacity for clinical prognosis and management of SCI patients.

Injury to the human SC, regardless of the mechanism, results in a complex cascade of events at the cellular level that may or may not have an effect on the neurovascular coupling mechanisms that underlie the signal changes detected with spinal fMRI.

The pathological processes that occur at the cellular level include ischemia, vasospasm, ion-mediated cellular damage, excitotoxicity, oxidative cellular damage, neuroinflammation, and cell death. Changes in the correspondence between fMRI signal changes and neural activity may therefore also depend on the time since the injury occurred, thus complicating interpretation. There are a number of clinical outcomes that follow traumatic SCI as a consequence of either adaptive or maladaptive plasticity. Adaptive plasticity refers to the concept of natural recovery whereby an individual who sustained motor deficits, sensory impairment or both following SCI recovers to some degree in the months after injury [81]. Maladaptive plasticity refers to neurological symptoms that arise as a result of spinal circuits reorganizing themselves in a way that provides no useful function such as neuropathic pain, spasticity, disruption of autonomic function and the lack of motor and sensory recovery [82]. One potential advantage of spinal fMRI will be to investigate the longitudinal effects of various stimulation paradigms as they relate to clinical symptoms such as the recovery of motor function, sensation or the development of neuropathic pain. A better understanding of the spinal circuit changes that are associated with maladaptive plasticity may lead to more accurate diagnoses and to the ability to objectively monitor treatment.

Studies of the effects of SCI that have been carried out to date using SC fMRI have all focused on the chronic stages at 1 year or more after the injury occurred. Potentially confounding effects include on-going changes in cellular function and ionic metabolism, each of which may alter the mechanisms of neurovascular coupling and the subsequent hemodynamic response. Nonetheless, the studies carried out to date have demonstrated that fMRI of the SC can detect important changes as a result of traumatic injury in both the cervical and lumbar regions of the SC [7, 22, 83]. The first SC fMRI

study carried out on participants with SC injuries investigated activity in the lumbar SC, below the level of injury, in response to a noxious cold stimulus applied to the leg (L4 dermatome) [7] . This study demonstrated significant activity in all participants, including SCI patients, in the lumbar segments of the SC, below the level of injury. Moreover, participants with SCI who could feel or had some altered sensation of the cold stimulus, had spatial patterns of activity that were similar to those observed in healthy participants. A more recent study of thermal responses in the cervical SC and brainstem investigated responses to warm thermal stimuli in regions both above and below the level of injury [84]. Results corresponded with the level and extent of injury, with responses above the level of injury being generally similar to those seen in healthy participants, and responses below the level of injury being altered depending on the injury severity. Right- and left-side differences were also demonstrated, as well as corresponding activity in the brainstem (Figure 1.3). Collectively, these results demonstrate the sensitivity of the fMRI method to changes as a result of trauma and the feasibility of using fMRI as a research tool for studying the effects of injury.

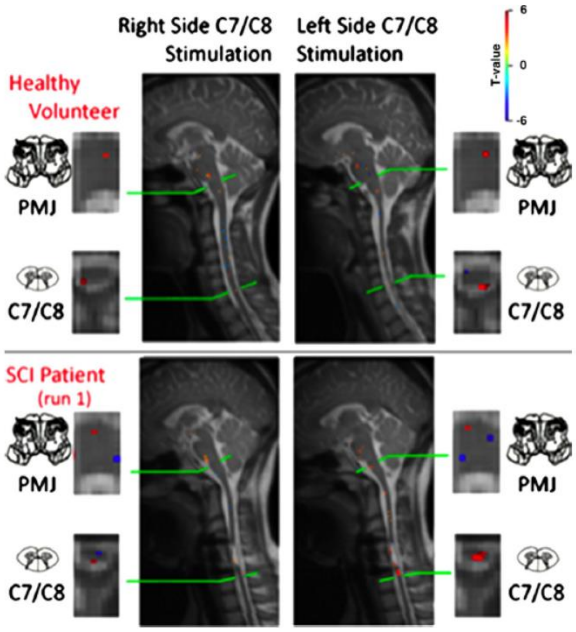

Figure 1.3: Example of results obtained in a healthy female participant (top) and an age-matched participant with an incomplete SC injury in the cervical level. Four dermatomes were stimulated, corresponding to the right and left C5 and C8 SC segments, and results are shown in selected axial and sagittal slices showing the responses to right- and left-side stimulation of the little finger side of the palm (C8 dermatome). Results obtained in the healthy participant show activity in the ipsilateral dorsal horn of the SC in the C8 segment, with a high degree of laterality corresponding to the side of the body being stimulated, as well as activity in the medulla of the brainstem. Results obtained in the participant with SCI show nearly normal responses on the left side of the SC, and slightly altered responses on the right side, as well as corresponding activity in the medulla. In spite of an apparently extensive span of tissue damage in the cervical SC, the neural activity detected is only slightly altered [24, 84].

Future clinical applications will require demonstration that the results obtained in each participant are sufficiently sensitive and reliable to be suitable for diagnostic purposes or for the monitoring of

treatment outcomes. As spinal fMRI emerges as a tool to investigate SCI, we must tread cautiously with the interpretation of results. One limitation, for example, is our lack of understanding of how the neurovascular coupling response may change after injury. Currently, the hemodynamic response function utilized in model-based fMRI data analysis is derived from healthy neural tissue. It will be important to investigate if damaged neural tissue also exhibits the same hemodynamic response function (both in temporal as well as spatial aspects) to a given stimulus, because the accuracy of the predicted response can impact on the sensitivity of the fMRI method for detecting neural activity. In addition, the technical challenges of SC fMRI, as discussed in the initial part of this chapter, may need to be reduced or eliminated before its sensitivity and reliability are acceptable for clinical applications.

Pain

The SC (together with the brainstem) is the first point in the central nervous system that processes the nociceptive signals arriving from the body, and which ultimately may produce a sensation of pain. Functional imaging of the SC aims to record this activity and can help to better understand how these signals are processed and whether an altered SC function underlies chronic or neuropathic pain states in humans. The development of non-invasive imaging techniques to record spinal activity provides critical information needed to interpret nociceptive processing in health and disease, and may help explain the patterns of brain activity observed in response to noxious stimulation in healthy controls and in patients suffering from pain. Furthermore, it has already provided important information about the modulation of spinal nociceptive processing induced by analgesic drugs or by other non-pharmacological treatments. The studies of pain that have been reported in the literature demonstrate that by using spinal fMRI, researchers are already asking challenging questions relating to the interaction of brain, brainstem and SC and of our ability to endogenously control pain. In BOLD fMRI studies of the SC [85, 86], patterns of cervical spinal activity were recorded in response to painful thermal and punctate stimulation and compared across a group of 18 subjects; a predominantly ipsilateral response was demonstrated using a mixed effects model and corrected (voxel-level) statistics [85]. However, not all reports of spinal activity in response to nociceptive stimuli have demonstrated lateralized activity in the cord. In response to painful laser stimulation of the dorsum of the left hand, activity was observed to be bilateral in the cervical SC (see Figure 1.4) [87]. Importantly, this was the first study to directly assess the false-positive detection rates in SC activity, and the number of activated voxels in response to laser stimulation was found to exceed the false-positive level.

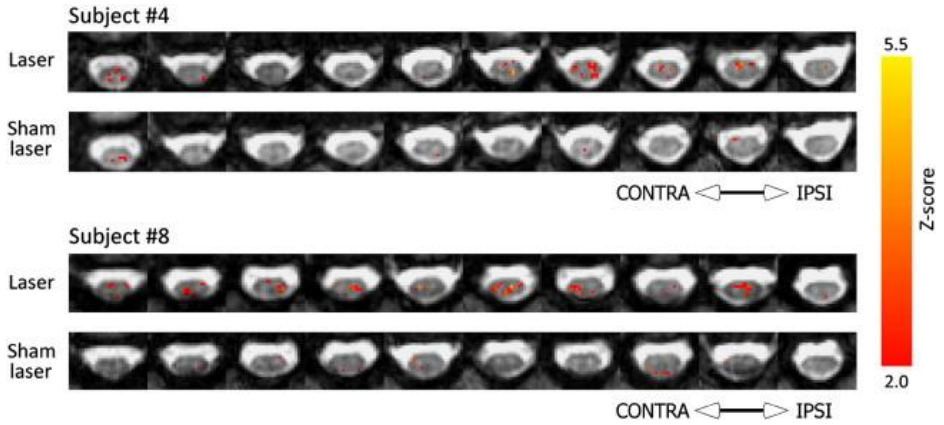

Figure 1.4: Representative maps from two subjects, showing the spatial location of voxels preferentially responding to noxious stimulation in the Stimulation run (Laser), or during corresponding time periods in the Rest run (Sham Laser). The uppermost slice is displayed to the right of each row. "Contra" and "Ipsi" refer to the sides of the cord contralateral and ipsilateral to the stimulated hand, respectively [87].

Concerning the absence of lateralized signals in response to nociceptive stimulation, it should be noted that this assessment was made on the basis of sub-dividing the cord into right and left halves, so any bilateral motor-reflex activity in response to stimulation (involving activity in both anterior horns) might have concealed increased ipsilateral dorsal horn activity. By using a combination of BOLD and SEEP contrast, Ghazni and co-workers reported changes in SC and brainstem activity in response to painful and non-painful punctate stimuli [88]. Activity in response to stimulation was observed throughout the SC, brainstem and thalamus. Surprisingly, activity in the ipsilateral cervical dorsal horn and brainstem was highest for the light-weight probe, which was interpreted as reflecting descending modulation from the brainstem. Of direct relevance to the study of descending pain modulation, two recent studies have recorded the brainstem and SC response during endogenous analgesia due to placebo effects [89, 90]. In response to thermal stimulation of the left forearm, in a region treated with an inert cream as a placebo, increased activity in periaqueductal grey matter (PAG) and rostral ventromedial medulla (RVM) was observed [89]. Conversely, BOLD evoked signal increases were reduced in a restricted region of the SC during placebo analgesia; this was interpreted as reflecting decreased nociceptive processing in the SC due to descending pain modulation [90]. The role of attention on patterns of brainstem and SC activity in response to cold stimulation (18 or 15 °C) that produced "mild" to "strong discomfort", was investigated by Stroman and his colleagues [15]. Similar to previous data examining brainstem responses following painful thermal stimulation [91], increased activity was found in the PAG during distraction conditions, perhaps relating to altered levels of discomfort. However, activity at the level of the SC was opposite to what might be expected on the basis of descending inhibition of nociceptive input, with decreased activity during the no-distraction "rating" period when compared to the distraction condition. On the other hand, a recent

study by Sprenger et al. [92] has demonstrated that during a mentally demanding distraction task (n-back task), SC activity, in response to a concurrent painful thermal stimulation is reduced when the cognitive demand is high. In addition, the reduction in pain ratings (when compared to the low cognitive demand condition) is significantly correlated with the change in BOLD signal. It is worth noting that developments in MR data acquisition, e.g., the use of slice dependent z-shimming [93] and region-selective radiofrequency (RF) excitation pulses [24, 94, 95], may improve our ability to record BOLD signal changes in the human SC. In particular, z-shimming has been already used to study spinal responses to noxious stimulation [89, 90, 92].

Multiple sclerosis

MS is the disease that has benefitted mostly from advanced quantitative SC imaging techniques, spanning from cord atrophy measurements, fMRI, DTI and also magnetization transfer ratio (MTR). MS is a disease that is being studied quite extensively with fMRI, in both the brain and SC [96]. A key challenge that has been identified for fMRI assessments of MS is that interpretation may be affected by disease-driven differences in task performance. In order to overcome this challenge, studies have been carried out with larger populations, and through the use of several motor, visual and cognitive tasks in groups representing all major clinical phenotypes of the disease. However, this solution will not be effective for individual patient assessments. One key finding from fMRI studies to date is that cortical reorganization occurs in patients affected by MS. As a result, patients adapt and their abilities do not necessarily match the axonal/neuronal loss seen with imaging, until the disease burden becomes too great and they are no longer able to adapt further. This adaptation is seen in fMRI results as recruitment of areas of the brain that are not active with the same task or stimulus in healthy control subjects [96]. Studies, performed via fMRI of the SC also showed MS-related changes in the response to proprioceptive and tactile stimulation [20, 21]. Specifically, the signal changes during stimulation were 20% higher, and the areas of activity were altered by on over-recruitment of the ipsilateral posterior cervical cord. Consistently, fMRI results demonstrate the adaptation of regions of the CNS to compensate for the deficits caused by MS lesions in order to maintain motor, sensory, and cognitive abilities.

Also, an increased activation of the cervical cord has been demonstrated in all the major MS clinical phenotypes and has been related to the severity of clinical disability and the extent of tissue damage [23, 24, 97, 98].

1.3.2.c Potential Clinical Applications

Currently, the American Spinal Injury Association (ASIA) [99] assessment scale is the standard for classifying SC injuries. This involves a battery of light touch and pin prick examinations to assess where a patient has preserved sensory perception. To determine preserved motor function, the patient's ability to move specific key muscle groups is assessed. This physical examination technique reveals information regarding SC function but does not reveal information about the condition of the SC caudal to an injury site. Further information regarding the condition of the SC caudal to the level of injury must be obtained by invasive measures or deduced from reflex actions. Electrophysiological techniques such as somatosensory-evoked potential, H-reflex, or stretch reflexes are capable of assessing the residual function after a SCI. The utility of these techniques is limited by the incomplete scope of the information obtained with each measure, such that a combination of measures is required to determine the residual function. For example, somatosensory-evoked potentials examine conduction along large areas of the body, and the results can be affected by peripheral damage, nerve root damage, or SC damage without revealing where along the pathway the damage has occurred. Similarly, an increase in reflexes denotes an upper motor neuron disorder but will not reveal the degree of damage, or whether the damage is complete or incomplete. Although these methods are useful for many research applications, they require specific equipment and are time-consuming. Therefore, these methods are not in routine clinical use. Thus, the ability of spinal fMRI to detect neuronal activity below the injury site in SC–injured patients is of considerable value for those assessing an injury, planning a treatment strategy, or monitoring recovery of function during and after treatment. Although spinal fMRI is not yet ready for routine clinical use in examining SC injuries, it is certainly fit for use in assessing recovery of function strategies. However, spinal fMRI will become more useful as intervention strategies develop, because it can detect differences in neuronal activity pre- and post-treatment. Spinal fMRI could become an important tool for assessing the efficacy of interventions. Currently, the ASIA assessment scale is used to follow progress in research interventions, and this, as mentioned, is unable to detect neuronal changes. Similarly, spinal fMRI could serve in assessing pharmacologic treatment effects on SC and nerve root function. Likewise, spasticity drug trials also could greatly benefit from the use of spinal fMRI, again because presently there are few non-invasive measures available to objectively see changes in neuronal activity. Spinal fMRI is able to show where functional activity occurs in response to a stimulus, regardless of a patient's ability to feel the stimulus—a feature that the ASIA assessment scale lacks. Therefore, in the case of SCI, the neuronal activity in the SC both above and below the injury site can be monitored after initial injury for prognosis and recovery-of-function strategy decisions (see the paragraph about SC injuries), as well as throughout rehabilitation and in response to pharmacologic treatment. A

protocol can be developed such that a standard battery of tests may be conducted to assess ascending, descending, and reflex activity. fMRI has been used to investigate nociceptive processing and central sensitization in the brain to better understand pain [100, 101]. Spinal fMRI can be used to study the structural and functional correlates of pain and advance our understanding of the mechanisms of nociceptive processing, central sensitization, and chronic neuropathic pain. In addition, the neural mechanisms underlying attentional modulation of pain are not known, but data suggest the involvement of multiple levels of the central nervous system, including the dorsal horn of the SC [102]. Dorsal horn involvement has yet to be shown in functional neuroimaging studies. Future research using functional neuroimaging in this area is warranted and is likely to have a significant impact on therapeutic interventions. Combined imaging of the SC, brain stem, and brain will provide information regarding the neuronal activity of the entire central neural axis, advancing scientific knowledge on how clinical chronic pain states are generated and maintained. The ability to image from the SC to the brain, as well as descending modulatory pathways back to the SC, will allow for the investigation of plasticity changes associated with chronic pain conditions and provide the opportunity to evaluate changes in both the disease state and the response to peripherally and centrally acting treatments. With spinal fMRI, objective means of assessing the neural function in patients with chronic pain will thus be available. Spinal fMRI could be useful in identifying the pathogenesis of many chronic pain conditions, whereas presently this is not understood. Spinal fMRI could expose the neuronal abnormalities underlying several pain conditions such as irritable bowel syndrome, chronic lower back pain, or fibromyalgia. It is possible that central sensitization is involved in many chronic pain conditions, and great potential exists for spinal fMRI to reveal the underlying initiation or maintenance of this state.

Although anatomical spinal MRI is used to detect a number of specifically SC– related conditions such as a Chiari malformation, a defect causing Brown-Sequard syndrome, or hydromyelia, a functional image of these conditions would be useful for monitoring the effects of lesion or structural abnormality on physiologic response and subsequent alterations in neuronal function. It might also help differentiate a neurodegenerative disorder such as tabes dorsalis, which involves a breakdown of sensory fibers but has symptoms that include weakness, loss of proprioception, and decreased coordination and reflexes, in addition to the sensory disturbances and pain. The ability of spinal fMRI to capture the activity of dorsal column neurons will aid in the diagnosis, prognosis, and monitoring of disease states such as this. As with many conditions, symptoms may not occur immediately after the initial insult but may appear gradually over time, resulting in a situation in which it may not be immediately clear where to begin investigation. When it is difficult to identify the cause of symptoms, spinal fMRI could indicate areas of abnormal neuronal function or identify the point at which the

breakdown is occurring. For example, spinal fMRI could determine whether it is an upper motor neuron disorder, a lower motor neuron disorder, or both, as in amyotrophic lateral sclerosis. Whether neurons are firing normally but the breakdown is at the neuromuscular junction or with the muscle fibers themselves, as in muscular dystrophies, could similarly be determined. MRI is used to locate lesion sites in multiple sclerosis, but use of spinal fMRI would aid in tracking disease progression and prognosis. The functional characterization of disease could be carried out with spinal fMRI. In cases of transverse myelitis, inflammation of a SC segment occurs, which can cause myelin damage, thereby impairing nerve conduction and interfering with neuronal communication. The benefit of functional imaging for these types of conditions is clear. Pre-surgical mapping localizes function in cortical tissue near areas intended for surgery or resection. Functional and anatomically distinct regions of cortex vary between different people. The use of fMRI can identify areas associated with specific functions, so that these areas may be targeted or avoided during resection. This method is a less invasive alternative to electrophysiological cortical mapping commonly used for obtaining this type of information. Functional imaging of the SC could be useful for diagnosis and prognosis of nerve decompression surgery. For example, in patients with cervical or lumbar radiculopathy, it is often unclear which nerve root is irritated or injured. Noxious stimulation of the affected region with simultaneous spinal fMRI would help localize the specific region affected. In another example, for diabetic neuropathy, the relief of pressure on a trunk is achieved by the excision of the constricting band or the widening of the bony canal to alleviate pain symptoms. Based on patient reports, it is not always clear which spinal nerves are implicated, as often a number of nerves are involved in creating the symptomatology. With spinal fMRI, it could be possible to better identify the specific nerves involved in particular symptoms, therefore improving surgery planning and decreasing surgical risk. The ability of spinal fMRI to detect changes in neuronal function in the absence of overtly physical manifestations could be valuable for patients undergoing recovery of function, rehabilitation, or pharmacologic treatment. Aside from physiologic information obtained by the clinician, patients could benefit psychologically. In the initial stages of a treatment strategy, it may be discouraging to patients when signs of improvement are not yet detectable. In the absence of measurable physical improvements, the “proof” of improvement in neuronal activity (increases or decreases in conduction, condition-specific) could provide the encouragement and motivation to continue with rehabilitation strategies. Alternately, spinal fMRI could reveal a strategy to be ineffective and accelerate the search for alternate strategies.

1.3.2.d Challenges in clinical application

The technical limitations of spinal fMRI must be addressed for the technique to be useful clinically. The need for greater signal-to-noise ratio in SC functional imaging is an issue. Future spinal fMRI studies will likely benefit from a reduction of the noise of cardiac origin. Indeed, modelling the time course of non-neuronal–related activity should reduce or eliminate noise caused by cardiac-driven motion. Increased use of the 3 Tesla magnet will help increase signal and sensitivity to magnetic susceptibility. More work is needed to resolve this issue. The identification and elimination of errors (falsely activated pixels) is also required. Addressing these issues will improve the reliability and sensitivity of spinal fMRI, resulting in an imaging method suitable for use on an individual basis.

The scanning parameters ideal for contrast in spinal fMRI result in slow imaging acquisition, whereas a faster imaging technique would be desirable. Also, at present, fMRI is expensive and requires highly trained personnel for data acquisition and analysis. Progress has been made in the advancement of spinal fMRI toward clinical use. Obtaining functional images in sagittal orientation allows for activity maps to be displayed in axial, coronal, and sagittal orientation, with improved spatial resolution in the superior/inferior direction [103]. In addition to demonstrating details of sub-segmental organization in the SC, neuroanatomic details such as spinous processes and the position of nerve roots, as well as cervical and lumbar enlargements, were identifiable. In addition, results can be normalized and consistent right/left and anterior/posterior dimensions constructed, which facilitates comparison within and across SCs. With further development of this method, optimal normalization dimensions can be produced and a SC atlas could be assembled, which may facilitate a standard method of documenting the results. Recently, there has been some progress about the construction of a standard Atlas for the SC based on high-resolution MRI at cervical and thoracic levels [104]. Ideally, a software program would be available for technicians and clinicians to use for simple and quick data analysis. Packaging a standardized spinal fMRI assessment protocol with an efficient and comprehensible analysis program could expedite spinal fMRI into clinical use. Although advances have been made in this area, further work is required before the method is optimal for clinical purposes. In addition to the technical advances required before spinal fMRI is ready for clinical use, other issues need to be considered. Careful study design is required for spinal fMRI to be effective. The task paradigm should ideally isolate the specific behaviour under investigation to the exclusion of other behaviours. This can be especially difficult in the situation of impaired functioning or loss of function. As pointed out by Detre [105], it is difficult to acquire a functional image of an impairment, both because of the difficulty in designing a well-characterized paradigm for examining the particular

aspect of the deficit, and because of the difficulty in imaging neural correlates of a behaviour the patient cannot properly perform. This is not specific to spinal fMRI but holds true nonetheless. It is probable that the utility of spinal fMRI will provide supplementary information to that obtained with other tools, rather than replace them. Although spinal fMRI may prove the optimal tool in particular cases, it is more likely that the pairing of spinal fMRI with other tools will be used to provide a more complete picture. For example, combining information from electrophysiology with spinal fMRI could resolve issues with greater temporal and spatial resolution, thus overcoming the limitations of each technique while building on the strengths of both. Diffusion tensor imaging provides structural information regarding the orientation of white matter tracts in a non-invasive manner. Anatomic and functional connectivity may be mapped to provide important information regarding neural circuitry, essential information for surgical purposes. Spinal neuronal activity is altered in the absence of descending modulation from supraspinal centers, and thus the effects of resection or stimulation may be detectable at the SC level. Magnetic resonance spectroscopy allows for the investigation of tissue metabolism and biochemistry; combined with fMRI, it can impart insight into SC normal and disease states.

To summarize, structural and functional MRI techniques have clear potential to provide clinicians with a powerful tool for directing rehabilitation and for predicting outcome in patients with neurodegenerative disease or injury. However, this is a novel application, in which many of the existing studies report results from small sample sizes. Though these results are promising, more research must be conducted before these techniques can be used for clinical purposes.

1.4 Future directions for non-invasive SC techniques

The technical challenges common to SC imaging methods have been clearly identified as being: 1) magnetic susceptibility differences, 2) physiological motion, and 3) small cross-sectional dimensions of the SC. These properties of the imaging environment in the human SC will not change, and so future advances require development of better methods to overcome these challenges. Improvements in imaging methods are needed to simultaneously increase the signal-to-noise ratio and the spatial resolution. For imaging methods such as PET and CT this may be obtained with improvements in detector technology, and similarly for MRI this goal may be reached owing to advances in radio-frequency coil design. Improvements in MRI methods are also needed to reduce sensitivity to magnetic field inhomogeneity. This may be achieved with improvements in localized magnetic field shimming methods, and changes in data sampling schemes to trade off shorter data sampling periods

with more sampling periods. Trade-offs in image sampling are possible if pulse-sequence designs are optimized for the SC environment, such as has been done for DTI [106-109]. Such advances in methods were realized with the advent of brain fMRI, and research groups, software developers, and MRI system manufacturers responded to these demands. The future development of SC imaging methods similarly requires researchers to engage with equipment manufacturers and software developers to communicate needs and encourage a two-way sharing of methods and technology. Researchers developing the methods need MRI and PET system manufacturers to make the methods more widely accessible, and in particular, accessible to clinical environments.

Summary and conclusions

Significant advances in SC imaging methods have been realized in the past decade. The great potential of such methods to support research into basic neuroscience and novel treatment strategies -as well as to improve clinical diagnoses, and the monitoring of treatment and rehabilitation outcomes- has been well-demonstrated. The realization of methods to provide the desired research and clinical tools still requires technological development. This chapter briefly reviews the recent developments in SC non-invasive techniques, with particular regard on fMRI. In particular, we discuss the feasibility of the application of spinal fMRI to the clinic and pre-clinic field as well as the limitations that must be overcome in order to achieve the full potential of this technique.

The relatively small number of publications in this area likely reflects the difficulty in acquiring functional images of the SC. However, the available literature has shown spinal fMRI to be a reliable tool for assessing SC neuronal function, and it is currently used for research purposes. Studies thus far have suggested that the clinical use of spinal fMRI is conceivable. However, further work is required before the method is optimal for clinical purposes. Issues related to spatial resolution, registration of subsequently acquired volumes, partial volume effects with the CSF, as well as the lack of a standard common template and the effects of physiological noise are still limiting the adoption of spinal fMRI into the clinical setting. In addition the application of fMRI to the SC requires specific modification to the conventional brain fMRI methodology, but the theory of conventional brain fMRI applies.

This chapter is a necessary starting point for this thesis, which will hopefully help the reader in understanding the importance of studying:

1) The bio-physical characterization of the spinal BOLD functional response.
2) The structure of the SC vascular and neuronal networks, which together contribute to the BOLD signal in fMRI. The information on gathered on these networks will be used to develop an optimized spinal BOLD model. Indeed the currently used fMRI model is a mathematical abstraction of the vascular/metabolic response in the rat brain cortex, which may not be appropriate for the SC.

This study will improve the methodological strategies for the non-invasive investigation of the SC function in physiological and pathological conditions, thereby accelerating the introduction of the SC fMRI in the clinical setting.

CHAPTER 2

CENTRAL NERVOUS STYSTEM: SC PHYSIOLOGY

The SC is the long bundle of nerves fibers and neurons that runs down the middle of the back. It is enclosed in the vertebral column (spine) and is considered part of the CNS. The SC is a complicated processor of sensory and motor information. It regulates sensory inflow and contributes to the control of movements. In short, the SC looks and often functions like a cable bringing sensory information from the body to the brain and sending movement commands from the brain to the body. In addition, the SC also processes sensory and motor signals.

Primary afferent fibers typically make their first synaptic connection in the dorsal portion of the SC, the "dorsal horn"; these connections are subject to top–down and local neuronal influences, which will modulate the transmission of nociceptive signals to the brain, and thus have a great impact on pain sensation. On the other hand, the last synapse before motor neurons leave the SC is located in its ventral part. These synapses represent a site of neural activity not available to conventional fMRI studies and, thus, SC fMRI has the potential to be useful in basic neurosciences research as well as in clinical practice.

Indeed, a noninvasive tool capable of monitoring the function, and thus complementing the available anatomical information, is a crucial need in these fields. However, the main difficulties facing researchers attempting to image the SC function are its small cross-sectional area, its proximity to structures (vertebrae, intervertebral discs) giving rise to large variations in magnetic susceptibility. In addition, the influence of physiological effects that displace the cord or generate noisy signal intensity changes near its superficial layers, and passive displacements of the cord in response to limb movement. However the vascular anatomy of SC is optimally organized for the generation of strong and spatially specific BOLD effect. This can help in overcoming the numerous other difficulties that involves the SC fMRI. Moreover, it must be pointed out that some cases of activation following the shape of small radial veins have been reported [110]. Thus anatomy has implications for the developments and applicability of Spinal fMRI. In this Chapter, we shall consider important general definitions about the SC physiology that constitute the prerequisites for understanding this thesis.

2.1 Neuronal System

The most general functional definition divides neuronal systems into *sensory systems*, like vision or hearing that acquires and process information from the environment, and *motor systems* that allow the organism to respond to such information by generating movements [111-113]. There is however, large number of cells and circuits that lie between these relatively well defined input and output systems. They are collectively referred to *associational systems*, and they carry out the most complex and least well characterized brain functions. In addition to these broad functional distinctions, neuroscientists and neurologists have conventionally divided the vertebrate nervous system anatomically into central and peripheral components (Figure 2.1). The CNS comprises the *brain* (*cerebrum, cerebellum and brainstem*) and the *SC*. It is composed of neurons and other specialized cells called glia, that aid in the function of the neurons [111]. The *peripheral nervous system* includes sensory neurons, which link sensory receptors on the body surface, as well as in specialized receptor structures like the ear, with processing circuits in the central nervous system.

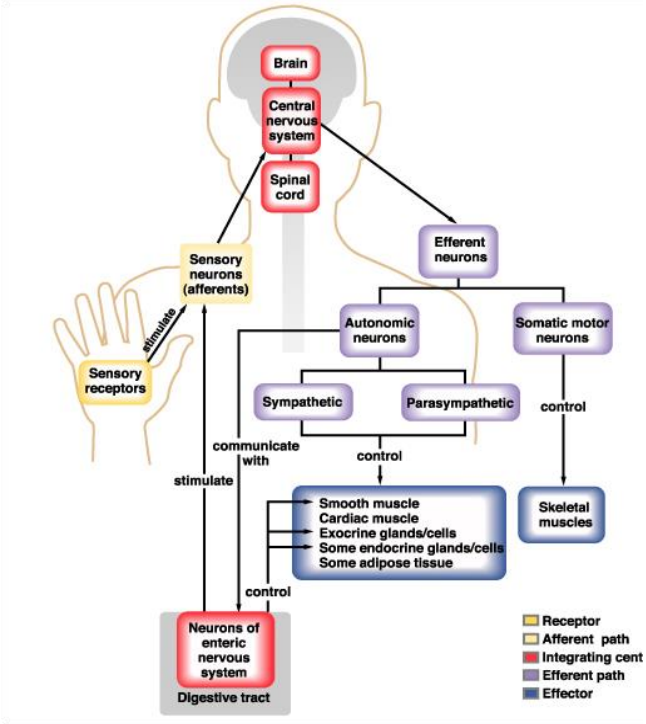

Figure 2.1: diagram of the major components of the central and peripheral nervous systems and their functional relationships. Stimuli from the environment convey information to processing circuits within the brain and the SC, which in turn interpret their significance and send signals to peripheral effectors that move the body and adjust the workings of its internal organ [112].

The motor portion of the peripheral nervous system consists of two components. Motor axons that connect the brain and the SC to skeletal muscles make up the *somatic motor division* of the peripheral nervous system. The visceral or autonomic motor division consists of cells and axons that innerve smooth muscles, cardiac muscles, and glands. In the peripheral nervous system, nerve cells are located in ganglia, which are simply local accumulations of nerve cell bodies (and supporting cells). Peripheral axons are gathered into *nerves*, which are bundles of axons; many of them are enveloped by the glial cells of the peripheral nervous system, the Schwann cells [111, 112, 114].

Grey matter refers to any accumulation of cell bodies and neuropil in the brain and in SC (e.g., nuclei or cortices), whereas the *white matter* refers to axons tracts. In the sensory portion of the peripheral nervous system (Figure 2.2(a)) *sensory ganglia* lie adjacent to either the SC (where they are referred to as a dorsal root ganglia (Figure 2.2 (b)) or the brainstem (where they are called cranial nerve ganglia). The nerve cells in sensory ganglia send axons to the periphery that end in (or on) specialized receptors that transduce information about a wide variety of stimuli [113].

The central processes of these sensory ganglion cells enter the SC or brainstem. In the somatic motor portion of the peripheral nervous system, axons from motor neurons in the SC give rise to peripheral motor axons that innervate the striated muscles to control skeletal movements and, consequently, most voluntary behaviours. The organization of the automatic division of the peripheral nervous system is a bit more complicated. Preganglionic visceral motor neurons in the brainstem and SC form synapses with peripheral motor neurons that lie in the autonomic ganglia. The motor neurons in autonomic ganglia innervate smooth muscles, glands, and cardiac muscle, thus controlling most involuntary (visceral) behaviour. In the sympathetic division of the autonomic motor system, the ganglia are along or in front of vertebral column and send their axons to a variety of peripheral targets. In the parasympathetic division the ganglia are found within the organ, they innervate. Another component of the visceral motor system, called the enteric system, is made up of small ganglia scattered throughout the wall of the gut [113].

After this overview of all the neuronal system [112] we focus our attention on the physiology of the SC, its constituents and the nervous pathway because it is important to understand the main difficulties to image the SC function and underline the importance of a spinal fMRI in the preclinical and clinical field.

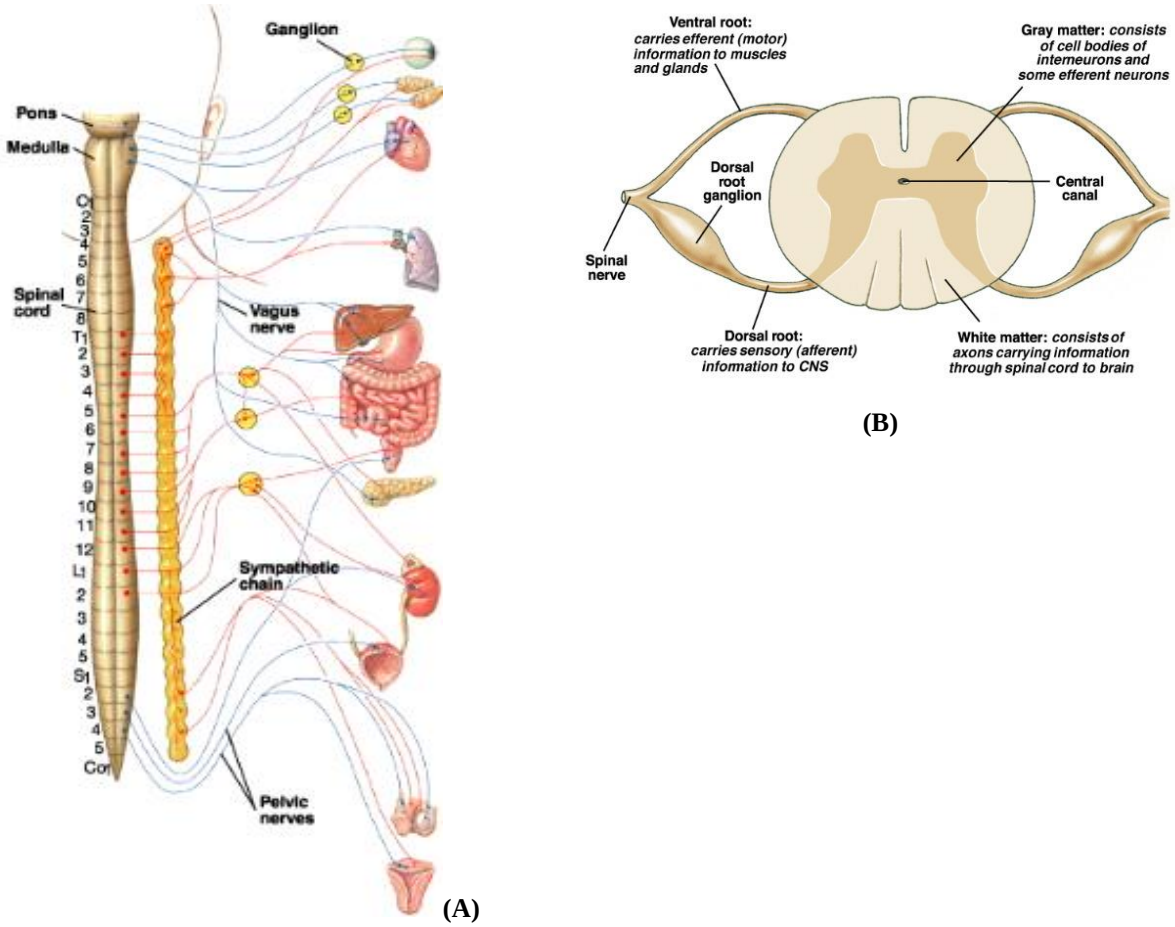

Figure 2.2 a) a pictorial view of the peripheral system **b)** section of SC segments, showing the grey and white matter and the dorsal root ganglion [113].

2.1.1 Central Nervous System

The central Nervous system is composed of seven parts (

Figure **2.3**) [111]:

The SC: the most caudal part of the central nervous system, receives and processes sensory information from the skin, joints, and muscles of the limbs and trunk and controls movement of the limbs and the trunk. It is subdivided into cervical, thoracic, lumbar, and sacral regions. The SC continues rostrally as the brain stem, which consists of the medulla, pons, and midbrain (see below). The brain stem receives sensory information from the skin and muscles of the head and provides the motor control for the muscles of the head. It also conveys information from the SC to the brain and from the brain to the SC, and regulates levels of arousal and awareness, through the reticular formation. The brain stem contains several collections of cell bodies, the cranial nerve nuclei. Some of these nuclei receive information from the skin and muscles of the head; others control motor output to muscles of the face, neck, and eyes. Still others are specialized for information from the special senses: hearing, balance, and taste.

The medulla oblongata, which lies directly above the SC, includes several centers responsible for vital autonomic functions, such as digestion, breathing, and the control of heart rate.

The pons, which lies above the medulla, conveys information about movement from the cerebral hemisphere to the cerebellum.

The cerebellum lies behind the pons and is connected to the brain stem by several major fiber tracts called peduncles. The cerebellum modulates the force and range of movement and is involved in the learning of motor skills.

The midbrain, which lies rostral to the pons, controls many sensory and motor functions, including eye movement and the coordination of visual and auditory reflexes.

The diencephalon lies rostral to the midbrain and contains two structures. One, the thalamus, processes most of the information reaching the cerebral cortex from the rest of the central nervous system. The other, the hypothalamus, regulates autonomic, endocrine, and visceral function.

The cerebral hemispheres consist of a heavily wrinkled outer layer- the cerebral cortex- and three deep –lying structures: the basal ganglia, the hippocampus, and the amygdaloid nuclei. The basal ganglia participate in regulating motor performance; the hippocampus is involved with aspects pf memory storage; and the amygdaloid nuclei coordinate the autonomic and endocrine responses of

emotional states. The cerebral cortex is divided into four lobes: frontal, parietal temporal, and occipital.

The brain is also commonly divided into three broader regions: the hindbrain (the medulla, pons, and cerebellum), midbrain, and forebrain (diencephalon and cerebral hemispheres). The hindbrain (excluding the cerebellum) and midbrain comprise the brain stem. One reason this conclusion eluded investigators for so many years lies in another organizational principle of the nervous system known as *parallel distributed processing*. As we shall see below, many sensory, motor, and cognitive functions are served by more than one neural pathway. When one functional region or pathway is damaged, others may be able to compensate partially for the loss, thereby obscuring the behavioural evidence for localization. Nevertheless, the neural pathways for certain higher functions have been precisely mapped in the brain.

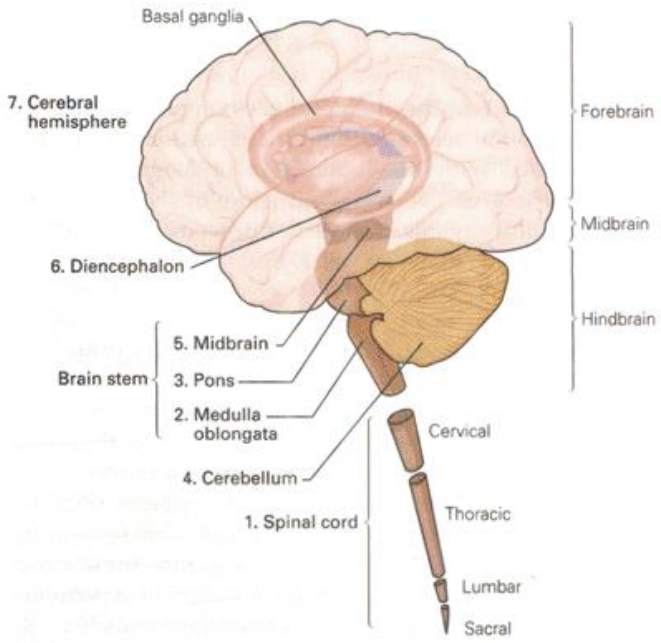

Figure 2.3: Pictorial view of the seven parts that compose the central Nervous system [111].

2.1.2 Cell types

As we have said before, the nervous system is composed of two general categories of cells: glial cells and nerve cells [111, 112]. Glial cells, or *neuraglia*, support the neurons by controlling their access to blood borne substances, by isolating neurons from each other, and by supporting neurons structurally. Nerve cells, or *neurons*, are cells that can encode and process information electrically and bio-chemically and can transmit it long distances in very short periods of time. Although the cells of the human nervous system are in many ways similar to those of other organs, they are unusual in their extraordinary numbers (The brain, SC and nerves contains 100 billion neurons and several times as many supporting cells). Most importantly, the nervous system has a greater range of distinct cell types- whether categorized by morphology, molecular identity, or physiological activity- than any other organ system. This rich structural and functional diversity, and the interconnection of nerve cells via synapses to form intricate ensembles, or circuits, is the foundation on which sensor processes, perception, and behaviour are ultimately built.

2.1.2.a Neuroglia cell

The nervous system contains many times more glial cells than neurons. Named from the Greek words for nerve glue, neuroglia or glial cells or simply glia, do not produce or transmit electrical signals, as do neurons. However, their presence is very important to the functioning of neurons.

Glia are thought to have at least seven other vital roles, that we report in the following [111].

● Glia cells support neurons. They also separate and sometimes insulate neuronal groups and synaptic connections from each other.
● Two types of glial cells: oligodendrocytes and Schwann cells produce the myelin used to insulate nerve cell axons, the cell outgrowths that conduct electrical signals.
● Some glial cells are scavengers, removing debris after injury or neuronal death.
● Glia cells perform important housekeeping chores that promote efficient signalling between neurons. For example, some glia also take up chemical transmitters released by neurons during synaptic transmission.
● During the brain's development certain classes of glial cells (“radial glia”) guide migrating neurons and direct the outgrowth of axons.
● In some cases, as at the nerve-muscle synapse of vertebrates, glial cells actively regulate the properties of the presynaptic terminal.

● Some glial cells (astrocytes) help form an impermeable lining in the brain's capillaries and venules— the blood-brain/spinal barrier—that prevents toxic substances in the blood from entering the brain or the SC.

● Other glial cells apparently release growth factors and otherwise help nourish nerve cells. Although this role has been difficult to demonstrate conclusively.

Microglia and Macroglia

In the vertebrate nervous system, glial cells are divided into two major classes: *microglia* and *macroglia* (e.g oligodendrocytes, Schwann cells, and astrocytes) (Figure 2.4)[111, 112].

Microglia are phagocytes that are mobilized after injury, infection, or disease. They arise from macrophages outside the nervous system and are physiologically and embryologically unrelated to the other cell types of the nervous system. Not much is known about what microglia do in the resting state, but they become activated and recruited during infection, injury, and seizure. The activated cell has a process that is stouter and more branched than that of inactivated cells, and it expresses a range of antigens, which suggests that it may serve as the major antigen presenting cell in the central nervous system. Microglia are thought to become activated in a number of diseases including multiple sclerosis and AIDS-related dementia, as well as various chronic neurodegenerative diseases such as Parkinson's disease and Alzheimer's disease [111].

Three types of *macroglial* cells predominate in the vertebrate nervous system: oligodendrocytes, Schwann cells, and astrocytes (Figure 2.4).

Oligodendrocytes and *Schwann* cells are small cells with relatively few processes. Both types carry out the important job of insulating axons, forming a myelin sheath by tightly winding their membranous processes around the axon in a spiral. Oligodendrocytes, which are found in the central nervous system, envelop an average of 15 axonal internodes each. By contrast, Schwann cells, which occur in the peripheral nervous system, each envelop just one internode of only one axon. In the case of the SC and brainstem there is a distinct junction between the Peripheral Nervous System- and CNS-type myelin called transitional zone and characterized by a complex glial structure.

The types of myelin produced by oligodendrocytes and Schwann cells differ to some degree in chemical makeup.

Astrocytes, the most numerous of glial cells, owe their name to their irregular, roughly star shaped cell bodies. They tend to have rather long processes, some of which terminate in end-feet. Some astrocytes form end-feet on the surfaces of nerve cells in the brain and SC and may play a role in bringing nutrients to these cells. Other astrocytes place end-feet on the brain's and SC' s blood vessels and cause the vessel's endothelial (lining) cells to form tight junctions, thus creating the protective

blood-brain/ SC barrier. Astrocytes also help to maintain the right potassium ion concentration in the extracellular space between neurons. In addition, astrocytes take up neurotransmitters from synaptic zones after release and thereby help regulate synaptic activities by removing transmitters. But the role of astrocytes is largely a supporting one.

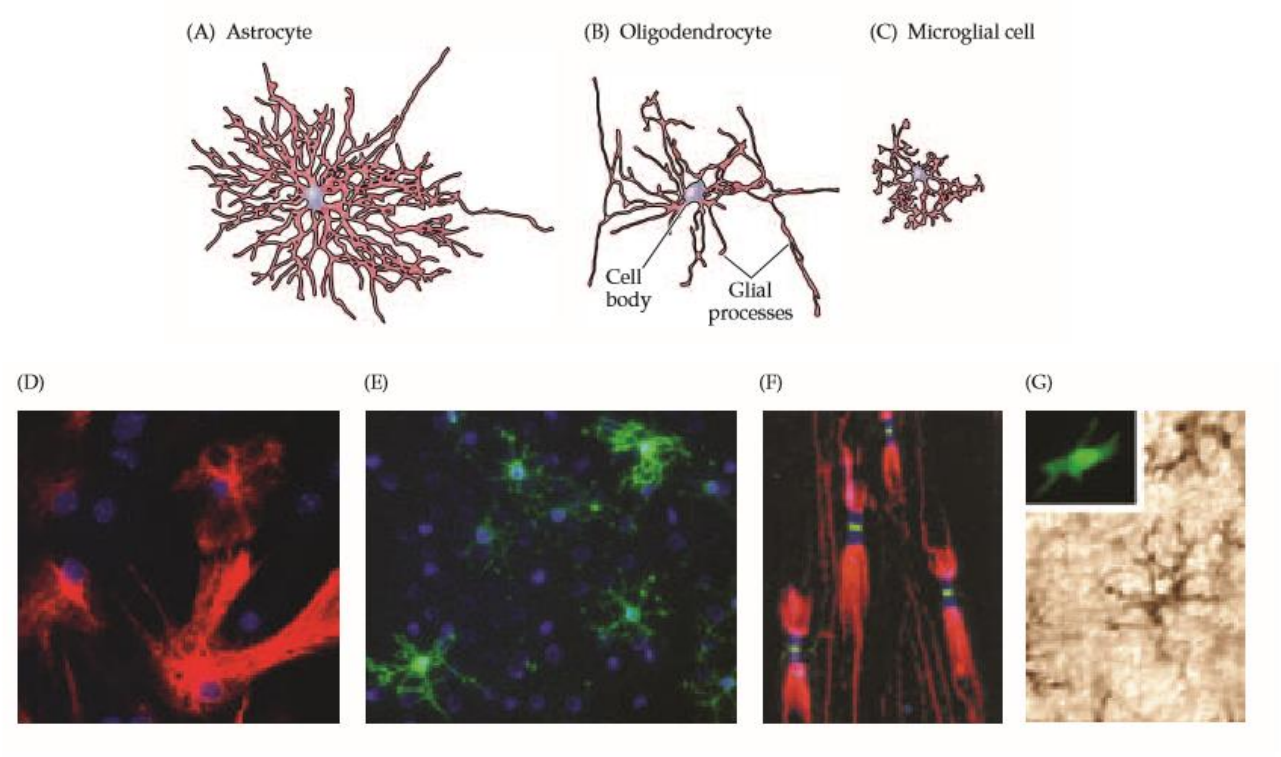

Figure 2.4: Varieties of neuroglial cells. Tracings of an astrocyte (A), an oligodendrocyte (B), and a microglial cell (C) visualized using the Golgi method. The images are at approximately the same scale. (D) Astrocytes in tissue culture, labelled (red) with an antibody against an astrocyte-specific protein. (E) Oligodendroglial cells in tissue culture labelled with an antibody against an oligodendroglial-specific protein. (F) Peripheral axon are unsheathed by myelin (labelled red) except at a distinct region called the node of Ranvier. The green label indicates ion channels concentrated in the node; the blue label indicates a molecularly distinct region called the paranode. (G) Microglial cells from the SC, labelled with a cell type-specific antibody. Inset: Higher-magnification image of a single microglial cell labelled with a macrophage-selective marker [112].

2.1.2.b Neurons

Neurons exist in a variety of shapes and forms, but they all have some common features. Each neuron has a *cell body or soma* where the nucleus and other important organelles are located. Emanating from the cell body are any number of small, branch-like extensions called *dendrites* and a single, very thin process called *axon*. That is specialized to transmit signals faithfully along its entire length

(Figure 2.5). The *dendrites* serve to increase the surface area of the soma, but do not contain large organelles [111, 112].

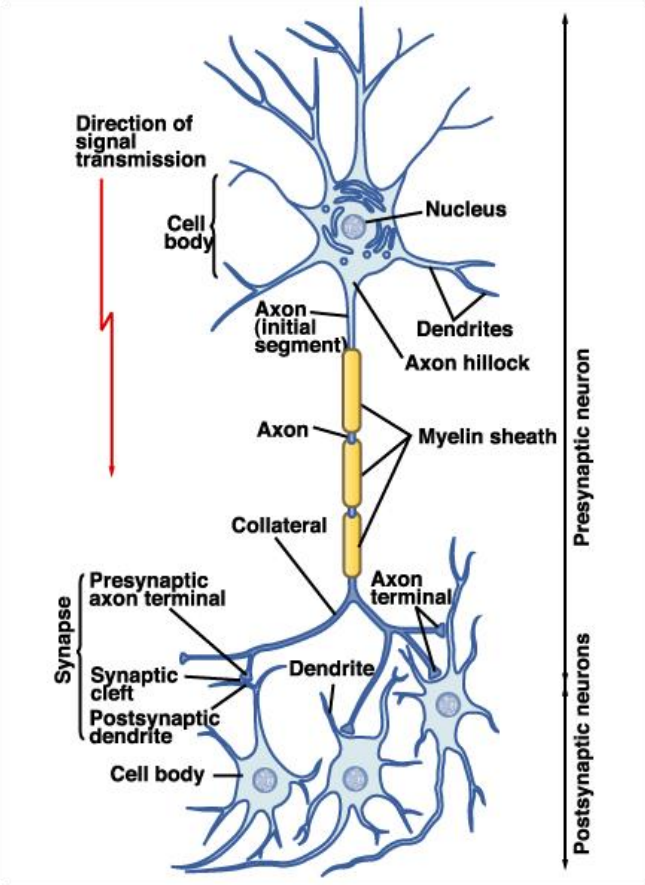

Figure 2.5: the structure of a typical neuron showing: input region with soma, organelles, and dendrites conducting region with axon hillock and axon output region with axon terminals [111].

The soma and dendrites contain receptors for signal molecules that are secreted from other cells [111, 112]. Dendrites of some neurons extend for many millimetres away from the cell body, allowing the cell to receive an enormous number of signals. The dendrites and soma represents the *input region* of the neuron. The *axon* extends for anywhere from a few micrometers to a couple of meters where it branches considerably. At the ends of these branches, the axon becomes swollen. These swellings contain small sacks, made of bilipid membrane, that contain high concentrations of *neurotrasmitter*. Another feature common to most neurons is the direction of the flow of information. The dendrites and cell body receive and put together the signals arriving from other neurons. The axon is used to transmit signals from the cell body to the terminals, without any loss of power, and to signal the terminals to secrete molecules that will act as messengers and signal other cells to change their activity in some way. The distinguishing characteristic of nerve cells is their specialization for intracellular

communication. This attribute is apparent in their overall morphology, in the specialization of their membranes for electrical signalling, and in the structural and functional intricacies of the synaptic contacts between them. A particularly salient morphological feature of most nerve cells is the elaborate arborisation of the dendrites. In fact the number of inputs that particular neuron receives depends on the complexity of its dendritic arbor: nerve cells that lack dendrites are innervated by just one or few other nerve cells, whereas those with increasingly elaborate dendrites are innervated by a commensurately larger number of other neurons [111, 112]. The dendrites (together with the cell body) provide the major site for synaptic terminals made by the axonal endings of other nerve cells. The *synaptic* contact itself is a special elaboration of the secretory apparatus found in most epithelial cells. Typically, the *presynaptic* terminal is immediately adjacent to a *postsynaptic* specialization of the contacted cell (Figure 2.6).

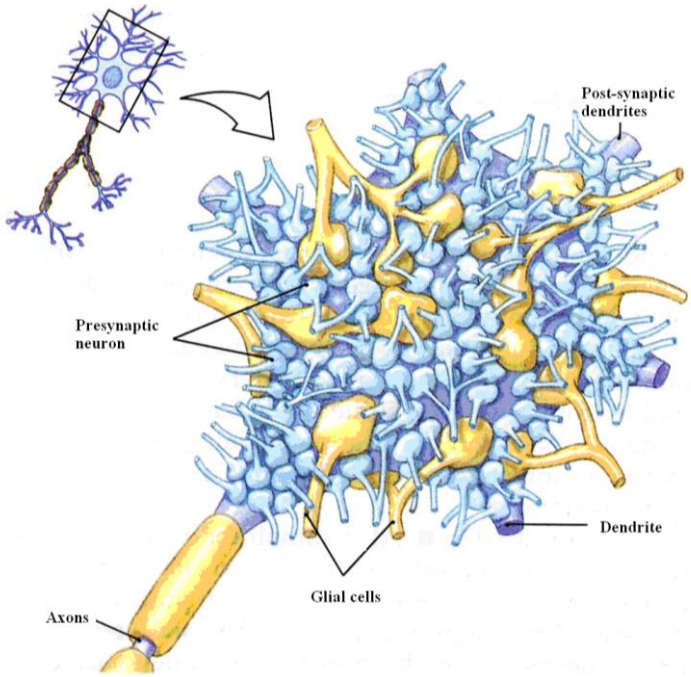

Figure 2.6: view of the neuronal soma. It is represented post-synaptic dendrites and presynaptic neuron [115].

The pre-and postsynaptic components communicate via secretion of molecules from the pre-synaptic terminal that binds to receptors in the postsynaptic specialization (Figure 2.7). These molecules must traverse the extracellular space between the pre- and postsynaptic elements; this interruption is called the *synaptic cleft*. The number of synaptic inputs received by each nerve cell in the human nervous system varies from 1 to 100,000 [112]. This range of inputs reflects a fundamental purpose of nerve cells, namely to integrate information from other neurons [111, 112]. The number of inputs onto any

particular cell is therefore an especially important determinant of neuronal function. The information from the inputs that impinge on the neuronal dendrites is integrated and "read out" at the origin of the axon, the portion of the nerve cell specialized for signal conduction to the next site of synaptic interaction.

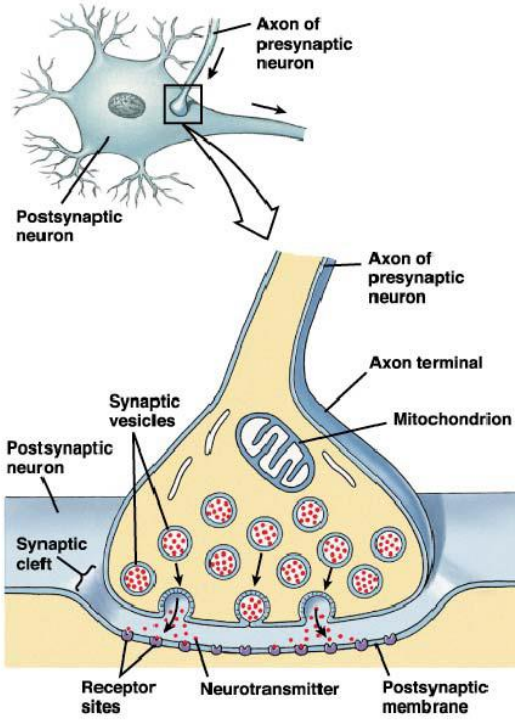

Figure 2.7: pictorial view of the synapse and synaptic events [115].

The axon is a unique extension from the neuronal cell body that may travel a few hundred micrometers or much farther, depending on the type of neurons and on the size of the species. Many nerve cells in the human brain have axons no more than a few millimetres long, and a few have no axons at all [111, 112]. These short axons are a defining feature of local circuit neurons or inter-neurons throughout the brain. Many axons, however, extended to more distant targets. For example, the axons that run from the human SC to the foot are about a metre long. The axonal mechanism (Figure 2.8) that carries signals over such distances is called the *action potential*, a self-regenerating wave of electrical activity that propagates from its point of initiation at the cell body (called the axon hillock) to the terminus of the axon. At the axon ending, another set of synaptic contacts is made on yet other cells. The target cells of neurons include other nerve cells in the brain, SC, and autonomic ganglia, and the cells of muscles and glands throughout the body. The process by which information encode by action potentials is passed on at synaptic contacts to the next cell in the pathway is called synaptic transmission. Presynaptic terminals (also called synaptic endings, axon terminals or terminal

boutons) and their postsynaptic specializations are typically chemical synapses, the most abundant type of synapse in the nervous system. The secretory organelles in the presynaptic terminal of chemical synapses are called synaptic vesicles, which are filled with neurotransmitter molecules. The neurotransmitters released from synaptic vesicles modify the electrical properties of the target cell by binding to neurotransmitter receptors, which are localized primarily at the postsynaptic specialization. Neurotransmitters, receptors, and the related transduction molecules are the machinery that allows nerve cells to communicate with one another, and with effectors cells in muscles and glands.

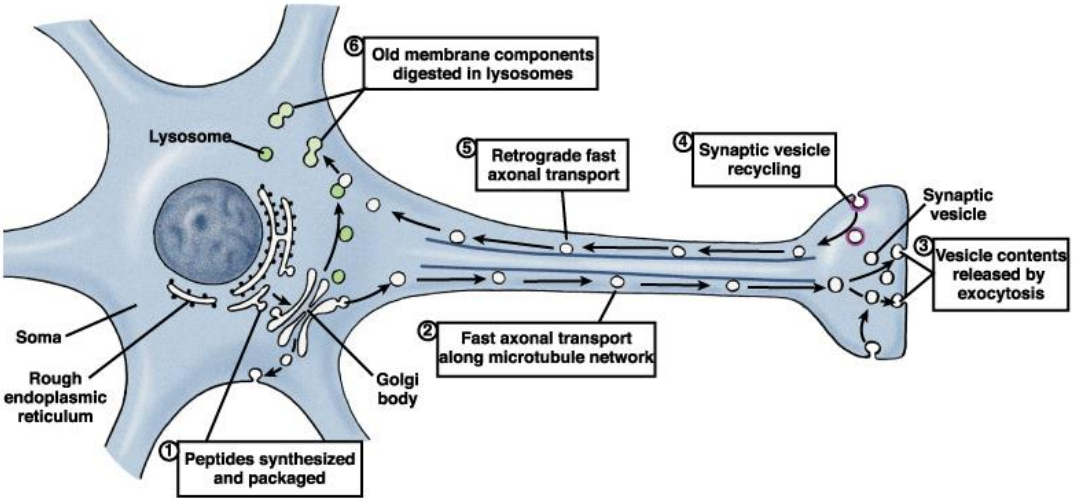

Figure 2.8: Schematic view of the axonal transport from the soma to the synapse [115].

Neurons can be broadly classified into three categories based on the arrangements and shapes of the dendrites, cell body, and axon [111]:

Unipolar neurons have cell bodies without any dendrites (Figure 2.9 a). These cells have only one process, the axon that branches to form a signal receiver at one end and signal emitters (axon terminals) at the other end. These cells predominate in the nervous systems of invertebrates; in vertebrates they occur in the autonomic nervous system.

Bipolar neurons have two processes emanating from the cell body (Figure 2.9 b). A lone dendrite originates from one end of the soma and a single axon arises from the other end.

Many sensory cells are bipolar cells, including those in the retina of the eye and in the olfactory epithelium of the nose. The mechanoreceptors that convey touch, pressure, and pain to the SC are variants of bipolar cells called *pseudo-unipolar* cells. These cells develop initially as bipolar cells; later the two cell processes fuse to form one axon that emerges from the cell body. The axon then splits into two; one branch runs to the periphery (to sensory receptors in the skin, joints, and muscle), the other to the SC.

The greatest number of neurons in our nervous system belongs to the multipolar category. *Multipolar* cells (Figure 2.9 c) possess many dendrites emanating from all over the surface of the cell body and one axon. They are the most common type of neuron in the mammalian nervous system.

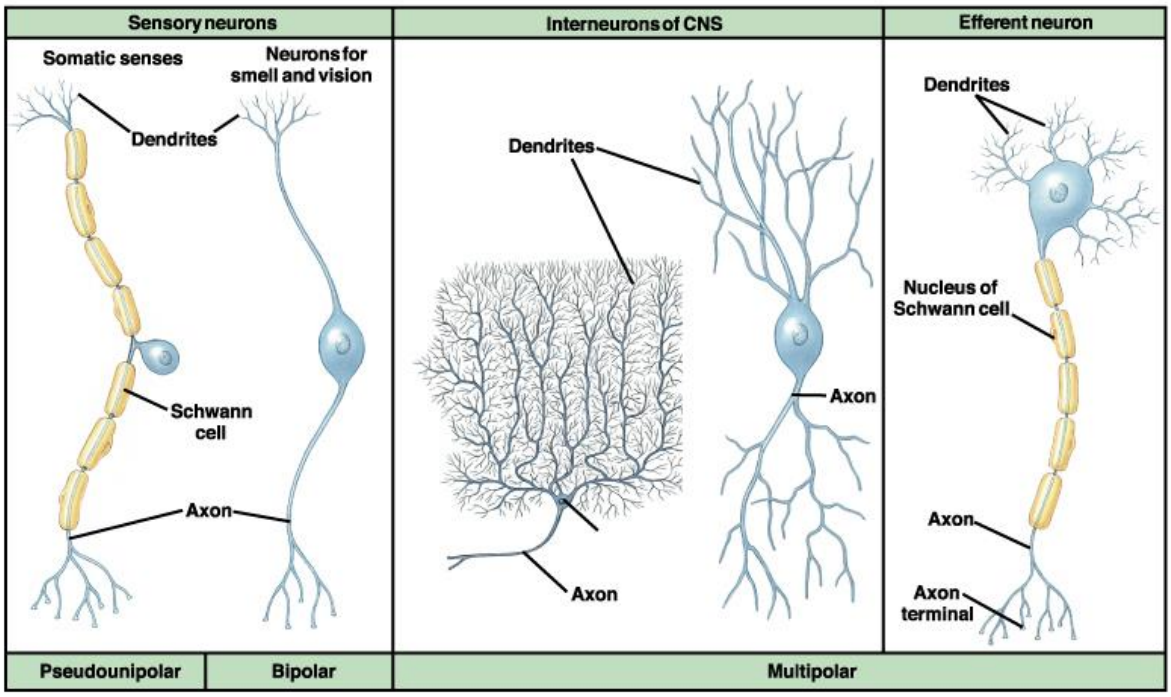

Figure 2.9: a)sketches of unipolar, b) bipolar, and c) multipolar neurons swing cell bodies with nuclei, dendrites (except for the unipolar neuron, which has no dendrites), axon and axon terminal [111].

Three examples illustrate the large diversity of these cells. Spinal motor neurons (Figure 2.10) innervate skeletal muscle fibres. A spinal motor cell with a relatively modest number of dendrites receives about 10,000 contacts—2000 on its cell body and 8000 on its dendrites [111]. Pyramidal cells (Figure 2.10) have a roughly triangular cell body; dendrites emerge from both the apex (the apical dendrite) and the base (the basal dendrites). Pyramidal cells are found in the hippocampus and throughout the cerebral cortex. Purkinje cells of the cerebellum (Figure 2.10) are characterized by the rich and extensive dendritic tree in one plane. Such a structure permits enormous synaptic input. A Purkinje cell in the cerebellum is much larger and bushier, as well it might be—it receives approximately 150,000 contacts [111].

The three major functional neurons groups are: *sensory*, *motor*, and *inter-neuronal* [111].

Sensory neurons carry information from the body's periphery into the nervous system for the purpose of both perception and motor coordination. Thus, a sensory neuron transmits impulses from

a *receptor*, such as those in the eye or ear, to a more central location in the nervous system, such as the SC or brain.

Motor neurons carry commands from the brain or SC to muscles and glands.

In particular the motor neurons regulate the contraction of muscles; other neurons stimulate other types of cells, such as glands.

Interneurons constitute by far the largest class, consisting of all nerve cells that are not specifically sensory or motor. Interneurons are subdivided into two classes. Relay or projection interneurons have long axons and convey signals over considerable distances, from one brain region to another. Local interneurons have short axons and process information within local circuits [112].

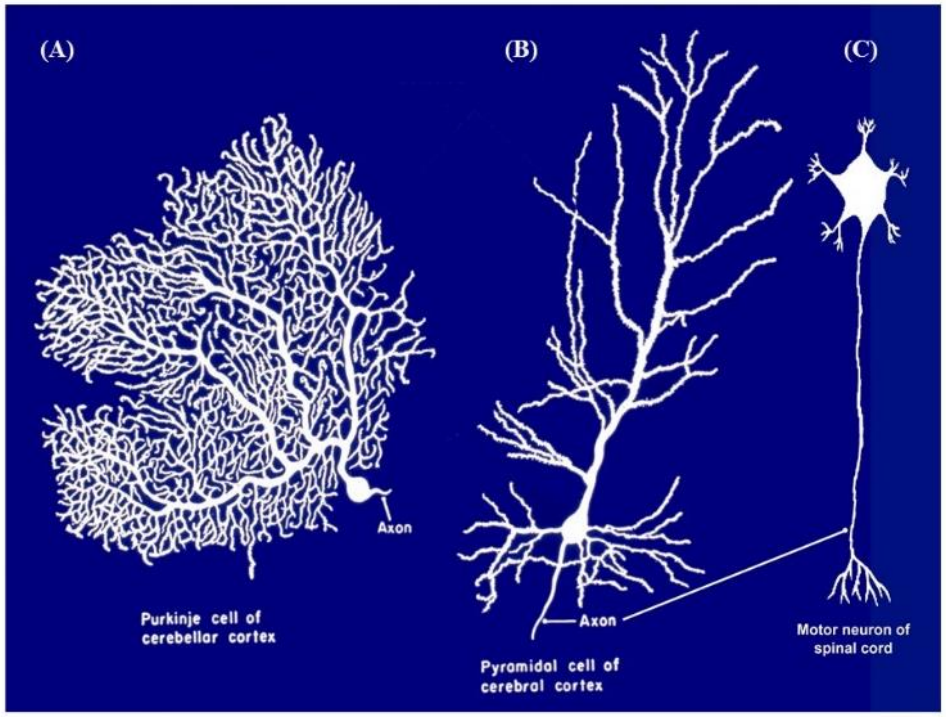

Figure 2.10: pictorial view of (a) Purkinje cell of cerebellar cortex. (b) Pyramidal cell of cerebral cortex. (c) Motor neurons of SC [116].

2.2 Gross anatomy of the SC

The SC participates to the active and passive control of sensory-motor functions (eg, locomotion, motility, pain perception) [117]. It is about 44 cm long in humans, and it follows an S-shaped curve in the sagittal, anterior/posterior direction. It is uniformly organized and it is divided into four regions (Figure 2.12 a): cervical (C), thoracic (T), lumbar (L), and sacral (S) [118].

The SC diameter in cross-section is about 1 cm to 1.5 cm, and it is ovoid-shaped, with enlargements in the cervical region which extends between C3 to T1, with a circumference of about 38 mm—and

in the lumbar region, with a circumference of about 35 mm, which extends between L1 and S2. The transverse diameter is largest at segment C5, and decreases progressively to segment T8. However, the sagittal diameter of each segment does not change distinctly with the segment. Segment C5 had the largest cross sectional area, at 75 mm^2, and segment T6 is the longest, averaging 22.4 mm in length [118].

The cervical enlargement corresponds with the attachments of the large waves, which supply the upper limbs. Its maximum circumference is on a level with the attachment of the sixth pair of cervical nerves. The lumbar enlargement gives attachment to the nerves, which supply the lower limbs [113]. The cord is covered by the meningeal membranes, and it is surrounded by cerebral spinal flux (CSF). An anterior median fissure and a posterior median sulcus incompletely divide the SC into two symmetrical parts (Figure **2.11**), which are joined across the middle line by a commissural band of nervous matter. The Anterior Median Fissure (*fissura mediana anterior*) has an average depth of about 3 mm, but this is increased in the lower part of the SC. It is perforated by blood vessels on their way to or from the central part of the SC. The Posterior Median Sulcus (*sulcus medianus posterior*) is very shallow; from it a septum of neuroglia reaches rather more than half-way into the substance of the SC; this septum varies in depth from 4 to 6 mm, but diminishes considerably in the lower part of the spine [102, 113, 119].

Thirty-one pairs of spinal nerves spring from the SC, each nerve having a ventral (anterior), and a dorsal (posterior) root, the latter being distinguished by the presence of an oval swelling, the spinal ganglion, which contains numerous nerve cells. The dorsal root contain all the sensory nerve fibres, their, cell bodies being in a ganglion on the course of each root (Figure **2.11**); in some vertebrates they may also contain a few motor fibres. The ventral root (motor root) of each spinal nerve consists of axons from motor neurons whose cell bodies are found within the grey matter of the SC.

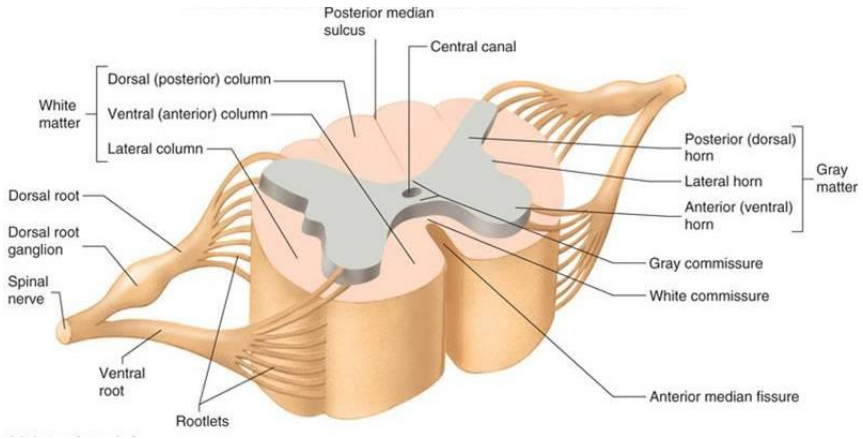

Figure 2.11: SC cross section [113].

A ventral root and a dorsal root unite to form a spinal nerve (Figure **2.11**), which passes outward from the vertebral canal through an intervertebral foramen (bone opening). A posterior branch (posterior ramus) of each spinal nerve turns toward the posterior to innervate muscles and skin of the back. The main portion of the nerve, the anterior branch (anterior ramus), continues forward to supply muscles and skin on the front and sides of the trunk and limbs. The spinal nerves in the thoracic and lumbar regions have a fourth or visceral branch, which is part of the autonomic nervous system [102, 113, 119].

Each root consists of several bundles of nerve fibres, and at its attachment extends for some distance along the side of the SC. The pairs of spinal nerves are grouped as follows: cervical 8, thoracic 12, lumbar 5, sacral 5, coccygeal 1. In the rat the SC is made up of 34 segments: 8 cervical (named C1 to C8), 13 thoracic (T1 to T13), 6 lumbar (L1 to L6), 4 sacral (S1 to S4), and 3 coccygeal (Co1 to Co3). Most mammals have a regional segmental pattern similar to the rat, except those animals with substantial tails have many more coccygeal segments [102].

In cross-section, the peripheral region of the cord contains myelinated axons that constitute the spinal white matter and form ascending and descending tracts to and from supra-spinal regions. In contrast to the brain, the SC white matter surrounds the butterfly-shaped grey matter, containing neuron bodies and glial cells [102] . The grey matter is further subdivided into a posterior horn and an anterior horn. The thoracic and upper two lumbar SC segments also display a wedge-shaped, intermediate lateral horn (Figure 2.12b).

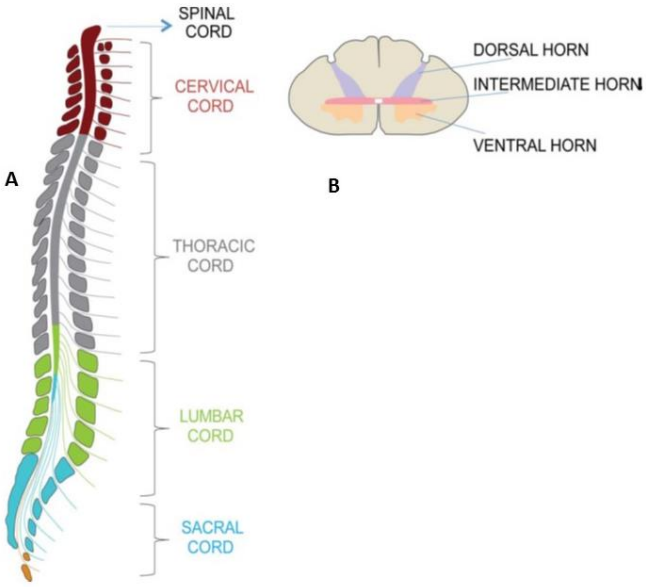

Figure 2.12: Schematic view of the human SC. Left side: (a) view of the SC four sections from cervical, thoracic, lumbar, and sacral levels. Right side : (b) view of the cervical SC cross-section. The grey matter is subdivided into a posterior (dorsal) horn (column), an anterior (ventral) horn (column), and an intermediate lateral horn [79].

The dorsal horn is along the entire SC and comprises sensory nuclei that receive and process incoming somatosensory information [102, 113, 119]. From there, ascending projections emerge to transmit the sensory information to the midbrain and diencephalon. The intermediate lateral horn includes autonomic neurons that innervate visceral and pelvic organs. The ventral horn comprises motor neurons that innervate skeletal muscles (Figure 2.13).

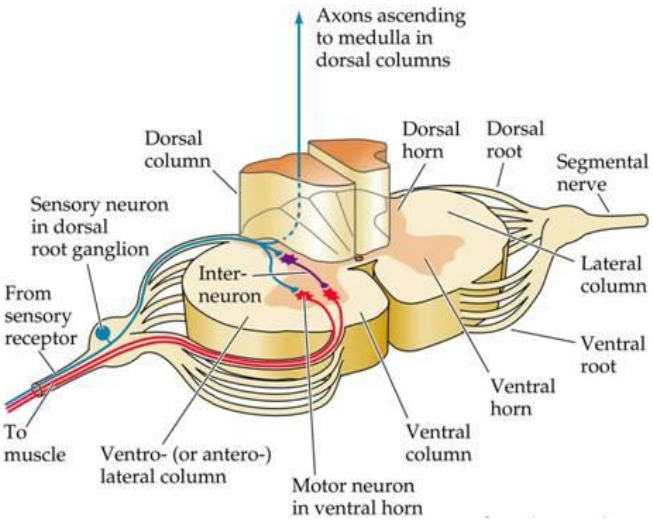

Figure 2.13: cross section of the SC withe and grey matter. In the ventral horn are reported the motor neurons and the interneurons with the sensory neuron in the dorsal root [113].

The central region, which connects the dorsal and ventral horns, is called the intermediate grey matter [102, 113, 119]. In the thoracic SC and in the upper lumbar segments, there is a small lateral projection of the intermediate grey matter called the inter mediolateral horn. The inter mediolateral horn contains the cells of origin of the autonomic nervous system. The thoracic inter mediolateral horn contains preganglionic sympathetic neurons. In upper sacral segments, the sacral parasympathetic nucleus, which is composed of preganglionic parasympathetic neurons, is present.

2.3 Internal Structure of the SC

On examining a transverse section of the SC it is seen to consist of grey and white nervous substance [102, 113, 119], the former being enclosed within the latter.

2.3.1 Grey matter

The grey substance consists of two symmetrical portions, one in each half of the SC: these are joined across the middle line by a transverse commissure of grey substance, through which runs a minute canal, the central canal (Figure **2.11**).

The quantity of grey substance, as well as the form, which it presents on transverse section, varies markedly at different levels. In the thoracic region it is small (Figure 2.14), not only in amount but relatively to the surrounding white substance. In the cervical and lumbar enlargements (Figure 2.14), it is greatly increased: in the latter, and especially in the conus medullaris, its proportion to the white substance is greatest. In the cervical region, its posterior column is comparatively narrow, while its

anterior is broad and expanded. In the thoracic region, both columns are attenuated, and the lateral column is evident; in the lumbar enlargement, both are expanded; while in the conus medullaris the grey substance assumes the form of two oval masses, one in each half of the cord, connected together by a broad grey commissure.

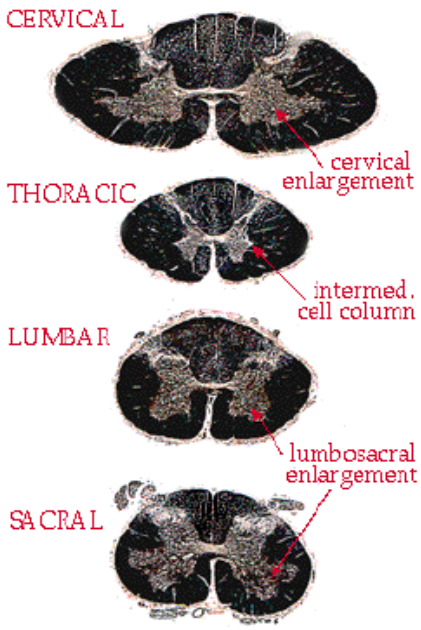

Figure 2.14: axial cross section of the SC at different level: Cervical, Thoracic, Lumbar and Sacral (http://www.bioon.com/bioline/neurosci/course/spinal.html).

2.3.1.a Structure of the Grey Substance

The grey substance consists of numerous nerve cells and nerve fibres held together by neuroglia [111, 112, 119]. Throughout the greater part of the grey substance, the neuroglia presents the appearance of a sponge-like network, but around the central canal and on the apices of the posterior columns it consists of the gelatinous substance. The nerve cells are multipolar, and vary greatly in size and shape [111, 112, 119]. They consist of (1) motor cells of large size, which are situated in the anterior horn, and are especially numerous in the cervical and lumbar enlargements; the axons of most of these cells pass out to form the anterior nerve roots, but before leaving the white substance they frequently give off collaterals, which re-enter and ramify in the grey substance. (2) Cells of small or medium size, whose axons pass into the white matter, where some pursue an ascending, and others a descending course, but most of them divide in a T-shape manner into descending and ascending processes. They give off collaterals, which enter and ramify in the grey substance, and the terminations of the axons behave in a similar manner. The lengths of these axons vary greatly: some are short and pass only

between adjoining spinal segments, while others are longer and connect more distant segments. These cells and their processes constitute a series of association or intersegmental neurons, which link together the different parts of the SC. The axons of most of these cells are confined to that side of the SC in which the nerve cells are situated, but some cross to the opposite side through the anterior commissure, and are termed crossed commissural fibres. Some of these latter end directly in the grey substance, while others enter the white substance, and ascend or descend in it for varying distances, before finally terminating in the grey substance. (3) Cells of the type II of Golgi, limited for the most part to the posterior column, are found also in the substantia gelatinosa of Rolando; their axons are short and entirely confined to the grey substance, in which they break up into numerous fine filaments. Most of the nerve cells are arranged in longitudinal columns, and appear as groups on transverse.

2.3.1.b Fine organization of the SC grey matter

Microscopic analysis of the spinal grey matter reveals a complex structure, characterized by successive layers of cells from dorsal to ventral. The landmark description of these layers by Rexed in 1952 and 1954 has formed the basis of the majority of detailed anatomical and studies of the SC in recent times. The laminar distribution (Figure 2.15) main advantage is its simple and comprehensive scheme of SC organization and physiological properties can also be correlated to this structural arrangement [102, 120].

Cytoarchitectural laminae are characterized by the density and topography of spinal neurons in the grey matter and can usually be identified on thick cross sections. In addition, each lamina has its own characteristics which are particularly distinct at the level of cervical and lumbar enlargements. In addition to the laminar arrangement in the coronal plain, in the ventral horn the cervical and lumbar motor neurons form rostro-caudal motor columns [114] .

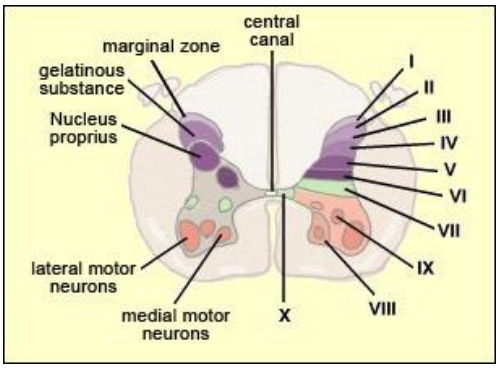

Figure 2.15: Cross section of the lumbar portion of the SC showing the layered arrangement of the hemicord (http://neuroscience.uth.tmc.edu/s2/chapter03.html).

Lamina I covers the tip of the dorsal horn. It has a loosely packed neuropil and a low neuronal density with neurons of variable size and distribution. The most typical neuron is the so-called Waldeyer[8]cell: large, fusiform neuron with disk-shaped dendritic domain. However, in cat and rat also small and medium-sized pyramidal neurons were identified in this lamina and characterised as fusiform, pyramidal and multipolar cells.

Lamina II appears as a darkly stained band in Nissl-stained sections due to its high neuronal density (substantia gelatinosa). The neuronal population consists of small fusiform neurons. There are two main cell types which form the majority of the population of lamina II: the islet cells with a rostrocaudal axis and the stalked cells with a dorsoventral dendritic tree. Other types of neurons have been described such as arboreal, curly, border, vertical, filamentous and stellate cells. It is possible, however, that some of these latter neurons correspond to each other or to the two main cell types. Islet cells contain GABA therefore they are considered as the inhibitory cells of this lamina.

Lamina III This was previously called the superficial part of the nucleus proprius (proper sensory nucleus) of the dorsal horn. There are many myelinated fibers in this lamina. The neurons are less densely packed and larger than those in lamina 2. Laminae 2 and 3 are functionally related and consist mostly of Golgi type 2 neurons [112].

Lamina IV Formerly known as the base of the nucleus proprius, or head of the dorsal horn, the lamina is about twice as thick as lamina 3. Its medial end curves ventrally along the margin of the dorsal horn and makes contact at the midline with its counterpart of the opposite side. In thoracic and upper lumbar levels, its medial extent is interrupted by the dorsal nucleus (of Clarke). Internal basilar nucleus is also present in lamina 4 of C1-C6 segments. Its neurons project to the midbrain and brainstem and send processes to lamina IV itself.

Lamina V-VI have a similar cyto- and dendroarchitecture. The medial part contains fusiform and triangular neurons. The lateral part is not clearly separated from the dorsolateral funiculus. This part corresponds to the reticular formation in the brainstem and consists of medium-sized multipolar neurons.

Lamina VII occupies the intermediate zone of the grey matter and is formed by an homogeneous population of medium-sized multipolar neurons. In the appropriate segments it contains some well-defined nuclei, such as the intermediolateral nucleus (T1-L1; medially) and the dorsal nucleus of Clarke (T1-L2; laterally). The intermediolateral nucleus plays a role in the autonomic sensory and motor functions and the axons of neurons from the dorsal nucleus of Clarke form the ascending fibres of the dorsal spinocerebellar tract.

Lamina VIII has, unlike laminae I-VII a dorso-ventral extension. It contains a variety of neurons with dorsoventrally polarized dendritic tree. The largest multipolar neurons can be distinguished from motor neurons only by their finer Nissl bodies by using conventional morphological techniques.

Lamina IX is made up of groups of cells that form motor nuclei. Motor neurons have a unique position in this lamina, being the only SC neuron which has its axon almost entirely in the peripheral nervous system. The α-motor neurons have the largest somata in the cord (50 x 70 μm) whilst the γ-motor neurons are smaller. Motor neurons can be easily recognized by the abundance of Nissl bodies in their cytoplasm and their multipolar shape. Their dendrites extend for long distances, dorsally as far as lamina VI. Small neurons at the medial border of the motor nucleus are identified as the short-axoned inhibitory interneurons, the Renshaw cells. Although Rexed's classification did not differentiate between motor neuron groups in lamina IX, these neurons can be divided into four separate columns in the human cord: the ventromedial, ventrolateral, dorsolateral and central columns (Figure 2.16).

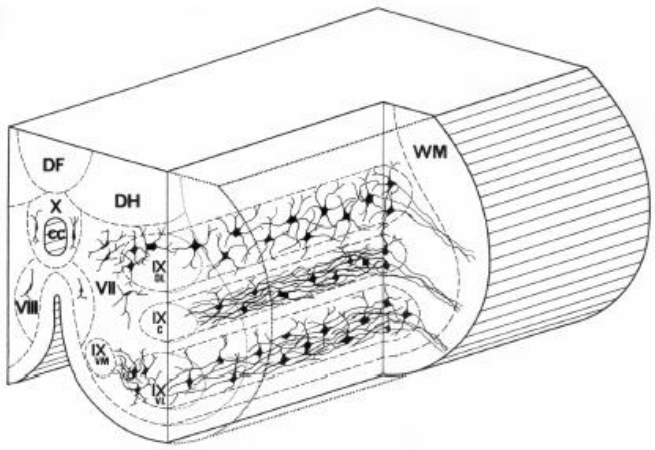

Figure 2.16: Schematic representation of the dendro-architecture of spinal motor neurons in various motor columns. The ventromedial motor neurons (IX-vm) form vertical and longitudinal dendritic branches (not shown), motor neurons in the ventrolateral (IX-vl) and central (IX-c) columns tend to form dendritic bundles in the longitudinal and transverse planes. Motor neurons in these columns have long overlapping areas. On the contrary, dorsolateral motor neurons (IX-dl) have no such a dendritic bundle formation and their branches mostly branch out in the transverse plane. WM: white matter; DF= dorsal funiculus; DH= dorsal horn; CC= central canal [102].

Motor neurons projecting to the axial muscles are found in the ventromedial column, those innervating proximal musculature of the limbs occupy medial and ventral position while neurons innervating distal limb muscles are located in dorsal and lateral positions. In all but one (dorsolateral) motor neurons-neuron column the dendritic polarization is longitudinal and dendritic trees overlap for a long distance (Figure 2.16). Such a dendritic organization favours synchronization and synergy

for axial, proximal and calf muscles. In contrast to these columns, motor neurons-neurons in the dorsolateral column have radially oriented dendritic trees without much overlap of their dendrites. This dendritic arrangement favours precise contacts with segmental afferents and may contribute to a more precise control of movements of distal muscles.

Lamina X This lamina corresponds to the substantia grisea centralis, the grey matter around the central canal. Two cell types can be recognized: (1) Bipolar cells with fan-shaped dendritic tree (dorsal portion of lamina X) and (2) bipolar cells with poorly ramified longitudinal dendrites (ventral portion).

Lateral spinal nucleus

This consists of a small group of cells lying ventral to the dorsolateral tip of the dorsal horn (Figure 2.15). They are thought to receive subcutaneous sensory information and to project to the midbrain, thalamus, and hypothalamus [102].

Lateral cervical nucleus

This nucleus is lateral to the lateral spinal nucleus in upper cervical levels. It is a sensory nucleus which projects to the cerebellum, midbrain, and thalamus [102].

Onuf's nucleus A distinct group of motor neurons-neurons in the caudal lumbar and rostral sacral SC in mammals, called Onuf's nucleus, is seen in the ventrolateral part of the ventral horn. Onuf's nucleus supplies the perineal muscles and the anal and urethral sphincters. The perineal muscles, bulbocavernous (called bulbospongious in humans) and ischiocavernous, are those involved in penile erection and ejaculation in males. The nucleus is sexually dimorphic, the motor neurons-neurons being larger in males. In humans these motor neurons-neurons are aggregated into a single column, but in the rat and mouse they are divided into two groups, a ventrolateral group which supplies the external urethral sphincter and the bulbocavernosus muscle, and a dorsomedial linear nucleus, which supplies the external anal sphincter and the ischiocavernosus muscle [102].

2.3.2 White matter

A layer of white matter surrounds the grey matter except for where the dorsal horn touches the margin of the SC. The white matter consists mostly of longitudinally running axons and also glial cells [102, 113, 119]. A large group of axons, which are located in a given area, is called a funiculus (e.g.

posterior funiculus). Smaller bundles of axons, which share common features within a funiculus are called fasciculus (e.g. fasciculus gracilis). Tracts and pathways are terms applied to nerve fibre bundles that have a functional connotation. A tract is a group of nerve fibres with the same origin, course, termination and function (e.g. spinothalamic tract). A pathway is a group of tracts with a related function (e.g. postsynaptic dorsal column pathway). The horns of grey matter divide the white matter into three columns (funiculi): dorsal, lateral and ventral (Figure 2.17). The boundary between the lateral and ventral columns is not distinct. It is generally taken to be in line with the emerging axons of the most lateral motor neurons neurons. The two dorsal columns are located between the two dorsal horns of grey matter and lie side by side with a common medial border. A deep fissure, the ventral median fissure, which extends almost as far as the commissural grey matter, separates the two ventral columns. Blood vessels travel through the deep fissure as way of reaching the centre of the grey matter. At the dorsal limit of the ventral median fissure is a band of white matter (the ventral white commissure) which connects the two ventral columns.

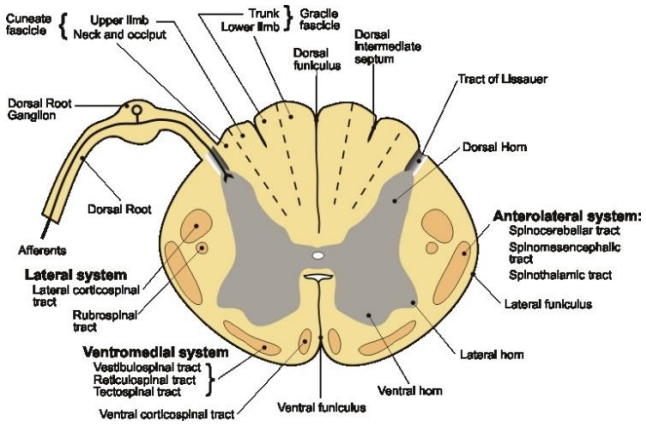

Figure 2.17: SC white matter cross section. The white matter organization is reported [119].

At the region where the dorsal horn reaches the pial surface of the SC, there is a prominent band of fibers called the dorsolateral fasciculus (the tract of Lissauer) (Figure 2.17). This tract contains primary afferent fibers, which either ascend or descend for a few segments before entering the dorsal horn. The dorsal column of white matter is chiefly made up of the central processes of dorsal root ganglion cells. These large myelinated axons form the main pathway conveying skin sensation and position sense (proprioception) from the limbs and trunk to the brain. Because more fibres are added at each segment in a caudorostral order, the dorsal column is very small in sacral segments, and largest in the rostral cervical SC [102, 113, 119]. As the fibres from one segment enter the dorsal column, they move to form a strip as close to the medial edge as possible. Fibres from the next segment move

as far medially as they can and form a strip lateral to those of the more caudal segment. When viewed at high cervical levels, the fibres from lower thoracic, lumbar and sacral segments (segments below T6) form a distinct medial strip, the gracile fasciculus. The more lateral group is wedge-shaped and is called the cuneate fasciculus. It primarily contains afferents from the upper thoracic and cervical segments. This group constitutes the dorsal corticospinal tract. Because it contributes fibres to each segment as it descends, this tract diminishes in size from rostral to caudal levels. The dorsal corticospinal tract fibres terminate in the dorsal horn, intermediate grey matter, and, to a lesser extent, on the interneuron pools of the ventral horn. The lateral and anterior columns contain a variety of ascending and descending fibre groups (Figure 2.18). The ascending tracts include the spinothalamic, spinocerebellar and spinotectal tracts and the descending tracts include the corticospinal, vestibulospinal, tectospinal and reticulospinal tracts [102, 113, 119]. As well as these long ascending and descending tracts, there are many fibres in the white columns that connect one SC segment with another. These fibres are called propriospinal, because they often lie very close to the grey matter. The largest propriospinal pathways connect the brachial and lumbosacral enlargements to coordinate limb movements.

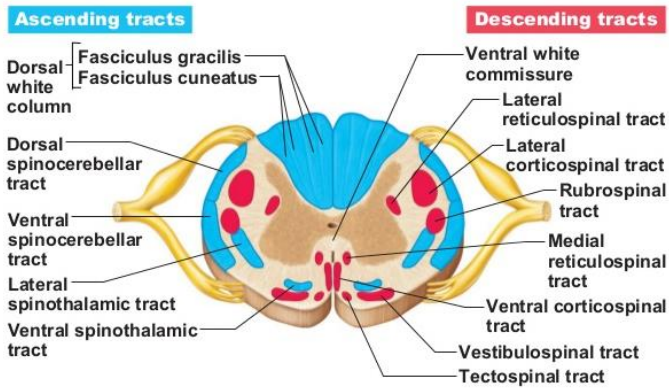

Figure 2.18: white matter cross section. In red the Descending tracts and in blue the ascending tracts are reported [113].

2.4 Connections of the SC with Other Parts of the CNS and its function

The SC has its own intrinsic pathways which are called propriospinal connections. The rest of the fibre tract system connects the SC to other parts of the CNS and are described here as descending and ascending pathways [102, 113, 119].

2.4.1 Ascending Pathways

The ascending pathways are formed by the central axons of dorsal root ganglion cells entering the SC via the dorsal roots (Figure 2.19). They either enter an ascending fibre tract (dorsal column pathways) or terminate in the spinal grey matter. About two-third of these fibres are fine, unmyelinated, slowly-conducting C fibres. The myelinated fibre components can be classified as fast-conducting, large, terminate in the dorsal column nuclei of the medulla or in the superficial dorsal horn according to a segregated pattern. Thin fibres related to temperature and pain terminate in laminae I and II, whereas coarse fibres terminate in deeper layers (laminae III-V) and in the ventral horn as well (proprioceptive afferents).

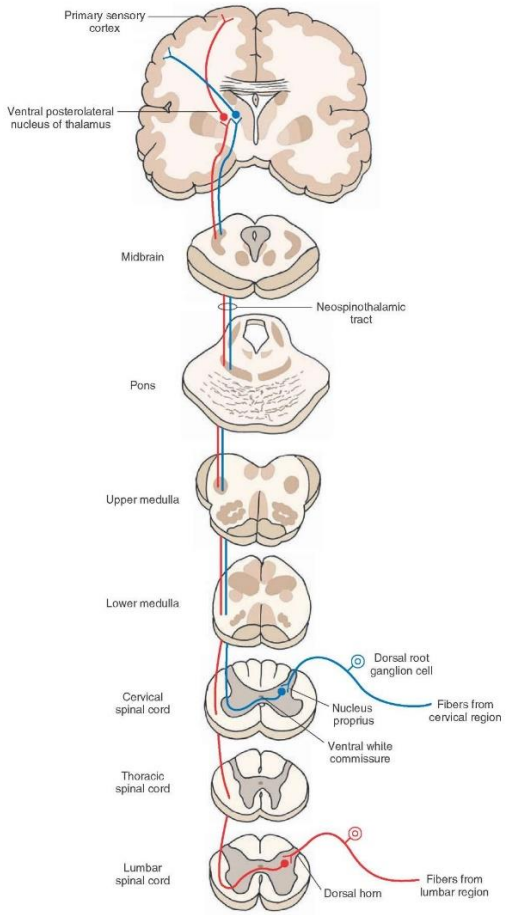

Figure 2.19: Ascending pathway**:**the peripheral processes of these dorsal root ganglion cells end as receptors sensing pain, temperature, and simple tactile sensations. The central processes of these dorsal root ganglion cells synapse with the neurons of the nucleus proprius. The axons of these second-order neurons cross via the anterior white commissure, enter the contralateral white matter, ascend in the lateral funiculus, and synapse on third-order neurons located in the ventral posterolateral nucleus of the thalamus. The axons of third-order neurons project to the primary sensory cortex [113].

The dorsal column pathways include the medially located fasciculus gracilis (Goll) and the laterally situated fasciculus cuneatus (Burdach). The fasciculus gracilis contains dorsal root afferents from the lower limbs and lower part of the body, the fasciculus cuneatus from the upper limb and upper part of the trunk. The fibres synapse on neurones of the nucleus gracilis and nucleus cuneatus, respectively. These pathways play role in discriminative sensory tasks, such as two-point discrimination, detection of speed and direction of movements and judging of cutaneous pressure. The spinothalamic tract originates from neurons in laminae I,V,VII and VIII, however the distribution of spinothalamic neurons shows significant species differences [102, 120]. In humans the axons cross to the ventrolateral column and terminate in the ventral posterolateral and in the central lateral nuclei of the thalamus. In other mammals they terminate mainly in the posterior thalamic nuclear complex. Functionally, this tract conveys the accurate localization of pain and thermal stimuli. Ventrolateral cordotomies presented evidence that other tracts may also transmit pain stimuli [120]. The spinoreticular tract originates from cells situated bilaterally throughout the spinal grey matter. The ascending fibres in the ventral and lateral funiculi terminate in several nuclei of the reticular formation. Many spinothalamic ascending fibres also give collaterals to reticular nuclei. This pathway is responsible for carrying a variety of sensory information. The spinocervicothalamic tract uses an intermediate nucleus in the SC, the lateral cervical nucleus, which is consistent in lower mammals but often absent in human SCs. Afferent fibres to this nucleus arise from the ipsilateral lamina IV in all cord segments. Neurons from the lateral cervical nucleus project to the contralateral thalamus via the medial lemniscus. This system is involved in tactile conditioned reflexes, tactile and proprioceptive placing and size discrimination. The spinocerebellar tracts (dorsal and ventral) carry information primarily arising from the lower extremities. Axons of the ipsilateral nucleus dorsalis of Clarke (present in Th1-L2 segments in humans) and projects to the vermis and the paravermal regions of the cerebellum form the dorsal spinocerebellar tract. It conveys information from muscle spindles, Golgi tendon organs, joints and mechanoreceptors of the lower extremities. Axons of cells situated in laminae V and VII in the lumbosacral SC form the ventral spinocerebellar tract. It projects to the vermis and paravermal region of the cerebellum and probably carries information about the interrelationship of different muscle groups. Equivalent information from the upper extremities are conveyed by the cuneocerebellar and the rostral spinocerebellar tracts of the SC.

2.4.2 Descending Pathways

The descending pathways from the brainstem and cortex modulate both facilitatory and inhibitory process of the spinal reflexes (Figure 2.20). The descending pathways also control voluntary movement and some sensory-driven reflex actions. In particular, the corticospinal system controls motor neurons and interneurons in the SC and the corticobulbar system controls brainstem nuclei that innervate cranial muscles. The corticospinal tract is most developed in higher primates and species differences are most pronounced for this tract. The cells of origin are located in the motor cortex and their axons form the pyramidal tract. In most mammals, fibres from neurones in the postcentral gyrus also contribute to this tract. In humans, the bulk of the fibres cross in the lower medulla and form the lateral corticospinal tract whereas uncrossed fibres remain in the ventral funiculus and then cross in the ventral commissure. In some species, the organization of this tract is different. Functionally, the corticospinal pathway exerts a fine and amplified motor control by influencing other descending pathways. The primary pathway carries the motor commands that underlie voluntary movement. In particular, the lateral corticospinal tract is responsible for the control of the distal musculature and the anterior corticospinal tract is responsible for the control of the proximal musculature.

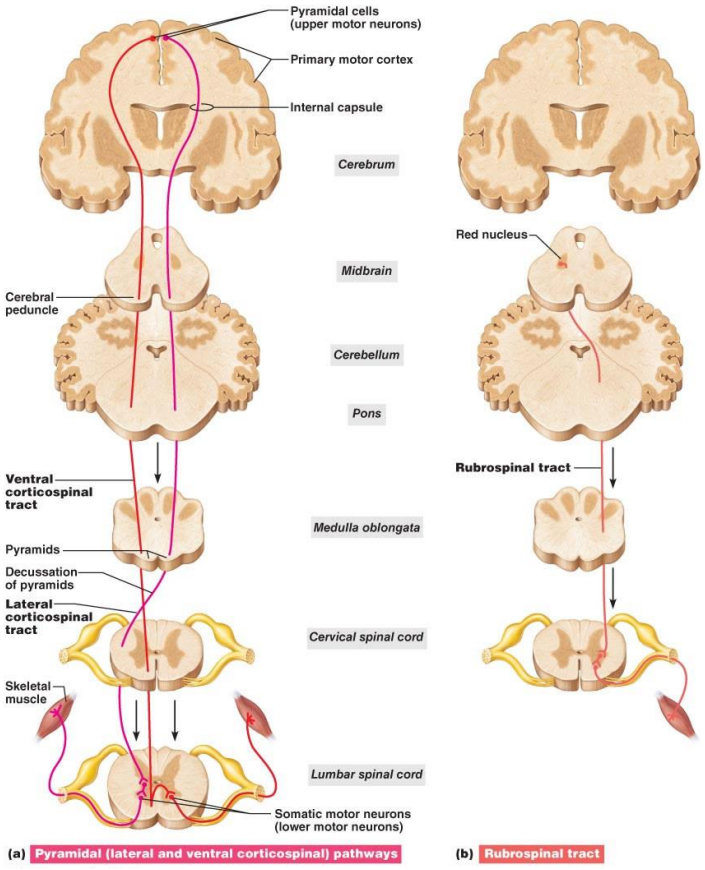

Figure 2.20: Descending pathways from the brainstem and cortex modulate both facilitatory and inhibitory process of the spinal reflexes. **(A)** Lateral and ventral corticospinal pathways **(B)** Rubrospinal tract [113].

A particularly important function of the lateral corticospinal tract is the fine control of the digits of the hand. The corticospinal tract is the only descending pathway in which some axons make synaptic contacts directly onto alpha motor neurons (Figure 2.20a). This direct cortical innervation presumably is necessary to allow the powerful processing networks of the cortex to control the activity of the spinal circuits that direct the exquisite movements of the fingers and hands. The percentage of axons in the corticospinal tract that innervate alpha motor neurons directly is greater in humans and nonhuman primates than in other mammals, presumably reflecting the increased manual dexterity of primates. Damage to the corticospinal tract results in a permanent loss of the fine control of the extremities. Although parallel descending pathways can often recover the function of more coarse movements, these pathways are not capable of generating fine, skilled movements. In addition to the fine control of distal muscles, the corticospinal tract also plays a role in the voluntary control of axial muscles.

Fibres of the reticulospinal tracts originate from the dorsal and central parts of the medulla and the pontine tegmentum. The terminal distribution of medial reticulospinal fibres is very dense in the

ventral horn of the enlargements while the lateral reticulospinal tract fibres terminate in laminae I and V. The fibres of the vestibule spinal tract originate from the lateral and medial vestibular nuclei. Both lateral and medial tract fibres terminate ipsilaterally in laminae VII and form mono- or polysynaptic inhibitory connections with motoneurons, especially with those of neck and back muscles. The rubrospinal tract is well developed in lower mammals and less developed in humans. Its fibres originate from the caudal magnocellular part of the red nucleus and project according to a somatotopic pattern contralaterally to laminae V-VII (Figure 2.20b). The tectospinal tract originates from the superior colliculus and terminates contralaterally in the ventral horn of the upper cervical cord where its fibres establish multisynaptic connections with motor neurons of neck muscles.

Apart from the major descending tract, there are many minor fibre bundles originating from the interstitial nucleus of Cajal, solitary and retroambiguous nuclei, and the paraventricular nucleus of the hypothalamus. Noradrenergic fibres descend from the locus coeruleus and the lateral pontine nuclei to the grey matter and to the intermediolateral nucleus, respectively. Serotonergic projections arise from the raphe magnus and raphe pallidus and obscurus nuclei terminate either in laminae I and V (raphe magnus fibres) or in the ventral horn (rest of the fibres).

2.5 Motor Control

One of the major principles of the motor system is that motor control [113], requires sensory input to accurately plan and execute movements. The SC is the first level of the motor hierarchy. It is the site where motor neurons are located. It is also the site of many interneurons and complex neural circuits that perform the “nuts and bolts” processing of motor control. These circuits execute the low-level commands that generate the proper forces on individual muscles and muscle groups to enable adaptive movements. The SC also contains complex circuitry for such rhythmic behaviours as walking. Because this low level of the hierarchy takes care of these basic functions, higher levels (such as the motor cortex) can process information related to the planning of movements, the construction of adaptive sequences of movements, and the coordination of whole-body movements, without having to encode the precise details of each muscle contraction.

2.5.1 Motor Neurons

Alpha motor neurons (also called **lower motor neurons**) innervate skeletal muscle and cause the muscle contractions that generate movement. Motor neurons release the neurotransmitter

acetylcholine at a synapse called the neuromuscular junction [111]. When the acetylcholine binds to acetylcholine receptors on the muscle fiber, an action potential is propagated along the muscle fiber in both directions. The action potential triggers the contraction of the muscle. If the ends of the muscle are fixed, keeping the muscle at the same length, then the contraction results on an increased force on the supports (i**sometric contraction**). If the muscle shortens against no resistance, the contraction results in constant force (**isotonic contraction**). The motor neurons that control limb and body movements are located in the anterior horn of the SC, and the motor neurons that control head and facial movements are located in the motor nuclei of the brainstem. Even though the motor system is composed of many different types of neurons scattered throughout the CNS, the motor neuron is the only way in which the motor system can communicate with the muscles. Thus, all movements ultimately depend on the activity of lower motor neurons. Motor neurons are not merely the conduits of motor commands generated from higher levels of the hierarchy. They are themselves components of complex circuits that perform sophisticated information processing. Motor neurons have highly branched, elaborate dendritic trees, enabling them to integrate the inputs from large numbers of other neurons and to calculate proper outputs (for more information see Appendix A: Motor neurons pools and motor unit).

2.5.2 Discending Motor pathways

The motor system is organized hierarchically; the hierarchy is not a simple chain of processing from higher to lower areas. Many pathways enable the different levels of the hierarchy to influence each other. Thus, the flow of information through the motor system has both a serial organization (communication between levels) and a parallel organization (multiple pathways between each level). Descending motor pathways arise from multiple regions of the brain and send axons down the SC that innervate alpha motor neurons, gamma motor neurons, and interneurons (see Appendix B: Descending Motor Pathways) [113]. The motor neurons are topographically organized in the anterior horn of the SC according to two rules: the flexor-extensor rule and the proximal-distal rule.

Flexor-extensor rule: motor neurons that innervate flexor muscles are located posteriorly to motor neurons that innervate extensor muscles.

Proximal-distal rule: motor neurons that innervate distal muscles (e.g., hand muscles) are located lateral to motor neurons that innervate proximal muscles (e.g., trunk muscles).

Descending motor pathways are organized into two major groups:

1. **Lateral pathways** control both proximal and distal muscles and are responsible for most voluntary movements of arms and legs. They include the
    a. lateral corticospinal tract
    b. rubrospinal tract
2. **Medial pathways** control axial muscles and are responsible for posture, balance, and coarse control of axial and proximal muscles. They include the
    a. vestibulospinal tracts (both lateral and medial)
    b. reticulospinal tracts (both pontine and medullary)
    c. tectospinal tract
    d. anterior corticospinal tract.

2.6 Vasculature of the SC

The SC is supplied by a single ventral spinal artery and two dorsal spinal arteries. The ventral spinal artery originates from the vertebral artery and descends within the ventral median fissure of the SC (Figure 2.21). The dorsal spinal arteries originate either from the vertebral artery or its inferior posterior cerebellar branch, and descend in the dorsolateral sulcus of the SC. Segmental branches from the vertebral, deep cervical, intercostal, and lumbar arteries anastomose with the ventral and dorsal spinal arteries (Figure 2.21 a). The veins of the SC form a surface plexus, which drain rostral into the cerebellar veins and cranial sinuses and through the intervertebral veins and external venous plexuses to the azygous system [102].

Given that fMRI relies on the recording of hemodynamic changes related to neuronal activity, it is worth describing vascular architecture providing the blood supply in the SC. In the fallowing, we report a detailed description of the vascular network of the SC.

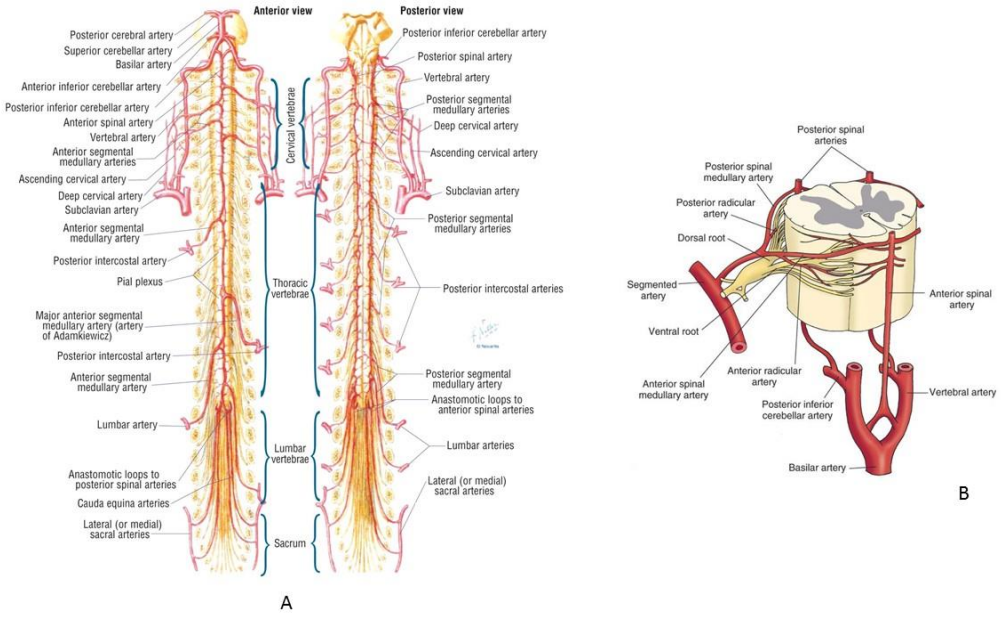

Figure 2.21: A) SC vascular distribution, all spinal nerves roots have associated radicular or segmental medullary arteries **B)** SC axial cross section [113].

2.6.1 Arterial anatomy

The arterial supply to the SC originates from ventral, posterolateral and dorsal systems that extend throughout the entire cord (Figure 2.21a). One ventral (anterior) spinal artery (vsp) is virtually a continuous channel that extends from the cervical segments to the filum terminale (Figure 2.22). This vessel can be found at the entrance of the ventral median fissure. Two dorsal spinal arteries (dsp) located just ventral to the entrance of the dorsal roots, also tend to form continuous channels along the cervical, thoracic and lumbar cords. The lateral spinal arteries (lsp) are found about midway between the attachment of the dorsal and that of the ventral roots. A median dorsal spinal artery (mdosa), situated at or close to the dorsal septum, is found along all segments of the cord (Figure 5.4). The ventral spinal artery originates rostrally from two caudally directed branches stemming off the two vertebral arteries before they join to form the basilar artery. Radicular arteries, branching off deep cervical, intercostal, lumbar and sacral arteries, enter the spinal canal through the intervertebral foraminae along with the spinal nerves and are variable in diameter. They divide, outside the dura mater, into branches that follow the course of ventral and dorsal roots (ventral and dorsal radicular arteries respectively). Some of the central radicular arteries supply blood only to the ventral roots but a number of them are larger and merge into the ventral spinal artery, either directly or after dividing into a rostral and a caudal branch. A similar arrangement is found for the dorsal spinal arteries. The number of the larger ventral and dorsal root arteries that contribute to the ventral and dorsal spinal arteries is quite variable. They are more abundant in the cervical and lumbar enlargements and almost

absent in the thoracic cord found that dorsal radicular arteries were more numerous and evenly distributed, but of a smaller size, than the ventral radicular arteries. The ventral spinal artery gives off, at regular intervals, the ventromedian or sulcal arteries (Figure 2.22). These vessels ascend in the ventromedian sulcus, usually in pairs destined one to a side, and reach the medial junction between the gray commissure and the ventral horn. They are then distributed widely within the grey matter, giving one or more branches to the ventral horn with collaterals to the commissure, lateral grey column, and base of the dorsal horn. They supplies the anterior two thirds of the cord. In particular posterior spinal arteries supply the dorsal white matter and the dorsal horns, for about one third of the cord. The capillary loops that originate in these distribution vessels travel beyond the boundary between grey and white matter and supply the anterior and ventral portion of the lateral white columns. The rest of the SC is supplied by perforating rami from the pial arterial network that interconnects the dorsal, dorsolateral, and lateral longitudinal arterial channels described above. These perforating arteries are arranged in a radial orientation and travel through the white matter, giving occasional small branches, (Figure 2.22) to a final distribution in the grey matter [102].

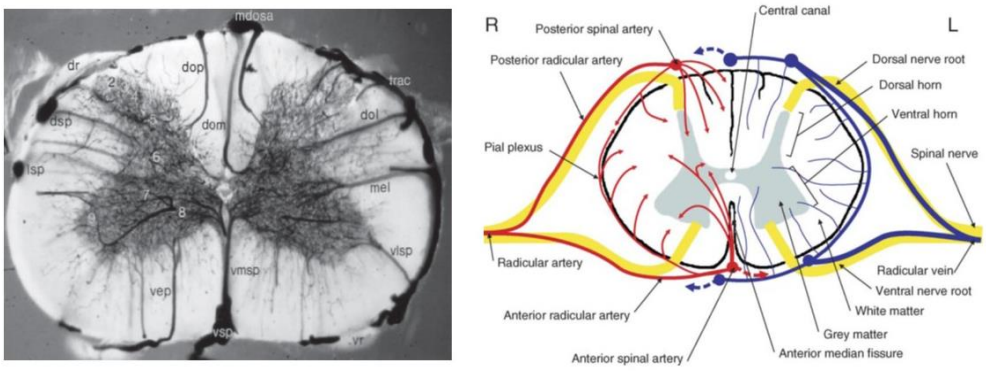

Figure 2.22: (on the left) SC arterial system demonstrated with an injected contrast medium. A coronal section, 1 mm thick, of the SC (C5) injected Intra arterially with neoprene latex-black ink mixture, which does not penetrate capillaries. Ventral (vsp), dorsal (dsp), median dorsal (mdosa), and lateral (lsp) spinal arteries are labelled. Contrast is provided by the presence of injection material in small arteries and precapillary vessels. The remarkable difference in microvascular density of gray and white matter is apparent in this unstained section [102]. **(on the right)** Schematic of the human SC. For clarity reasons, arteries are drawn only on the right side of the cord, veins only on the left [77].

Therefore we can summarize that larger arteries (0.1-0.2 mm in humans) lie externally to the SC and have longitudinal symmetry while only small arteries (maximum 50 μm) penetrate radially into the cord.

2.6.2 Venous anatomy

An intricate venous plexus is found on the surface of the SC. The veins draining the SC are arranged roughy like the arteries (Figure 2.22). There are usually three anterior and three posterior spinal veins (in general larger), one medial and two lateral that run longitudinally [102].

On the ventral side, a ventral spinal vein (vsv) is found dorsal or adjacent to the ventral spinal artery. Like its arterial counterpart, this vessel spans the entire length of the cord, but with notable variations in calibre. The cervical portion of the vsv parallels in size the vsa, but it is more slender at the thoracic segments. Approximately at the junction between the thoracic and lumbar cords, a large ventral radicular vein divides into a cranial small vessel continuous with the thoracic vsv and a much larger caudal vessel continuous with the similar sized lumbar vsv. This vein ends as a continuous channel that follows a tortuous path along the sacral segments and cauda equina. On the dorsal cord surface, a dorsal spinal vein (dsv) is found ventral or adjacent to the dorso-median spinal artery. The ventral and dorsal spinal veins are connected by a large number of smaller veins that surround the cord, although occasionally, and particularly at the cervical and lumbar enlargements, prominent venous transverse anastomotic circles can be found. Internal spinal veins drain into the ventral or dorsomedian veins and into other vessels of the cord surface plexus. Also for the veins, the main vessels are external to the cord and longitudinally disposed, while the internal drainage is provided by small, radial vessels (diameter less 50 μm).

2.6.3 Capillaries of the SC

The SC white matter is not served by capillary beds as abundantly as in the grey matter. In fact, the density of the capillary bed is 5 times greater in grey matter than in white matter. The capillary beds in white matter are also uniform, stretching longitudinally in the direction of the nerve fibres. Where the grey and white matter meet, the capillary bed are denser than those in white matter are alone. Within the grey matter, the density of the beds depends on the location of the cell bodies. This arrangement reflects the greater metabolic requirements of cell bodies compared with axons.

The lateral horns, anterior horns, and base of the posterior horns (especially the substantia gelatinosa) have the thickest capillary beds, although the remainder of the posterior horns is not well supplied.

Summary and conclusions

The SC is part of the CNS and participates to the active and passive control of sensory-motor functions (e.g. locomotion, motility, pain perception). It is uniformly organized and it is divided into four regions: cervical, thoracic, lumbar, and sacral. In cross-section, the peripheral region of the cord contains myelinated axons that constitute the spinal white matter and form ascending and descending tracts to and from supraspinal regions. In contrast to the brain, the SC white matter surrounds the butterfly-shaped grey matter, containing neuron bodies and glial cells. The grey matter is further subdivided into a posterior horn and an anterior horn. The thoracic and upper two lumbar SC segments also display a wedge-shaped, intermediate lateral horn (intermediolateral cell column). The dorsal horn is along the entire SC and comprises sensory nuclei that receive and process incoming somatosensory information. From there, ascending projections emerge to transmit the sensory information to the midbrain and diencephalon. The intermediate lateral horn includes autonomic neurons that innervate visceral and pelvic organs. The ventral horn comprises motor neurons that innervate skeletal muscles. Although the SC is the output station of the central motor system, little is known about the relationships between its functional activity and willed movement parameters in humans. Thanks the help of the fMRI applied to SC may be possible to understand this relationship. However many difficulties in spinal fMRI arise from the specific anatomic features of the SC. In particular, the small cross-sectional area and large rostrocaudal extent of the SC, and its variable curvature imply a low signal, because of the constraints they impose on the voxel size. In spite of the small voxel size usually employed, a significant and variable contamination of the signal occurs because of partial volume effect and motion. The proximity of the SC to several structures of different density (vertebrae, intervertebral discs) gives rise to large variations in magnetic susceptibility and determines a relatively poor local magnetic field homogeneity, causing image distortion and low signal intensity in standard T_2^* -weighted fMRI with echo planar imaging (EPI)[2] readout.

However, the particular SC distribution of large vessels, only on the surface of the SC, should enhance the specificity of fMRI BOLD signal, even with T_2^* weighting, because of the inherent elimination of the confounding, unspecific effect of larger vessels from the grey matter signal. Similarly, the disposition of small vessels, all radial and thus orthogonal to magnetic field should emphasize the dephasing effect of deoxyhemoglobin. Therefore, the vascular anatomy of SC is optimally organized

[2] In EPI the entire spatial encoding and acquisition for the slice is completed after a single radiofrequency (RF) pulse using multiple gradient echoes, leading to acquire an image in only 25 - 100 ms. This allows for the partial reduction of the physiological fluctuations of the signal induced by processes such as blood vessel pulsation, vaso motion and respiration. Nevertheless, high resolution images can be very difficult to obtain with EPI, especially at high magnetic fields where the signal loss is faster, given that T2 reduces as the field increases.

for the generation of strong and spatially specific BOLD effect. This can help in overcoming the numerous other difficulties that involves the SC fMRI.

In this Chapter, we have described the structure of the SC and of some neuronal functions in such detail to understand the SC function and the origin of the fMRI limitation.

CHAPTER 3

SC fMRI: BASIS AND ISSUES

fMRI based on BOLD contrast [1-5] has gained a primary role in the study of human brain, both for the characterization of normal brain activity and in clinical practice. Up to now, however, several studies of the human SC by functional imaging have been presented, starting from the work published in 1996 by Yoshizawa et al. [6], with a subsequent strong contribution of Stroman et al. [7-16]. SC fMRI may be of immediate application in neuroradiology, and in particular for the assessment and follow-up of spinal injuries, pain, and neurodegenerative diseases (e.g. multiple sclerosis), as well as in the development and evaluation of new therapies. Indeed, a non-invasive tool capable of monitoring the function, and thus complementing the available anatomical information, is a crucial need in these fields. Patients' studies provide further evidence of response sensitivity to pathological changes suggestive of a neuronal basis for spinal cord activity. Preliminary studies of people with SCI and MS have demonstrated altered activity in the SC depending on the injury severity or disease state [7, 20-24] (see paragraph 1.3.2 for detailed information). From clinical perspective, it is important to recognize that Spinal fMRI has been demonstrated for group analyses but that there are still sources of variability or uncertainty that count against its use for individual studies. Once these sources of variability and errors are characterized and understood, it is expected that methods can be adapted to optimize the sensitivity to study and assess individuals. SC fMRI activations in response to thermal, sensory, motor and painful stimuli, as well as evidence of the descending modulation of activity [121], have been reported thus far [7, 19, 22, 122], and substantial efforts have been devoted to develop appropriate methodologies [16]. Nonetheless, the application of fMRI to the SC remains confined to a few laboratories, mainly because of the vagaries of the activation patterns and of their characteristics [25-27]. This can be explained, at least in part, by a poor control of physiological noise. The most challenging issue in SC fMRI, significantly impairing its potential, is the limited overall quality of the functional series, that emerges as geometrical distortion, signal loss, and poor contrast to noise ratio. The relevant solution can be found in appropriate experimental procedures at acquisition stage, and in a suitable post processing. In the following sections, after a short introduction to relevant features of MRI and BOLD contrast, we will discuss the main characteristics of the SC BOLD signal and sources of physiological noise in SC fMRI and possible approaches to its

mitigation, taking into account the possible impact of the biophysical origin of activity-related signal changes. This chapter is the basis to understand the next chapters about our study of the physiological origin of the SC BOLD response.

3.1 MRI basic principles

MRI may be the most widely used method for detecting pathology in the CNS because of the high tissue contrast and relatively high spatial resolution that it provides. MRI also provides several different methods for visualizing tissues and pathology in addition to detailed anatomical imaging, including functional imaging.

3.1.1 Source of the MRI signal

One of the great strengths of MRI is that the signal originates from endogenous sources, as does the contrast between different tissues, or between healthy tissue and that affected by injury or disease. For the purposes of biological imaging, the MR signal originates from the nuclei of hydrogen atoms, primarily within water and lipids. Although other nuclei can provide an MR signal, no others have the natural abundance in the body, or signal strength, that is provided by hydrogen nuclei. The MR signal originates specifically from the magnetic properties of hydrogen nuclei. When a body is placed within the strong magnetic field of an MRI system, called B_0 (with typical strengths of 1.5–3 T), the body becomes weakly "magnetized", meaning that each tiny volume of water within the body has the properties of a tiny magnet. It is important to note that this magnetization is weak, and it does not alter any chemical processes, diffusion, thermal motion, fluid movement, surface tensions, etc., and as a result, it has no known physiological effects. The magnetization is large enough, however, to be detected. After a body is placed within an MRI system, the magnetization becomes established in an equilibrium state within 1 or 2 s, it is not an instantaneous process. This state is a balance between the magnetic forces that tend to align the magnetic fields of the hydrogen nuclei in specific orientations, and the thermal motion and interactions between individual hydrogen nuclei that tend to push them into a random distribution. The equilibrium magnetization within the tissues is oriented parallel to B_0 and it has a fixed magnitude that is determined by how many hydrogen nuclei are contributing, and by the strength of the magnetic field B_0 and the temperature (although for biological imaging the temperature can be considered to be fixed). Higher magnetic fields tend to produce stronger magnetization, and therefore higher MR signal. In this equilibrium state, no MR signal can be detected though. It is necessary to push the magnetization out of equilibrium in order to detect a signal. If the net magnetization of a tiny volume of water is rotated away from alignment with B_0 it

will not simply snap back into alignment, but instead it will "precess" or rotate around the direction of B_0 .This precession is very much like the motion of a spinning top or a gyroscope when its axis of rotation is not vertical. This frequency, ω, is given by the Larmor equation:

(1) $$\omega_0 = \gamma B_0$$

The rotating magnetization creates a time-varying magnetic field that is detected, and this is the MR signal. The magnetization can be pushed out of equilibrium, in order to produce the MR signal, by a brief pulse of a magnetic field that rotates at the Larmor frequency. Because the frequency of rotation is typically in the radio-frequency range frequency range (64MHz for MRI at 1.5 T, and 128MHz for MRI at 3 T), this is referred to as a "radio- frequency" or "RF" pulse. The rotating magnetic field, B_1 must be directed transverse to B_0 and by rotating at the Larmor frequency it rotates in synchrony with the precessing magnetization so that it can be relatively weak (typically under 0.0001 T, or 1 G), and yet have a very large influence on the magnetization. The duration of the pulse can be calibrated to rotate the equilibrium magnetization any desired angle away from B_0. A 90◦ rotation will result in the strongest MR signal being detected [123].

3.1.2 "Relaxation" times

An important feature of the MR signal for imaging is the time needed to re-establish the equilibrium magnetization, after it has been disturbed by an RF pulse. As soon as the magnetization is pushed away from equilibrium it begins to "relax" back to equilibrium, with its transverse component decaying exponentially towards zero, and its component parallel to B_0 (i.e. longitudinal) growing exponentially towards its equilibrium magnitude. The rates of relaxation are different in the two directions, although they are somewhat related. They depend primarily on the interactions between hydrogen nuclei which are driven by the random thermal motion. As a result, relaxation rates depend strongly on the mobility of the water and the concentrations of macromolecules, etc., which influence this mobility. The relaxation rates reflect the chemical environment of the water within the various fluids and tissues in the body, and so they reflect physiological information. The recovery of magnetization towards the equilibrium value is an exponential process characterized by the longitudinal relaxation time, T_1. The decay of the transverse relaxation towards zero is also an exponential function characterized by the transverse relaxation time, T_2. In practice, the observed

transverse relaxation, characterized by T_2^* is the net effect of the true transverse relaxation that is driven by random thermal motion (characterized by T_2), and the effects of spatial variations in the static magnetic field. In fact, despite the efforts to obtain the most homogeneous magnetic fields possible, spatial inhomogeneities of B_0 cannot be entirely avoided. It leads to a spectral linewidth enlargement caused by spin precession at different Larmor frequencies. As a result, spin phases spread and spins coherency damps faster than according to T_2decay. In this case, the reference time-constant is T_2^* , related to the transverse time decay constant T_2 by the equation:

(2) $$\frac{1}{T_2^*} = \frac{1}{T_2} + \gamma \Delta B$$

Where, ΔB is the difference in strength of the locally varying field, so $T_2^* \leq T_2$.

In particular, the value of T_1 depends on the tissue water content, and is higher with greater water content, but also depends on lipid con- tent and tends to be lower in white matter, presumably because of the lipid content of myelin. The value of T_2 also depends on tissue water content because it depends on the mobility of hydrogen nuclei. The transverse relaxation rate $\frac{1}{T_2}$ has been shown to depend linearly on the concentrations of proteins in solution. With more macromolecules or cellular structure to interact with, the transverse relaxation tends to be faster. Although T_2^* is related to T_2, the contribution of spatial variations in B_0 can depend on the MR system and the position within the body. The information provided does not necessarily reflect the physiological condition of the tissues, and so this relaxation is not very often exploited for diagnostic imaging. However, it is extremely important for functional MRI because of how its value around blood vessels is related to the oxygenation level of the blood [123].

3.1.3 Imaging

Spatial information can be “encoded” into the MR signal by making the magnetic field strength depend on the position within the body. While the MR signal is being recorded, a magnetic field can be turned on that is static, and adds to B_0 but varies linearly in intensity across one direction. This is termed a “gradient”. In this situation, the signal that is detected will be a mix of many different frequencies. The Fourier Transform of the signal will reveal how much signal is at each frequency. Given that the frequency depends on the magnetic field strength, and the field strength depends on the position in one direction, knowing how much signal is at each frequency is the same as knowing how much signal is at each position. This approach cannot be used in two directions at the same time, but it is possible to turn on a gradient in a second direction, for a brief period of time, and then shut it off prior to recording the signal. This will make the phase of the signal depend on the position in

this second gradient direction. With enough combinations of different strengths of gradients in the second direction, applied prior to acquiring the signal with a gradient in the first direction, it is possible to have enough data to construct an unambiguous two- dimensional image. In fact, by applying a two-dimensional Fourier Transform to the data that is acquired, we can get the image that is desired. This idea can be extended to a third dimension for three- dimensional imaging. Alternatively, it is possible to apply an RF pulse while a gradient is on in a third direction, and affect only the hydrogen nuclei within a narrow range of space along this third direction, where the Larmor frequency is close to the frequency of the RF pulse. In this way a thin slice can be excited and 2D spatial encoding can be applied to this slice to create an image.

The size of the field-of-view (FOV) that is imaged depends on the strength of the gradient that is applied, and the frequency range that is sampled. This frequency range is also called the "receiver bandwidth" or BW. This value is important because it also determines the sampling rate, given that the time between successively sampled points is generally equal to 1/BW. So, it not only influences the field-of-view that can be imaged, but also how long the sampling will take. The receiver bandwidth has yet another influence, as random noise is also sampled with the signal, and the noise is proportional to the square root of the bandwidth $\sqrt{(\mathrm{BW})}$. As with any measurements, the influence of the noise can be reduced by recording more data. If data is sampled for a 2D image with N_x points along one axis and N_y points along the other, then the signal-to-noise ratio (SNR) of the resulting image depends on $\sqrt{(N_x N_y)}$. Another very important factor determining the overall signal strength, and therefore the SNR, is the volume ,V, from which the signal is being measured for each point in the image. This volume is called a "voxel". A larger volume of tissue gives more signal because it contains more hydrogen nuclei. This volume is also important because higher image resolution means smaller voxels (i.e. lower V). Putting this all together:

(3) $$\mathrm{SNR} \propto \frac{V\sqrt{N_x N_y}}{BW}$$

A final important point is that the image SNR ultimately also depends on the relaxation-time weighting that is applied to the MRI signal in order to obtain contrast between different signals. Stronger relaxation time weighting will generally cost a reduction of signal intensity, and therefore lower SNR. As a consequence of this need to balance the desired properties of the resulting images, such as speed, spatial resolution, and signal- to-noise ratio, there is no single "best" imaging method. The optimal balance of these desired properties must be found to meet the needs of each specific application, and the determination of "optimal" can be subjective [123].

3.2 BOLD-based fMRI

Since its development about twenty years ago, BOLD [2] based fMRI has become the leading research tool for non-invasive mapping of neuronal activity. The signal detected with this technique relies on the levels of oxygen in the blood and involves complex changes in regional cerebral/spinal blood volume, blood flow and deoxy-haemoglobin levels that are associated with the neuronal activation and result in altered signal intensity in T_2 and T_2^* − weighted MR images (Figure 3.1). The contrast generated is widely known as BOLD contrast (see also paragraph 1.3.2 and 1.3.2.a). The fMRI studies are usually performed with stimuli that involve anatomically distinct regions of motor, sensory or cognitive functions. The statistical analysis of the voxel time courses highlights the stimulus-correlated modulation of the MRI signal and reproduces the activation patterns in terms of statistical parametric maps.

In the following, we report an overview about the main physiological and bio-physics characteristics of the BOLD contrast.

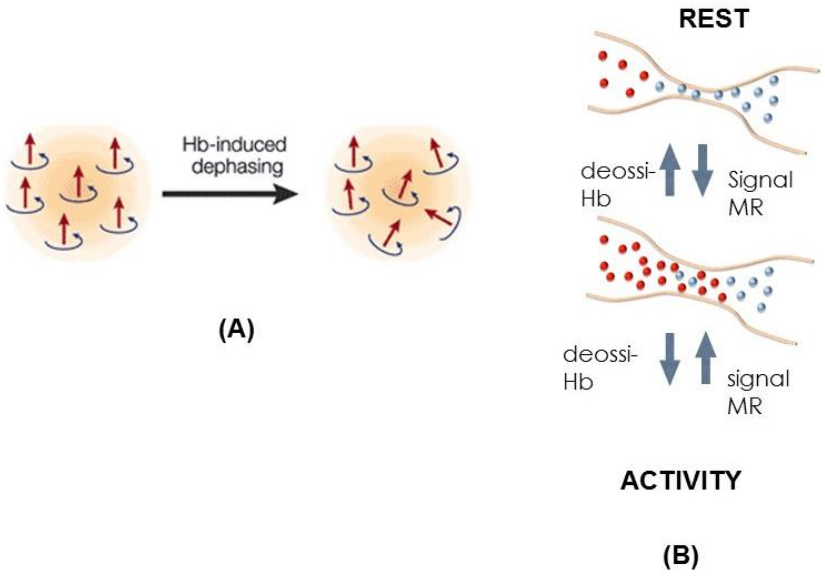

Figure 3.1: (A) The de-oxygenated state produces a loss of coherence among spins primarily detectable in the T_2^* weight. **(B)** Magnetic characteristic of the haemoglobin [70].

3.2.1Blood susceptibility

A particular treatment, due to its important role in fMRI, has to be reserved for blood susceptibility and its dependence on oxygenation. The formation of oxy-hemoglobin in red blood cells yields concomitant changes in the red blood cells susceptibility relative to its surrounding.

A model for the susceptibility of the total blood system is:

$$\chi_{blood} = H_{ct}\left(Y\chi_{oxy} + (1-Y)\chi_{deoxy}\right) + (1-H_{ct})\chi_{plasma} \quad (4)$$

where Y is the fractional oxygenation in the red blood cells and H_{ct} is the fraction of red blood cells in blood (hematocrit). It has been observed that arterial (oxygenated) blood appears to have the same susceptibility as the surrounding tissue (i.e. $\chi_{oxy} \cong \chi_{sorraound}$)[3]. Then, if $\chi_{plasma} \cong \chi_{oxy}$ (this happens for (1-Y) = 0,05, [124]), the difference in susceptibility between blood and surrounding tissue can be simply calculated by equation (4) and results:

$$\chi_{blood} - \chi_{sorround} \cong \chi_{blood} - \chi_{oxy} = (1-Y)H_{ct}(\chi_{deoxy} - \chi_{oxy}) \quad (5)$$

that is :

$$\Delta\chi_{blood,sorround} = (1-Y)H_{ct}\Delta\chi_{deoxy,oxy} \quad (6)$$

The change in blood susceptibility from fully oxygenated to deoxygenated blood has been measured to be 0.264 ppm per unit H_{ct}.

The equation (6) expresses the changes in susceptibility induced by changes in oxygenation of the blood compartment (Figure 3.1 B). This relationship can be used to calculate the corresponding induced phase variations, once the field changes are a known function of the susceptibility variations. Geometrical models, such as for example the spherical and cylinder models (the latter is discussed in the following paragraph), are helpful to describe these field changes induced by susceptibility variations in the blood compartment, since the effect depends on the geometry of the object with differing χ and its orientation to the applied field.

3.2.2 The physical source of the BOLD effect

The BOLD based fMRI technique takes advantage of the fact that no intravenous contrast medium is required: the magnetic properties of the haemoglobin, the blood oxygen-carrying protein, act as endogenous contrast agent. The haemoglobin is diamagnetic when bound to oxygen and paramagnetic

[3] This is also the reason why the functional studies are based on the susceptibility changes that occurs during neural activation only in venous blood.

when deoxygenated (dHb). Therefore, a change in the haemoglobin oxygenation state leads to changes in the local distortions of a magnetic field applied to it (Figure 3.1). In particular, the confinement of paramagnetic dHb in the intracellular space of the red blood cells (RBCs) produces a difference in the magnetic susceptibility between the RBCs and the surrounding plasma and tissue. As a result there is a spatial inhomogenity in the local magnetic field around the RBCs, and ultimately around the blood vessels (Figure 3.2). The water spins, which diffuse around the blood vessels containing dHb, are affected by these inhomogeneities and lose phase coherence. A net decrease in the transverse magnetization and a signal loss in T_2 and T_2^*-weighted images (respectively spin echo (SE) images and gradient echo (GE) images) proportional to the intravascular concentration of dHb is produced[4]. BOLD contrast was first reported by Ogawa *et al.* in 1990 [3]. They demonstrated that the signal coming from the surrounding of a capillary tube has a decrease in intensity when the tube is filled with deoxygenated blood but not when it is filled with oxygenated blood. The feasibility of BOLD contrast was subsequently shown by Ogawa *et al.* [1] in vivo on a rat model. They also verified *in vitro* other expected features of the BOLD effect, typical of susceptibility effects, such as the orientation dependence with respect to the static field. They specifically observed that the inhomogeneities were apparent only when the tube was oriented perpendicularly to the static field, because in this case the magnetic field lines crosses the susceptibility discontinuities at the interface between the dissimilar materials.

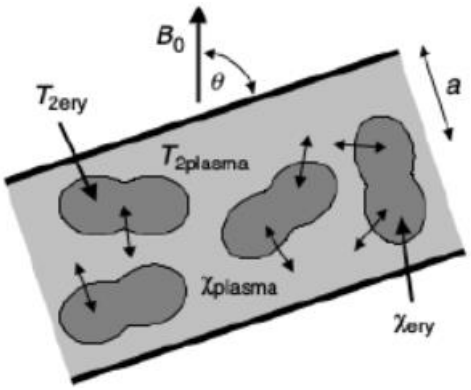

Figure 3.2: A blood vessel scheme: erythrocytes submerged in plasma [70].

[4] Field inhomogeneity due to dHb does not artefact the spin-lattice relaxation time (T_1), given that there is no motional component at frequencies near the Larmor frequency to promote energy transfer.

3.2.3 BOLD and neural events

As much as told till now, the BOLD technique works by detecting the levels of oxygen in the blood, point by point, throughout the brain or SC. The increase of metabolism triggered by neuronal activity induces an enhancement of oxygen consumption and a subsequent increase of local blood flow and volume. The overcompensating increase of hemodynamic parameters produces an overall decrease of tissutal deoxyhemoglobin content and thus an increase of T_2 and T_2^*; consequently, T_2 and T_2^* −weighted images show an intensity increase in activated regions. Such an increase enables the localization of the underlying neuronal activity with BOLD fMRI. In other words, BOLD fMRI uses hemodynamic responses as surrogates for neural function. The locally increased blood flow in regions of the brain or SC that become active appears to be a consequence of increased energy utilization. The neural basis of the fMRI signal was demonstrated directly in experiments using combined imaging and intra-cortical recordings [5]. The exact nature of this relationship was clearly assessed by Logothetis et al. [5], that obtained simultaneous fMRI responses and intracortical recordings of neural signals in monkeys. They observed that the BOLD responses can be estimated from Local Field Potentials (LFPs), thus suggesting that the BOLD contrast mechanism reflects the input and intracortical processing of a given area rather than its spiking output. In particular, the relationship between pre-synaptic input and BOLD signal changes has been demonstrated by the observation that hemodynamic changes correlate better with LFPs than either single-unit or multi-unit recordings [5]. LFPs represent the input to a given region, as well the local processing. The consequence of this relationship for fMRI based on BOLD contrast is that the signal changes reflect the net change in pre-synaptic input, whether excitory or inhibitory, presumably regardless of the net change in neuronal output. A strong coupling between LFP's and changes in tissue oxygen concentration has even been demonstrated in the absence of spiking output, supporting the conclusion that hemodynamic changes reflect synaptic more than spiking activity.

3.2.4 BOLD signal timecourse

In order to understand the biological and physical origins of the measured signal it is required to outline a typical BOLD response. This waveform response has variable shape and amplitude. Short pulse stimuli can produce an almost invariant shape waveform which can be modelled as a gamma function. The BOLD reponse can be divided into 3 epochs [70] (Figure 3.3):

- **Initial dip**: the initial dip corresponds to an apparent increase in deoxyhemoglobin when stimulation starts [125]. This phenomenon is probably due to an increase in oxygen consumption during stimulation in conjunction with a slow vascular response to the stimulus.

- **Positive BOLD response**: it is an increase in response signal that reaches a peak around 5-8*s* from the beginning of the stimulation. An intense stimulation leads to the increase of the rate of cerebral perfusion around 50 / 70%, causing an increase in the capillary oxygenation that accelerates the oxygen transport through the capillary walls. Thus the amount of deoxyhemoglobin in veins decreases, leading to an activation induced signal increase of 2 - 3% with respect to the baseline at 1.5T.

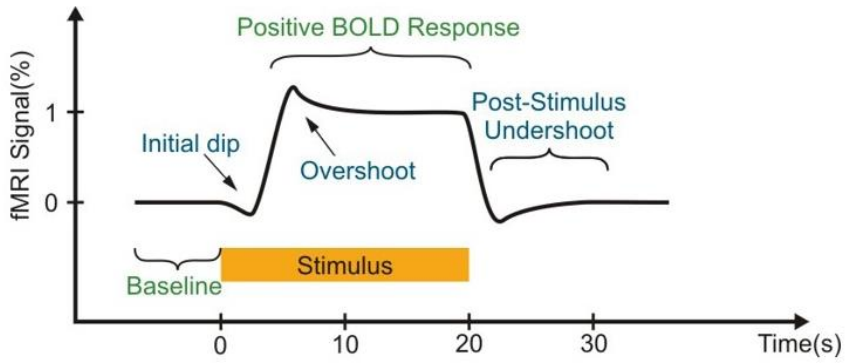

Figure 3.3: BOLD response scheme. BOLD signal can be divided in 3 dierent epochs: initial dip, overshoot and positive response, post-stimulus undershoot [70].

Oxygen does not affect the BOLD response, only deoxyhemoglobin influence the MR signal but the complementarity between oxyhemoglobin and deoxyhemoglobin leads to consider the fMRI signal as dependent upon blood oxygenation level. The positive response often shows an overshoot at its beginning, followed by an exponential decay that keeps the signal back to the positive steady-state level. The extent of this overshoot is variable and generally speaking there is no correlation between the amount of positive response and the presence or absence of the overshoot.

- **Post-stimulus undershoot:** after turning-on stimulation, the signal comes back to the off baseline. Yet, there is often a further signal decrease under the baseline, during which signal can remain negative even for tens of seconds.

3.2.5 Theoretical model of BOLD effect

A single blood vessel can be treated as an isolated compartment. In fact, during the time course of a single TE[5] (EchoTime) (typically 50 ms or less, depending on the static magnetic field intensity applied) the intravascular water diffuses freely between red blood cells and serum, but cannot exchange across the vessel wall to a significant extent. As a consequence, its resonance frequency shifts because of the rapidly changing magnetic fields immediately around and inside each red blood cell. As the blood oxygen content decreases, the magnitude of these local magnetic field differences increases with the proportion of haemoglobin that change from a diamagnetic to paramagnetic state. The extravascular water closely surrounding the vessel containing deoxygenated blood experiences a significant local field gradient, the magnitude of which depends on the proximity and relative orientation of the vessel with respect to the static magnetic field.

Modelling the vessel as an infinitely long cylinder with axis R_0, the perturbation to B_0, in terms of angular frequency, in a point *P* outside the vessel, can be expressed as follows [4]:

(7) $$\Delta\omega_B^{in} = 2\pi\Delta\chi_0(1-Y)H_{ct}\gamma B_0\left\{cos^2(\theta) - \frac{1}{3}\right\},$$

Where outside the cylinder it is:

(8) $$\Delta\omega_B^{out} = 2\pi\Delta\chi_0(1-Y)H_{ct}\gamma B_0\left\{\frac{R_0}{r}\right\}^2 \sin^2(\theta)\cos(2\Psi),$$

Where: "$\Delta\chi_0$" is the maximum susceptibility difference expected in the presence of fully deoxygenated blood; “Y” is the fraction of oxygenated blood; "H_{ct}" is the haematocrit value; "R_0" is the radius of the vessel; “r” is the distance between the point of interest and the center of the cylinder in the plane normal to the cylinder; "Ψ" is the angle between the direction of the magnetic field and the projection of the vector, indicating the position of the spin in a plane perpendicular to the vessel and the vessel orientation related to the applied field (see Figure 3.4) "$2\pi\Delta\chi_0(1-Y)H_{ct}\gamma$" represents the frequency shift (measured in Hz) induced by the degree of blood deoxygenation (1-Y) (see also equ.(6)).

[5] The **echo time** refers to time between the application of radiofrequency excitation pulse and the peak of the signal induced in the coil. It is measured in milliseconds. The amount of T2 relaxation is controlled by TE

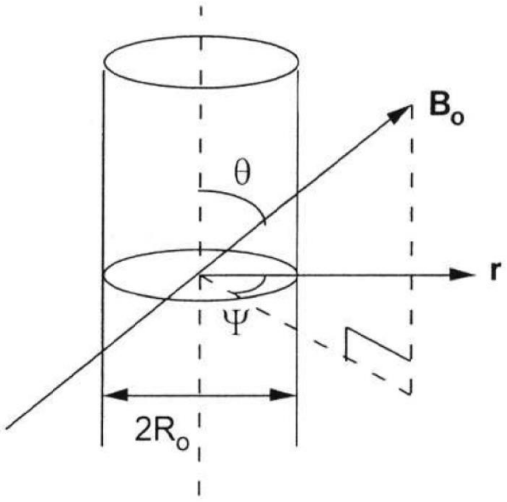

Figure 3.4: Schematic Overview of the cylinder-vessel model

The effects of the field inhomogeneities induced by dHb on the NMR signal critically depend on the comparison between the distance covered by the diffusing water spins during the echo time and the extent of the magnetic field gradient around the compartment containing the dHb (this can either be a vessel or a RBC). The variation in magnetic field across the voxel leads to a T_2^*; signal loss. Additional T_2 loss occurs if the water diffuses significantly through the field gradient. The ratio between T_2 and T_2^*; components depends essentially on the vessel size: the T_2^* component prevails when the radial diffusion path of the water molecules is small related to the typical vessel size generating the gradient, or, in other words, in proximity of large vessels, while the T_2 component prevails in proximity of small vessels.

The model developed in 1993 by Ogawa et al. [4] was able to successfully account for the main peculiarities of BOLD contrast, as the dependence on the kind of sequence utilized, the dependence on the orientation of the magnetic field, and the dependence on the degree of blood oxygenation. The physical analysis of BOLD phenomena has been extended by other groups [97, 126], which described the BOLD signal in terms of static and dynamic[6] averaging differentiating between intravascular and extravascular effects.

[6] **Static averaging:** if the magnetic field gradients extend over a scale much larger than the diffusion length, as in the case of large vessels, a water molecule at a given point in space experiences a locally time-averaged magnetic field, which varies according to its proximity to the large vessel. Consequently, the global signal S(t) is dephased and lost with increasing TE. (Remember that $S(t) \propto \sum_k e^{-i\phi_k}$, where $e^{-i\phi_k}$ is the so-called phase factor, and ϕk is the phase accumulated by each spin during TE,
expressed as $\phi(\theta)_k = \int_0^{TE} \omega_k\left(\theta, r(t)\right)dt = \varpi_k TE$.
Dynamic averaging: if the magnetic field gradients extend over a scale comparable with the diffusion length, as in the case of capillaries and RBCs, each spin experiences the full range of external fields, which, being symmetrically positive

3.2.6 Intravascular and Extravascular BOLD Signal Component

The fMRI signal changes originate from an intravascular contribution of the water molecules contained in blood and an extravascular contribution due to tissue water. Signal changes are characterized by a capillary and venous blood contribution. The arteries, rich with oxygenated blood, generally do not determine signal variations, thus they can be excluded. A voxel of an fMRI image is larger than a vein or a capillary, therefore signal coming from inside the vein or the capillary results from an average of intra- and extra-vascular effects.

3.2.6.a Extravascular BOLD Signal Component

When Ogawa *et al.* [4] proposed their physical model of BOLD effect; they considered only the contribution of the extravascular (EV) (Figure 3.6) spins, without considering the exchange that ultimately takes place between intra- and extravascular water across the capillary walls[7].

Two important formulas can be derived from their simulation:

(9) $R_2^* = \alpha\{\Delta\chi_0\omega_0(1-Y)\}b_{Vl}$ (Large vessels)

(10) $R_2^* = \eta\{\Delta\chi_0\omega_0(1-Y)\}b_{Vs}p$ (Small vessels) .

Where $R_2^* = 1/T_2^*$, α and η are constants, ω_0 is the static magnetic field in angular units, b_{Vl} and b_{Vs} are the blood volumes for large vessels and small vessels, *p* is the fraction of active small vessels (i.e. filled with dHb containing red blood cells). Eqs. (9) and (10) show the signal behaving differently depending on the blood vessel radius. In particular, for smaller vessels, the functional sensitivity increases with the square of the main magnetic field strength, while for larger vessels the dependence is merely linear. This explains the drive in fMRI to use an ever-higher main magnetic field, given that the contribution of smaller vessels, which are generally closer to the activation site, will be emphasized. Even for the capillaries, however, the quadratic dependence of the extravascular BOLD effect will not persist indefinitely with increasing magnetic fields, since at some (as yet unknown) values of B0, the frequency shifts around the capillaries will be sufficiently large to make the static dephasing dominant. Eqs. (9) and (10) have the key features of linking the measured signal with those physiological parameters which vary during activation. The deoxygenated blood fraction is related to oxygen consumption (Metabolic Rate of Oxygen Consumption $CMRO_2$) and blood flow (Cerebral

---

and negative (average zero (ϖ_k = 0). In such cases, there is no net phase change, but the wide range of susceptibility-induced magnetic fields experienced by the spins leads to diffusional signal loss, which results in a T_2 decrease).

[7] The typical life-time of water in capillaries exceeds 500 ms , significantly longer than the typical T_2 and $T2$ measured in the brain (at 1.5 T they are respectively » 100 and 70 ms, while at 4 T they are » 60 ms and 35 - 40 ms), and longer than the echo time typically used in fMRI (about 20 - 40 ms at 3T).

Blood Flow CBF) according to (1-Y) = $CMRO_2$=CBF. From Eq. (9) and (10) it is evident that an increase of blood volume or oxygen consumption results in a signal decrease, while a CBF increase corresponds to a signal rise.

Previous data obtained by means of PET strategies [127, 128] indicated a small increase of $CMRO_2$ (0 - 5%) compared to the large increase of CBF (30 - 50%) during elevated neuronal activity. Qualitatively, the BOLD signal increase is certainly consistent with this finding [127, 128]when considering the extravascular effects alone[8]. Nonetheless, the changes in neuronal physiology in response to a stimulation remains a matter of intense debate, since the BOLD signal derives from the multiple interaction of CBF, CBV and $CMRO_2$ (

Figure **3.5**), each of which may have a characteristic temporal behaviour.

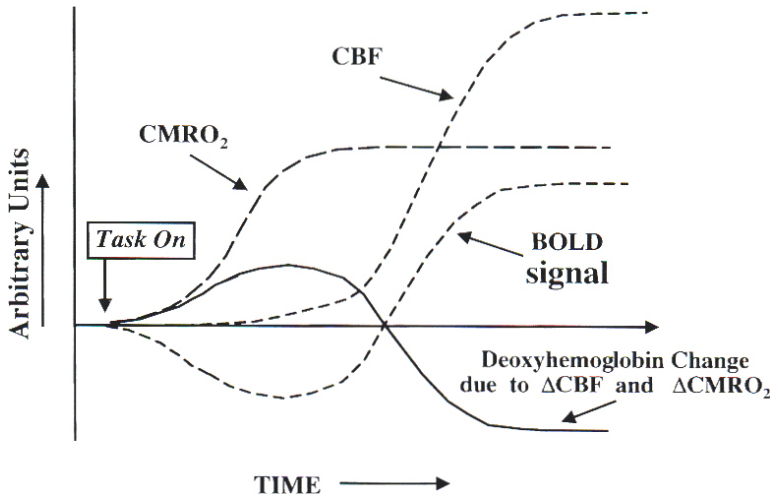

Figure 3.5: Time-courses of CBF, CBV and $CMRO_2$

3.2.6.b Intravascular effects

In order to complete the description of BOLD effect, the intravascular (IV) component must also be considered (Figure 3.6). dHb is compartmentalized within RBCs. Due to the small dimensions of RBC compared to the diffusion distances, the effects of the presence of gradients around the RBC are dynamically averaged. Given that the RBC membrane is highly permeable to water, the blood T_2 itself decreases in the presence of dHb; this effect was also shown to increase quadratically with field,

[8] This interpretation implicitly suggests that the decrease in NMR signal resulting from the elevation of CBV during activation (see Eqs.(9 and (10 and) must be smaller than the positive effect on BOLD.

as expected from dynamic averaging. Blood contribution influences the BOLD signal in a particular way when there is a large blood vessel in the voxel. Such a voxel can be considered as being composed of two large bulk magnetic moments, one associated with blood, and one with tissue. Neglecting the gradients near the blood vessels, these magnetic moments process at slightly different frequencies (the difference in frequency is given by Eq.(9), and lead to magnetization dephasing and signal loss, similar to the extravascular effect in the static regime. This effect is nulled in a SE sequence, and can be ignored either when the voxel is made up of capillaries alone (in this case the blood volume occupies a 2% fraction), or when the voxel is entirely occupied by a blood vessel.

The BOLD dependence on the vascular composition of the voxel is important and has to be considered in signal evaluation: if the voxel is constituted by a superposition of microvessels, the signal can be calculated by averaging over vessels orientations[9]; if the voxel is constituted by a single macrovessel the distinction between intravascular (IV) and extravascular (EV) spins is important, both in magnitude signal decay evaluation (where deviation from mono-exponential decay can be found) and in phase signal analysis (Figure 3.6).

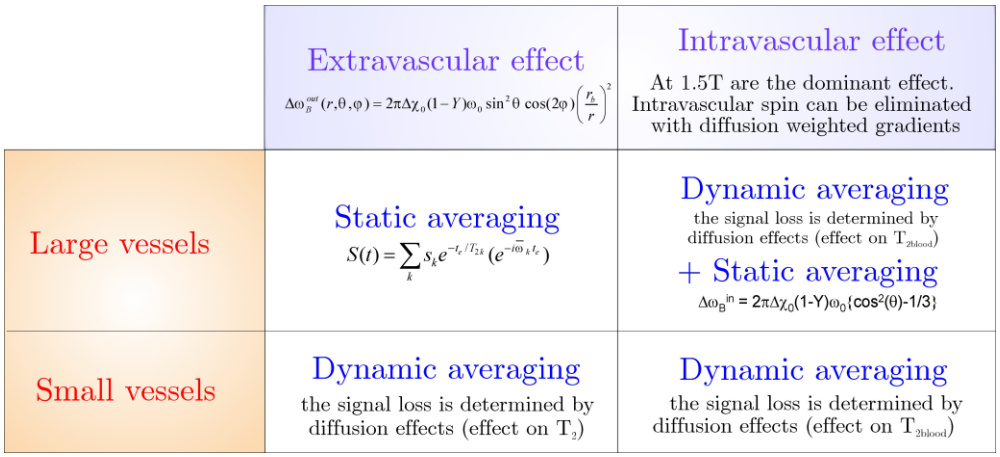

Figure 3.6: Schematic representation of the contributions to the BOLD signal from large and small vessels. The vessels here considered are always veins, or at least capillaries, since BOLD effect originates only from the venous compartment. Note that the effects due to static averaging can be eliminated by using a SE sequence.

[9] This is because in a voxel constituted by micro-vessels, contrary to techniques that use exogenous contrast agents whose susceptibility effects are an order of magnitude larger than the effects produced by BOLD contrast, the overlap of the susceptibility generated fields by neighbouring blood vessels is small and the detailed knowledge of vasculature is therefore not necessary.

3.3 Main characteristic of the BOLD contrast in the SC

As we have seen in the previous paragraph, the BOLD fMRI response in the healthy brain is an indirect measure of neural activity, related to synaptic function. Applying BOLD fMRI to the SC assumes that a similar relationship between a change in neuronal activity and BOLD signal change is present in the SC. Invasive studies have previously demonstrated mechanisms of stimulus induced alteration of spinal synaptic activity, and activity modulated changes in glucose metabolism and blood flow [129]. Recent experiments conducted using hypercapnia suggest that the vasoactive aspect of this coupling is present in the human SC and leads to BOLD signal changes [130]. In a rat model, experiments by Zhao et al. have further compared the locations of SC blood volume and BOLD contrast changes during noxious and non-noxious electrical stimulation [131, 132]. As yet, however, direct exploration of the relationship between neural activity and BOLD signal change in the SC is lacking. However, there are several reasons to expect that the function of the SC could be successfully explored using BOLD fMRI. First, the metabolic signal changes, at least during nociceptive stimuli, are larger in the SC than in the brain [133]. Second, as we have seen in the paragraph (2.6), the particular distribution of large vessels, only on the surface of the SC, should enhance the specificity of BOLD signal, even with T_2^*–weighting, due to the inherent elimination of the confounding, unspecific effect of larger vessels [134] from the grey matter signal.

Third, the grey matter of the SC, where the synaptic activity that relates to the observed BOLD response takes place, is largely surrounded by white matter, while the larger draining veins are positioned peripherally, at the cord surface. Thus, the white matter may protect the BOLD signal arising in the grey matter from partial volume effects with both the cerebrospinal fluid (CSF), which is heavily prone to motion-related signal variations, and from the confounding BOLD signals arising in the distal draining veins [135].

These advantages are counterbalanced, however, by several factors that make the collection of functional MR images of the SC difficult to achieve. The SC has a relatively deep location, a small cross-section and a long rostro-caudal extent; these anatomical properties lead to inefficient MR signal reception. The surrounding vertebral structures and the conformation of the head, neck and body impose significant magnetic field inhomogeneities that can lead to image distortion and signal loss. In addition, the SC lies in close proximity to the heart and the lungs that are strong sources of physiological noise [5, 11, 77, 79]. In the next paragraphs we will described the different kind of noise that affect the SC BOLD signal.

3.3.1 Sources of physiological noise in the BOLD based fMRI spinal imaging

Physiological noise in SC fMRI time series shows some specific features that differentiate it from the noise routinely encountered during the brain fMRI. Particularly many difficulties in spinal fMRI arise from:

1) The specific anatomic features of the SC, as described above. In particular, the small cross-sectional area and large rostro-caudal extent of the SC, and its variable curvature imply a low signal, because of the constraints they impose on the voxel size. In spite of the small voxel size usually employed, a significant and variable contamination of the signal occurs because of partial volume effect and motion.
2) The proximity of the SC to several structures of different density (vertebrae, intervertebral discs) gives rise to large variations in magnetic susceptibility and determines a relatively poor local magnetic field homogeneity, causing image distortion and low signal intensity in standard T_2*-weighted fMRI with EPI readout.
3) The motion due to the task itself can be of particular concern in studies employing motor tasks. Indeed, limb movements give rise to millimetre displacements in the position of the nerve root(s) serving the moved limb, which might translate to small stimulus-correlated movements of the cord, but may also, in the case of neck flexion, give rise to large longitudinal shifts of the entire cord
4) The physiological motion displaces the cord and generates signal intensity changes near its superficial layers. These movements are primarily due to the cardiac-driven pulsation of cerebrospinal fluid (CSF) within the subarachnoid space surrounding the cord [136]. Another potential source of cardiac-related noise is the systole-induced pulsation in spinal arteries. In particular, it was observed by Piché et al. [137] that cardiac noise is distributed irregularly along the full rostrocaudal extent. In addition, respiratory effects may either take the form of bulk movements of spinal and connective tissue, due to shifting tissue mass as the chest wall rises/falls, or to bulk changing susceptibility effects. This problem was previously noted in the brain [138], but it is of much greater significance to functional imaging of both the SC and the brainstem [139].

Whatever the origin of SC motion, it produces time-dependent partial volume effects along the cord/CSF or cord/vessels interfaces. In addition longitudinal motion of tissues between adjacent slices may change the effective repetition time (TR), depending on the direction of motion and the slice orientation. In the (Appendix C: Physiological noise) we analyse the different noise sources.

In SC, as in the brain, physiological changes are often aliased into frequency regions of interest for the functional paradigm, thereby mimicking it and reducing the statistical significance of actual task-related signal changes. In particular, low-frequency noise, due to the phenomena previously described, is a very large source of systematic error in spinal fMRI studies, contributing to both false-positive and false-negative result. Effects of CSF flow and physiological noise in general have been investigated using flow-sensitive EPI [140]. It was shown that it is possible to observe cardiac and respiratory effects in critically sampled (short TR =160 ms) single-slice EPI data, taken along the SC. In addition, it was found that CSF flows caudally during systole and rostrally during diastole, showing its cardiac dependence. The signal changes, that are proportional to the flow rate, occur as fresh CSF spins flow into the imaging slice. The effect was also shown to be dependent on the phase of the respiratory cycle at the image acquisition time [141]. Possible methods and strategies for reducing physiological noise, which take into account its features and the interactions between its causes, are discussed in the following section (paragraph 3.4).

3.3.2 SC fMRI time course

The temporal resolution of the SC fMRI studies is often limited by the temporal averaging or filtering [8, 9, 11, 18, 26, 142]. Stroman and Ryner [12] obtained the best temporal resolution, about 10 s, using EPI and breath holding to reduce motion. The poor temporal resolution is a strong limiting factor for the resolution of the shape of the transient phases of the hemodynamic response. The time to reach the maximum effect is substantially longer than in brain and has been evaluated in 20–30 s for motor task and in about 15 s for sensory stimulation [12]. The slow rise of signal during the stimulation has been regarded as an indirect proof that the observed variation is related to physiology and is not artefactual, as most confounding effects (like motion or task-related flow) should increase immediately after the onset of the task [12]. The ostensible slowness of fMRI signal during blocked tasks strongly suggests an impulsive hemodynamic response function (HRF)[143, 144] different and slower than in brain. The physiological reason for this feature is not clear. Giulietti et al. [17] determined the impulse response function (IRF) of the BOLD response in the cervical SC to a 1-Hz ball-squeezing task performed for periods of 3, 6, 9, 15, 21, 27, and 42 s. They estimated a full width at half maximum of 9.14 s and a peak latency of 9.34 s, both values being longer than the corresponding ones in the brain. This indicates that greater temporal damping of the hemodynamic response occurs in the spine. At the minimum task duration of 3s, the response did not fit the modelled HRF, suggesting a non-linearity in the response at short durations.

3.3.3 Signal specifity:

Anatomical localization of the response

fMRI is able to reflect functional responses along polysynaptic pathways, even activation of a simple network may be associated with widespread responses within the spinal grey matter.

In the last decade, experiments based on the task-dependent modulation of spinal cord fMRI activations signal in response to innocuous and painful sensory stimuli or motor tasks have been performed. The resultant fMRI signal was found to increase in sites consistent with the known functional neuroatonomy of the spinal cord. Different groups observed activity changes in the cervical spinal cord during a motor task of the upper limb movements [6, 11, 12, 18, 26]. Yoshizawa et al. performed one of the first studies about the intensity changes in BOLD signal between rest and hand exercise (*i.e*., opening and closing the right hand) [6]. In particular, their preliminary results demonstrated a local regional activation in the fMRI signal of the human spinal cord during motor tasks in correspondence of the two cord segments interested by hand movements. Stroman and his colleagues identified the corresponding anatomical location in the ventral grey matter of the spinal cord during a motor task that consisted in squeezing a rubber bulb with one hand. fMRI intensity changes, corresponding to motor areas ipsilateral to the hand being exercised, between the C6 and T1 segments [11, 12, 142]. Also Madi et al. [18] first attempted to demonstrate a spatial specificity of spinal activity related to movements of the finger, wrist and elbow (Figure 3.7). In a small subject population, they found a rostro-caudal ordering of the foci of activity consistent with the functional organization of sensory and motor circuits, albeit located slightly caudal to the expected spinal level.

At 1.5 T, bilateral lumbar activation accompanying both passive and active pedalling has been demonstrated by Kornelsen and Stroman [145] in the dorsal horns of SC segments S3 and S2, and in the ventral horns of the L4 through L1 segments. Compared to passive pedalling, active pedalling yielded a significantly stronger response in the dorsal horn between the L1 and L4 levels, and in the ventral horns at L5.

The characterization of the somatosensory activity in the human SC was investigated by fMRI, performing a sensory task applied to the hand, forearm and lower leg using spin-echo or gradient-echo MR sequence. Stracke et al.[146] , using skin indentation applied to individual fingers, reported that only stimulation of the thumb gave rise to consistent activation at the expected level in the majority of subjects. In addition, a focus of activity was found in the C3-C4 region in all subjects, independent of the stimulated digit. The authors attribute this rostral focus of activation to propriospinal neurons that have been demonstrated in the cat to integrate and project input from several descending pathways (corticospinal, rubrospinal, tectospinal and reticulospinal), possibly

mediating the command for reaching movements [147]. A C3-C4 propriospinal neuron system has been demonstrated in macaque monkeys [148], and indirect evidence suggests that the system also exists in humans [149, 150]. In a pair of studies, a thermal stimulus was applied to a series of dermatomes on the arm [9] and to the calf [13] , while in the other [151], vibratory stimulation of Aβ fibres (see CHAPTER 2) was applied to the hand palm and to the joints of the arm and of the leg.

Thermal stimulation of the median aspect of the palm elicited a response in SC segments C5 to C8 (peaking at C6), while thermal stimulation of the ulnar side of the palm elicited a response in SC segments C7 and C8. Vibratory stimulation of the palms and wrist yielded apparent peaks of activation at the C7 level. Thermal stimulation of the forearm and vibratory stimulation of the biceps yielded activation over the C5-C7 and C6-C7 spinal levels, respectively. In the lumbar SC, activation was observed throughout the T12-L5 range in response to thermal stimulation of the calf (L4 dermatome). Vibratory stimulation of both the knee and the Achilles tendon elicited a response centred at the T11 and T12 levels [151].

In a recent study using BOLD contrast, Summers et al. [87] recorded the SC responses to noxious and innocuous somatosensory stimuli (induced by laser heating and brush strokes, respectively) applied to a portion of the hand dorsum corresponding to the C6-C7 dermatomes. Significant responses were found to both noxious and innocuous stimuli in both the ipsi- and contralateral sides of the cord. Crucially, these responses were significantly larger than the noise levels measured in a corresponding scan at rest. In accordance with the results of Summers et al previous studies [152, 153], BOLD signal increases following noxious stimuli were significantly higher than those elicited by innocuous stimuli. The resultant fMRI signal was found to increase in sites consistent with the known functional neuroatonomy of the SC.

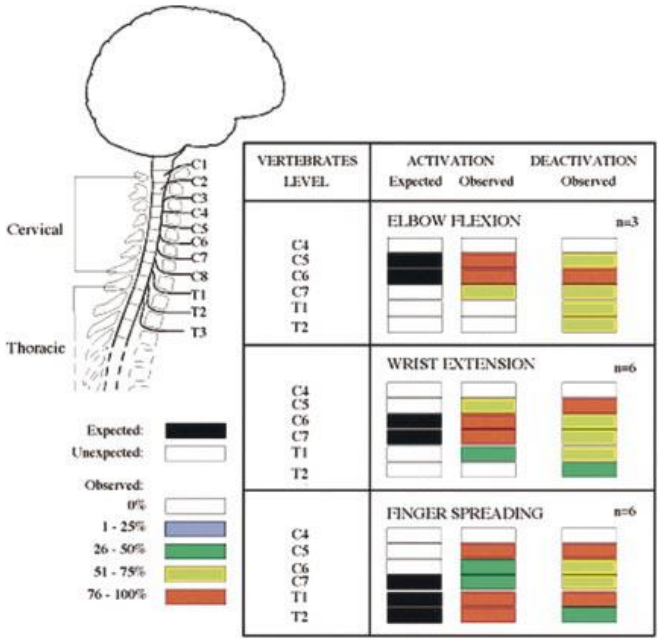

Figure 3.7: Activation/deactivation sites (increased/decreased BOLD signal) evoked by three different motor tasks: elbow flexion, wrist extension, and finger spreading. Chart shows frequency of significant signal increases or decreases, on a segment-by-segment basis, across the subjects imaged (elbow flexion, n 5 3; wrist extension and finger spreading, n 5 6)[18].

Distribution neuronal activity with motor and sensory stimulation

As we have seen in the (CHAPTER 2) the main activation in SC is expected to be ipsilateral with the stimulation. Nonetheless, also contralateral activation was often observed [6, 9, 11-13, 26, 145], occasionally intense as the ipsilateral one [6, 26]. This is somewhat unexpected, and probably, interneuron activity cannot completely account for this phenomenon. It is not clear whether the contralateral activations are expression of real contralateral activity, or they are simply artefacts. In order to explain these activations, the regulation of motor control, or even the execution of unobserved shadow movements or their conscious inhibition, has been involved [6] . Contralateral activation is expected when muscle pain is involved, but a more prominent ipsilateral activation was instead observed with thermal noxious stimulation [13]. Very often, motor stimulation resulted in an activation of the mediolateral zone of the grey matter, with a slight enhancement of ventral horns. Sometimes, also dorsal horns resulted active [6, 11], with intensity comparable or even major than in ventral areas. The presence of unexpected dorsal activation during motor tasks can be partially ascribed to proprioceptive input and -less probably- touch, in particular for larger hand movements. In any case, it is likely to reflect also the insufficient in-plane resolution and the incorrect registration of images. Ventral activation in correspondence to thermal stimulus [9, 13, 145] is less surprising because of interneurons activity. Dermatomes are innervated by fibres from a single nerve that connects to a single spinal segment, but dermatomes partially overlap; the stimulation of single

dermatomes has been shown to roughly map to the corresponding spinal areas [9, 12, 13, 145]. A certain degree of distribution of activation among adjacent SC segments is nonetheless expected, in particular, for thermal stimulation, as interneurons can spread the input to several spinal segments [9, 13, 145]. Unfortunately, some differences in the fMRI patterns corresponding to the stimulation of different dermatomes are observed only after the application of a clustering post-processing routine that facilitates the emergence of such a feature. If no clustering is applied, the stimulation of different hand dermatomes induces fMRI activation patterns that are indistinguishable from each other, and partially referable to false activations [9]. The activation spreading among segments was observed also during motor tasks [18, 26, 145]. When specific motor tasks are used, designed to require the movement of individual muscle groups innervated by nerves proceeding from different spinal segments, the observed activation spreads on more segments than expected, but the activation in extra segments is less consistent across subjects [18]. This finding suggests a prominent inter-subject variability, perhaps in relation of different ability in the accurate execution of the task or also in the muscle innervation. A possible artefactual origin of some unexpected features of the signal can be hypothesized as well. Interestingly, also, areas of reduced BOLD response were observed; negative response was more diffused than positive one, and it was similarly clustered [18]. The spreading of activation beyond the expected areas suggest conducting electromyography studies in conjunction with spine fMRI to exactly assess the activated muscles.

3.4 Addressing physiological noise in SC fMRI

Physiological noise mitigation in SC fMRI requires strategic actions at both experimental and post-processing stage. In the following two sections, we will discuss these points separately.

3.4.1Acquisition strategies

Several methods have been developed for reducing physiological noise in fMRI time series, but until now, a consensus method for spinal fMRI studies does not exist. To date, fMRI studies of the brainstem and SC based on conventional brain fMRI methods (T_2^*-weighted EPI) [76, 110, 154] have succeeded in detecting activity with reasonable reliability.

The very first and conceptually easy mitigation approach for physiological noise, in SC fMRI, was applied from the very beginning of research in this area [6]. It consists in a tailored choice for voxel size, with smaller dimensions than in comparable studies performed on the brain, and possibly a larger rostro-caudal dimension than transversal one. This choice capitalizes on both the anatomy of SC, showing a roughly axial symmetry, with putative activations spanning for at least one spinal segment,

and smaller transversal area, as well as on features of the physiological motion, that shows reduced transversal versus longitudinal displacements, as discussed earlier. This approach attempts at minimizing time-varying partial volume effects at tissue interfaces, and intravoxel signal cancellation because of magnetic field bulk inhomogeneity. The obvious trade-off between physiological noise reduction and intrinsic signal to noise ratio (SNR) loss limits the effectiveness of this method.

In principle, the effects of physiological motion have been assessed for both GRE and SE spinal fMRI techniques but, in spite of this knowledge, further improvements in the sensitivity, specificity and reproducibility of SC fMRI measurements are needed.

Half Fourier turbo spin echo imaging is considerably less sensitive to magnetic field inhomogeneity than gradient-echo methods, and fast spin-echo methods suffer less distortion than spin-echo methods with an echo-planar spatial encoding scheme. Stroman et al. have suggested a SC fMRI method based on a single-shot fast spin-echo (SSFSE) [14]. Of course, the choice of image weighting has a significant impact on the sensitivity to specific biophysical contrast mechanisms (i.e. SEEP vs BOLD). Early experiments suggested that cardiac gating yielded modest advancements in the sensitivity of GRE spinal fMRI [154]. However, because of the complex nature of CSF and SC [72] motion, it is doubtful that cardiac gating alone is sufficient to fully eliminate motion-related noise [72]. Uneven TR is also a concern because of variable T_1 saturation, if TR is kept short. However, it was shown recently that quantitative T_2^* data (derived from dual echo EPI series) allowed to reduce drastically the cardiac noise in fMRI of the brainstem, mitigating the non-equilibrium magnetization problems related to uneven TR during cardiac gating [155]. Considering that cardiogenic pulsatile motion is a major source of physiological noise in both brainstem and SC, this approach can offer advantages for spinal fMRI, as well. In general, multi-echo EPI approaches have been shown to be useful in brain fMRI, particularly in the areas most affected by susceptibility effects [156]. All the advantages reported in the brain, including equalization of contrast between areas with different T_2^*, enhanced sensitivity, and reduced artifacts, appear to be especially beneficial in the context of SC fMRI, assuming that a sufficiently fast readout can be obtained. This condition is needed in order to avoid distortion at later echoes, and to obtain a range of TE values wide enough to confirm the advantages reported in the brain. The implementation of a SE fluid-attenuated inversion recovery sequence for reducing CSF inflow artefacts did not show consistent task-related signal changes [157], probably due to the inherent T1-weighting added as a result of the inversion recovery module. Motion artefacts have been shown to be reduced by means of flow compensation gradients and spatial saturation pulses, to eliminate signals arising from anterior to the spine (i.e., from the heart, lungs and throat) and surrounding it.

To obtain high resolution SC images, most studies have used axial orientation with relatively large slice thickness and high in-plane resolution [17-19, 26, 71, 131, 158] Another strategy is to image in sagittal orientation using isotropic voxels and thin slices. The latter approach offers the benefits of extensive spinal coverage using only a few slices [27, 146], and of reduced partial volume contamination. Moreover, the sagittal approach produces better resolution in the R/C direction, which is of interest to localize properly the location of activated clusters. Because of the limited SNR, the disadvantage of having isotropic voxels is represented by the difficulty to reach high spatial resolution in the SC cross-section. This is desirable to precisely assess the lateralization of the activation, [19]. The choice of imaging plane has also an effect on distortions. The dimension with lower bandwidth (Phase encoding in EPI, usually readout in conventional imaging) is expected to carry on higher distortion and signal cancellation if inhomogeneous areas are spanned, thus possible choices include sagittal or coronal acquisition, with orientation set so that the direction more sensitive to artefacts crosses the least inhomogeneous tissues. Alternatively, axial slices can be prescribed unevenly spaced, to be centered either on a vertebral body, or on an intervertebral disc. No quantitative assessments exist about the effectiveness of these optimizations.

Spiral EPI sampling has been shown to be less sensitive to motion artefacts in the brain [159]. Methods combining spiral in/out trajectories have further advantages in terms of diminished susceptibility-induced signal dropout and increased BOLD signal. This technique provide a good choice for many fMRI applications, and can be especially beneficial. Very recently, double-shot spiral-in spiral-out trajectory was exploited for the characterization of somato-topic organization of nociception in the human SC [160]. Albeit results can be questioned, the approach is promising, and it could be a possible solution for some of the quality problems in SC fMRI.

Motion effect are more easily corrected and physiological noise can be more effectively filtered during post-processing if high sampling rate is employed. A substantial reduction of TR, with no intrinsic SNR disadvantages, can be obtained with simultaneous multislice (multiband) EPI excitation and sampling[161]. The method was never applied on SC, however can offer significant advantages; given that it relies on the same unfolding approaches used for parallel imaging, a proper design of the coil is needed, a not trivial task for coils suitable for SC fMRI.

3.4.2Post-processing strategies

Physiological noise represents a nontrivial issue. In fact, it reduces the statistical power of fMRI experiments, and causes temporal signal correlation of otherwise uncorrelated areas, altering the

analysis of fMRI data. Several methods have been proposed for reducing physiological noise in spinal fMRI, generally derived from approaches developed for applications in brain studies.

These methods can be divided into two main groups, characterized by different analytical approaches:

1) Approaches based on General Linear Model (GLM) *fitting* of non-interest (noisy) signals at inference stage (see Appendix D: Several approaches to fMRI data analysis can enhance the detection of signals within or across subjects. and Appendix E: General linear modelling. Generally, physiological recordings (or derived quantities) are used as regressors for physiologically-generated variance.
2) Direct *subtraction or filtering* of noise components during pre-processing. Noisy signals are identified because of their spatio-temporal features, also exploiting explicit recording of physiologic parameters.

There is some degree of overlap between these 2 groups, because a given noise model can be equally suited to be included in GLM or in some pre-processing step, however we will discuss them separately, taking into account the implementations presented in the literature up to now.

3.4.3Noise fitting

Albeit statistical inference on fMRI data can be conducted in many ways, GLM gained a dominant position in the neuroimaging community, and this fact is reflected by its use in noise fitting approaches in SC fMRI. It is based on a linear regression using a stock of functions that are assumed to model fMRI time series (supposed to be linearly dependent on neural activity). Thus, it allows to statistically test the contribution of each explanatory variable, at every voxel of the volume series. The physiological counterpart of this statistical test is that neuronal activity – whose timing is usually under control – induces a local hemodynamic response, giving rise to the BOLD. In the case of spinal fMRI, the physiological noise significantly contributes to the total variance of time series [25]. Hence, when modelling the signal with the GLM, the physiological noise can be taken into account, using specific regressors.

The RESPITE method (Retrospective SC motion time-course estimates), specifically tailored on SC fMRI, is the main method of this class. This method is incorporated [162] into an automated GLM analysis, creating subject and slice- specific models of SC motion to reduce physiological noise. RESPITE is an extension of previous attempts at mitigating physiological noise in brain studies [163], exploiting recordings of respiratory and cardiac activity during fMRI series acquisition.

RESPITE was developed after extensive characterization of SC motion during heartbeats in the context of fMRI [72]. In particular the cardiac-related components of anterior/posterior (AP) and right/left SC motion have been studied with cardiac-gated fast imaging [72, 164], showing that SC motion depends on the cardiac phase at the imaging time, assuming that readout time is kept short enough. It was shown that the first 3 principal components (PCs) of SC motion in AP direction as a function of cardiac phase (collectively evaluated on a group of 10 subjects) are sufficient to estimate the SC motion of each subject [163].

RESPITE terms are generated from the 3 PCs mentioned above, replicated for periodicity, temporally stretched or compressed to match the cardiac phase during fMRI acquisition, and finally resampled on the slices acquisition raster [162, 163]. RESPITE terms are then included as nuisance regressors in the GLM. The method is merged to processing steps that lead to spatial normalization and motion correction of fMRI data spanning the entire brainstem and cervical SC [164]. An intrinsic advantage of this comprehensive approach is that the labelling of anatomic regions (i.e. CSF areas) can be useful in further processing steps.

RESPITE methods performed well in comparison to uncompensated analysis approach, showing sensitivity and specificity improvements by ~ 15-20 % and ~ 5-6 %, respectively [162]. The crucial feature of RESPITE is that nuisance regressors are derived by assuming a stereotyped motion response as function of cardiac phase. An intrinsic advantage is that overfitting is avoided, because of the very low number of regressors. However, the applicability of PCs measured on a small group of subjects to the whole population is not granted, especially considering impaired people with possibly abnormal SC motion features.

3.4.4 Noise suppression

The broad category of noise suppression includes processing steps aimed at reducing the prevalence of noise in fMRI series before statistical inference. Some trivial steps, like low-pass filtering, are supposed to help, albeit they are not specifically tailored on physiological noise, which is characterized by extensive aliasing at the usual TR range. Adaptive filtering has been shown to be effective in brain fMRI data [165], and it can be effective, in principle in SC fMRI. However, it was recently shown that in SC fMRI explicit noise modelling (see below) outperforms the selective averaging filter (SAF) in terms of the residual signal variations and activation statistics [163, 165].

Hu et al. [164] and Glover et al. [166] have introduced two similar approaches for physiological noise fitting and filtering. Both methods assign cardiac and respiratory phases to each acquired image slice, based on simultaneous recordings of respiration and cardiac pulsation. These parameters are then

modeled using a low-order Fourier expansion, fitted to the data and then subtracted. These method differ, in that the former operates on k-space date, and the latter (dubbed the retrospective image correction method (RETROICOR)) on the images domain. It should be noted that the RETROICOR technique has been implemented also through a GLM approach [166, 167].

Physiological noise correction methods were refined for applications in the brain at higher field [168] [169], showing that the introduction of a higher number of noise repressors is beneficial. Several new regressors derived from physiological recordings were introduced, including the heart rate (HR), respiration volume per unit time (RVT), motion correction, and the associated cardiac and respiratory response functions [86]. All these improvements are expected to be beneficial in SC fMRI, as well. Indeed, it was demonstrated the utility of RETROICOR in the context of GE-EPI based SC fMRI [170].

Recently, Brooks and colleagues [25] systematically studied the features of physiological noise in SC fMRI, introducing a new physiological noise model (PNM) based on RETROICOR, which, as usual, exploits cardiac and respiratory traces. Their model relies on the probabilistic independent component analysis (PICA)-based assessment of signal sources in SC fMRI time series, in order to define additional terms to the Fourier expansion used by RETROICOR. These latter terms essentially account for the interaction between cardiac and respiratory noise. Furthermore, PNM considers additional regressors, taking into account the presence of low-frequency signals, which are not directly attributable to simple cardiac or respiratory effects. These regressors are: blood CO_2 concentration, respiration volume per unit time (RVT), estimated using the methods of Birn et al. [169] and representing the rate and the depth of breathing, and finally the temporal derivative of RVT.

It was shown that the optimal PNM included cardiac and respiratory terms, their interaction, and low-frequency regressors. It included in total 37 regressors. (RETRO37). In comparison with standard RETRO10, it resulted in a reduction of false-positives. In addition, it was observed that the inclusion of the CSF signal regressor was crucial, as it explained a significant amount of otherwise unmodeled signal variance in the cord and increased the number of active cord voxels. Finally it was found that the use of pre-whitening[171] – together with PNM regressors on spinal fMRI data – reduces non-white noise, which was not accounted for by physiological noise correction, and decreases false positive detection rates. This approach was successfully exploited for the assessment of cervical spinal activations during painful thermal stimulation.

Alternatively to RETROICOR, there are methods based on the extraction of the physiological noise from the fMRI data itself. One such method, introduced by Perlbag et al [172], performs a correction

of structured noise using Spatial Independent Component Analysis (CORSICA). CORSICA is based on the estimation of a noise map using the spatial independent component analysis (ICA) and removing the corresponding components from the functional data before testing for the effect of interest. The noise components can be identified in two different ways: 1) using anatomical priors [172], or 2) using a separate data acquisition with a short TR to assess the spatial distribution of noise at rest. In this way it is possible to avoid aliasing for the cardiac signal (which typically ranges from 0.8 to 1.4 Hz). CORSICA was demonstrated to be useful in reducing the physiological noise in brain fMRI time series by Schrouff et al. [173]. The main assumption of CORSICA is that physiological noise is spatially structured; indeed, it was demonstrated by Piché et al [137]that cardiac-related noise is spatially structured and stable within each individual.

Recently, Xie et al showed that CORSICA can improve the sensitivity and specificity of BOLD responses to nociceptive stimuli in the cervical SC [173].

An approach conceptually similar, but different in its implementation, is Component based noise correction (CompCor) method, that builds noise regressors on the principal components of the signal extracted from anatomically defined noisy areas (chiefly CSF, aCompCor), or from areas showing higher temporal fluctuations (tCompCor) [174]. The method was never applied to the SC. In the tCompCor flavor, it can possibly include some functionally eloquent areas in the noise model, because of the high expected functional response [17].

Another strategy to reduce physiological noise, recently introduced in brain fMRI, is the inclusion of signal derived from the first, very short, TE in a dual echo (spiral) sequence as a nuisance regressor for filtering the data of the second echo, acquired at conventional TE. Short TE data were reported to show variance mainly related to physiological fluctuations and motion [175]. It could be applied for the correction of physiological noise in the SC fMRI, assuming a purely BOLD origin of the contrast. Of course, this approach preserves only susceptibility effects, and would filter-out any proton density SEEP component, and thus can be useless in SC fMRI, depending on the active contrast.

Summary and conclusions

fMRI of the human spinal cord offers a novel means of non-invasively studying the processing of information to and from the body. The studies of spinal somatosensory and motor systems performed to date provide reasonable evidence that task-related activity of physiological origin can be detected with spinal fMRI.

In this chapter, a review of the current knowledge and major issues about fMRI in the human spinal cord is presented, with emphasis on the main methodological and technical problems.

In addition, in the first part of the chapter we have described the principles of the MRI and the basis of the BOLD.

In particular the objectives of this chapter are to describe:

1) the features of the BOLD based spinal fMRI and the differences with the brain fMRI;
2) the current state-of-the-art of human SC fMRI (also see paragraph 1.3.2.b about SC fMRI capabilities and applications);
3) the main difficulties facing researchers attempting to image the spinal cord function that gives rise to large variations in magnetic susceptibility, the influence of physiological effects that displace the cord or generate noisy signal intensity changes near its superficial layers, and passive displacements of the cord in response to limb movement;

to identify the greatest current needs, from a research and clinical point of view.

This chapter is a necessary starting point for this thesis, which will hopefully help the reader in understanding the next chapter.

CHAPTER 4

CHARACTERIZATION OF FUNCTIONAL MRI SIGNAL IN THE HUMAN SC: STUDY OF THE LINEARITY IN BOLD CONTRAST

fMRI has emerged during the last decade as the main non-invasive technique for the investigation of human brain function. As we have seen in the previous chapters, similar approaches have been repeatedly attempted in the SC, but have not yet been widely adopted as a tool for the assessment of SC function. One of the reasons for this slow adoption is that features of the functional contrast in the SC are still to be established. Several studies on humans [9, 11, 16, 18, 26, 77, 79, 121, 142, 145] have reported signal amplitudes similar to the brain ones, with an increase spanning from 3 to 5% above the baseline [19, 71]. In addition Previous works had shown a linear relationship between the intensity of an isometric task and the amplitude of the fMRI signal [18] and a modulation of the response amplitude induced by the intensity of a cold thermal stimulus [9]. However, despite the increasing numbers of reports of spinal fMRI studies in the literature, there is not a clear and full knowledge about the characteristics of the functional signal.

The investigation of the characteristics of the SC functional signal, and in particular its linearity, is crucial for the physiological characterization of the BOLD response and also because the analysis of fMRI time series is generally based on the assumption that the signal is linearly linked with the underlying neural activity.

In this framework, we studied the relationship between the intensity of the stimulation and the amplitude of the functional response in humans during a controlled motor task (graded isometric force) with the dominant hand.

In the following we report the results obtained, we found the SC BOLD response to be characterized by a strong parametric dependence on the stimulation strength. In particular, stimulation elicited a response roughly proportional to the applied force. The results confirm the physiological origin of the response, and will be of great help in model-based spinal cord fMRI inference.

4.1Intensity dependence of the BOLD response in spinal fMRI

fMRI techniques based on the BOLD signal [2, 176] are well established for the indirect study of the neuronal activity in the brain [5]. Extension to the spinal cord [2] has proven to be difficult. [24]. Beyond technical issues, that are still partially unresolved [16, 79], general acceptance of spinal cord fMRI is hampered by the fact that features and origin of the functional contrast are not fully understood yet. In particular, it is still unknown the exact relationship between stimulation features and fMRI response. Indeed, being fMRI an indirect effect of neural activation, the properties of this relationship are governed by a combination of the neural response with the spinal cord neurovascular coupling.

The features of spinal neurons activation are fairly well understood at neural level, thanks electrophysiological studies on animals. In particular, electrophysiological evidence with thermal stimuli demonstrated a clear stepwise response with each increase in temperature (from 36 to 52 °C), while the sustained heat application, results in a stillness response [177, 178]. In addition it was found that a painful cold sensation induced a rapidly rate increases at temperatures from 15 °C to 10 °C [179].

Repeated noxious thermal stimuli were found to induce an enhancement of background rather than a change of evoked response in monkey spinotalamic tract [180], whereas spinotalamic cat neurons showed a variegate response to increasing heat or cold stimuli, according to their class. Each class of neurons indeed broadly showed a linear stimulus-response function within a given temperature interval, and divergence from linearity (in the form of either an acceleration of response or a plateau) outside that interval [181].

Spinal motor neurons were functionally characterized on monkeys performing motor tasks. A linear relationship between the contractile force and the firing rate of the elements of the spinal circuitry involved was generally found, with some ceiling effect at the highest forces [80, 182, 183].

In humans, an inverse relationship between the recruitment threshold and the firing rate of motor neurons in voluntary isometric contractions was found by electromyography. However, at any given recruitment threshold the firing rate increased monotonically with applied force [184]. Interestingly, the hierarchical firing rate organization of motor units is altered during high frequency oscillatory contraction (frequencies $\geq$ 2Hz), when higher-threshold motor units increase their activation, while response of lower-threshold ones decrease; the phenomenon was attributed to a gradual switch from a graded activation response towards an on-off response when the applied force is quickly modulated [185].

The spinal cord fMRI response to graded stimuli is not yet fully characterized. Several works reported task-dependent modulations of spinal cord fMRI signal in response to various classes of stimuli.

Functional response to motor task of the upper or lower limb was reported at various levels of the spinal cord, broadly corresponding to the expected localization of the neural response [6, 11, 12, 18, 26, 142, 145, 186].

Yoshizawa et al. performed one of the first studies about the intensity changes in BOLD signal between rest and hand exercise (*i.e.*, opening and closing the right hand) [6]. In particular, their preliminary results demonstrated a local regional activation in the fMRI signal of the human SC during motor tasks in correspondence of the two cord segments interested by hand movements.

In particular, Madi and colleagues observed either positive or negative correlations between the functional response in multiple locations of the spinal cord and the applied force in an isometric motor task [18]. They found preliminary results about the existence of a linear functional relationship between the BOLD signal amplitude and the force applied, performing an isometric exercise of the biceps muscle using variable resistance weight. This result represents a substantial evidence that the BOLD signal level is modified by the neural activity level and the increased neural activity is associated linearly with the increasing of the force during the task. While Kornelsen failed to identify a response change in the lumbar spinal cord between active and passive pedalling. However, active pedalling resulted in larger activated areas in the relevant spinal cord segments [145]. In addition, Maieron et al. demonstrated the existence of a rate-dependent increase in spinal fMRI associated to a finger tapping motor task at two different frequencies [19] (see Figure 4.1).

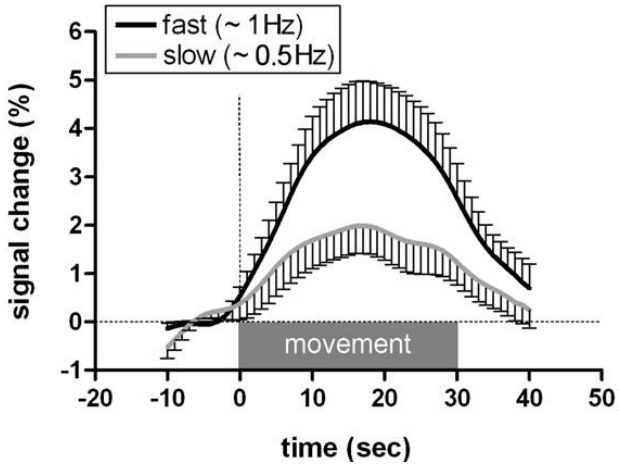

Figure 4.1: Time courses of fMRI signals averaged around the movement (perimovement plots) in clusters related to movements of the right hand at low or high frequency. Note the higher signal changes during high frequency movement. From Maieron et al.[19].

The modulation of the somatosensory activity in the human spinal cord was investigated by fMRI, performing a sensory task consisting in thermal stimuli applied to the hand, forearm and lower leg using spin-echo or gradient-echo MR sequence.

Response to graded somatosensory stimulation was reported as well. Graded temperature reductions (32 °C - 10 °C), induced a clear increase of the fMRI response for temperatures below 15°C [7, 9, 13] and response independent of temperature for moderately cold stimulations. Stepwise increase of thermal stimulus (from 32°C to 45°C) was found to induce higher functional response that an abrupt switch to the same target temperature (45°C) in the spinal cord, namely in the ipsilateral dorsal horn [187], in agreement with the known properties of heat fibers [177].

Finally, a recent paper found excellent mesoscale matching between fMRI activated areas and the expected response site to either tactile or nociceptive thermal stimulations in lightly sedated monkeys. Amplitude of the response clearly depended on stimulus properties, in a region-dependent manner [188].

In spite of the results obtained until now, the exact features and the biophysical origins of the functional response in the spinal cord are still unclear. In this framework, our study is aimed at characterizing the functional response to a graded motor task in the human spinal cord, with the goal of assessing the properties of the relationship between the hemodynamic response and the intensity of the inducing task, in a broad range of isometric force levels. We found congruent task-related fMRI responses, with positive signal changes mostly detected at C5–C7 vertebral levels. The functional response amplitude was roughly a linear function of the applied force, but divergences from linearity were observed. This parametric dependence indirectly confirms the physiological origin of the functional response in the human spinal cord and will help the design and analysis of spinal cord fMRI studies.

4.2Materials and Methods

4.2.1 SC fMRI: technical issues

In order to determine the technical conditions that would provide the best NMR-image quality, we have been carried out of the preliminary experimental sessions.

For fMRI of the SC, as with any fMRI method, fast imaging is essential. We observed that for our experiment the best methods is the GE-EPI (Figure 4.2). In particular, we observed motor-related signal changes for gradient-echo EPI that were about double those of Turbo SE. The distinction between GE and SE methods has particular relevance in the spinal cord because the superficial draining veins are separated from the grey matter of the spinal cord by the white matter tracts. It has been well-recognized in brain fMRI studies that GE sequences are sensitive to BOLD changes in these veins and so may be prone to dissociation between the site of signal change and the site of neuronal activity [134, 189]. This is given further support by a hypercapnia challenge study that showed the GE BOLD response to be dominated by signal changes at the SC surface [190].

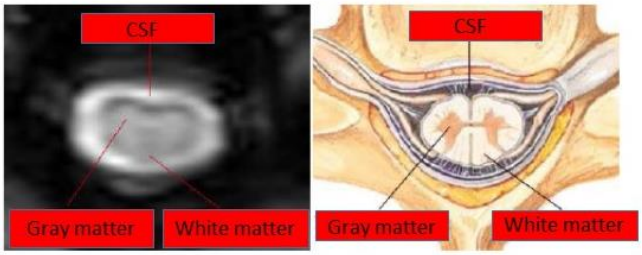

Figure 4.2: On the left, the slice acquired with a GE EPI. **On the right** a pictorial view of the axial cross section of the SC. Thanks the god contrast it is possible to distinguish the white matter from the grey matter and the CSF canal

Regardless of acquisition method, the image orientation, the SNR, the number of images in the time-series and the extent of signal changes are important factors in determining the ability to detect a functional response. These factors must be taken into consideration when designing an experiment: indeed, inadequate statistical power can lead to either over- or under- estimation of the magnitude of functional response, thus making a valid characterization difficult to attain.

We acquired the images in axial, sagittal and coronal section. The choice of image orientation has largely been based on the fact that sagittal and coronal images provide the advantage of covering a greater extent of the SC, while axial images tend to offer better dorsal-ventral and left-right resolution, and allow greater slice thickness (and, consequently, better SNR) with less partial volume effect. However we observed, in the preliminary experimental sections, that the range of the time SNR in the axial acquisition is about (5-21) while in the coronal section is about (7-15) (Figure 4.3).

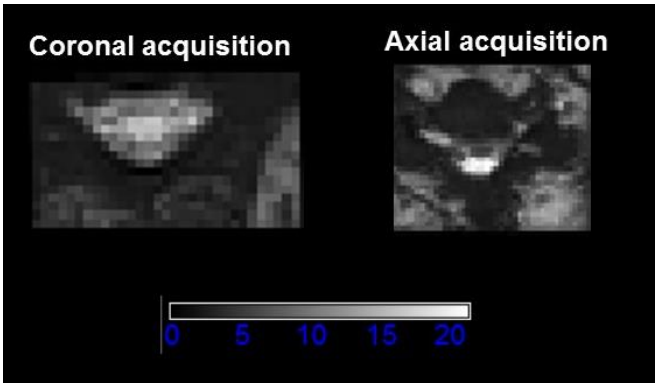

Figure 4.3: Comparison between axial tSNR slice acquired in coronal (on the left) and axial (on the right)

In addition we compare the realignment parameter and we can observed from the plot in Figure 4.4 (an example of the results obtained for the preliminary section), that the translation is order of 5 mm and the rotation is about 3 mm in axial acquisition. Thus the noise is so high that the signal is covered. Probably it is due to the small cross section of the SC. For these reasons we acquired coronal images. In the following, we report the imaging methods that we used for the experiment.

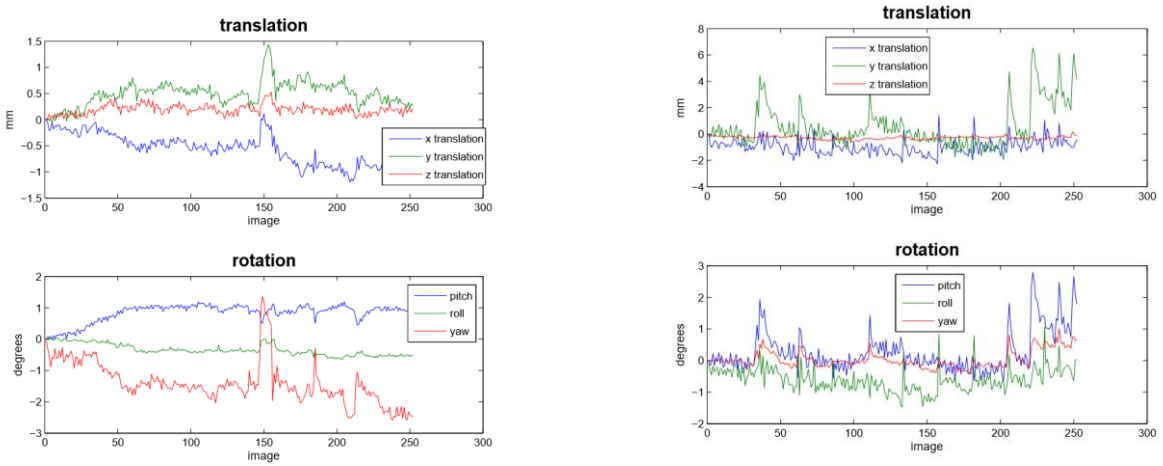

Figure 4.4: on the right the realignment parameter in the coronal acquisition. **On the left** the realignment parameter in the axial acquisition

4.2.2 Imaging methods

4.2.2.a Partecipants

Fifteen healthy right-handed volunteers (ten males and five females) with a mean age of 23 ±6 years participated in this study. None of them had a known history of any neurological or psychiatric disease

or was under medication. Each participant gave his written informed consent to the study, according to institutional and EU regulations. The study was approved by the local Committee on Ethics.

4.2.2.b Stimulation devices

The motor stimulation was provided via a custom made device, which included a hand-held force transducer and a visual feedback system (Figure 4.5).

The force transducer included a plastic housing and two pressure bars, to be operated between the first and the second finger.

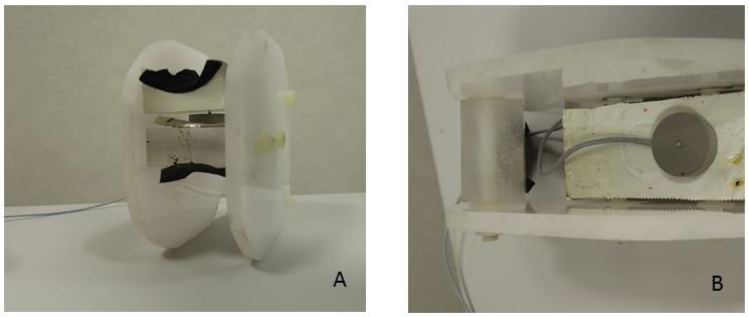

Figure 4.5:(A) motor stimulation device lateral view. (B) a sub-miniature resistive load cell (FUTEK MODELL LLB302 www.futek.com) inside the device.

The exerted pressure was converted to a proportional electrical signal with a sub-miniature resistive load cell (FUTEK MODELL LLB302 www.futek.com), that have a good accuracy and stability for use in compression force measurement applications. The base output from these load cells is about 2 mV/V. So if you supply 10V DC power to the load cell, you get about 20 milliVolt of change for full scale.

Then the signal was routed via shielded cables to an EM shielded amplifier and finally outside the magnet room to an 8 bits analogue to digital converter (ADC), that included a low-pass filter with a time constant of about 0.75 s before its first stage. Digital data were fed to a real-time custom-made microprocessor system interfaced to the scanner and to the stimulation PC. The latter generated the visual feedback and recorded the sampled force, synchronously with the fMRI acquisition (Figure 4.6 A). Visual feedback was a red bar, whose length was proportional to the applied force. Scale of the red bar was set on a subject by subject basis and automatically changed between epochs, so that target force was always set at mid length, identified by yellow marks. Visual feedback was shown on a LCD screen (compatible with the MR) and seen by the subject via an overhead mirror.

4.2.2.c Stimulation paradigm[10]

Immediately before the fMRI session, subjects underwent a training phase with the stimulation device. In a first trial the Maximum sustainable voluntary contraction force (MSF) was determined. Subject were asked to press the device up to their maximum sustainable force, and to keep the force for 20s, followed by 20s of rest, without visual feedback. Each block was repeated 5 times. MSF force was computed as the 90th percentile of the recorded force. Then, subjects were trained to steadily apply a given level of force (60% of MSF) for 30s, followed by 30s of rest, based on the visual feedback described above. Each block was repeated 4 times, to allow assessment of subject compliance. In this phase the amplifier gain was set to optimize the ADC resolution without causing overflow.

The fMRI task was organized in blocks, pseudorandomly ordered. Each run started and ended with a 60s rest epoch. After the first rest epoch, 9 epochs of motor task were alternated to rest epochs, each lasting 30s, for a total duration of 630 s. During force task epochs, subjects were required to steadily apply force up to a predetermined level, set either to 10%, 20%, or 50% of the MSF. The subjects were previously notified that a different amount of force would be needed to reach the target during each epoch. All Subjects were asked to perform 3 runs, that featured different pesudorandomizations and were randomly ordered, but were equal for all subjects.

The participants were fitted an arm restraint to the right arm to limit upper arm and forearm motion, and were instructed to relax their muscles, direct their attention to the feedback bar, and not to move in response to the stimuli throughout both the training phase and the actual fMRI experiments (Figure 4.6).

[10] The choice of the experimental paradigm involves the definition of the stimulation and the task that must be performed by the subject. The choice should be optimal to get greater contrast in the areas of interest. In addition to the stimulation conditions, a control condition is important to define the baseline signal with respect to which stimulus induced BOLD signal changes can be evaluated. Thus the experimental paradigm consists in acquisition runs during which functional volumes are acquired at a time distance TR. The experimental paradigm can be distinguished into blocked-design and even-related design.
The blocked-design paradigm consists in discrete time intervals of stimulation, i.e. blocks or eras with a duration of 30 seconds in our case, in rapid succession within a functional run. The signal acquired during a block is compared to the signal acquired in blocks of different stimulation conditions to obtain a BOLD contrast signal. The repetition time between a block and another with the same functional condition makes a cycle. Subjects might get tired during long stimulation experimental runs, anyway a stronger BOLD signal can be obtained by integrating response over the stimulation time.

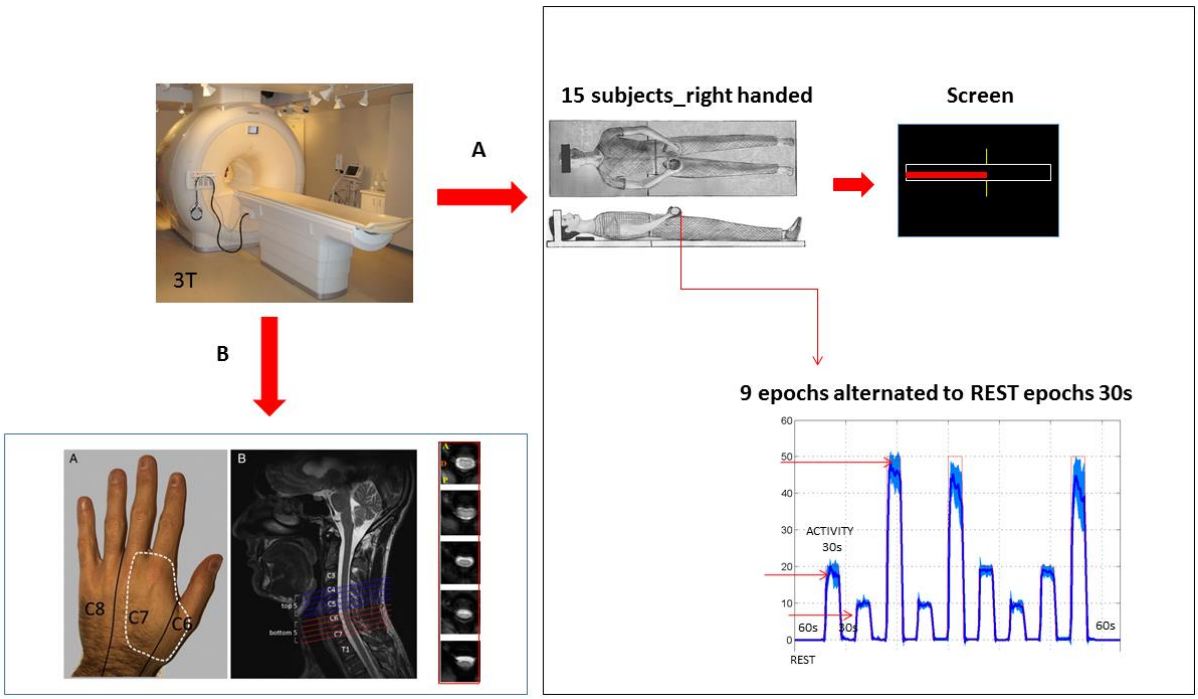

Figure 4.6: pictorial view of the experimental designed used

4.2.2.d Imaging

fMRI data were acquired using a neurovascular coil array, on a 3T scanner (Philips Medical Systems, Best, The Netherlands).

For the planning of the functional runs, a survey scan and sagittal T2 turbo-spin-echo scan (TE/TR, 120/3000 ms, FOV 340x340x21 mm, Resolution 0.48x0.48x3 mm) were performed to allow identification of the vertebral levels. The 3 functional scans consisted of a pseudo coronal –GE EPI (TE/TR = 25/2500 ms, Flip angle = 75°, FOV =144x144x32 mm3, Acquisition Matrix: 76x97x20, Reconstruction Resolution = 1.5x1.5x1.57 mm3, lateral saturation bands), and included 252 repetitions (plus dummy scans). The functional volumes were centred on the intervertebral disc between the fifth and sixth cervical vertebrae, and covered with good quality the spinal region of interest (from the seventh to the fourth cervical vertebra) (Figure 4.6). Respiratory and cardiac signals were recorded during the functional scans.

Between the second and third functional scan, additional images were acquired to provide anatomical reference as well as to mitigate fatigue, and included a 3D T1-weighted gradient echo sequence (TE/TR 5.89/9.59 ms, flip angle 9°, FOV 240x240x192 cm, resolution 0.75x0.75x1.5mm)

4.2.2.e fMRI data analysis

There are three stages to the analysis of the data from any fMRI experiment. Firstly, there are the pre-processing steps, which can be applied to the data to improve the detection of activation events. These include realignment of the images, to correct for subject movement during the experiment, and the smoothing to improve the signal to noise ratio. Next, the statistical analysis, which detects the pixels in the image which show a response to the stimulus, is carried out. Finally, the activation images must be displayed, and probability values, which give the statistical confidence that can be placed in the result, quoted.

We processed each session independently, using routines from SPM [191], AFNI [192] and FSL [193] packages, within a custom programmed Matlab® framework. Force recordings were resampled to the TR of the fMRI sequence (2.5 s). We report in the following the different phase of the data analysis (Figure 4.7).

Pre-processing (see Appendix D: Several approaches to fMRI data analysis can enhance the detection of signals within or across subjects.

We select only a subject-specific sub-region containing the entire spinal canal. Images were cropped to reduce the area around the spinal cord in order to eliminate tissue lateral to the vertebral bodies, and rostral to the C3 vertebra.

Then the data were motion corrected by a rigid body transformation realigning all of them to the mean image. Specifically the realignment step corrects for motion effects across and within sessions of an individual subject. This routine realigns a timeseries of images acquired from the same subject using a least squares approach and a 6 parameter (rigid body: 3 translational + 3 rotational parameters) spatial transformation [194]. Realignment is necessary because the fMRI analysis is based on signal differences induced by different stimulation conditions, therefore signal must be de-noised from unrelated effects such as subject's movements.

Then a RETROICOR [166] based routine was used for physiological noise reduction, including respiratory and cardiac harmonics up to the 2d order, RVT and one interaction term, as well as the relevant first derivatives [25] (see paragraph 3.4). Voxel time courses were despiked on a voxel-by-voxel basis, and slicetiming correction was applied. Finally, data were spatially smoothed with a Gaussian kernel of 6x6x6 mm^3 and temporal high-pass filtered (0.022 Hz). SC EPI images were then automatically segmented into SC and surrounding CSF [17], and segmentation was manually refined, using the T1 scans as a visual reference (Figure 4.7).

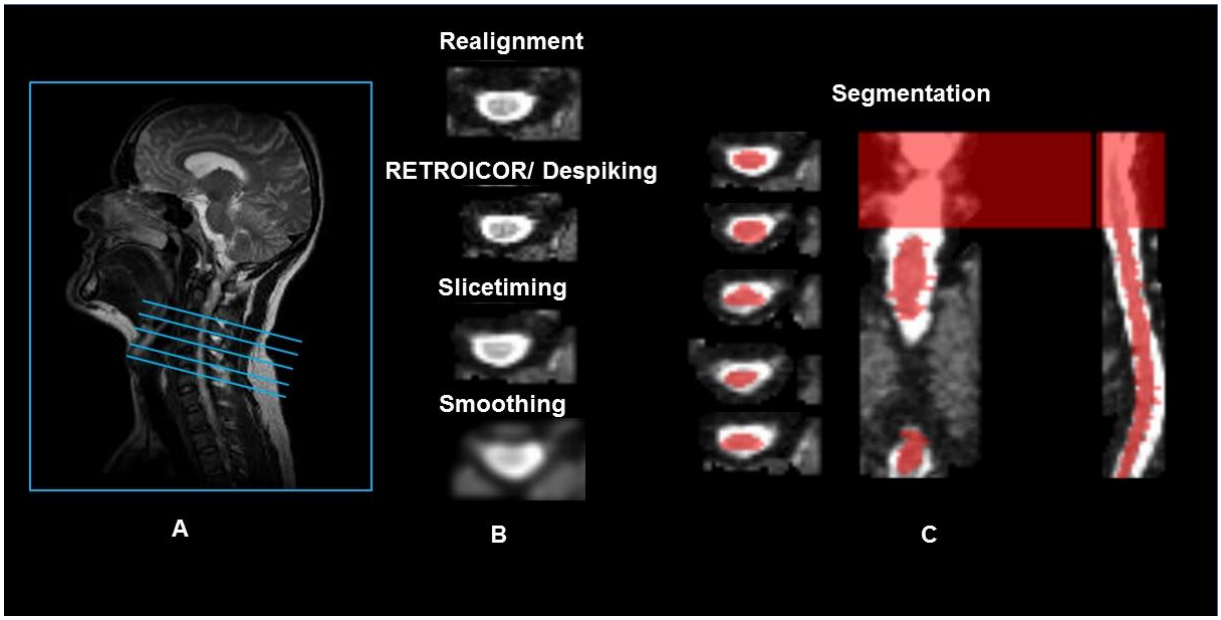

Figure 4.7: (A) A representative subject is shown (T1 weighted GE sagittal image). Slices prescription (in blue) for the T_2^* experiment and the functional sessions. (B) Axial slice at the different phases of the pre-processing. (C) SC segmentation mask was in axial (different slice) and coronal and sagittal slice respectively were reported.

Statistical analysis

To assess the features of the BOLD response the signal was deconvolved only within the segmented region (Afni 3Ddeconvolve) using the recorded force.

More specifically, given the input stimulus function and the measured fMRI signal data, program "3dDeconvolve" first estimates the impulse response function then convolves it with the stimulus time series to yield the estimated response. To estimate the goodness of the fit various statistics are calculated (F-test, t-test).

A Volterra kernel analysis [195] of the data from the designed runs was used. A Volterra kernel analysis was performed for the average time series from the joint ROI

The signal was modelled as a superimposition of linear and non linear terms (up to the 3rd order) as defined by the following equation written in matrix form:

(11) $$y=\boldsymbol{X_1}\,\boldsymbol{h_1}+\boldsymbol{X_2}\boldsymbol{h_2}+\boldsymbol{X_3}\,\boldsymbol{h_3}+\boldsymbol{e}$$

Where y are the observed data $\boldsymbol{h_{1,2,3}}$ are column vectors representing the (unknown) kernels, in particular the first-order kernel, the second-order kernel terms, and the third-order kernel terms respectively, according to a truncated Volterra series expansion [195]. $\boldsymbol{X_{1,2,3}}$, are design matrices

including the resampled force elevated to 1st, 2nd, and 3rd powers and centered around 0. "*e*" is the additive noise.

When using the Volterra signal model in eq. 11, an estimate of the kernels $h_{1,2,3}$ serves as an estimate of the hemodynamic response function.

The kernels were extracted with a deconvolution analysis, using the resampled force acquired during the task.

Responding areas were identified by thresholding the F maps to $p<0.001$. Clustering was then applied, with a cluster size threshold of at least 20 contiguous voxels, corresponding roughly to $p<0.05$ corrected for multiple comparisons (permutation test).

We extrapolate the hemodynamic response as the theory of Kernel by custom made algorithm written in Matlab®.

Kernels from each run were then independently averaged within the responding areas. The 1st order kernels of all runs were then normalized to a common reference, and the same normalization factor was applied run by run to the relevant non linear kernels.

4.3 Results: biophysical characterization of the BOLD response

Subject were generally able to correctly perform the task. 15 subjects were unable to complete the 3rd run, or during a run (usually the 3rd) showed an unacceptable compliance with the task. These runs were selectively deleted from any further processing. Figure 4.8 reports the resampled force averaged between subjects for each run type, and the relevant 95% confidence band. A steady, but slow decline of applied force is apparent at the highest level of force (50% MSF), especially when the maximal force is required during the later epochs.

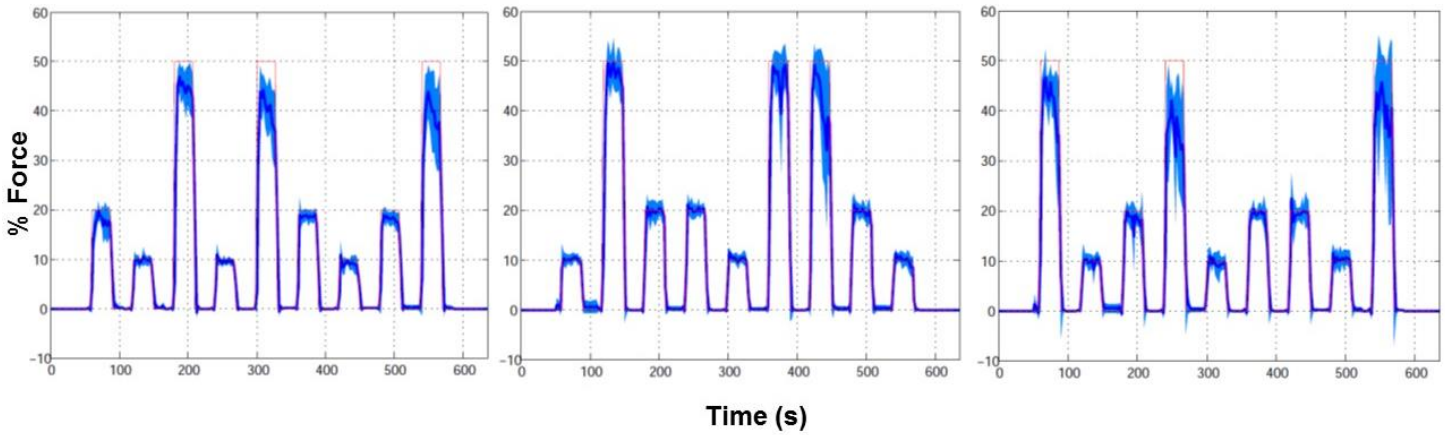

Figure 4.8: Force developed during the three runs (order is random). Force is expressed in percentage of the MSF

In Figure 4.9, an example of the axial functional map of two subjects, using the recorded force data acquired, is reported. We found a congruent task-related fMRI response. Positive signal changes were principally detected at C5–C7 vertebral levels, which is consistent with studies employing motor stimuli of the hand, with no apparent tendency to lateralize (Figure 4.9)

However BOLD responses to motor stimuli of the thumb were expected to occur mostly in the spinal cord at around C5 vertebral level, which roughly corresponds to the position of spinal level C6, this discrepancy could be depend from different factors due to the experimental perform. Responding areas were identified by thresholding the F-test maps to $p<0.0011$. The F statistic tests if all of the stimuli combined are statistically significant, but does not indicate whether an individual stimulus is significant. In order to test for the significance of an individual stimulus, the partial F statistic is calculated.

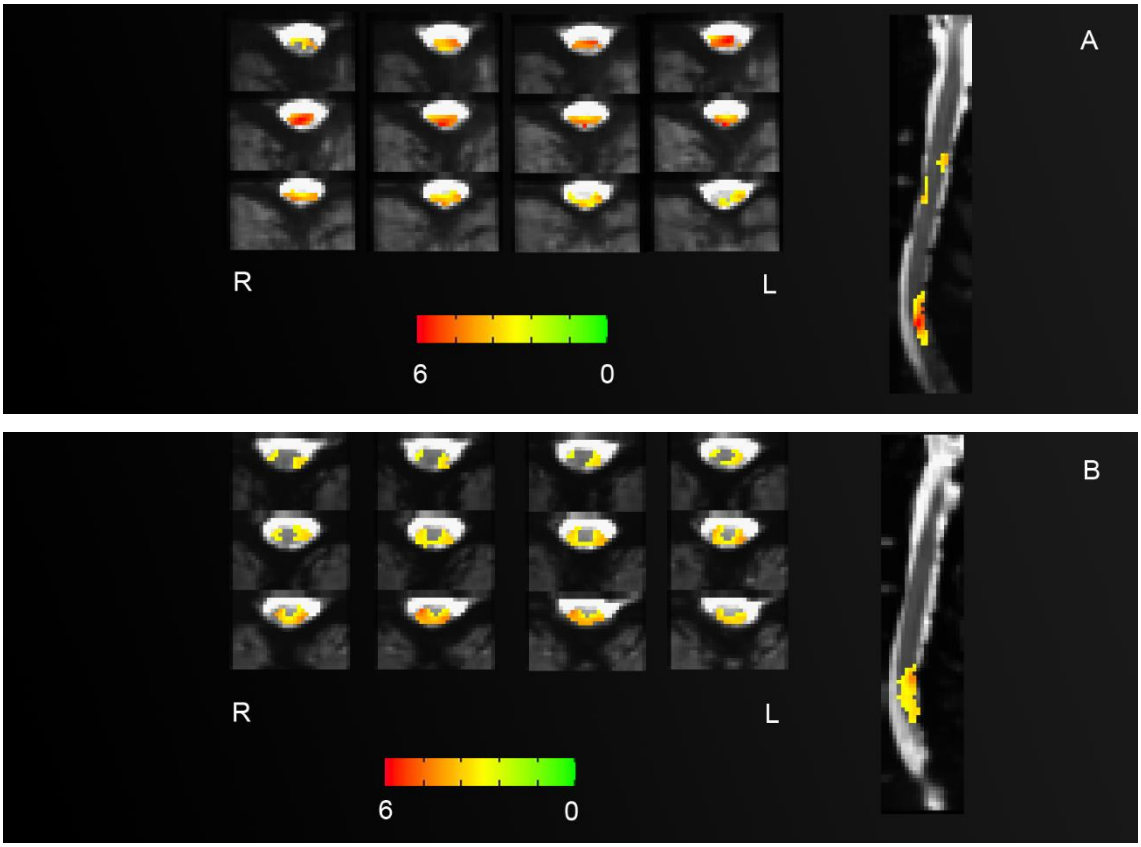

Figure 4.9: Activation maps of two representative subjects (A,B) at lower cervical level during a graded isometric force.

We extrapolate the hemodynamic response as the theory of Kernel [196] exerted force. In particular, a Volterra kernel analysis was performed for the average time series from the joint ROI [197].

We found a linear dependence of voxel-wise functional response on the task intensity (i.e. exerted force, Figure 4.10). We note that the force values are the result of the recorded force across all the subject during the task, that span between 0 and about 55% of MSF across subjects, because of the subjects' inability to keep a steady force.

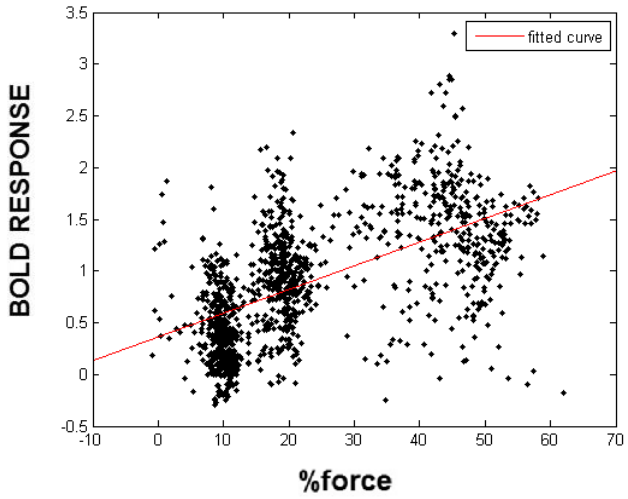

Figure 4.10: (A) plot of the BOLD response as a function of the measured force, in red the linear fit linear fit

As shown in Figure 4.10 the BOLD response presents a linear trend. There is a great variability between the epochs. We analyse the data with a linear model with a 95% confidence bounds: f(x) = p1*x + p2 and we obtained a trend of about 1.3±0.3 ($p < 0.05$) with p2=0.7. This result suggest a strong parametric dependence of functional response in the spinal cord on the stimulation strength in an isometric motor task. This dependence is important, because confirms the physiological origin of the BOLD response, and it is of great help in model-based fMRI inference. In order to better verify the linearity of the BOLD response, in Figure 4.11 we report the mean hemodynamic functional response, between the subjects, as a function of the time.

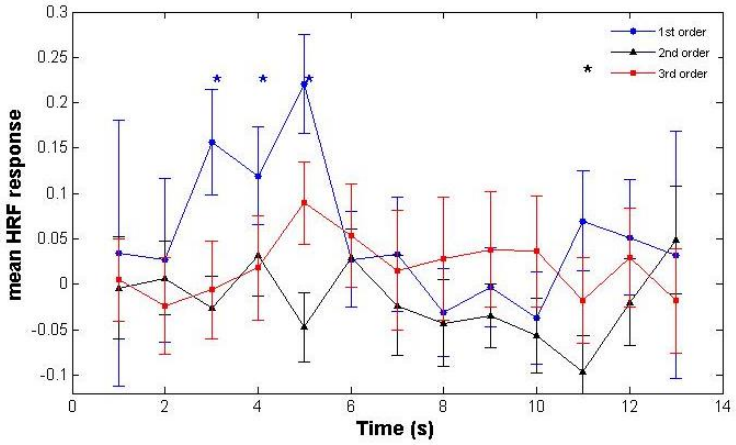

Figure 4.11: The hemodynamic response function, obtained using the Volterra kernel analysis for the first order, (blue one), the second order (black one) and the third order (red one).

The three plots are an estimation of the first order- kernel h1(the blue one), of the second order-kernel h2 (black one) and of the third order- kernel h3 (red one), respectively, extracted with a deconvolution analysis (using the Volterra signal model reported in equation (11)). As we can observe from Figure 4.11, the first order kernel h1 (the blue one) produced a significant response between 0 and 6 sec, showing a temporal linearity response.

It is possible to note that the undershoot presents a quadratic behaviour, probably due to the low statistics. Thus taken together our results clearly demonstrate strong linear characteristics of the task-related BOLD signal. We also performed a t-test (with a significance of 5%) to verify the hypothesis that the data are compatible with a normal distribution with mean=0 (and unknown variance). The datasets that fail the test (i.e. that do not have mean=0) are highlighted by stars in the figure. In Figure 4.12 we report the mean between the HRF of the 1st, 2nd, and 3rd order, which closely resembles the 1st order trend.

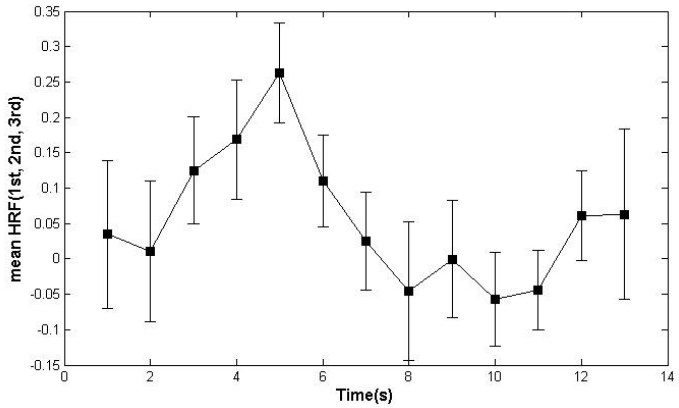

Figure 4.12: mean between the first, second and third order kernel.

In Figure 4.13, we report box plots for the HRF of the 1st, 2nd and 3rd order, respectively.

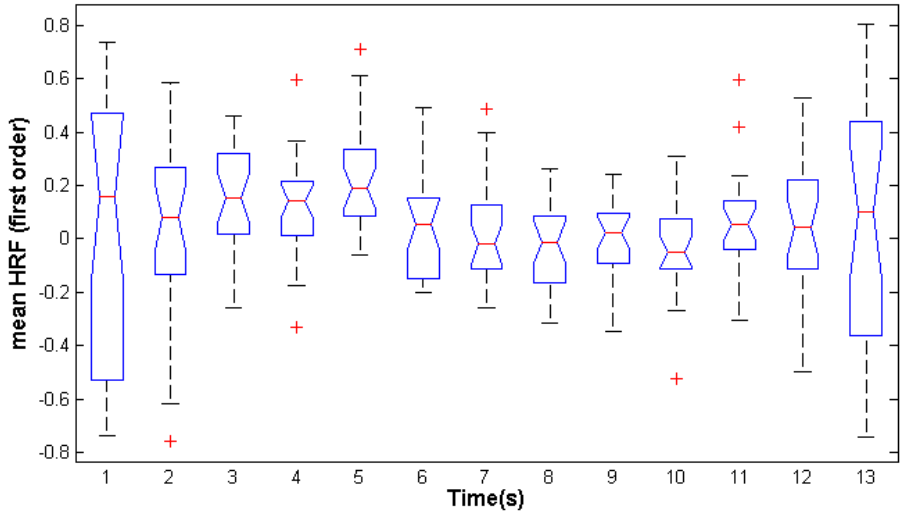

(A)

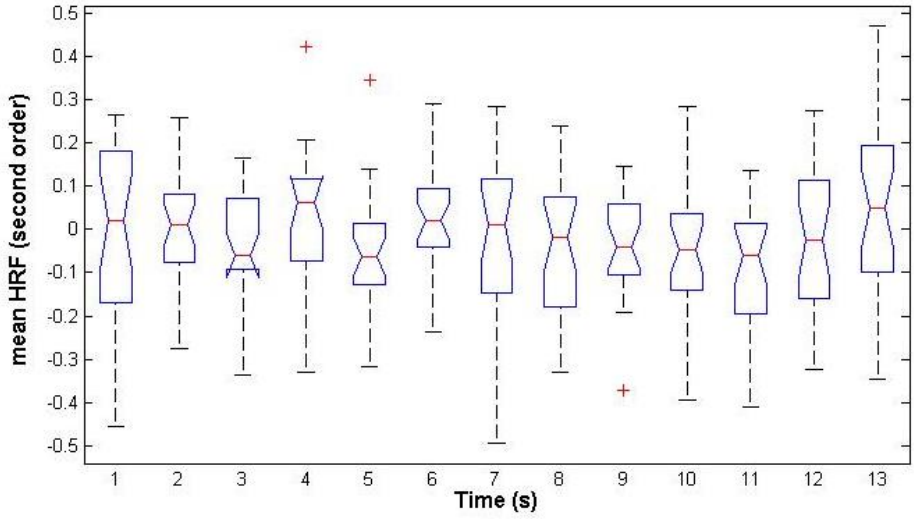

(B)

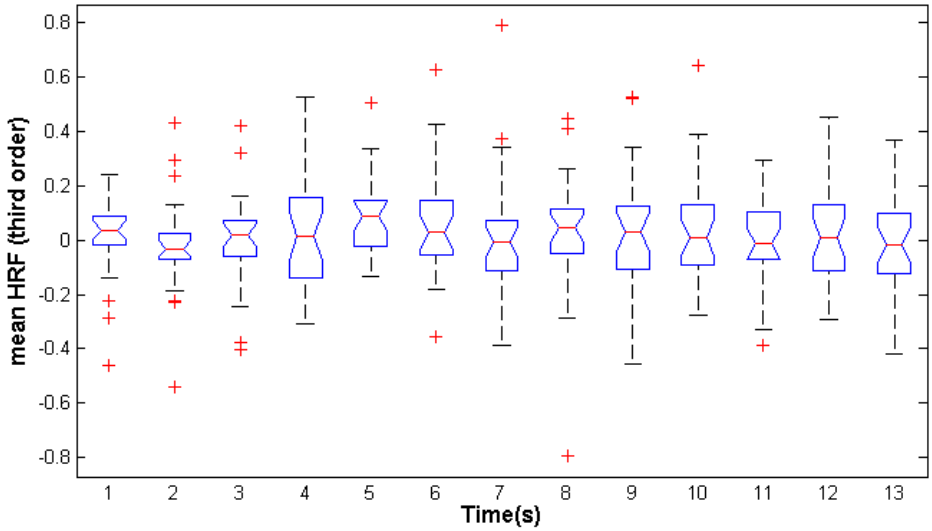

(C)

Figure 4.13: box plots of each HRF order (A,B,C).The box plot plots the median of each group along with the interquartile ranges for each group, providing a visual display of trend in the raw data. Large differences in the center lines of the box plots correspond to large values of *F-test* and correspondingly small p-values.

For each order we performed a balanced one-way ANOVA[11] test [198], obtaining a p-value smaller than 0.05 (p= 0.037) for the first order, and >0.05 for the 2nd and 3rd order. This confirms the linearity of the SC BOLD response.

In order to verify univocally the linearity we compare the results obtained deconvolving the response from a known area of activation with the stimulus function, with data analysis using the standard SC hemodynamic function proposed by Giulietti et al. [17].

In particular, the activation map underwent pre- processing with RETROICOR physiological noise reduction, spinal cord masking, motion, slice timing correction and smoothing. Subject-specific activation maps were obtained by GLM fitting to regressors computed by convolution of the measured force with the spinal cord hrf [17]. The functional response was then averaged from the functional data within thresholded maps ($p<0.001$) (Figure 4.14), and compared with the normalized exerted force. We found a congruent task-related fMRI response. Positive signal changes were principally detected at C4–C7 vertebral levels. Comparing the maps of the same subjects in Figure 4.9 (A) with the activation map in Figure 4.14 we can observed that the activation is the same but the region of activation in the first case is less spread than the second case due to the higher statistical parameter value (2^6).

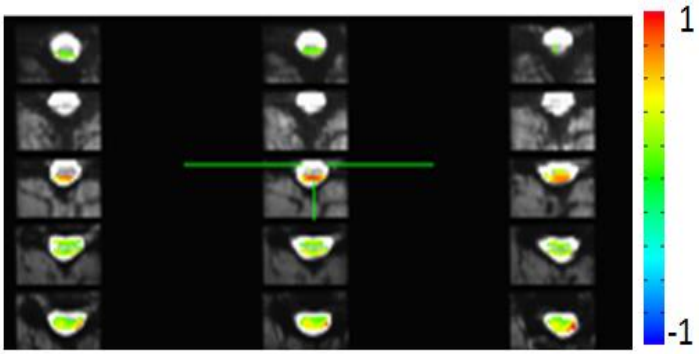

Figure 4.14: Activation maps of a representative subject (P<0.001) using the recorded force data acquired

Thus taken together our results clearly, demonstrate strong liner characteristics of the task related BOLD signal.

[11] The ANOVA F–test (of the null-hypothesis that all treatments have exactly the same effect) is recommended as a practical test, because of its robustness against many alternative distributions.

4.4 Discussion

In comparison to the sparse results obtained in the spinal cord, the relationship between stimulation intensity and functional response has been extensively studied in the animal and human brain, based roughly on a common strategy, i.e. the use of graded stimulation to detect changes in both electrophysiological and hemodynamic signals.

Logothetis et al.[5] was the first who simultaneously measured electrophysiological and BOLD responses in monkeys' visual cortex to investigate the relationship between neuronal activity and BOLD signal. They found that both BOLD and electrophysiological responses increased linearly with the stimulus. Recently electromigraphyc studies on monkeys show that the relation between activation of various muscles and activity in the primary motor cortex and cerebellum can best be described as being linear [199].

In addition Brain fMRI studies have shown exstensively the presence of force related effects in motor areas and a linear relationship between the fMRI response and different applied force. Buschbeck et al. [200]f ound a linear increase of the Bold response with a grip force, although they show that the force-related modulations of the cortical activity were comparable for the precision grip with the power grip force. In addition Thickbroom et al. [201] shown an increase in the maximum voxel signal with force during a sustained finger flexion task at a number of force levels related to maximum voluntary contraction, while the mean signal per voxel was relatively constant at each level of contraction.

We have demonstrated the linearity of the functional response to motor stimulations in the spinal cord. This is one of the first study reporting a linear properties of the functional signal in the spinal cord related to a motor task. Previous Brain fMRI studies demostrated exstensively the presence of task related effects in motor and sensitive areas and a linear relationship between the fMRI response and applied stimulus performing isometric motor or visual task [200, 201]. Spinal cord fMRI activations in response to thermal, sensory, motor and painful stimuli, as well as evidence of the descending modulation of activity have been reported thus far[7, 19, 78, 122], and substantial efforts have been devoted to develop appropriate methodologies. By detailing the biophysical features of the BOLD signal, we used an isometric motor task to study parametrically the relationship between stimulation strength and functional response in the SC of healthy subjects. We found a congruent task-related fMRI activation in the region C5-C7 (Figure 4.9, Figure 4.14) as demonstrated by the work of Madi et al. [18], which demonstrated that the detected activity varied with the task for the

most part, and by the work of Stroman et al. that identified the corresponding anatomical spinal cord location in the ventral grey matter of the spinal cord during a motor task [11, 12, 202] that consisted in squeezing a rubber bulb with one hand. fMRI intensity changes, corresponding to motor areas ipsilateral to the hand being exercised, between the C6 and T1 segments.

However the responses were expected to occur roughly in the position of spinal level C6, the task were designed to emphasize a single muscle group, the hand muscles. This difference could be depend from some factors due to the experimental perform. For example, even though the subjects arm was blocked with a specific arm band and the subjects were instructed to limit their movements during the task, variation in task performance, such as not voluntary additional motion, may have occurred. In addition, it is important to consider two physiology characteristics [203]:

1) the fact that all muscles groups are innerved by at least two adjacent spinal roots .
2) The differences in the innervations of muscles.

In Figure 4.10, Figure 4.11 and Figure 4.13 we report a strong linear dependence of functional response in the spinal cord as a function of an isometric motor task. It was shown a first evidence about the correlation of the spinal BOLD response with the force applied in a voluntary isometric motor task, by Madi et al. [18]. In addition Maieron et al. shown that there is a linear correlation between the BOLD activation and the different frequency –fast versus self-selected– at which a finger-tapping task is performed [130] Furthermore, Summers et al. demostrated that the BOLD signal changes from the baseline during noxius stimuli, while no signal changes were observed during innocuous stimuli in humans, confirming physiological information obtained in animals [87]. Finally, Stroman et al. found a clear increase in the signal intensity for temperatures below 15°C in response to thermal stimulation based on a graded temperature reductions (32° C- 10 °C) [9]. These compelling demonstrations of an intensity-dependent response in spinal fMRI support our present results. The main results, reported in figure 4, are obtained using a Volterra kernel analysis approach. This analysis approach compared to other parametric approach, has the advantage of providing kernel estimates that completely characterize the linearities/nonlinearities of the BOLD response up to the second order. In Figure 4.11 the linearity of the BOLD response is clearly represented, in fact the size of the first-order kernel increases (between 0- 6 sec) relative to the size of the second-order kernel and the third-order kernel.

Summary and Conclusions

fMRI approaches have been sparsely attempted for the study of the SC function; however, the exact features of functional response, and even the biophysical origin of the signal, are still unclear.

In the present work, we performed a controlled motor task (graded isometric force) of the right dominant hand, and we parametrically studied the relationship between stimulation strength and functional response.

Each subject performed a block design motor task in which they were asked to press a force-sensitive, custom-made device between their first and second finger, until a real-time visual feedback confirmed the achievement of a specific target force. Subjects underwent 3 functional runs, each including alternating 30s rest and motor task epochs, during which the target forces were 10%, 20% and 50% of the subject's maximal sustained force in a pseudorandom order. The exerted force was digitized and recorded.

The data analysis of spinal cord fMRI consisted in a series of steps, performed using different computer programs. In this framework, we developed a user interface incorporating the functionalities of the different fMRI programs. In particular, the activation map were processed with physiological noise reduction, spinal cord masking, motion, slice timing correction and smoothing.

To assess the features of the BOLD response the signal was deconvolved only within the segmented region using the recorded force. By deconvolving the response from a known area of activation with the stimulus function, the haemodynamic response function can be obtained.

We compared the results obtained with the Subject-specific activation maps, obtained by GLM fitting to regressors computed by convolution of the measured force with the standard SC hemodynamic response function.

We demonstrated a strong parametric dependence of functional response in the spinal cord on the stimulation strength in an isometric motor task. Such a dependence is important, because confirms the physiological origin of the response. In addition this result is of great importance because demonstrate that SC fMRI may be of immediate application in neuroradiology, and in particular for the assessment and follow-up of spinal injuries, pain, and neurodegenerative diseases (e.g. multiple sclerosis), as well as in the development and evaluation of new therapies. Indeed, a non-invasive tool capable of monitoring the function, and thus complementing the available anatomical information, is a crucial need in these fields.

CHAPTER 5

CHARACTERIZATION OF MOUSE SC VASCULAR AND NEURONAL NETWORK USING HIGH RESOLUTION X-RAY PHASE CONTRAST TOMOGRAPHY TO DEVELOP A SC BOLD MODEL

The present Chapter tackles the study of the SC vascular and neuronal networks (VN and NN), which together contribute to the BOLD signal in fMRI. The state-of the-art BOLD model currently used in fMRI studies is a mathematical abstraction based on the vascular/metabolic response in the rat brain cortex, which may not be appropriate for the SC. The absence of adequate models of the functional anatomy of the SC currently prevents the unambiguous interpretation of SC fMRI data and its application to the clinical practice [79]. The development of an accurate vascular model of the SC would thus be of paramount importance. A 3D high-resolution micro-imaging technique is required to define the complex structure of the vascular and neuronal networks in the SC. The spatial resolution limit of MR or PET techniques raises the question of a possible micro-vascular organization at a scale smaller than the resolved one. Synchrotron X-ray phase contrast µTomography (SXPCµT), has great potential to reveal the structures that generate poor contrast by absorption, providing stacks of high resolution images and allowing for 3D reconstruction and analysis. Therefore by using SXPCµT, a high-quality, quantitative morphometrical and structural analysis of the VN and NN can be performed [204]. For these reasons we investigate the vascular network of the mouse spinal cord with SXPCµT. The purpose of our study is to further delineate the arterial and venous network along the entirety of the mouse SC with a 3D technique with micrometric resolution, without an invasive contrast agent that could modify the appearance of the vasculature network. The results obtained will be useful to develop an fMRI optimised BOLD signal model for the spinal cord, on the basis of its real vascular geometry. In addition studying simultaneously the complexity of the VN and NN in a large volume of tissue, with a resolution sufficient to access the smallest capillaries and the neurons ultra-structure, appears then as a key point for a better understanding of the neuro-vascular coupling in healthy and neurodegenerative-diseased samples.

This study will improve the methodological strategies to investigate SC function non invasively in physiological and pathological conditions, thereby accelerating the introduction of the SC fMRI in the clinical setting.

5.1 Advantages of XrPCT for the study of Vascular and Neuronal Network in the SC

Micro-vascular and neuronal structural organization is an important physiological issue [205] for which quantitative structural analysis is a key step. Indeed, there is growing interest in high-resolution imaging of vascular and neuronal structures in several pathological issues. It appears essential to define morphological and topological quantitative parameters characterizing neuronal network and vascular networks, to a better understanding of the cellular control of blood flow, and thus of the neuro-vascular coupling. Up to date a number of different approaches, in vivo and ex vivo, are used to understand this issue, but all of them have serious limitations.

In the last years, methods targeting large cerebral volumes have been developed. Post-mortem methods, such as the corrosion cast technique, provide impressive pictures of the human cortical and rat spinal cord using SEM (Scanning Electron Microscopy) but do not offer the possibility of quantitative analyses [206, 207]. This is achieved only by complementing the SEM measurement with 3D micro-tomography [208] but this combination of techniques makes this approach of difficult application in preclinical investigations and moreover it requires an invasive sample preparation which can alter the 3D morphology of the system. Techniques such as histological sectioning or SEM, as well as optical confocal microscopy [209], have been used for a systematic in situ study of vessel morphometry, at the micrometre scale. Albeit the accuracy of these methods, they are restricted to the investigation of tissue volume within a depth of a few hundreds of micrometres because of a finite penetration ability (typically 10 microns). Hence imaging of larger volumes of tissue in any microscope requires sectioning them to an appropriate thickness, a procedure inherently destructive, and prone to induce damage within the imaged sections.

More recent techniques, such as two-photon microscopy, provide important 3D information and offer optical biopsy, for which high speed imaging is required. However, it is restricted by the low penetration depth (100 mm) and moderate size of the region of interest (100–200 mm) [210].

On the other hand, MRI or PET allow for structural and functional imaging. However, their spatial resolution (in the order of millimeters) limits the possibility of investigating the micro-vascular organization (typical scale: 10–100 mm).

MR angiography and volumetric-CT are powerful 3D techniques used to image arteries (and, less commonly also veins) in order to evaluate abnormalities. They have been applied to demonstrate the diffuse organization of tumor vessel architecture in vivo. However, small vessels (smaller than 50 mm in diameter) cannot be visualized with either modality.

However, small vessels (smaller than 50 mm in diameter) cannot be visualized with either modality. Conventional X-ray angiography is commonly used to image neural vasculature in clinical practice, but it also has a detection limit of some hundreds of microns, which is inappropriate for imaging the micrometric vessels and capillaries. Thus, a 3D high resolution micro-imaging technique is required to investigate the complicated structure of microvascular and neuronal networks. The high-resolution SXPCT applied in combination with a contrast agent has been proposed for 3D imaging of micro-vascular networks inside several cubic millimeters of ex-vivo cerebral tissue and adapted to the analyses of primate vessel networks, as well as to brain tumors in an implanted rat model [211, 212]. Such a method not only permits to image the entire ex-vivo volume of tissue, but it also allows a systematic digitalization of the vessels. This technique reaches spatial resolution close to microns, when invasive contrast agent are used. In addition it was demonstrated that vessels of about 30 microns could be detected using phase contrast x-ray imaging without the use of such agents [213, 214]. Up to date, SXPCT appears the most promising ex vivo technique for a 3D imaging of the vasculature [214, 215].

In this framework we study the entire ex vivo mouse spinal cord with the applications of SXPCT exploiting the spatial resolution of 0.6 microns and 3.5 microns.

The data analysis and the 3D rendering enable the distinct visualization of the VN and neuronal systems in the same image.

The results reported in this study are unique in providing a detailed three-dimensional analysis of the micro-vascular network and simultaneously the relevant interactions with neural cells of the healthy mouse's SC, without any contrast agent and with non-invasive contrast agent [204].

In the following we report same experimental detail and the most important results obtained.

5.2 Materials and methods

This thesis consists in three main parts: the first one that we have described in CHAPTER 4 is relative to the biophysical and physiological characterization of the SC BOLD response. The second one consists in the structural delineation by SXPCT, of the Neuronal and micro-vascular networks, involved in the BOLD response, along the entirety of the mouse SC. The last one consist in the 3D quantification of the NN and VN to detect the vessels, neurons and axons by means of their characteristic geometry. These information will later be employed to refine the vascular model used in fMRI, which was developed only for a specific real geometry of the VN, i.e. for the rat brain [4], and may be not be applicable to the SC. The last two part of this thesis are characterized by the use

of SPCT for the quantification of the VN and NN. In this paragraph we report the sample preparation, the experimental approach and data analysis method used in order to achieve these goals.

5.2.1 Sample preparation

In this project we studied adult male C57 Black mice (20–22 g, body weight) were purchased from Charles River, Calco, Italy and kept under controlled conditions (temperature: 22°C; humidity: 40%) on a 12-h light/dark cycle with food and water ad libitum.

Mice were divided into three groups: one group was perfused with saline solution, one group was perfused with MICROFILL® [216], a low-viscosity radio opaque polymer (Flow Tech, Inc., Carver, MA), which is well suited for penetrating vessels of different diameters. In addition these kind of contrast avoid the sedimentation of suspensions containing radio-opaque materials as barium sulphate. The last group was used for histology and immunohistochemistry analysis.

All experimental animal procedures were carried out in the IRCCS AOU San Martino –IST Animal Facility (Genoa, Italy), in the respect of the national current regulations regarding the protection of animals used for scientific purpose (D.lgsvo 27/01/1992, n. 116). Research protocols have been evaluated and approved by the IRCCS AOU San Martino –IST Ethical Committee for animal experimentation (CSEA) as Animal use project n. 336 communicated to The Italian Ministry of Health, having regard to the article 7 of the D.lgs 116/92.

5.2.1.a Group 1 & 2 sample preparation (for SXPCT): Perfusion with saline solution and with MICROFILL®

Mice were anesthetized by an intraperitoneal injection of ketamine (80 mg/kg)/xylazine (10 mg/kg) mixture and perfused transcardially with saline solution containing heparin (50 U/ml). One group was afterward perfused transcardially by MICROFILL® agent. At the end of perfusion, the animals were stored overnight at 4 °C to permit the solidification of the MICROFILL®. Afterwards spinal cords were dissected out, fixed in 4% paraformaldehyde for 24 h. Fixation time and volume of fixative solution depends on the size of the sample, both of which should be increased in proportion to the volume of the sample. At the end of the fixation, it proceeds with the washing of the sample from the fixative (the duration of which depends on the volume of the sample), after that the samples are transferred in 70% alcohol, which allows the conservation. Before the experiments mice undergo laminectomy and the spinal cord is taken off, dehydrated using graded ethanol and immersed in methyl salicylate for 24-48h.

Figure 5.1: spinal cord dissected with MICROFILL® contrast agent

5.2.1.b Group 3: Histology and immunohistochemistry.

For morphological evaluation, mice were sacrificed and spinal cords were dissected out and immediately fixed for 24 h in ethyl alcohol (60%), acetic acid (10%) and chloroform (30%). After embedding in paraffin, spinal cord sections were cut at 20 mm and stained with thionin (Nissl staining) and hematoxylin/eosin (H&E).

For immunohistochemical analysis of MBP, mice were anesthetized by ketamine (100 mg/kg, i.p.)/xylazine (10 mg/kg, i.p.) and perfused transcardially with 4%paraformaldehyde in phosphate buffered saline. Spinal cords were removed, fixed for 24 h in ethyl alcohol (60%), acetic acid (10%) and chloroform (30%) and embedded in paraffin. Twenty mm sections were first soaked in 3% hydrogen peroxide to block endogenous peroxidase activity and then incubated overnight with rabbit polyclonal anti-MBP (152000, Chemicon International, Billerica, MA).

For immunohistochemical analysis of SMI-32 or laminin, mice were killed, spinal cords were removed, fixed for 24 h, as above, and embedded in paraffin. Twenty mm sections were first soaked in 3% hydrogen peroxide to block endogenous peroxidase activity and then incubated overnight with mouse monoclonal anti-SMI32 (151,000, Covance, Princeton, NJ) or rabbit polyclonal anti-laminin (15200, Novus Biologicals, Littleton, CO). Slices were then incubated then for 1 h with secondary biotinylated anti-mouse or biotinylated anti-rabbit antibodies (15200; Vector Laboratories, Burlingame, CA). 3,3-Diaminobenzidine tetrachloride was used for detection (ABC Elite kit; Vector Laboratories, Burlingame, CA). Control staining was performed without the primary antibodies.

5.2.2 High resolution Synchrotron Phase Contrast Tomography

Studying the complexity of the VN and NN in a large volume of tissue, with a resolution sufficient to access the smallest capillaries and the neurons ultra-structure, appears a key point for a better understanding of the neuro-vascular coupling. Within this context, XPCμT has great potential for the investigation of the structures that generate poor contrast by absorption, since the XPCuT sensitivity to light elements is about 1000 times higher than by X-ray absorption contrast methods [217]. In this project Synchrotron XPCμT is used for the simulataneous investigation of micro-vascular structures (with and without contrast agents) and neurons structure in healthy mouse's SC, at both the local and global level. The attainment of a 3D imaging and the quantification of the SC-VN should considerably improve our knowledge of the effects of pathological processes, such as injuries and neurodegenerative diseases, where secondary vascular effects have been implicated.

5.2.2.a XPCT basis

The refractive index of the materials in the X-ray region can be expressed as:

(12) $$n(x,y,z) = 1 - \delta(x,y,z) + i\beta(x,y,z)$$

$\beta(x,y,z)$ describes the absorption of X-rays in the sample. It is related to the widely used linear X-ray attenuation coefficient $\mu(x,y,z)$ by:

(13) $$\mu(x,y,z) = \frac{4\pi}{\lambda} \times \beta(x,y,z)$$

Where λ is the incident X-ray wavelength. Conventional absorption tomography yields virtual slices or volume data corresponding to the local X-ray absorption coefficient $\mu(x,y,z)$. PCT, on the other hand, provides the real part of the refractive index, expressed in terms of its decrement from unity $\delta(x,y,z)$. It is related to the electron density distribution $\rho_e(x,y,z)$ by

(14) $$\delta(x,y,z) = \frac{r_e \lambda^2}{2\pi} \rho_e(x,y,z),$$

for X-ray energies far away from the absorption edges.

The absorption component β falls off very fast with respect to δ ($\beta(E) \propto \frac{1}{E^4}$; $\delta(E) \propto \frac{1}{E^2}$) and hence for high-energy X-rays ($E \geq 8keV$, “hard” X-rays) δ is orders of magnitude larger than β. This is especially true for biological sample made up of light elements (Figure 5.2).

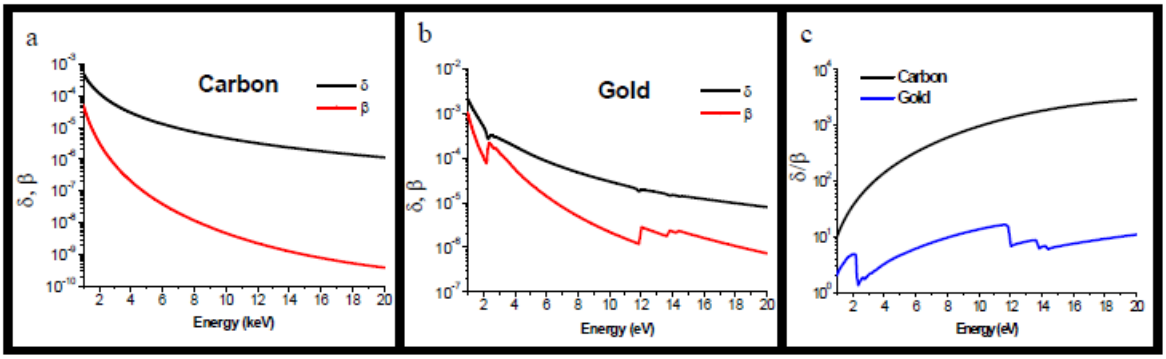

Figure 5.2: and β as a function of the energy of the incoming radiation a) for Carbon, b) for Gold. c) Ratio $\frac{\delta}{\beta}$ as a function of the energy for both cases. In the X-ray energy range δ is orders of magnitude bigger than the imaginary part β and this is especially true for light elements.

XRPCT methods:

The goal of XRPCT imaging is to determine 2D (radiography) or 3D (tomography) distributions of the scattering properties of an object (related to the electron density, see equations (12) by recording attenuation and phase changes of the transmitted x-ray beam.

Since the detector can record only absorption information the phase has lost. To solve this problem there is different techniques have been developed to exploit the phase-contrast in the x-ray regime. They can be classified into five main categories: the propagation-based imaging (PBI) methods [218], the analyzer-based imaging (ABI) methods [219, 220], the interferometric methods based on the use of crystals [217], the grating interferometric (GI) [221] and the grating non-interferometric methods [222].

A simple yet effective phase contrast method for hard x-rays is based upon in-line imaging after free space propagation (Figure 5.3). When synchrotron x-rays illuminate the sample, variations in optical path length produce slight local deviations (refraction) of the x-ray beam from its original path. In absorption radiography the detector is generally placed close enough to the sample that these variations are unnoticed. On the contrary, when a free space propagation distance is allowed between sample and detector, the recorded image contains the refraction information in the form of interference fringes appearing at the interfaces between different materials within the sample [223]. The fringes thus enhance the visibility of low absorbing features. Nevertheless, the image captured by in-line propagation always contains mixed absorption and phase effects. Therefore, specific algorithms have to be used to recover the morphological distribution of absorption and phase within the object [224, 225]. Strictly speaking the quantitative estimation of the object projected thickness is possible only for mono-elemental samples under monochromatic illumination [224]. On the other hand, although the refractive indices of different soft tissues are very similar for hard x-rays, a semi-

quantitative phase imaging is still possible taking into account the specific interfaces between tissues [225].

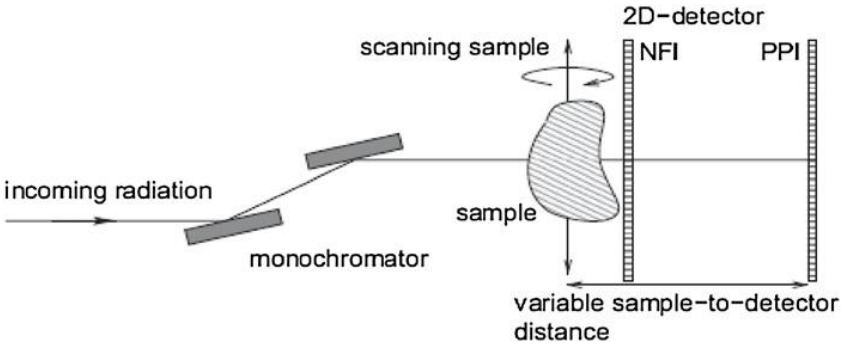

Figure 5.3: The experimental set-up of PBI. A monochromatic, transversally coherent x-ray fan beam traverses the sample, and is recorded by a 2D detector at different distances. PPI, phase propagation x-ray imaging (another name of PBI); NFI, near field imaging [215].

For more specifically information see [215].

5.2.2.b Experimental approach used

The SXPCT has been performed on the samples of groups 1 and 2. We used phase contrast method based upon in-line imaging after free space propagation. As we have said in the paragraph above, the image captured by in-line propagation always contains mixed absorption and phase effects. Therefore, specific algorithm has been used to decouple absorption from phase information [224]. Phase contrast images were acquired with pixel size of 0.64 µm or 3.5 µm, respectively after administration or not of the MICROFILL® contrast agent. The phase retrieval algorithm proposed by Paganin et al. [224] was applied to all projections of the tomographic measurements.

The experiment of the un-stained sample was carried out at TOMCAT beamline at the Swiss Light Source (SLS) in Villigen (Switzerland). The monochromatic incident X-ray energy was 17 keV and a CCD camera with a pixel size of about 0.64 µm was set at a distance of 5 cm from the sample. The tomography has been acquired with 1601 projections covering a total angle range of 360°.

The experiment of the stained sample was carried out at ID17 at ESRF in Grenoble (Figure 5.4). The monochromatic incident X-ray energy was 30 keV. The sample was set at a distance of 2.3 m from the CCD camera with a pixel size of 3.5 µm. The tomography has been acquired with 2000 projections covering a total angle range of 360° with acquisition time of 1 second per point. In both experiments we explored the entire volume of the spinal cord.

Figure 5.4: sketch of the experimental set up @ ESRF

5.2.2.c Data analysis.

The phase retrieval algorithm proposed by Paganin et al. [226] has been applied to the projections of the tomographic scans using the ANKAphase [227] code. The phase tomograms display different grey-level regions corresponding to different tissues. The algorithm produces the projected thickness of the object which is proportional to the refractive index decrement if the object is homogeneous. When applied to all tomographic projections, the retrieved phase maps can be fed to a standard filtered back-projection algorithm to obtain phase tomograms.

The rigorous application of the phase retrieval algorithm is restricted to a mono-elemental object of known composition and density (i.e. known refractive index). On the other hand, in many practical applications one does not require the quantitative knowledge of the projected thickness or the phase of the tissue. If only an approximate value of the refractive index is known, the algorithm will still produce a phase map which will differ from the real one by a constant factor [221]. Similarly, if different tissues with similar refractive index are present in the specimen, the phase shift generated from each of them will be reconstructed up to an unknown constant. For the aims of the tomographic reconstruction though, this is a minor problem if the tissues are relatively similar and the tomograms will display different grey-level regions corresponding to different tissues which enormously facilitate the image segmentation.

Also, on multiple occasions we performed a segmentation of the obtained images, both to display the tissues independently and to reduce the artifacts. Such segmentations have been performed using both commercial (Volview and ImageJ) and home-developed program software (Matlab® routines by Inna Bukreeva from the TomaLab of CNR-NANOTEC).

5.2.3 Simultaneous submicrometric 3D imaging of the micro-vascular network and the neuronal system in mouse SC

As we have seen in the previous paragraph SC angio-architecture and regional segregation of functional SC regions are key elements for advancing understanding on neurovascular functions in fMRI and clinical research fields. In this framework we measured the entire mouse SC with XSPCT. In particular we report the simultaneous 3D imaging of micro-vascular and neuronal system of the lumbar/sacral region. In Figure 5.5 we report a 2D images of a 3D reconstruction of 300 µm thick volume of the SC lumbar-sacral region acquired with XSPCT without using contrast agent, with spatial resolution of 0.6 µm, obtained at TOMCAT beamline at SLS. In particular we report this spinal level because the various region of the SC are disproportionally vascularized, and the lumbar/sacral region have a small peripheral and large central supply and has more grey matter, particularly in the ventral horns, where lower motor neurons for the arms and the legs reside [102].

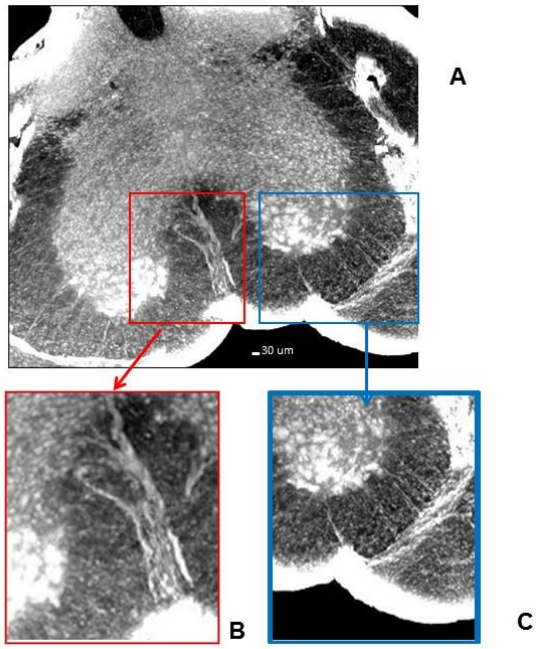

Figure 5.5: A) X-ray Phase Contrast Tomography reconstructed volume of 500 slices of the lumbar-sacral region of the spinal cord. The image is obtained at a spatial resolution of 0.64 mm without contrast agent at TOMCAT beamline. the grey matter is represented in white while the white matter is represented in grey. B) (Red square) Detail of the radial vessels of one of the vascular tree penetrating the grey matter. C) (Blue square) Zoom of the grey/ white matter interface. The white spots in the gray matter are the neuronal cell bodies [204].

The image shows an amazing contrast between white and grey matter of the spinal cord (inverted grey-levels in the figure). The ‘‘H’’ typical shape of the grey matter (of anterior horn and of the posterior horn) [102] can be well distinguished from the surrounding white matter (see CHAPTER 2

Figure **2.11**). The central and the radial vessels penetrating the grey matter from the outer part of the spinal cord, are perfectly discernible and well imaged.

In the Figure 5.5 B, it is possible to distinguish the central/sulcal arteries that supply the SC central region. The sulcal arteries are usually straight in the anterior sulcus and they don't branch in the anterior median sulcus. At the grey/white matter interface (Figure 5.5 C) it is possible to discern the neuronal cell bodies, white spots in the grey matter, and the nerve fibres surround the grey matter.

In Figure 5.6 (A) we report a 3D reconstruction of a 1.2 mm (with spatial resolution of 0.6 µm) of the same sample, where it is possible to observe the grey matter bordering the central canal. In addition the image shows two different vascular trees that appear at different depths in the sample, corresponding to two lumbar/sacral spinal segments. Thanks the high spatial resolution it is possible to distinguish the sulcal veins from the sulcal arteries, because the sulcal veins, that are superficial, exhibit an undulating course and received branches in the anterior median sulcus [207].

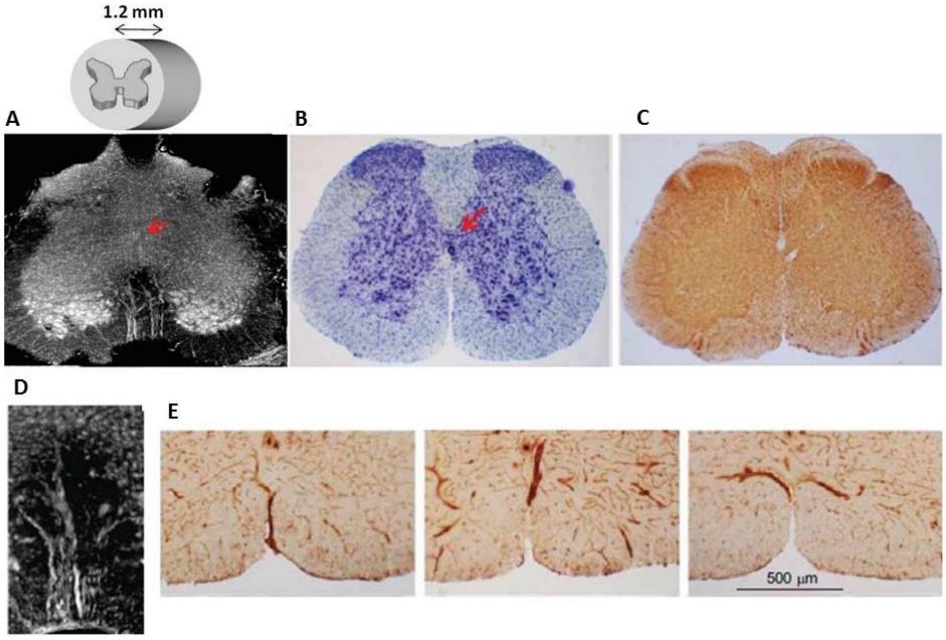

Figure 5.6: A) X-ray Phase Contrast Tomography reconstructed volume of 1.2 mm thick of the lumbar-sacral region of the spinal cord. The image is obtained at a spatial resolution of 0.64 mm without contrast agent at TOMCAT beamline. The inset is a sketch of the imaged volume of the spinal cord. B) Nissl staining of the lumbar-sacral spinal cord. C) Immunohistochemical analysis of SMI-32, a marker of motor neurons, in the lumbar-sacral region of the spinal cord. D) Detail of the radial vessels of one of the vascular tree penetrating the grey matter. E) Immunohistochemistry of laminin, a marker of blood vessels, in the anterior portion of the lumbar-sacral SC obtained at different levels. The red arrows in a) and b) indicate the central SC canal [204].

We compare the results obtained about the neuronal and vascular system with histology performed on twin samples. The Nissl staining and the immunohistological analysis of SMI-32, a marker of motor neurons confirm the neuronal structure observed with XSPCT. Figure 5.6 (D) shows one of the vascular trees imaged in Figure 5.6 (A). Immunohistochemistry images of laminin show the

presence of blood vessels in the anterior portion of the lumbar-sacral SC obtained at different levels (Figure 5.6 (E)) very likely corresponding to the structure observed to XSPCT Figure 5.6 (D).
The unprecedented spatial resolution combined with the large field of view of the tomographic images allows to access information coming from both the VN and the neuronal system in the same image in the entire volume (Figure 5.7).

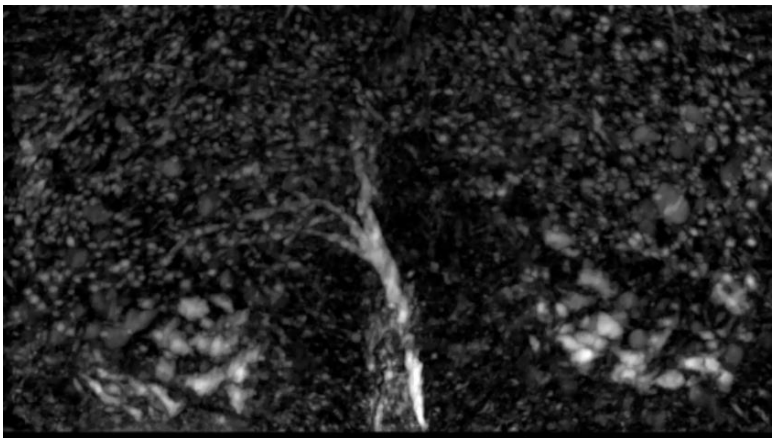

Figure 5.7: We report a 3d rendering of the lobal/sacral section (500 slices with spatial resolution of about 0.64 micron) where we can see the distribution in the volume of the neuron cell and vessels.

In order to better investigate the VN and the NN of the spinal cord we performed an image segmentation of the Figure 5.6 A. The contours of the SC micro-vasculature and of the neuron fibres are clearly reported. In particular the vessels and the fibres look differently: the vessels appear ramified while the nerve fibres bear a resemblance to ‘‘branches of a weeping Willow’’. The smallest vessels that could be identified, as shown in Figure 5.8 (A), were approximately capillary of about 9 to 5 ± 1μm in diameter. Together the micro-vessels the intricate neuron fibres (from 5.5 to 9.5 ± 1μm in diameter) are shown in Figure 5.8 (A). In Figure 5.8 (B) is reported a magnified region of Figure 5.8 (A), where the capillaries are segmented in red and the nervous fibres in green. Immunohistochemical analysis of spinal cord uses an antibody against myelin basic protein (MBP), a major constituent of the myelin sheath of oligodendrocytes and Schwann cells in the CNS and the peripheral nervous system. It shows the presence of neuronal fibres in the spinal cord, as shown in Figure 5.8 (C), which parallel the complexity of neuron fibres imaged by XSPCT. Comparative images of spinal cord labelled with antibodies against laminin shows the vascular system (Figure 5.8 D). The images in Figure 5.8 C and Figure 5.8 D confirm the segmentation of Figure 5.8 (B).

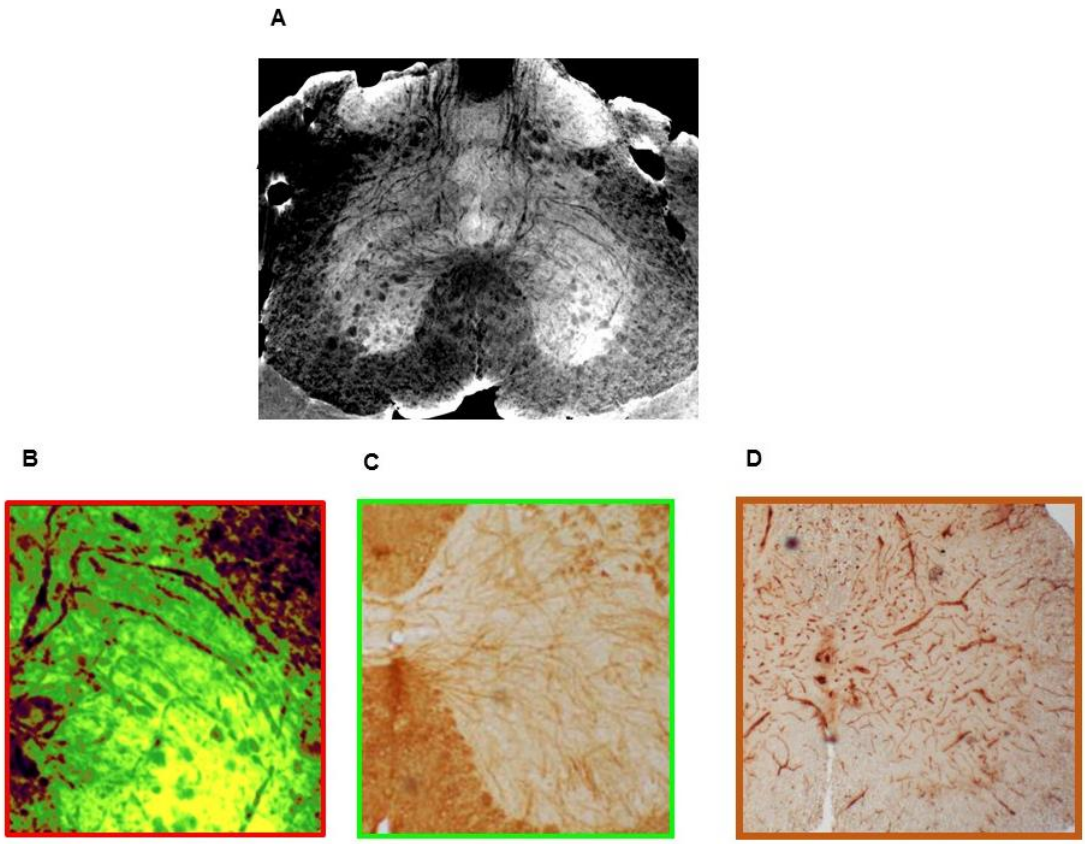

Figure 5.8: VN investigation: a) X-ray Phase Contrast Tomography reconstructed volume of lumbar-sacral region of the spinal cord. The image, obtained with a pixel size of 0.64 mm without contrast agent at TOMCAT beamline, was segmented to show the capillaries and the nerve fibers. b) Magnified region of a): the vessels are red and the nerve fibers are green. c) Immunohistochemical analysis of laminin, a marker of blood vessels, in the lumbar-sacral spinal cord showing a coronal section of the vascular system. d) Immunohistochemical analysis of myelin basic protein (MBP), a marker of the myelin sheath of nerve fibers in the spinal cord [204].

5.2.4 3D imaging of the Vascular network in mouse SC

In order to investigate only the VN of the spinal cord we made a segmentation, based on the different grey level (that correspond to different electronic density) of the volume presented before, using custom-made program "Volview". We shows in red the high-resolution 3D digitalized angio-architectual maps (vascular and the microvascular network), cut off by the segmentation in the previous image (Figure 5.8).

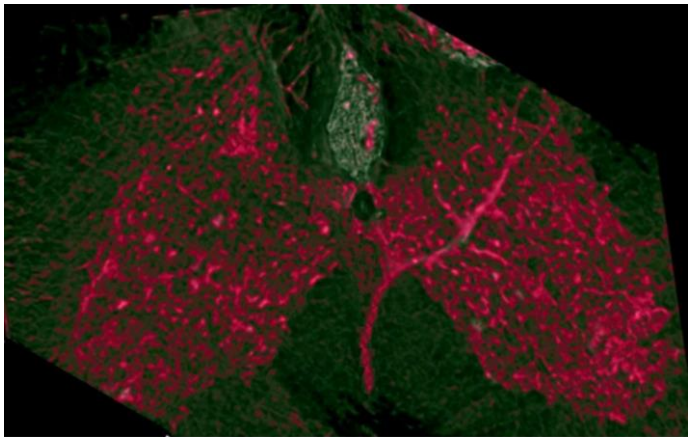

Figure 5.9: 3D segmentation of the VN in mice SC without contrast agent , in red the sulcal artery and the micro-vessels are reported (see paragraph 2.6)

We compare the VN imaged without contrast agent with the case of a twin sample prepared with MICROFIL®, a compound that fills and enhances the opacity of the microvascular network. These images were recorded at the ID17 beamline at ESRF using a 3.5 µm pixel size detector. The architecture of the vascular network is shown in (Figure 5.10) (axial view). The spatial distribution of the VN in Figure 5.10 confirms that there is a small peripheral and large central vascular supply that is characteristic of the lumbar-sacral region.

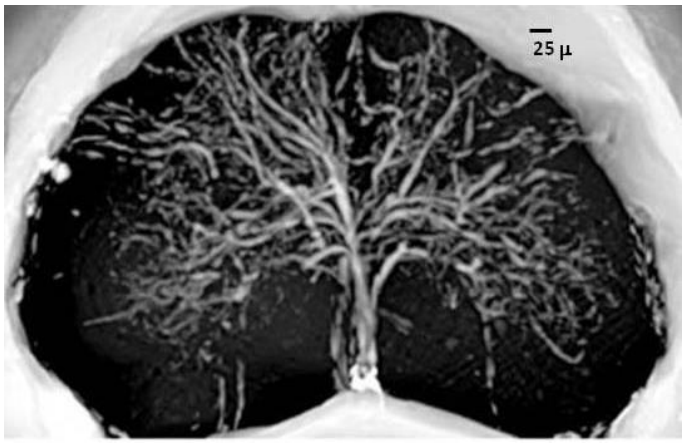

Figure 5.10: VN investigation: X-ray Phase Contrast Tomography reconstructed volume of about 1 mm thick of the lumbar-sacral region of the spinal cord with MICROFIL®, as contrast agent. The image is obtained with a pixel size of 3.5 µm at ID17 at the ESRF.

In Figure 5.11 the longitudinal view of the volume in the Figure 5.10 is reported. A volume of about 1 mm has been processed.

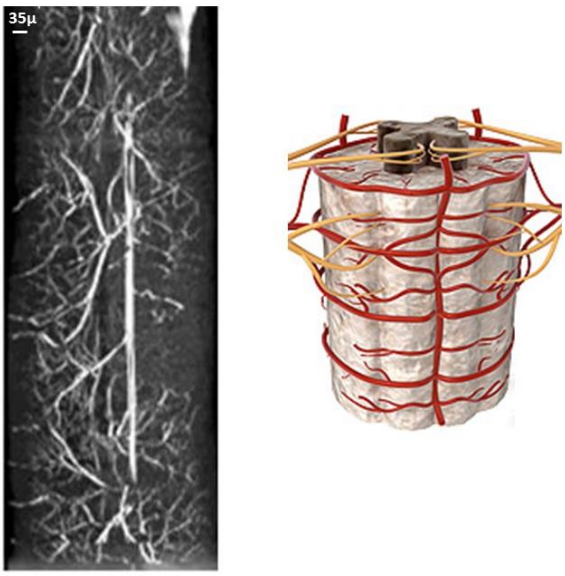

Figure 5.11: on the left Longitudinal view of Figure 5.10, 1 mm long. On the right a pictorial view of the SC vascularization coronal cross section.

It is clear the modulation at SC vertebral level of the vascular network along the spine (see paragraph 2.6). Main vessels are longitudinal and the micro-vasculature is radial.

SXrPCµT is able to reveal the micro-architecture of the SC with unprecedented spatial resolution and without the use of contrast agents, a hopeless task with conventional Xray techniques.

The results, obtained will be useful in principle to improve a classic BOLD model (based on infinite cylindrical model), used in fMRI where the equivalence with a realistic vascular model was demonstrated only for a specific geometry of the vasculature (i.e. the superficial cortex of the rat brain), but may be not preserved in the case of the SC vasculature geometry, thus it is needed at least explicit theoretical calculations, based on realistic modelling of the SC VN properties.

5.2.5 3D imaging of the Neuronal network in mouse SC

The very high spatial resolution of 0.6 µm imaging achieved in the experiment without contrast agent, allows the identification of a striking contrast between white and grey matter with single cells and nerve fibres, which are well distinguishable at the white/grey matter interface in the anterior horn of the spinal cord (In Figure 5.12 A). This SC region is highly enriched with somatic motor neurons (that are rendered in white) with a characteristic stellate morphology. Histology by Nissl staining (Figure 5.12 B) and hematoxylin/eosin staining (Figure 5.12 C) confirmed the images obtained by XSPCT. Moreover, immunohistochemical analysis with an antibody against the non-phosphorylated epitopes in neuro-filament B (SMI-32) labelled motor neurons (Figure 5.12 D), which show the same morphology of Figure 5.12 A. Higher magnification images of SMI-32 labelled cells (Figure 5.12 F)

and hematoxylin/eosin staining (Figure 5.12G) parallel the morphology of a single motor neuron shown in Figure 5.12 E.

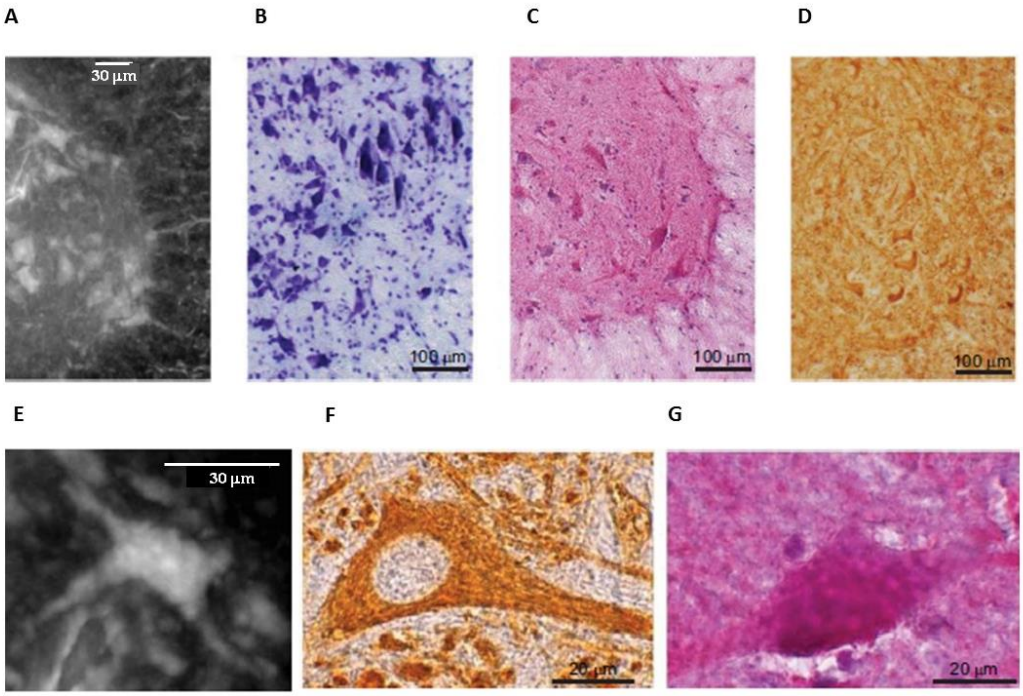

Figure 5.12: Neural population investigation: A) White/grey matter interface, imaged with inverted colour, of a thick slab selected in the anterior horn of the lumbar-sacral spinal cord. B) Nissl staining, C) Hematoxylin/eosin staining and D) Immunohistochemical analysis of SMI-32, a marker of motor neurons, at the white/grey matter interface of the anterior horn of the lumbar-sacral spinal cord. E) Magnification of a single neuronal cell. Zoom of image F) SMI-32 labelled cells and G) hematoxylin/eosin staining showing a single neuronal cell [204].

To study the morphology and the interaction between the white and the grey matter at micro scale order, we report in Figure 5.13 a zoom of the Figure 5.12, where the nerve fibres, rendered in light grey, are imaged at the interface with the grey matter (red box). In addition thanks to the sub-micron spatial resolution it is possible to distinguish the myelinated axons Figure 5.13 C, that motor neurons send out the spinal cord via the ventral nerve root filaments.

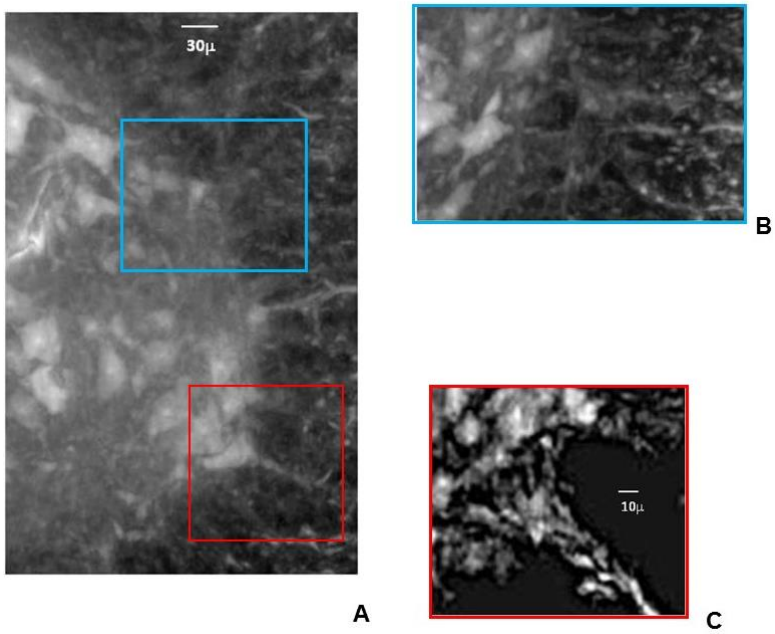

Figure 5.13:A) grey /white matter interface in the ventral horn. **B)** (blue square) Nerve fibers are imaged at the interface with the grey matter . **C)** nerve fiber of the ventral root [204]

In order to study the neuronal network interaction and its morphology, we performed a longitudinal projection (of about 1 mm in length) in the ventral horn, at the interface between white and grey matter (Figure 5.14). This region is made up of groups of cells that form motor nuclei in Lamina IX (Figure 5.14 A). Motor neurons have a unique position in the lamina IX, being the only SC neuron which has its axon almost entirely in the peripheral nervous system (see CHAPTER 2). We clearly detailed the motor neuron pool or motor nucleus that innervate a limb muscle, because there is a one-to-one relationship between a muscle and a motor neuron pool (see Appendix A: Motor neurons pools and motor unit).

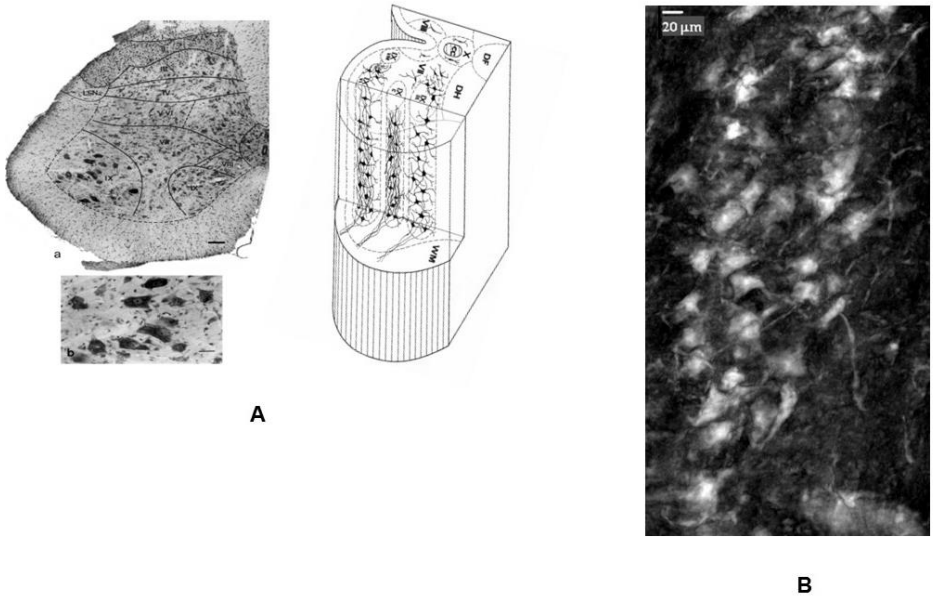

Figure 5.14: (A)Schematic representation of the laminae on the lumbar/sacral level (on the left) and dendroarchitecture of spinal moto-neurons in various motor columns (on the right) [102]. (B) Longitudinal view (length:1 mm) of the sample at the same interface [204].

In Figure 5.15 we show the interface between the central region, which connects the dorsal and ventral horns, called the intermediate grey matter, and the ventral horns. The insets of the figure are the magnification images of the motor neurons (red box) and small neurons at the medial border of the motor nucleus, which are identified as the short-axonal inhibitory interneurons (blue boxes).

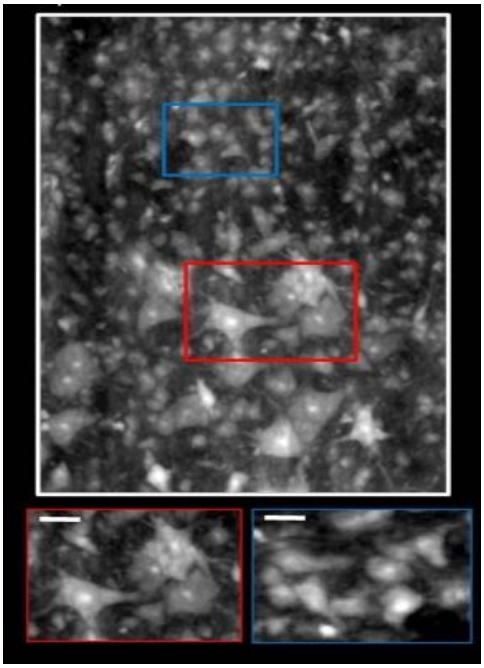

Figure 5.15: Longitudinal distribution of the cells, in the region crossing the motor neurons (red box), and the inter-neurons (blue box).

Thus, thanks this high resolution techniques it is possible to study the morphology of the SC not only structurally but also locally with high spatial resolution.

We study the distribution of the moto- and inter-neurons at different SC level. We select two Regions Of Interest (ROI) one in the ventral horn (Laminae 8/9-motor nucleus) and one in the intermediate grey matter, in particular the large central part of lamina 7, rich in interneurons cell. Then we calculated the Probability Density functions (PDF) in that ROIs.

We report in Figure 5.16A, B, C the tomographic SC cross section at cervical and thoracic level with the relative histology and laminae Rexed distribution studied. As we can observed from the PDF reported in Figure 5.16 D, the inter-neurons and motor neurons nucleus in the ROI selected, along the spine change, this is due to the fact that in the cervical and in the lumbar/sacral enlargements level the spine has more grey matter than at the thoracic level (see CHAPTER 2) .

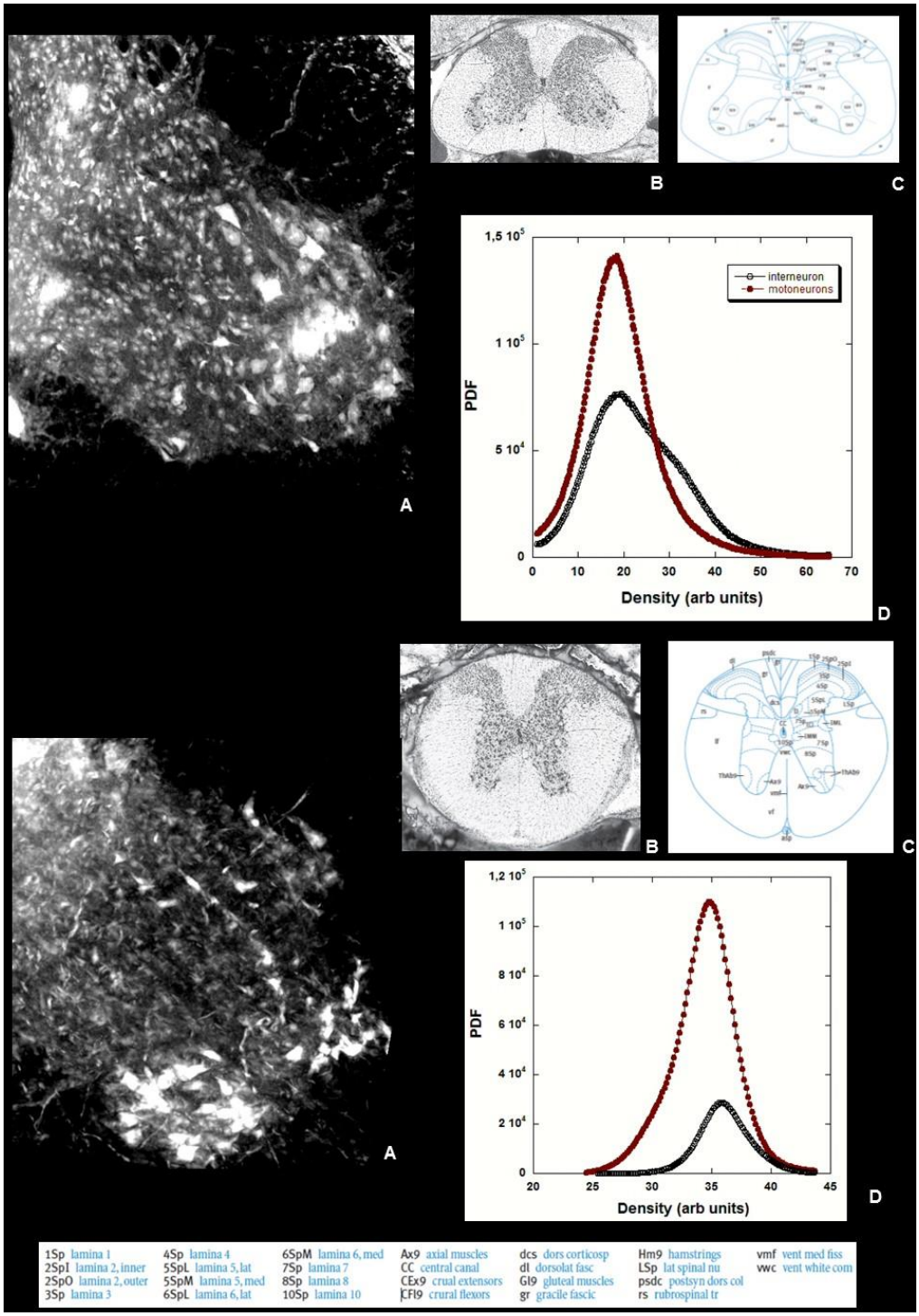

Figure 5.16: cross section in 2 level (up the cervical level and down the thoracic level) with the relative PDF, histology and laminae distribution [102].

After studying the neuronal network morphology and interaction, thanks of the tomography technique peculiarity to digitally sectioning the sample to investigate the electronic density distribution at different depths, we exploit this peculiarity to investigate the density distribution inside the single neuron soma and to quantify the different intracellular-compartments at the different depth inside the cell with a spatial depth resolution equal to the voxels size, 640x640x640 nm^3.

Figure 5.17 displays the electronic density distribution over individual slices (640 nm thick) in which we digitally sliced the neuron cell. The different grey levels of XSPCT image are proportional to electronic density of the different cellular elements inside the soma. Figure 5.17 B shows contour plot for different depth ranges. The intracellular-compartment in neuron soma, corresponds to a different functionality area.

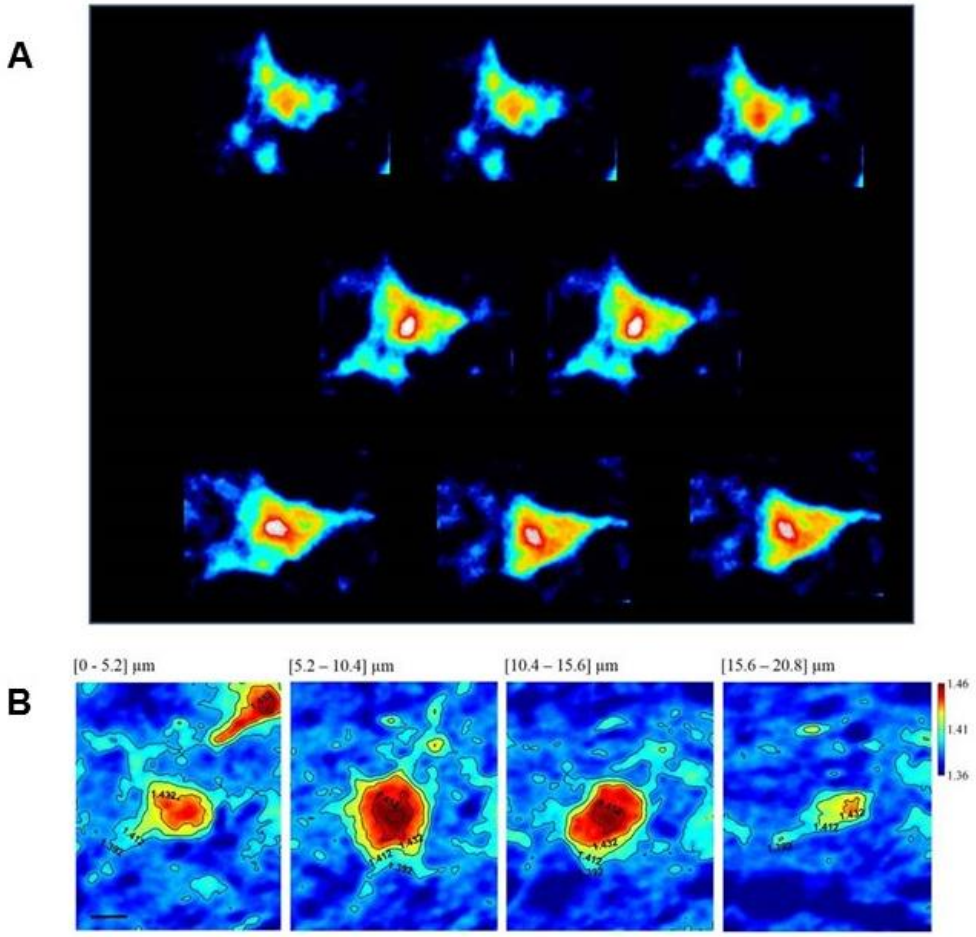

Figure 5.17: A) electronic density distribution over individual slices (640 nm thick) in which we digitally sliced the neuron cell. B) Contour plot for different depth ranges.

Summary and Conclusions

As we saw in this Chapter, SXPCμT offers the possibility to investigate simultaneously the structure of the CNS and of the vessels network (Figure 5.5), at a range of scales spanning from millimetres to sub-micrometre (Figure 5.6, Figure 5.7, Figure 5.8). This ability may have a strong impact in a large number of pre-clinical investigations of pathologies, such as neurodegenerative diseases, as well as in regenerative medicine. For example, pathology studies have found that a higher prevalence of vascular disease in the brain may result in an increased premorbid diagnosis of the Alzheimer Disease (AD) [228]. On the other hand, traumatic spinal cord injuries induce microvascular changes that may contribute to secondary injuries and deficits observed in patients [229, 230]. For example, the resulting ischemia and the extravasation of the blood components contribute to a series of effects such as edema formation, neuronal cell death, and damage to white matter tracts. Furthermore, regenerative medicine [231] shows promise for the treatment of traumatic diseases of the spinal cord.

All the above mentioned examples clearly underline the importance of the possibility to perform 3D imaging in an ex-vivo model with one single phase-contrast tomographic measurement, displaying simultaneously the complete architecture of the VN, neuronal populations (Figure 5.5), and axon bundles up to a single neuron soma (Figure 5.13, Figure 5.15). This technique allows for achieving a much higher spatial resolution than state-of-the-art SC MRI (see below Figure 5.18), with neither specific sample preparation nor contrast agent or sectioning. The ability to obtain excellent 3D resolution of the SC vasculature, allowing for the differentiation of arteries, veins and capillaries at the micrometric scale, will be instrumental to the definition of a more refined BOLD model, based on the real geometry of the spinal cord VN (a possibility that will be discussed in greater detail within the next Chapter). This improved model will greatly help our interpretation of the experimental data obtained in human-scale SC fMRI measurements, such as those presented in CHAPTER 4

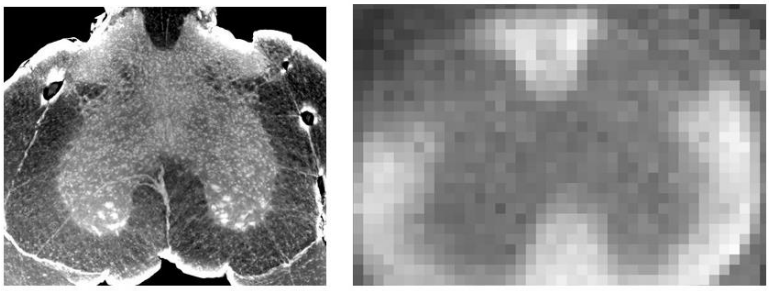

Figure 5.18: (on the right) 3D tomography reconstruction of the thoracic level compared with diffusion tensor imaging obtained with a Bruker 9.4T Avance system (in collaboration with NMR group of CNR-ISC), operating with a micro-imaging probe (10mm internal diameter bore) and equipped with a gradient unit characterized by a maximum gradient strength of 1200mT/m, and a rise time of 100μs. An imaging version of Pulse Gradient Stimulated Echo (PGSTE) sequence with Δ/δ=40/4.4ms, diffusion gradients along x, y and z axis, TR=5s, slice thickness 1mm, FOV=8mm

CHAPTER 6

SEGMENTATION OF MOUSE SC VN AS A BASIS TO DEVELOP A REALISTIC SC BOLD MODEL

As we have seen in the previous chapter, from the very beginning of brain fMRI, significant effort was devoted to the biophysical characterization of the signal, and in particular to the theoretical prediction of functional contrast features. In comparison, only modest theoretical knowledge is available for SC fMRI contrast, the origin of which is still unknown. This chapter propose a starting point to the development of numerical models of the fMRI signal in the SC based on the real geometry of the SC vascularization. In particular we analysed the vessel tree, which we have measured with SXPCμT, using a custom made program based on the structural feature (e.g. length, diameter and tortuosity) of the vessels. The results obtained will be useful in principle to improve a classic BOLD model, based on infinite cylindrical model (see CHAPTER 3), used in fMRI, where the equivalence with a realistic vascular model was demonstrated only for a specific geometry of the vasculature (i.e. the superficial cortex of the rat brain), but may be not preserved in the case of the SC vasculature geometry. It is not trivial to transfer the results obtained in a particular region of the body to another region, especially when, as in the case of BOLD, several metabolic and neuronal processes are interested.

In this framework it is needed at least explicit BOLD model, based on realistic SC vascular properties. For this reason we study the geometry and the size of the spine vessels that mainly contribute to its BOLD contrast. In particular, the attainment of a 3D imaging and quantification of the vascular network of the SC should considerably improve our knowledge of the effects of pathological processes, such as SC injuries and neurological diseases, where vascular secondary effects have been implicated.

In the following after a brief discussion about the BOLD contrast and its origin, we report the main results obtained by the segmentation of the XRPμT images that will be used to refine a SC BOLD model

6.1Current hypotheses about the origin of the SC functional contrast

The knowledge about the specificity and the characteristics of the fMRI signal in the SC is still poor. While the vascular, BOLD–like origin of the functional signal in the brain is well known, the topic is still debated for the spinal cord. At present, no satisfactory model for the functional signal in the spinal cord is available. A theoretical prediction of the functional contrast features in the spinal cord is very much needed. For this reason we put the basis to develop a SC BOLD model.

6.1.1Origin of functional signal

In the BOLD model, the fractional signal change ΔS/S in T_2^*-weighted images of gray matter tissues can be approximated as a decay linear on TE [232]:

(15)

$$\frac{\Delta S}{S} \approx -\mathrm{TE}\Delta\left(\frac{1}{T_2^*}\right)$$

Therefore, if no other phenomena are involved, the expected fractional signal change can be extrapolated to 0 for TE=0 s. Measures of ΔS/S vs. TE in T_2^*-weighted images of SC under motor or sensory stimulation gave a good linear fitting, but in the motor task data, a strange dependence of the slope of the linear fit on the order of data collection (from longer to shorter TE or vice versa) has been reported [12]. This unexpected characteristic that does not affect data acquired during sensory stimulation seems to be related to some systematic effect more than to a real physical feature. However, the fittings consistently showed a nonzero intercept, in the order of +2%. Further measures, conducted with shorter TE, seem to confirm the nonzero extrapolation, but suggest also a nonlinear dependence of ΔS/S on TE, at TE shorter than about 35 ms [8].

Stroman and Ryner [12]observed similar functional contrasts with GE EPI and SE EPI, in the same experimental conditions, while in the brain T_2^*-weighting provides a contrast considerably stronger than T_2 weighting [189]. Furthermore, the contrast is often higher than in brain under similar experimental conditions (see table 2 ref [77]).

A partial explanation for this feature can be found in the differences of vascular anatomy between brain and SC. As already discussed (see paragraph 2.6), the vessels of SC are optimally arranged for producing a strong and spatially specific BOLD contrast, with little intravascular contribution (that dominates the BOLD effect in brain at 1.5 T) and little static averaging (that is observed in T_2^*-weighted images but not in T_2-weighted ones)[4]. Thus, the signal loss is dominated by diffusion effects and therefore is mainly a T_2 effect, which produces similar contrasts in GE and SE images. A further factor is the anatomy of grey matter that has a simple shape, without tortuosity, and thus allows

the best functional homogeneity of imaging voxel, further enhanced by the good in-plane resolution often reached, giving less partial-averaging effects. However, while these components can account for similar (and increased) T_2 and T_2^* contrasts, they cannot explain the nonzero extrapolation of ΔS/S vs. TE at TE=0 s.

This phenomenon can be explained with a nonlinear trend of ΔS/S at short TE. Static dephasing and diffusion near vessels contribute nonlinearly to relaxation, but static dephasing is likely to have a minor role (see above) and diffusion effects should contribute with a component diverging from linearity only at longer TE and maintaining the zero value at TE=0 s. Stroman et al. hypothesize that the increase of SE contrast and the nonzero intercept of ΔS/S vs. TE are related to a functional increase of the baseline signal, not related to BOLD effect. They observe that as a consequence of the increased blood flow during activation, the intravascular pressure increases, in particular in arteries. Thus, the water flow across the vessel walls can increment and the extravascular water at equilibrium can have an overall increase. As a complemental alternative, an increase in intracellular water can be suggested by the functional decrease of apparent diffusion coefficient observed by Darquie´ et al. [233], attributed to neuronal swelling during activation. In both these conditions, an enhancement of MRI signal is observed because of the greater amount of resonant protons [12]. Stroman et al. [142] [8, 202] refer to this phenomenon as SEEP (see paragraph 1.3.2). In particular, in SC fMRI, it is supposed to account for at least half of the functional contrast.

6.1.2 General overview of the "work-in-progress" SC BOLD signal Model

In the SC, the BOLD signal arising from large venous vessels should be greatly reduced, due to their axial symmetry, parallel to the static magnetic field $\mathbf{B_0}$. Similarly, the disposition of small vessels, all radial and thus orthogonal to $\mathbf{B_0}$, should emphasize the dephasing effect of deoxyhemoglobin. In fact, modelling the vessel as an infinite cylinder, the perturbation to $\mathbf{B_0}$ in a point P outside the vessel can be expressed, in terms of angular frequency, as reported in equations (see CHAPTER 3):

(7)
$$\Delta\omega_B^{in} = 2\pi\Delta\chi_0(1-Y)H_{ct}\gamma B_0\left\{cos^2(\theta) - \frac{1}{3}\right\},$$
$$\Delta\omega_B^{out} = 2\pi\Delta\chi_0(1-Y)H_{ct}\gamma B_0\left\{\frac{R_0}{r}\right\}^2 \sin^2(\theta)\cos(2\Psi),$$

As it is apparent from Eq. (7) [232], the perturbation in P is maximal when the vessel is perpendicular to the static magnetic field and vanishes when the vessel is parallel to $\mathbf{B_0}$. Moreover, the intravascular contribution can be neglected for large vessels, as they lie externally to the SC.

The classical BOLD model is based on several assumption that only hold for the specific geometry of the brain (i.e. cerebral cortex) vasculature and whose validity may not be preserved in the case of the SC.

In particular the modelling of the BOLD signal in the brain assumes random distribution of vessels, and distance between vessels large if compared to the diffusion range of water molecules during the MRI scan [4]. Consequently, it is assumed that each water molecule experiences the dephasing field of a single vessel.

We sought to incorporate SC structural information into previously published models of neurovascular and neuro-metabolic coupling. In particular we assume that each water molecule experiences the dephasing field of a single vessel as in the brain BOLD model but conversely the vessels are not randomly distributed and are not far apart.

Numerical simulations will be conducted assuming the known SC anatomy, that we have characterized thanks the high resolution XrPCT images and segmentation algorithms. Dephasing will be computed numerically in a voxel, by dividing it in a reasonably high number of starting lattice points (almost 4096), and a set of 3D random walks (not discretized to the lattice) will be generated for a sample water molecule. At each time step (100 μs or shorter) the dephasing will be calculated as:

16) $$\phi(\theta) \int_0^{TE} w_b(P)dt$$

The signal attenuation (relative to the signal without phase dispersion) will be calculated with the appropriate averaging between the accumulated phases obtained with the set of random walks.

Vessel orientation (θ) and size (r_b), will be varied in the interval suggested by the SC anatomy. The global effect will be obtained from average between different orientations and sizes.

For this reason in this project it will be placed a particular emphasis on the study of the geometry and of the size of those spine vessels that mainly contribute to its BOLD contrast.

6.2 SC Vasculature

In our work, we mainly focus on the geometry of the spinal cord vasculature, and on the size of those vessel that mainly contribute to its BOLD contrast.

As we have seen in the CHAPTER 2, the blood supply to vertebral body, paraspinal muscles, dura, nerve root, and spinal cord is derived from segmental arteries. An extraspinal system connects the neighbouring segmental arteries longitudinally. The intraspinal extradural system is mainly a transverse anastomosis. The extra- and intraspinal anastomoses protect the spinal cord against ischaemia when pathologies such as arteriosclerotic disease of the aorta cause occlusion of the focal vessels. The distribution of blood to the spinal cord is achieved by a system of longitudinal anastomoses between the anterior spinal artery and the posterior/ posterolateral spinal arteries. These are reinforced by the radiculopial or radicu- lomedullary arteries at various segmental levels. Both the arterial and venous blood contributing to the BOLD contrast is driven by transverse vessels, with diameters inferior to 50 μm.

The Size of the vessels is a well-known issue in the modulation of the BOLD contrast [234], concerning both the relationship between the diffusion process and the loss signal coherence, and the vascular volumes topic (i.e. the intravascular extravascular ratio). Thus the peculiar size of those SC vessels contributing to BOLD signal constitutes an important issue for a SC specific model. But, as demonstrated by Pathak and co-workers, the pure geometric features (the shape) of the vascular bed may play a very important role [235]. The in the infinite cylindrical model itself give a clear evidence of the differences one can found when the vascular bed is characterized by a preferred orientation in relation to the static magnetic field (see eq. (8)). In the following we report the vasculature analysis. In particular we performed the segmentation of the vessel tree using a 2D/3D analysis tool that detects vessels by means of their characteristic geometry (tubular structure), rather than by a range of grey, allowing for the extraction of individual vessels from 3D datasets and for the estimation of several attributes such as length, diameter and tortuosity and voxel junction.

6.3 Skeletonize

To analyse the vascular network we used An ImageJ application "*Analyze-Skeleton"*, implemented with The Floyd Warshall algorithm [236]. After thresholding the 2D/3D stack, the binary image is transferred to a skeleton and the skeleton to a weighted graph using the ImageJ plugin.

6.3.1General Description

Analyze-Skeleton plugin tags all pixel/voxels in a skeleton image and then counts all its junctions, triple and quadruple points and branches, and measures their average and maximum length. The tags are shown in a new window displaying every tag in a different color.

The voxels are classified into three different categories depending on their 26 neighbors (

Figure **6.1**):

- **End-point** voxels: if they have less than 2 neighbors.
- **Junction** voxels: if they have more than 2 neighbors.
- **Slab** voxels: if they have exactly 2 neighbors.

End-point voxels are displayed in **blue**, slab voxels in **orange** and junction voxels in **purple**. However, following this notation, the number of junction voxels can be different from the number of actual junctions since some junction voxels can be neighbours of each other.

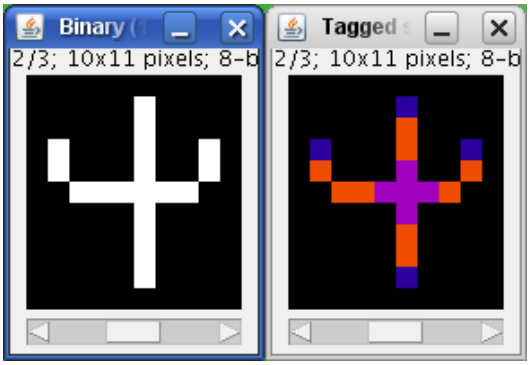

Figure 6.1: Example of skeleton classification (http://fiji.sc/AnalyzeSkeleton)

The Skeleton is treated as an undirected graph[12], where the end-points and junctions are the nodes and the slab-branches are the edges. While traversing the graph in the Depth-first search (DFS)[13] fashion, the edges/branches pointing to unvisited nodes are marked as *TREE* edges, while the edges to visited nodes are marked as BACK edges, which involves the presence of a loop. After the edge

[12] An undirected graph is a graph in which edges have no orientation. The edge (x, y) is identical to the edge (y, x), i.e., they are not ordered pairs, but sets {x, y} (or 2-multisets) of vertices. The maximum number of edges in an undirected graph without a loop is $n(n-1)/2$.

[13] Depth-first search (DFS) is an algorithm for traversing or searching tree or graph data structures. One starts at the root (selecting some arbitrary node as the root in the case of a graph) and explores as far as possible along each branch before backtracking.

classification, the BACK edges are backtracked following their predecessors in order to calculate all the edges belonging to each cycle and proceed with the pruning (Figure 6.2). The only known limitation of this approach is shown in the presence of nested loops. In those cases, a second call to the plugin is usually enough to eliminate all the remaining loops.

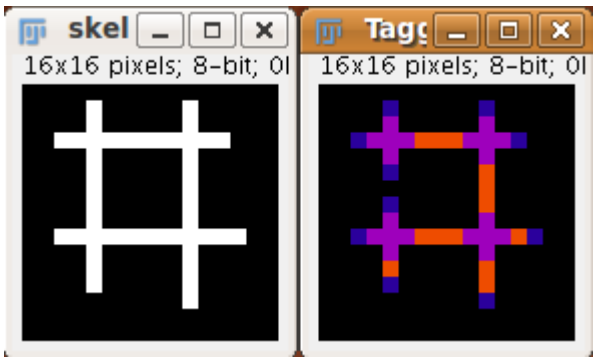

Figure 6.2: Example of cycle detection and pruning (http://fiji.sc/AnalyzeSkeleton)

After classification, for each skeleton in the image are defined:

- The number of branches (slab segments, usually connecting end-points, end-points and junctions or junctions and junctions). The special case of a circular skeleton is also contemplated here.
- The number of voxels of every type: end-point, slab and junction voxels.
- The number of actual junctions (merging neighbor junction voxels) with an arbitrary number of projecting branches.
- The number of triple points (junctions with exactly 3 branches) and quadruple points (4 branches).
- The average and maximum length of branches, in the corresponding units.

- Calibrated branch length,
- 3D coordinates of the extremes of the branch (the so-called V1 and V2 vertices),
- and the Euclidean distance between those extreme points. This value has proven to be a good indicator of the tortuosity of the 3D object.

Implementation with the Marshall algorithm: Longest shortest path estimation

As we have seen in the previous paragraph the tagged skeleton can be described as an undirected and weighted graph. The nodes are the end-point and junction pixels, the weighted edges are the summed Euclidian distances between every slab pixel and its neighbour in the edge. From graph theory it is known that there always is a shortest path between two nodes of a connected graph. So, in a graph

there always exists a longest, shortest path, which is the best approximation for the vessels length in our case. Dijkstra's algorithm [237], is a well-known graph search algorithm that solves the single-source shortest path problem for a graph with nonnegative edge path costs, producing a shortest path tree. The Floyd–Warshall algorithm [236] is a graph analysis algorithm for finding shortest paths in a weighted graph (with positive or negative edge weights). A single execution of the algorithm find the lengths (summed weights) of the shortest paths between all pairs of nodes though it does not return details of the paths themselves. The algorithm uses an adjacency matrix to determine the shortest path from every node to every other node. Initially this adjacency matrix contains the weight of the edge from node i to node j which respectively correspond to the row and column of the matrix, if there is no edge from i to j the weight is set to infinity. During these iterations the algorithm check if there exists a shorter path between nodes. If this is the case it replaces the old value in the matrix with the new. In this way, after $(n)^3$ iterations we get all the shortest paths, where n is the number of nodes.

The Warshall algorithm was implemented in the AnalyzeSkeleton plugin. The maximum length of all shortest paths was used as output of the algorithm.

The Warshall algorithm does not return details about the paths, but in order to be able to verify the results it is nice when the shortest path is visualized. Therefore we reconstructed the found shortest path using the predecessor matrix which is computed at the same time as the adjacency matrix. In the predecessor matrix all the shortest paths going from node i to any other node are coded in row i. The column j then contains the predecessor node (hence the name) in the shortest path going from i to j. In this way we can reconstruct the longest path as drawn in the final image (Figure 6.3).

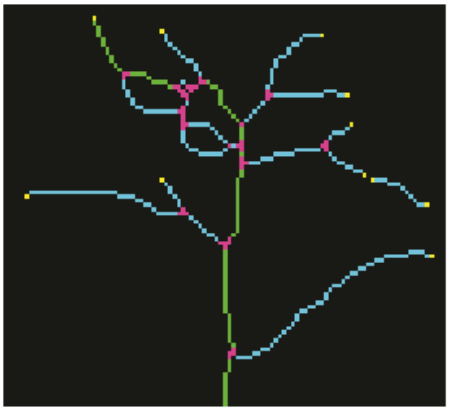

Figure 6.3: shows the result. The end-point pixels are coloured yellow, the junction pixels purple and the slab pixels cyan [236].

6.4 Vascular segmentation

To study the real morphology and the structure of the mouse SC we performed the segmentation on the mouse SC measured at ID17 at ESRF with a pixel size of 3.5 µm. The tomography has been acquired with 2000 projections covering a total angle range of 360° with acquisition time of 1 second per point. We explored the entire volume of the SC. After the analysis of the reconstructed tomography, we analyse with ImageJ- *Analyze-Skeleton* volumes of about 1mm to detect vessels by means of their characteristic geometry, allowing for the extraction of individual vessels from 3D datasets and for the estimation of several attributes such as length, diameter and tortuosity (see the paragraph above).

First a fixed threshold was applied on the reconstructed volume resulting in a binary image (Figure 6.4B). Figure 6.4C shows the skeleton of the binary image. Thresholding and skeletonizing were applied using standard ImageJ functions. After that, using the *Analyze-Skeleton* plugin the skeleton is annotated. This plugin tags all pixels in the skeleton image and then counts all its junctions, triple and quadruple points and branches, and measures their average and maximum length. In our case the SC vascularization has lots of leaves and side branches which results in a very complicated skeleton (about 25000 junctions) (Figure 6.4D).

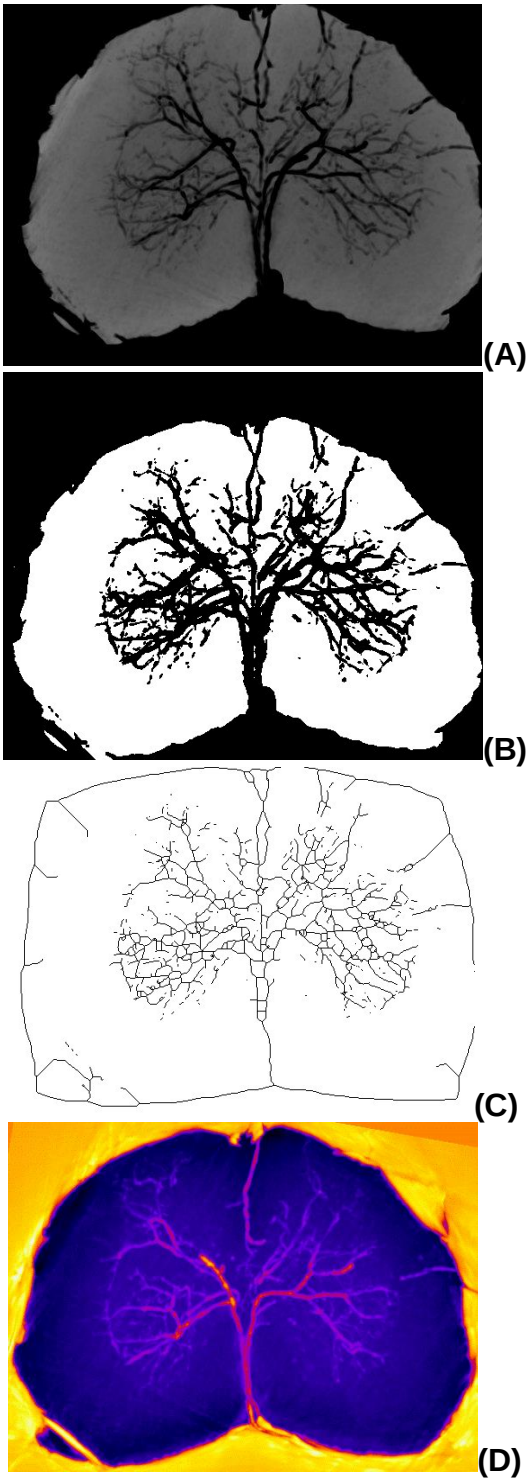

Figure 6.4:the different step of the SC segmentation

We performed the same procedure using a coronal view of the same volume to study the longitudinal distribution of the vessels. In this way we studied the vessels in two different cross section to have a complete overview of the vascular geometry of the SC.

Figure 6.5: SC coronal cross section of the volume in Figure 6.5 in the (A), (B) and (D) step

After the identification of the vessels in a slab of 1 mm, we performed the same procedure using small images stack, of about 200 micron, to segment only one or two vessels as a basis for the BOLD model signal (Figure 6.6).

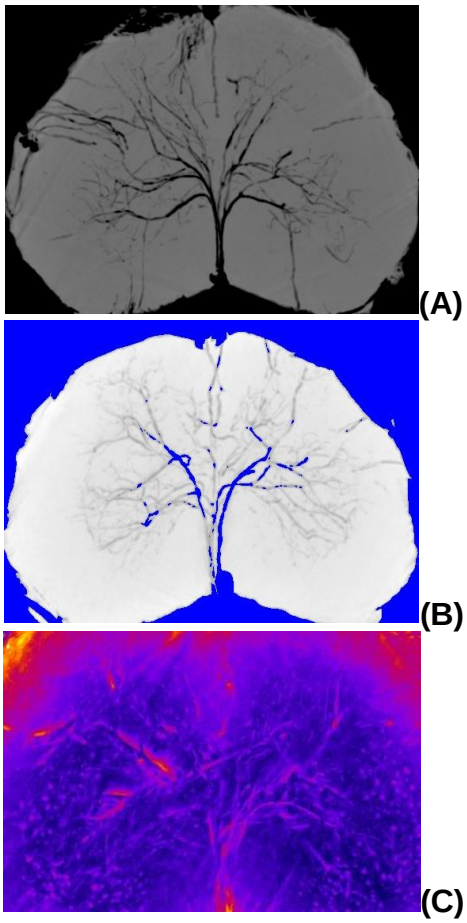

Figure 6.6: (A) a reconstructed slab of 200 micron. **(B)** thresholded and binarized volume **(C)** Skeleton

In order to measure the diameter of the vessels segmented we extracted from the skeleton the vessels and using the ImageJ-plugins Diameter. The DIAMETER plug-in uses a full width at half-maximum algorithm to estimate the inner vessel diameter based on the red blood cell column. In detail, the algorithm requires a line selection by the operator. This should cross the vessel and exceed the maximum vessel diameter during the investigated period on both sides. In Figure 6.7 we report on the left the skeletonized image obtained by the "Analyze-Skeleton" tool and on the right we report the size of three vessels (arteriole, small vein and the sulcal artery).

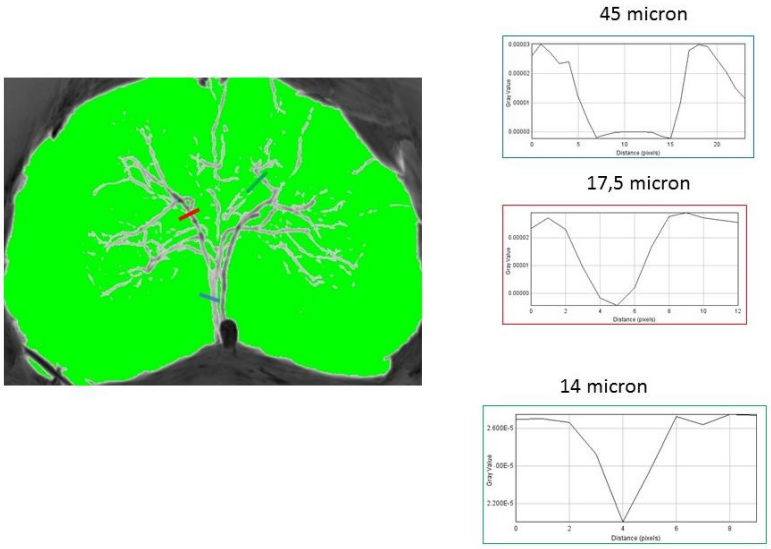

Figure 6.7: we report in the blue the measure of the sulcal artery, while in red square and in the green square the size of the arterioles and of the small veins are shown respectively.

This analysis will be used to refine the SC BOLD model, described in the paragraph, using realistic vascular geometry. For this reason in our work we place a particular emphasis on the study of the geometry and of the size of those spine vessels that mainly contribute to the BOLD contrast.

Summary and Conclusions

We plan to improve the classical model of the BOLD signal. The latter is based on several assumptions that only hold for the specific geometry of the brain (i.e. cerebral cortex) vasculature and whose validity may not be preserved in the case of the SC. The BOLD signal is the result of vascular and metabolic processes that strongly depend on the features of the tissue. We sought to incorporate structural information into previously published models of neurovascular and neurometabolic coupling. Thus we detect the vessels by means of their characteristic geometry from the high resolution SXPCµT images. SXPCµT is able to reveal the micro-architecture of the SC with unprecedented spatial resolution and without the use of contrast agents, a hopeless task with conventional Xray techniques. We use algorithms that allow to extract individual vessel features, such as length, diameter and tortuosity. We delineate the micro-vascular and VN of the mouse SC.

The attainment of a 3D imaging and the quantification of the vascular network of the SC should considerably improve our knowledge of the effects of pathological processes, such as SC injuries and neurological diseases, where vascular secondary effects have been implicated.

Conclusions

The present thesis proposes an interdisciplinary research combining biomedical and physical science, with the intent to develop a multidisciplinary network between advanced X-ray imaging techniques, fMRI and new algorithms to develop a solid multimodal method for pre-clinical research in the field of imaging field.

In particular, in this work we characterized the *spinal BOLD signal* using a multimodal approach. We investigated

1) The biophysical features of the spinal BOLD functional response.
2) The structure of the SC vascular and neuronal networks, which together contribute to the BOLD signal in fMRI. The information gathered on these networks will be used to develop an optimized spinal BOLD model. Indeed the currently used fMRI model is a mathematical abstraction of the vascular/metabolic response in the rat brain cortex, which may not be appropriate for the SC.

Part I:

Several fMRI approaches have been sparsely attempted for the study of the SC function; however, the exact features of the functional response, and even the biophysical origin of the signal, are still unclear.

In the present work, we performed a controlled motor task (graded isometric force) of the right dominant hand, and we parametrically studied the relationship between stimulation strength and functional response. We found a strong parametric dependence of the functional response in the SC on the stimulation strength in an isometric motor task. Such a dependence is important, because it confirms the physiological origin of the response. Chapter 4 we presented the results obtained on the study of the linearity of the hemodynamic response as a function of the intensity of a graded task in fMRI applied to the human SC. We developed approaches to study this linear relationship, and to verify univocally the results obtained. The first method is a direct one, assessing the features of the BOLD response by deconvolving the signal only

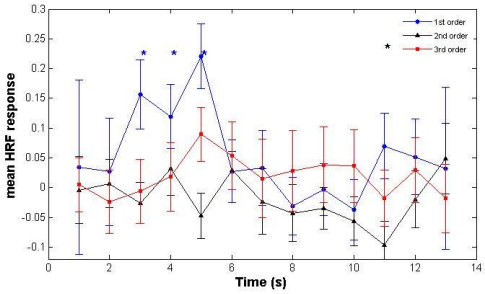

Hemodynamic response extracted from the kernel analysis

within the segmented region using the recorded force. By deconvolving the response from a known area of activation with the stimulus function, the hemodynamic response function can be obtained (using Volterra Theory).

The second method, on the other hand, analyses the data by using a standard SC hemodynamic function response [17]. With both methods we observed a linearity of the hemodynamic response as a function of the intensity of a graded task. In addition, the activation response is the same but the activation region is less spread in the first case than in the second case, due to the higher statistical parameter (2^6) in the former.

We also performed a systematic investigation of the different strength levels, employing a model that takes non-linear effects into account (Volterra series).

Part II:

The present thesis also tackled the study of the SC vascular (VN) and neuronal networks (NN), which together contribute to the BOLD signal in fMRI. The state-of the-art model currently used in fMRI studies is a mathematical abstraction of the vascular/metabolic response in the rat brain cortex, which may not be appropriate for the SC. In this thesis, we obtained detailed spatial information on the vascular geometry of the mouse SC, by means of SXPCμT. The gathered information will be instrumental for the development of an optimized SC BOLD model. This will improve the methodological strategies employed to investigate SC function non-invasively in physiological and pathological conditions, thereby accelerating the introduction of SC fMRI in the clinical setting. In Chapter 5 we report the main results obtained using SXPCT, which allowed us to simultaneously investigate the structure of the CNS and of the vessels network at a range of scales spanning from millimetres to sub-micrometres. The results reported in this study are unique in providing a detailed three-dimensional analysis of the micro-vascular network together with their relevant interactions with the neuronal cells of the healthy mouse SC, without the need for any contrast agent and for destructive sample preparation. In particular, we are able to image the 3D distribution both of the micro-capillary network and of the micrometric nerve fibres, axon bundles and neuron soma.

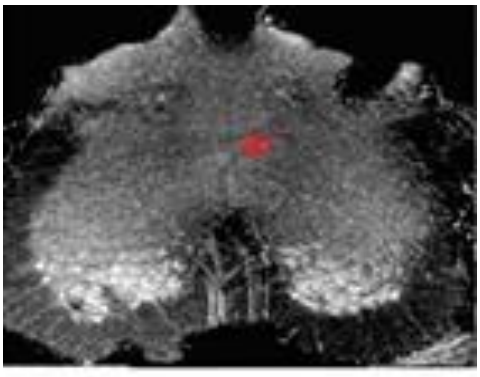

High resoluton SXPCT image. It is reported simultaneously the NN and the VN. The red row indicate the CFS canal.

Finally, in Chapter 6 we treated the high-resolution images obtained by SXPCμT to segment the vascular architecture of the mouse SC by means of its characteristic geometry using an algorithm implemented in ImageJ software.

In particular, this algorithm allows for the extraction of individual vessel features, such as length, diameter and tortuosity. In addition, the algorithm also allows for the extraction of a map of the vessels segmented in the volume. This map represents an excellent starting point for the definition of the refined BOLD model that we are developing in collaboration with the Fondazione Santa Lucia.

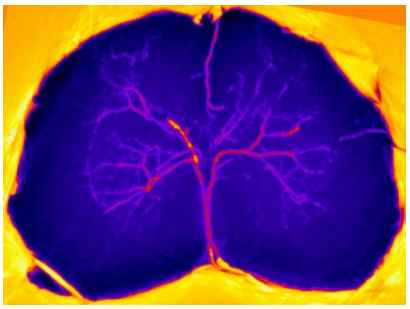

Vascular segmentation using ImageJ tool

In conclusion, this thesis opens an important path for the development of clinical applications of spinal fMRI. The study of the human SC in vivo may be of immediate and fruitful exploitation in the medical field, in particular in the treatment of SC injuries and of multiple sclerosis. Once SC fMRI becomes available to them, clinicians will benefit of a tool capable of verifying the effectiveness of treatments during the testing phase, and of monitoring their progression from the anatomical and structural viewpoints.

References

1. Ogawa, S. and T.M. Lee, *Magnetic resonance imaging of blood vessels at high fields: in vivo and in vitro measurements and image simulation.* Magn Reson Med, 1990. **16**(1): p. 9-18.

2. Ogawa, S., et al., *Brain magnetic resonance imaging with contrast dependent on blood oxygenation.* Proc Natl Acad Sci U S A, 1990. **87**(24): p. 9868-72.

3. Ogawa, S., et al., *Oxygenation-sensitive contrast in magnetic resonance image of rodent brain at high magnetic fields.* Magn Reson Med, 1990. **14**(1): p. 68-78.

4. Ogawa, S., et al., *Functional brain mapping by blood oxygenation level-dependent contrast magnetic resonance imaging. A comparison of signal characteristics with a biophysical model.* Biophysical journal, 1993. **64**(3): p. 803.

5. Logothetis, N.K., et al., *Neurophysiological investigation of the basis of the fMRI signal.* Nature, 2001. **412**(6843): p. 150-157.

6. Yoshizawa, T., et al., *Functional magnetic resonance imaging of motor activation in the human cervical spinal cord.* Neuroimage, 1996. **4**(3): p. 174-182.

7. Stroman, P., et al., *Noninvasive assessment of the injured human spinal cord by means of functional magnetic resonance imaging.* Spinal Cord, 2004. **42**(2): p. 59-66.

8. Stroman, P., et al., *Extravascular proton-density changes as a non-BOLD component of contrast in fMRI of the human spinal cord.* Magnetic resonance in medicine, 2002. **48**(1): p. 122-127.

9. Stroman, P., et al., *Functional magnetic resonance imaging of the human cervical spinal cord with stimulation of different sensory dermatomes.* Magnetic resonance imaging, 2002. **20**(1): p. 1-6.

10. Stroman, P., K. Malisza, and M. Onu, *Functional magnetic resonance imaging at 0.2 Tesla.* Neuroimage, 2003. **20**(2): p. 1210-1214.

11. Stroman, P., P. Nance, and L. Ryner, *BOLD MRI of the human cervical spinal cord at 3 tesla.* Magnetic resonance in medicine, 1999. **42**(3): p. 571-576.

12. Stroman, P. and L. Ryner, *Functional MRI of motor and sensory activation in the human spinal cord.* Magnetic resonance imaging, 2001. **19**(1): p. 27-32.

13. Stroman, P., et al., *Mapping of neuronal function in the healthy and injured human spinal cord with spinal fMRI.* Neuroimage, 2002. **17**(4): p. 1854-1860.

14. Stroman, P.W., *Magnetic resonance imaging of neuronal function in the spinal cord: spinal FMRI.* Clinical medicine & research, 2005. **3**(3): p. 146-156.

15. Stroman, P.W., B.C. Coe, and D.P. Munoz, *Influence of attention focus on neural activity in the human spinal cord during thermal sensory stimulation.* Magnetic resonance imaging, 2011. **29**(1): p. 9-18.

16. Stroman, P.W., et al., *The current state-of-the-art of spinal cord imaging: methods.* Neuroimage, 2014. **84**: p. 1070-1081.

17. Giulietti, G., et al., *Characterization of the functional response in the human spinal cord: Impulse-response function and linearity.* Neuroimage, 2008. **42**(2): p. 626-634.

18. Madi, S., et al., *Functional MR imaging of the human cervical spinal cord.* American journal of neuroradiology, 2001. **22**(9): p. 1768-1774.

19. Maieron, M., et al., *Functional responses in the human spinal cord during willed motor actions: evidence for side-and rate-dependent activity.* The Journal of neuroscience, 2007. **27**(15): p. 4182-4190.

20. Agosta, F., et al., *Tactile-associated recruitment of the cervical cord is altered in patients with multiple sclerosis.* Neuroimage, 2008. **39**(4): p. 1542-1548.

21. Agosta, F., et al., *Evidence for enhanced functional activity of cervical cord in relapsing multiple sclerosis.* Magnetic Resonance in Medicine, 2008. **59**(5): p. 1035-1042.

22. Kornelsen, J. and P. Stroman, *Detection of the neuronal activity occurring caudal to the site of spinal cord injury that is elicited during lower limb movement tasks.* Spinal Cord, 2007. **45**(7): p. 485-490.

23. Valsasina, P., et al., *Cervical cord functional MRI changes in relapse-onset MS patients.* Journal of Neurology, Neurosurgery & Psychiatry, 2010. **81**(4): p. 405-408.

24. Wheeler-Kingshott, C., et al., *The current state-of-the-art of spinal cord imaging: applications.* Neuroimage, 2014. **84**: p. 1082-1093.

25. Brooks, J.C., et al., *Physiological noise modelling for spinal functional magnetic resonance imaging studies.* Neuroimage, 2008. **39**(2): p. 680-692.

26. Backes, W.H., W.H. Mess, and J.T. Wilmink, *Functional MR imaging of the cervical spinal cord by use of median nerve stimulation and fist clenching.* American Journal of Neuroradiology, 2001. **22**(10): p. 1854-1859.

27. Bouwman, C., et al., *Spinal cord functional MRI at 3 T: gradient echo echo-planar imaging versus turbo spin echo.* Neuroimage, 2008. **43**(2): p. 288-296.

28. Mitchell, D.G., *MRI principles*. 1999: WB Saunders Company.

29. García-Panach, J., et al., *A voxel-based analysis of FDG-PET in traumatic brain injury: regional metabolism and relationship between the thalamus and cortical areas.* Journal of neurotrauma, 2011. **28**(9): p. 1707-1717.

30. Kato, T., et al., *Statistical image analysis of cerebral glucose metabolism in patients with cognitive impairment following diffuse traumatic brain injury.* Journal of neurotrauma, 2007. **24**(6): p. 919-926.

31. Floeth, F.W., et al., *Prognostic value of 18F-FDG PET in monosegmental stenosis and myelopathy of the cervical spinal cord.* Journal of Nuclear Medicine, 2011. **52**(9): p. 1385-1391.

32. Uchida, K., et al., *Metabolic neuroimaging of the cervical spinal cord in patients with compressive myelopathy: a high-resolution positron emission tomography study.* Journal of Neurosurgery: Spine, 2004. **1**(1): p. 72-79.

33. Uchida, K., et al., *Neurological Improvement Associated with Resolution of Irradiation-Induced Myelopathy: Serial Magnetic Resonance Imaging and Positron Emission Tomography Findings.* Journal of Neuroimaging, 2009. **19**(3): p. 274-276.

34. Uchida, K., et al., *High-resolution magnetic resonance imaging and 18FDG-PET findings of the cervical spinal cord before and after decompressive surgery in patients with compressive myelopathy.* Spine, 2009. **34**(11): p. 1185-1191.

35. Tewarie*, R.D.N., et al., *Positron emission tomography for serial imaging of the contused adult rat spinal cord.* Molecular imaging, 2010. **9**(2): p. 108.

36. Wang, X., et al., *Recovery from chronic spinal cord contusion after Nogo receptor intervention.* Annals of neurology, 2011. **70**(5): p. 805-821.

37. Huang, Y., et al., *Comparative Evaluation in Nonhuman Primates of Five PET Radiotracers for Imaging the Serotonin Transporters: [11C] McN 5652, [11C] ADAM, [11C] DASB, [11C] DAPA, and [11C] AFM.* Journal of Cerebral Blood Flow & Metabolism, 2002. **22**(11): p. 1377-1398.

38. Williams, W.A., et al., *First in human evaluation of [11 C] AFM, a novel PET tracer for the serotonin transporter.* Neuroimage, 2008. **41**: p. T42.

39. Zhu, Z., et al., *The new PET imaging agent [11 C] AFE is a selective serotonin transporter ligand with fast brain uptake kinetics.* Nuclear medicine and biology, 2004. **31**(8): p. 983-994.

40. Horsfield, M.A., et al., *Rapid semi-automatic segmentation of the spinal cord from magnetic resonance images: application in multiple sclerosis.* Neuroimage, 2010. **50**(2): p. 446-455.

41. Le Bihan, D., et al., *MR imaging of intravoxel incoherent motions: application to diffusion and perfusion in neurologic disorders.* Radiology, 1986. **161**(2): p. 401-407.

42. Basser, P.J., J. Mattiello, and D. LeBihan, *MR diffusion tensor spectroscopy and imaging.* Biophysical journal, 1994. **66**(1): p. 259.

43. Clark, C.A. and D.J. Werring, *Diffusion tensor imaging in spinal cord: methods and applications–a review.* NMR in Biomedicine, 2002. **15**(7-8): p. 578-586.

44. Barker, G., *Diffusion-weighted imaging of the spinal cord and optic nerve.* Journal of the neurological sciences, 2001. **186**: p. S45-S49.

45. Vedantam, A., et al., *Diffusion tensor imaging of the spinal cord: insights from animal and human studies.* Neurosurgery, 2014. **74**(1): p. 1-8.

46. Demir, A., et al., *Diffusion-weighted MR Imaging with Apparent Diffusion Coefficient and Apparent Diffusion Tensor Maps in Cervical Spondylotic Myelopathy 1.* Radiology, 2003. **229**(1): p. 37-43.

47. Shen, H., et al., *Applications of diffusion-weighted MRI in thoracic spinal cord injury without radiographic abnormality*. International orthopaedics, 2007. **31**(3): p. 375-383.

48. Mac Donald, C.L., et al., *Diffusion tensor imaging reliably detects experimental traumatic axonal injury and indicates approximate time of injury*. The Journal of neuroscience, 2007. **27**(44): p. 11869-11876.

49. DeBoy, C.A., et al., *High resolution diffusion tensor imaging of axonal damage in focal inflammatory and demyelinating lesions in rat spinal cord.* Brain, 2007. **130**(8): p. 2199-2210.

50. Zhang, J., et al., *Diffusion tensor magnetic resonance imaging of Wallerian degeneration in rat spinal cord after dorsal root axotomy*. The Journal of Neuroscience, 2009. **29**(10): p. 3160-3171.

51. Thurnher, M.M. and M. Law, *Diffusion-weighted imaging, diffusion-tensor imaging, and fiber tractography of the spinal cord.* Magnetic resonance imaging clinics of North America, 2009. **17**(2): p. 225-244.

52. Budde, M.D., et al., *Toward accurate diagnosis of white matter pathology using diffusion tensor imaging.* Magnetic resonance in medicine, 2007. **57**(4): p. 688-695.

53. Budde, M.D., et al., *Axial diffusivity is the primary correlate of axonal injury in the experimental autoimmune encephalomyelitis spinal cord: a quantitative pixelwise analysis.* The Journal of neuroscience, 2009. **29**(9): p. 2805-2813.

54. Kim, J.H., et al., *Noninvasive diffusion tensor imaging of evolving white matter pathology in a mouse model of acute spinal cord injury*. Magnetic Resonance in Medicine, 2007. **58**(2): p. 253-260.

55. Kozlowski, P., et al., *Characterizing white matter damage in rat spinal cord with quantitative MRI and histology*. Journal of neurotrauma, 2008. **25**(6): p. 653-676.

56. Song, S.-K., et al., *Dysmyelination revealed through MRI as increased radial (but unchanged axial) diffusion of water*. Neuroimage, 2002. **17**(3): p. 1429-1436.

57. Xie, M., et al., *Rostro-caudal analysis of corpus callosum demyelination and axon damage across disease stages refines diffusion tensor imaging correlations with pathological features.* Journal of neuropathology and experimental neurology, 2010. **69**(7): p. 704.

58. Herrera, J.J., T. Chacko, and P.A. Narayana, *Histological correlation of diffusion tensor imaging metrics in experimental spinal cord injury.* Journal of neuroscience research, 2008. **86**(2): p. 443-447.

59. Sun, S.W., et al., *Noninvasive detection of cuprizone induced axonal damage and demyelination in the mouse corpus callosum.* Magnetic Resonance in Medicine, 2006. **55**(2): p. 302-308.

60. Wheeler-Kingshott, C.A. and M. Cercignani, *About "axial" and "radial" diffusivities.* Magnetic Resonance in Medicine, 2009. **61**(5): p. 1255-1260.

61. Schmierer, K., et al., *Quantitative magnetization transfer imaging in postmortem multiple sclerosis brain.* Journal of Magnetic Resonance Imaging, 2007. **26**(1): p. 41-51.

62. Cohen-Adad, J., et al., *Demyelination and degeneration in the injured human spinal cord detected with diffusion and magnetization transfer MRI.* Neuroimage, 2011. **55**(3): p. 1024-1033.

63. Beaulieu, C., *The basis of anisotropic water diffusion in the nervous system–a technical review.* NMR in Biomedicine, 2002. **15**(7-8): p. 435-455.

64. Sen, P.N. and P.J. Basser, *A model for diffusion in white matter in the brain.* Biophysical Journal, 2005. **89**(5): p. 2927-2938.

65. Ellingson, B., et al., *Diffusion tensor MR imaging of the neurologically intact human spinal cord.* American Journal of Neuroradiology, 2008. **29**(7): p. 1279-1284.

66. Bastin, M.E., P.A. Armitage, and I. Marshall, *A theoretical study of the effect of experimental noise on the measurement of anisotropy in diffusion imaging.* Magnetic resonance imaging, 1998. **16**(7): p. 773-785.

67. Carballido-Gamio, J., et al., *Single-shot fast spin-echo diffusion tensor imaging of the lumbar spine at 1.5 and 3 T.* Magnetic resonance imaging, 2007. **25**(5): p. 665-670.

68. Pauling, L.C., CD., *The magnetic properties and structure of hemoglobin, oxyhemoglobin and carbon monoxy hemoglobin.* Proc Natl Acad Sci USA, 1936. **22**: p. 210–6.

69. Buxton, R.B., *Introduction to functional magnetic resonance imaging: principles and techniques*. 2009: Cambridge university press.

70. Smith, S.M., P.M. Matthews, and P. Jezzard, *Functional MRI: an introduction to methods*. 2001: Oxford University Press.

71. Govers, N., et al., *Functional MRI of the cervical spinal cord on 1.5 T with fingertapping: to what extent is it feasible?* Neuroradiology, 2007. **49**(1): p. 73-81.

72. Figley, C. and P. Stroman, *Investigation of human cervical and upper thoracic spinal cord motion: implications for imaging spinal cord structure and function.* Magnetic Resonance in Medicine, 2007. **58**(1): p. 185-189.

73. Stroman, P., B. Tomanek, and K. Malisza, *Functional magnetic resonance imaging of the human brain and spinal cord by means of signal enhancement by extravascular protons.* Concepts in Magnetic Resonance Part A, 2003. **16**(1): p. 28-34.

74. Stroman, P., et al., *Functional magnetic resonance imaging of the human brain based on signal enhancement by extravascular protons (SEEP fMRI).* Magnetic resonance in medicine, 2003. **49**(3): p. 433-439.

75. Stroman, P.W., et al., *Functional magnetic resonance imaging based on SEEP contrast: response function and anatomical specificity.* Magnetic resonance imaging, 2005. **23**(8): p. 843-850.

76. Fairhurst, M., et al., *Anticipatory brainstem activity predicts neural processing of pain in humans.* Pain, 2007. **128**(1): p. 101-110.

77. Giove, F., et al., *Issues about the fMRI of the human spinal cord.* Magnetic resonance imaging, 2004. **22**(10): p. 1505-1516.

78. Kornelsen, J. and S. Mackey, *Potential clinical applications for spinal functional MRI.* Current pain and headache reports, 2007. **11**(3): p. 165-170.

79. Fratini, M., et al., *On the impact of physiological noise in spinal cord functional MRI.* Journal of Magnetic Resonance Imaging, 2014. **40**(4): p. 770-777.

80. Maier, M.A., S.I. Perlmutter, and E.E. Fetz, *Response patterns and force relations of monkey spinal interneurons during active wrist movement.* Journal of neurophysiology, 1998. **80**(5): p. 2495-2513.

81. Fawcett, J., et al., *Guidelines for the conduct of clinical trials for spinal cord injury as developed by the ICCP panel: spontaneous recovery after spinal cord injury and statistical power needed for therapeutic clinical trials.* Spinal cord, 2007. **45**(3): p. 190-205.

82. Gwak, Y.S. and C.E. Hulsebosch, *GABA and central neuropathic pain following spinal cord injury.* Neuropharmacology, 2011. **60**(5): p. 799-808.

83. Goldfarb, J.W., et al., *Cyclic CINE-balanced steady-state free precession image intensity variations: Implications for the detection of myocardial edema.* Journal of Magnetic Resonance Imaging, 2011. **33**(3): p. 573-581.

84. Saranathan, M., et al., *A 3D balanced-SSFP Dixon technique with group-encoded k-space segmentation for breath-held non–contrast-enhanced MR angiography.* Magnetic resonance imaging, 2012. **30**(2): p. 158-164.

85. Brooks, J.C., et al., *Stimulus site and modality dependence of functional activity within the human spinal cord.* The Journal of Neuroscience, 2012. **32**(18): p. 6231-6239.

86. Kong, Y., et al., *Assessment of physiological noise modelling methods for functional imaging of the spinal cord.* Neuroimage, 2012. **60**(2): p. 1538-1549.

87. Summers, P.E., et al., *A quantitative comparison of BOLD fMRI responses to noxious and innocuous stimuli in the human spinal cord.* Neuroimage, 2010. **50**(4): p. 1408-1415.

88. Ghazni, N., C. Cahill, and P. Stroman, *Tactile sensory and pain networks in the human spinal cord and brain stem mapped by means of functional MR imaging.* American Journal of Neuroradiology, 2010. **31**(4): p. 661-667.

89. Eippert, F., et al., *Activation of the opioidergic descending pain control system underlies placebo analgesia.* Neuron, 2009. **63**(4): p. 533-543.

90. Eippert, F., et al., *Direct evidence for spinal cord involvement in placebo analgesia.* Science, 2009. **326**(5951): p. 404-404.

91. Tracey, I., et al., *Imaging attentional modulation of pain in the periaqueductal gray in humans.* the Journal of Neuroscience, 2002. **22**(7): p. 2748-2752.

92. Sprenger, C., et al., *Attention modulates spinal cord responses to pain.* Current Biology, 2012. **22**(11): p. 1019-1022.

93. Finsterbusch, J., F. Eippert, and C. Büchel, *Single, slice-specific z-shim gradient pulses improve T2*-weighted imaging of the spinal cord.* Neuroimage, 2012. **59**(3): p. 2307-2315.

94. Finsterbusch, J., C. Sprenger, and C. Büchel, *Combined T2*-weighted measurements of the human brain and cervical spinal cord with a dynamic shim update.* NeuroImage, 2013. **79**: p. 153-161.

95. Finsterbusch, J., *Simultaneous functional MRI acquisition of distributed brain regions with high temporal resolution using a 2D-selective radiofrequency excitation.* Magnetic Resonance in Medicine, 2015. **73**(2): p. 683-691.

96. Filippi, M. and M. Rocca, *Functional MR imaging in multiple sclerosis.* Neuroimaging clinics of North America, 2009. **19**(1): p. 59-70.

97. Agosta, F., et al., *Primary Progressive Multiple Sclerosis: Tactile-associated Functional MR Activity in the Cervical Spinal Cord 1.* Radiology, 2009. **253**(1): p. 209-215.

98. Agosta, F., et al., *Tactile-associated fMRI recruitment of the cervical cord in healthy subjects.* Human brain mapping, 2009. **30**(1): p. 340-345.

99. Kirshblum, S.C., et al., *Reference for the 2011 revision of the international standards for neurological classification of spinal cord injury.* The journal of spinal cord medicine, 2011. **34**(6): p. 547-554.

100. Jones, A., et al., *Cortical and subcortical localization of response to pain in man using positron emission tomography.* Proceedings of the Royal Society of London B: Biological Sciences, 1991. **244**(1309): p. 39-44.

101. Apkarian, A.V., et al., *Human brain mechanisms of pain perception and regulation in health and disease.* European Journal of Pain, 2005. **9**(4): p. 463-463.

102. Watson, C., G. Paxinos, and G. Kayalioglu, *The spinal cord: a Christopher and Dana Reeve Foundation text and atlas*. 2009: Academic press.

103. Stroman, P.W., J. Kornelsen, and J. Lawrence, *An improved method for spinal functional MRI with large volume coverage of the spinal cord.* Journal of Magnetic Resonance Imaging, 2005. **21**(5): p. 520-526.

104. Taso, M., et al., *Construction of an in vivo human spinal cord atlas based on high-resolution MR images at cervical and thoracic levels: preliminary results.* Magnetic Resonance Materials in Physics, Biology and Medicine, 2014. **27**(3): p. 257-267.

105. Detre, J.A., *Clinical applicability of functional MRI.* Journal of Magnetic Resonance Imaging, 2006. **23**(6): p. 808-815.

106. Dowell, N.G., et al., *Contiguous-slice zonally oblique multislice (CO-ZOOM) diffusion tensor imaging: Examples of in vivo spinal cord and optic nerve applications.* Journal of Magnetic Resonance Imaging, 2009. **29**(2): p. 454-460.

107. Finsterbusch, J. and J. Frahm, *Single-shot line scan imaging using stimulated echoes.* Journal of Magnetic Resonance, 1999. **137**(1): p. 144-153.

108. Wheeler-Kingshott, C.A., et al., *Investigating cervical spinal cord structure using axial diffusion tensor imaging.* Neuroimage, 2002. **16**(1): p. 93-102.

109. Wilm, B., et al., *Reduced field-of-view MRI using outer volume suppression for spinal cord diffusion imaging.* Magnetic Resonance in Medicine, 2007. **57**(3): p. 625-630.

110. Zambreanu, L., et al., *A role for the brainstem in central sensitisation in humans. Evidence from functional magnetic resonance imaging.* Pain, 2005. **114**(3): p. 397-407.

111. Kandel, E.R., J.H. Schwartz, and T.M. Jessell, *Principles of neural science*. Vol. 4. 2000: McGraw-Hill New York.

112. Purves, D., et al., *Neuroscience. 2nd.* Sunderland: Sinauer, 2001.

113. Blumenfeld, H., *Neuroanatomy through clinical cases*. 2014: Sinauer.

114. Brown, A.G., *Organization in the spinal cord: the anatomy and physiology of identified neurones*. 2012: Springer Science & Business Media.

115. Alberts, B., et al., *Molecular Biology of the Cell 3E*. 1994.

116. Sjöström, P.J., et al., *Dendritic excitability and synaptic plasticity*. Physiological reviews, 2008. **88**(2): p. 769-840.

117. Willis Jr, W.D. and R.E. Coggeshall, *Sensory Mechanisms of the Spinal Cord: Volume 1 Primary Afferent Neurons and the Spinal Dorsal Horn*. 2012: Springer Science & Business Media.

118. Ko, H., et al., *Gross quantitative measurements of spinal cord segments in human*. Spinal Cord, 2004. **42**(1): p. 35-40.

119. Williams, P.L., *Gray's anatomy*. 1980.

120. Nógrádi, A. and G. Vrbová, *Anatomy and Physiology of the Spinal Cord*, in *Transplantation of Neural Tissue into the Spinal Cord*. 2006, Springer. p. 1-23.

121. Stroman, P.W., *Spinal fMRI investigation of human spinal cord function over a range of innocuous thermal sensory stimuli and study-related emotional influences*. Magnetic resonance imaging, 2009. **27**(10): p. 1333-1346.

122. Stroman PW, C.C., *Functional magnetic resonance imaging of the human spinal cord and brainstem during heat stimulation.* In: Proc 14th Annual Meeting SMRM, Seattle, 2006.

123. Stroman, P.W., et al., *Advanced MR imaging techniques and characterization of residual anatomy*. Clinical neurology and neurosurgery, 2012. **114**(5): p. 460-470.

124. Spees, W.M., et al., *Water proton MR properties of human blood at 1.5 Tesla: Magnetic susceptibility, T1, T2, T* 2, and non-Lorentzian signal behavior*. Magnetic resonance in medicine, 2001. **45**(4): p. 533-542.

125. Malonek, D. and A. Grinvald, *Interactions between electrical activity and cortical microcirculation revealed by imaging spectroscopy: implications for functional brain mapping*. Science, 1996. **272**(5261): p. 551.

126. Uğurbil, K., et al., *Imaging brain activity using nuclear spins*. Proceedings of the International School of Physics "Enrico Fermi", IOS Press, Amsterdam, 1999: p. 261-310.

127. Fox, P.T., et al., *Nonoxidative glucose consumption during focal physiologic neural activity.* Science, 1988. **241**(4864): p. 462-464.

128. Fox, P.T. and M.E. Raichle, *Focal physiological uncoupling of cerebral blood flow and oxidative metabolism during somatosensory stimulation in human subjects.* Proceedings of the National Academy of Sciences, 1986. **83**(4): p. 1140-1144.

129. Mangia, S., et al., *Metabolic and hemodynamic events after changes in neuronal activity: current hypotheses, theoretical predictions and in vivo NMR experimental findings.* Journal of Cerebral Blood Flow & Metabolism, 2009. **29**(3): p. 441-463.

130. Maieron, M., et al. *Breath-hold-induced MRI signal changes in the spinal cord imply BOLD contrast.* in *13th Annual Meeting of the Organization for Human Brain Mapping (HBM), Chicago, USA*. 2007.

131. Zhao, F., et al., *BOLD and blood volume-weighted fMRI of rat lumbar spinal cord during non-noxious and noxious electrical hindpaw stimulation.* Neuroimage, 2008. **40**(1): p. 133-147.

132. Zhao, F., et al., *Pain fMRI in rat cervical spinal cord: an echo planar imaging evaluation of sensitivity of BOLD and blood volume-weighted fMRI.* Neuroimage, 2009. **44**(2): p. 349-362.

133. Porro, C.A., et al., *CNS pattern of metabolic activity during tonic pain: evidence for modulation by β-endorphin.* European Journal of Neuroscience, 1999. **11**(3): p. 874-888.

134. Gati, J.S., et al., *Experimental determination of the BOLD field strength dependence in vessels and tissue.* Magnetic resonance in medicine, 1997. **38**(2): p. 296-302.

135. Lai, S., et al., *Identification of vascular structures as a major source of signal contrast in high resolution 2D and 3D functional activation imaging of the motor cortex at l. 5T preliminary results.* Magnetic Resonance in Medicine, 1993. **30**(3): p. 387-392.

136. Greitz, D., A. Franck, and B. Nordell, *On the pulsatile nature of intracranial and spinal CSF-circulation demonstrated by MR imaging.* Acta radiologica, 1993. **34**(4): p. 321-328.

137. Piché, M., et al., *Characterization of cardiac-related noise in fMRI of the cervical spinal cord.* Magnetic resonance imaging, 2009. **27**(3): p. 300-310.

138. Windischberger, C., et al., *On the origin of respiratory artifacts in BOLD-EPI of the human brain.* Magnetic resonance imaging, 2002. **20**(8): p. 575-582.

139. Harvey, A.K., et al., *Brainstem functional magnetic resonance imaging: disentangling signal from physiological noise.* Journal of Magnetic Resonance Imaging, 2008. **28**(6): p. 1337-1344.

140. Friese, S., et al., *The influence of pulse and respiration on spinal cerebrospinal fluid pulsation.* Investigative radiology, 2004. **39**(2): p. 120-130.

141. Frank, L.R., R.B. Buxton, and E.C. Wong, *Estimation of respiration-induced noise fluctuations from undersampled multislice fMRI data†.* Magnetic Resonance in Medicine, 2001. **45**(4): p. 635-644.

142. Stroman, P., et al., *Characterization of contrast changes in functional MRI of the human spinal cord at 1.5 T.* Magnetic resonance imaging, 2001. **19**(6): p. 833-838.

143. Boynton, G.M., S.A. Engel, and D.J. Heeger, *Linear systems analysis of the fMRI signal.* NeuroImage, 2012. **62**(2): p. 975-984.

144. Handwerker, D.A., et al., *The continuing challenge of understanding and modeling hemodynamic variation in fMRI.* Neuroimage, 2012. **62**(2): p. 1017-1023.

145. Kornelsen, J. and P. Stroman, *fMRI of the lumbar spinal cord during a lower limb motor task.* Magnetic resonance in medicine, 2004. **52**(2): p. 411-414.

146. Stracke, C., et al., *Interneuronal systems of the cervical spinal cord assessed with BOLD imaging at 1.5 T.* Neuroradiology, 2005. **47**(2): p. 127-133.

147. Pettersson, L.-G., *Forelimb movements in the cat; kinetic features and neuronal control.* Acta physiologica Scandinavica. Supplementum, 1989. **594**: p. 1-60.

148. Alstermark, B., et al., *Disynaptic Pyramidal Excitation in Forelimb Motoneurons Mediated Via C3–C4 Propriospinal Neurons in theMacaca fuscata.* Journal of Neurophysiology, 1999. **82**(6): p. 3580-3585.

149. Nielsen, J. and E. Pierrot-Deseilligny, *Pattern of cutaneous inhibition of the propriospinal-like excitation to human upper limb motoneurones.* The Journal of physiology, 1991. **434**(1): p. 169-182.

150. Pierrot-Deseilligny, E., *Propriospinal transmission of part of the corticospinal excitation in humans.* Muscle & nerve, 2002. **26**(2): p. 155-172.

151. Lawrence, J.M., P.W. Stroman, and S.S. Kollias, *Functional magnetic resonance imaging of the human spinal cord during vibration stimulation of different dermatomes.* Neuroradiology, 2008. **50**(3): p. 273-280.

152. Porro, C., et al., *Functional activity mapping of the rat spinal cord during formalin-induced noxious stimulation.* Neuroscience, 1991. **41**(2): p. 655-665.

153. Coghill, R.C., D.J. Mayer, and D.D. Price, *The roles of spatial recruitment and discharge frequency in spinal cord coding of pain: a combined electrophysiological and imaging investigation.* Pain, 1993. **53**(3): p. 295-309.

154. Brooks, J. and I. Tracey, *REVIEW: from nociception to pain perception: imaging the spinal and supraspinal pathways.* Journal of Anatomy, 2005. **207**(1): p. 19-33.

155. Beissner, F., et al., *Dual-echo EPI for non-equilibrium fMRI—Implications of different echo combinations and masking procedures.* Neuroimage, 2010. **52**(2): p. 524-531.

156. Poser, B.A., et al., *BOLD contrast sensitivity enhancement and artifact reduction with multiecho EPI: parallel-acquired inhomogeneity-desensitized fMRI.* Magnetic Resonance in Medicine, 2006. **55**(6): p. 1227-1235.

157. Moffitt, M.A., et al., *Functional magnetic resonance imaging of the human lumbar spinal cord.* Journal of Magnetic Resonance Imaging, 2005. **21**(5): p. 527-535.

158. Endo, T., et al., *Reorganization of sensory processing below the level of spinal cord injury as revealed by fMRI.* Experimental neurology, 2008. **209**(1): p. 155-160.

159. Glover, G., *Spiral imaging in fMRI.* NeuroImage, 2012. **62**: p. 7.

160. Nash, P., et al., *Functional magnetic resonance imaging identifies somatotopic organization of nociception in the human spinal cord.* PAIN®, 2013. **154**(6): p. 776-781.

161. Summers, P.E., C.A. Porro, and F. Giove, *Somatotopy of nociceptive responses in the human spinal cord.* Pain, 2013. **154**(11): p. 2572-2573.

162. Moeller, S., et al., *Multiband multislice GE-EPI at 7 tesla, with 16-fold acceleration using partial parallel imaging with application to high spatial and temporal whole-brain fMRI.* Magnetic Resonance in Medicine, 2010. **63**(5): p. 1144-1153.

163. Figley, C.R. and P.W. Stroman, *Development and validation of retrospective spinal cord motion time-course estimates (RESPITE) for spin-echo spinal fMRI: Improved sensitivity and specificity by means of a motion-compensating general linear model analysis.* Neuroimage, 2009. **44**(2): p. 421-427.

164. Hu, X., et al., *Retrospective estimation and correction of physiological fluctuation in functional MRI.* Magnetic resonance in medicine, 1995. **34**(2): p. 201-212.

165. Stroman, P.W., C.R. Figley, and C.M. Cahill, *Spatial normalization, bulk motion correction and coregistration for functional magnetic resonance imaging of the human cervical spinal cord and brainstem.* Magnetic resonance imaging, 2008. **26**(6): p. 809-814.

166. Glover, G.H., T.Q. Li, and D. Ress, *Image-based method for retrospective correction of physiological motion effects in fMRI: RETROICOR.* Magnetic Resonance in Medicine, 2000. **44**(1): p. 162-167.

167. Corfield, D.R., et al., *Modulation of the corticospinal control of ventilation by changes in reflex respiratory drive.* Journal of Applied Physiology, 1999. **87**(5): p. 1923-1930.

168. Restom, K., Y. Behzadi, and T.T. Liu, *Physiological noise reduction for arterial spin labeling functional MRI.* Neuroimage, 2006. **31**(3): p. 1104-1115.

169. Birn, R.M., et al., *Separating respiratory-variation-related fluctuations from neuronal-activity-related fluctuations in fMRI.* Neuroimage, 2006. **31**(4): p. 1536-1548.

170. Brooks J, R.M., Schweinhardt P, Wise R, Tracey and I., *Functional magnetic resonance imaging (fMRI) of the spinal cord: a methodological study.* . In: Proc 23rd Annual Meeting American Pain Society, Vancouver, 2004.

171. Lund, T.E., et al., *Non-white noise in fMRI: does modelling have an impact?* Neuroimage, 2006. **29**(1): p. 54-66.

172. Perlbarg, V., et al., *CORSICA: correction of structured noise in fMRI by automatic identification of ICA components.* Magnetic resonance imaging, 2007. **25**(1): p. 35-46.

173. Schrouff, J., et al., *Brain functional integration decreases during propofol-induced loss of consciousness.* Neuroimage, 2011. **57**(1): p. 198-205.

174. Xie, G., et al., *Reduction of physiological noise with independent component analysis improves the detection of nociceptive responses with fMRI of the human spinal cord.* Neuroimage, 2012. **63**(1): p. 245-252.

175. Behzadi, Y., et al., *A component based noise correction method (CompCor) for BOLD and perfusion based fMRI.* Neuroimage, 2007. **37**(1): p. 90-101.

176. Bandettini, P.A., et al., *Time course EPI of human brain function during task activation.* Magnetic resonance in medicine, 1992. **25**(2): p. 390-397.

177. Duclaux, R., *Response characteristics of cutaneous warm receptors in the monkey.* Journal of Neurophysiology, 1980. **43**(1): p. 1-15.

178. Handwerker, H., A. Iggo, and M. Zimmermann, *Segmental and supraspinal actions on dorsal horn neurons responding to noxious and non-noxious skin stimuli.* Pain, 1975. **1**(2): p. 147-165.

179. LaMOTTE, R.H. and J.G. Thalhammer, *Response properties of high-threshold cutaneous cold receptors in the primate.* Brain research, 1982. **244**(2): p. 279-287.

180. Kenshalo, D., et al., *Facilitation of the responses of primate spinothalamic cells to cold and to tactile stimuli by noxious heating of the skin.* Pain, 1982. **12**(2): p. 141-152.

181. Craig, A., K. Krout, and D. Andrew, *Quantitative response characteristics of thermoreceptive and nociceptive lamina I spinothalamic neurons in the cat.* Journal of Neurophysiology, 2001. **86**(3): p. 1459-1480.

182. Prut, Y. and S.I. Perlmutter, *Firing properties of spinal interneurons during voluntary movement. I. State-dependent regularity of firing.* The Journal of neuroscience, 2003. **23**(29): p. 9600-9610.

183. Prut, Y. and S.I. Perlmutter, *Firing properties of spinal interneurons during voluntary movement. II. Interactions between spinal neurons.* The Journal of neuroscience, 2003. **23**(29): p. 9611-9619.

184. De Luca, C.J. and E.C. Hostage, *Relationship between firing rate and recruitment threshold of motoneurons in voluntary isometric contractions.* Journal of neurophysiology, 2010. **104**(2): p. 1034-1046.

185. De Luca, C.J., J.C. Kline, and P. Contessa, *Transposed firing activation of motor units.* Journal of neurophysiology, 2014. **112**(4): p. 962-970.

186. Ng, M.-C., et al., *Cervical spinal cord BOLD fMRI study: modulation of functional activation by dexterity of dominant and non-dominant hands.* Neuroimage, 2008. **39**(2): p. 825-831.

187. Bosma, R.L. and P.W. Stroman, *Spinal cord response to stepwise and block presentation of thermal stimuli: A functional MRI study.* Journal of Magnetic Resonance Imaging, 2015. **41**(5): p. 1318-1325.

188. Yang, P.-F., F. Wang, and L.M. Chen, *Differential fMRI Activation Patterns to Noxious Heat and Tactile Stimuli in the Primate Spinal Cord.* The Journal of Neuroscience, 2015. **35**(29): p. 10493-10502.

189. Bandettini, P.A., et al., *Spin-echo and gradient-echo EPI of human brain activation using BOLD contrast: a comparative study at 1.5 T.* NMR in Biomedicine, 1994. **7**(1-2): p. 12-20.

190. Cohen-Adad, J., et al., *BOLD signal responses to controlled hypercapnia in human spinal cord.* Neuroimage, 2010. **50**(3): p. 1074-1084.

191. Ashburner, J., *Computational anatomy with the SPM software.* Magnetic resonance imaging, 2009. **27**(8): p. 1163-1174.

192. Cox, R.W., *AFNI: software for analysis and visualization of functional magnetic resonance neuroimages.* Computers and Biomedical research, 1996. **29**(3): p. 162-173.

193. Jenkinson, M., et al., *Fsl.* Neuroimage, 2012. **62**(2): p. 782-790.

194. Friston, K.J., et al., *Characterizing dynamic brain responses with fMRI: a multivariate approach.* Neuroimage, 1995. **2**(2PA): p. 166-172.

195. Brockett, R.W., *Volterra series and geometric control theory.* Automatica, 1976. **12**(2): p. 167-176.

196. Korenberg, M.J. and I.W. Hunter, *The identification of nonlinear biological systems: Volterra kernel approaches.* Annals of biomedical engineering, 1996. **24**(2): p. 250-268.

197. Liu, T.T. and J. Liau, *Caffeine increases the linearity of the visual BOLD response.* Neuroimage, 2010. **49**(3): p. 2311-2317.

198. Hinkelmann, K. and O. Kempthorne, *Design and Analysis of Experiments, Special Designs and Applications*. Vol. 3. 2012: John Wiley & Sons.

199. Townsend, B.R., L. Paninski, and R.N. Lemon, *Linear encoding of muscle activity in primary motor cortex and cerebellum.* Journal of neurophysiology, 2006. **96**(5): p. 2578-2592.

200. Kuhtz-Buschbeck, J., et al., *Brain activity is similar during precision and power gripping with light force: an fMRI study.* Neuroimage, 2008. **40**(4): p. 1469-1481.

201. Thickbroom, G., et al., *Isometric force-related activity in sensorimotor cortex measured with functional MRI.* Experimental brain research, 1998. **121**(1): p. 59-64.

202. Stroman, P., et al., *Spin-echo versus gradient-echo fMRI with short echo times.* Magnetic resonance imaging, 2001. **19**(6): p. 827-831.

203. Benzel, E.C., *The cervical Spine.* 2012. **Lippincott Williams & Wilkins edition**(fifth edition).

204. Fratini, M., et al., *Simultaneous submicrometric 3D imaging of the micro-vascular network and the neuronal system in a mouse spinal cord.* Scientific reports, 2015. **5**.

205. Popel A.S., P.A.R.S.D.W., *Developments in the microcirculation physiome project.* . J. Neuro. Meth, 1998 **111**: p. 911-913.

206. Reina-De La Torre, F., A. Rodriguez-Baeza, and J. Sahuquillo-Barris, *Morphological characteristics and distribution pattern of the arterial vessels in human cerebral cortex: a scanning electron microscope study.* The Anatomical Record, 1998. **251**(1): p. 87-96.

207. Koyanagi, I., C.H. Tator, and P.J. Lea, *Three-Dimensional Analysis of the Vascular System in the Rat Spinal Cord with Scanning Electron Microscopy of Vascular Corrosion Casts. Part 2: Acute Spinal Cord Injury.* Neurosurgery, 1993. **33**(2): p. 285-292.

208. Heinzer, S., et al., *Hierarchical microimaging for multiscale analysis of large vascular networks.* Neuroimage, 2006. **32**(2): p. 626-636.

209. Cassot, F., et al., *Morphometric study of a human cerebral microvascular network.* Journal of Cerebral Blood Flow and Metabolism, 1999. **19**: p. S738-S738.

210. Stefanovic, B., et al., *Functional reactivity of cerebral capillaries.* Journal of Cerebral Blood Flow & Metabolism, 2008. **28**(5): p. 961-972.

211. Plouraboué, F., et al., *X-ray high-resolution vascular network imaging.* Journal of microscopy, 2004. **215**(2): p. 139-148.

212. Risser, L., et al., *From homogeneous to fractal normal and tumorous microvascular networks in the brain.* Journal of Cerebral Blood Flow & Metabolism, 2007. **27**(2): p. 293-303.

213. Zhang, X., et al., *Mouse blood vessel imaging by in-line x-ray phase-contrast imaging.* Physics in medicine and biology, 2008. **53**(20): p. 5735.

214. Momose, A., T. Takeda, and Y. Itai, *Blood Vessels: Depiction at Phase-Contrast X-ray Imaging without Contrast Agents in the Mouse and Rat—Feasibility Study 1.* Radiology, 2000. **217**(2): p. 593-596.

215. Bravin, A., P. Coan, and P. Suortti, *X-ray phase-contrast imaging: from pre-clinical applications towards clinics.* Physics in medicine and biology, 2013. **58**(1): p. R1.

216. Flowtech, I., Carver, Massachusetts.

217. Momose, A., et al., *Phase–contrast X–ray computed tomography for observing biological soft tissues.* Nature medicine, 1996. **2**(4): p. 473-475.

218. Snigirev, A., et al., *On the possibilities of x-ray phase contrast microimaging by coherent high-energy synchrotron radiation.* Review of Scientific Instruments, 1995. **66**(12): p. 5486-5492.

219. Förster, E., K. Goetz, and P. Zaumseil, *Double crystal diffractometry for the characterization of targets for laser fusion experiments.* Kristall und Technik, 1980. **15**(8): p. 937-945.

220. Davis, T., et al., *X-ray image contrast from a simple phase object.* Physical review letters, 1995. **74**(16): p. 3173.

221. Weitkamp, T., et al., *X-ray phase imaging with a grating interferometer.* Optics express, 2005. **13**(16): p. 6296-6304.

222. Olivo, A. and R. Speller, *A coded-aperture technique allowing x-ray phase contrast imaging with conventional sources.* Applied Physics Letters, 2007. **91**(7): p. 074106.

223. Wilkins, S., et al., *Phase-contrast imaging using polychromatic hard X-rays.* Nature, 1996. **384**(6607): p. 335-338.

224. Paganin, D., et al., *Simultaneous phase and amplitude extraction from a single defocused image of a homogeneous object.* Journal of microscopy, 2002. **206**(1): p. 33-40.

225. Beltran, M., et al., *Interface-specific x-ray phase retrieval tomography of complex biological organs.* Physics in medicine and biology, 2011. **56**(23): p. 7353.

226. Paganin, D., et al., *Phase retrieval using coherent imaging systems with linear transfer functions.* Optics Communications, 2004. **234**(1): p. 87-105.

227. Weitkamp, T., et al., *ANKAphase: software for single-distance phase retrieval from inline X-ray phase-contrast radiographs.* Journal of synchrotron radiation, 2011. **18**(4): p. 617-629.

228. Snowdon, D.A., et al., *Brain infarction and the clinical expression of Alzheimer disease: the Nun Study.* Jama, 1997. **277**(10): p. 813-817.

229. Whetstone, W.D., et al., *Blood-spinal cord barrier after spinal cord injury: Relation to revascularization and wound healing.* Journal of neuroscience research, 2003. **74**(2): p. 227-239.

230. Casella, G.T., et al., *New vascular tissue rapidly replaces neural parenchyma and vessels destroyed by a contusion injury to the rat spinal cord.* Experimental neurology, 2002. **173**(1): p. 63-76.

231. Lu, P., et al., *Long-distance growth and connectivity of neural stem cells after severe spinal cord injury.* Cell, 2012. **150**(6): p. 1264-1273.

232. Menon, R.S., et al., *4 Tesla gradient recalled echo characteristics of photic stimulation-induced signal changes in the human primary visual cortex.* Magnetic Resonance in Medicine, 1993. **30**(3): p. 380-386.

233. Darquié, A., et al., *Transient decrease in water diffusion observed in human occipital cortex during visual stimulation.* Proceedings of the National Academy of Sciences, 2001. **98**(16): p. 9391-9395.

234. Boxerman, J.L., et al., *MR contrast due to intravascular magnetic susceptibility perturbations.* Magnetic Resonance in Medicine, 1995. **34**(4): p. 555-566.

235. Pathak, A.P., S.D. Rand, and K.M. Schmainda, *The effect of brain tumor angiogenesis on the in vivo relationship between the gradient-echo relaxation rate change (ΔR2*) and contrast agent (MION) dose.* Journal of Magnetic Resonance Imaging, 2003. **18**(4): p. 397-403.

236. Hougardy, S., *The Floyd–Warshall algorithm on graphs with negative cycles.* Information Processing Letters, 2010. **110**(8): p. 279-281.

237. Skiena, S., *Dijkstra's Algorithm.* Implementing Discrete Mathematics: Combinatorics and Graph Theory with Mathematica, Reading, MA: Addison-Wesley, 1990: p. 225-227.

238. Lee, K.-H., et al., *Application of spatial modulation of magnetization to cervical spinal stenosis for evaluation of the hydrodynamic changes occurring in cerebrospinal fluid.* Korean Journal of Radiology, 2000. **1**(1): p. 11-18.

239. Schroth, G. and U. Klose, *Cerebrospinal fluid flow.* Neuroradiology, 1992. **35**(1): p. 16-24.

240. Henry-Feugeas, M., et al., *Temporal and spatial assessment of normal cerebrospinal fluid dynamics with MR imaging.* Magnetic resonance imaging, 1993. **11**(8): p. 1107-1118.

241. Enzmann, D. and N. Pelc, *Normal flow patterns of intracranial and spinal cerebrospinal fluid defined with phase-contrast cine MR imaging.* Radiology, 1991. **178**(2): p. 467-474.

242. Cooke, F., et al., *Quantitative proton magnetic resonance spectroscopy of the cervical spinal cord.* Magnetic resonance in medicine, 2004. **51**(6): p. 1122-1128.

Appendix A: Motor neurons pools and motor unit

Two terms are used to describe the anatomical relationship between motor neurons and muscles: the motor neuron pool and the motor unit.

1. Motor neurons are clustered in columnar, spinal nuclei called **motor neuron pools** (or motor nuclei). All of the motor neurons in a motor neuron pool innervate a single muscle, and all motor neurons that innervate a particular muscle are contained in the same motor neuron pool. Thus, there is a one-to-one relationship between a muscle and a motor neuron pool.
2. Each individual muscle fiber in a muscle is innervated by one, and only one, motor neuron (make sure you understand the difference between a muscle and a muscle fiber). A single motor neuron, however, can innervate many muscle fibers. The combination of an individual motor neuron and all of the muscle fibers that it innervates is called a **motor unit**. The number of fibers innervated by a motor unit is called its **innervation ratio**. If a muscle is required for fine control or for delicate movements (e.g., movement of the fingers or hands), its motor units will tend to have small innervation ratios. That is, each motor neuron will innervate a small number of muscle fibers (10-100), enabling many nuances of movement of the entire muscle. If a muscle is required only for coarse movements (e.g., a thigh muscle), its motor units will tend to have a high innervation ratio (i.e., each motor neuron innervating 1000 or more muscle fibers), as there is no necessity for individual muscle fibers to undergo highly coordinated, differential contractions to produce a fine movement.

Appendix B: Descending Motor Pathways

Corticospinal tracts. The corticospinal tract originates in the motor cortex. The axons of motor projection neurons collect in the internal capsule, and then course through the crus cerebri (cerebral peduncle) in the midbrain. At the level of the medulla, these axons form the medullary pyramids on the ventral surface of the brainstem (hence, this tract is also called thepyramidal tract). At the level of the caudal medulla, the corticospinal tract splits into two tracts. Approximately 90% of the axons cross over to the contralateral side at the pyramidal decussation, forming the lateral corticospinal tract. These axons continue to course through the lateral funiculus of the SC, before synapsing either directly onto alpha motor neurons or onto interneurons in the ventral horn. The remaining 10% of the axons that do not cross at the caudal medulla constitute the anterior corticospinal tract, as they continue down the SC in the anterior funiculus. When they reach the spinal segment at which they terminate, they cross over to the contralateral side through the anterior white commissure and innervate alpha motor neurons or interneurons in the anterior horn. Thus, both the lateral and anterior corticospinal tracts are crossed pathways; they cross the midline at different locations, however.

Function. The corticospinal tract (along with the corticobulbar tract) is the primary pathway that carries the motor commands that underlie voluntary movement. The lateral corticospinal tract is responsible for the control of the distal musculature and the anterior corticospinal tract is responsible for the control of the proximal musculature. A particularly important function of the lateral corticospinal tract is the fine control of the digits of the hand. The corticospinal tract is the only descending pathway in which some axons make synaptic contacts directly onto alpha motor neurons. This direct cortical innervation presumably is necessary to allow the powerful processing networks of the cortex to control the activity of the spinal circuits that direct the exquisite movements of the fingers and hands. The percentage of axons in the corticospinal tract that innervate alpha motor neurons directly is greater in humans and nonhuman primates than in other mammals, presumably reflecting the increased manual dexterity of primates. Damage to the corticospinal tract results in a permanent loss of the fine control of the extremities. Although parallel descending pathways can often recover the function of more coarse movements, these pathways are not capable of generating fine, skilled movements. In addition to the fine control of distal muscles, the corticospinal tract also plays a role in the voluntary control of axial muscles.

Rubrospinal tract. The rubrospinal tract originates in the red nucleus of the midbrain. The axons immediately cross to the contralateral side of the brain, and they course through the brainstem and the lateral funiculus of the SC. The axons innervate spinal neurons at all levels of the SC.

Function. The rubrospinal tract is an alternative by which voluntary motor commands can be sent to the SC. Although it is a major pathway in many animals, it is relatively minor in humans. Activation of this tract causes excitation of flexor muscles and inhibition of extensor muscles. The rubrospinal tract is thought to play a role in movement velocity, as rubrospinal lesions cause a temporary slowness in movement. In addition, because the red nucleus receives most of its input from the cerebellum, the rubrospinal tract probably plays a role in transmitting learned motor commands from the cerebellum to the musculature. The red nucleus also receives some input from the motor cortex, and it is therefore probably an important pathway for the recovery of some voluntary motor function after damage to the corticospinal tract.

Vestibulospinal tracts. The two vestibulospinal tracts originate in 2 of the 4 vestibular nuclei. The lateral vestibulospinal tract originates in the lateral vestibular nucleus. It courses through the brainstem and through the anterior funiculus of the SC on the ipsilateral side, before exiting ipsilaterally at all levels of the SC. The medial vestibulospinal tract originates in the medial vestibular nucleus, splits immediately and courses bilaterally through the brainstem via the medial longitudinal fasciculus (MLF) and through the anterior funiculus of the SC, before exiting at or above the T6 vertebra.

Function. The vestibulospinal tracts mediate postural adjustments and head movements. They also help the body to maintain balance. Small movements of the body are detected by the vestibular sensory neurons, and motor commands to counteract these movements are sent through the vestibulospinal tracts to appropriate muscle groups throughout the body. The lateral vestibulospinal tract excites antigravity muscles in order to exert control over postural changes necessary to compensate for tilts and movements of the body. The medial vestibulospinal tract innervates neck muscles in order to stabilize head position as one moves around the world. It is also important for the coordination of head and eye movements.

Reticulospinal tracts. The two reticulospinal tracts originate in the brainstem reticular formation, a large, diffusely organized collection of neurons in the pons and medulla (Figure 2.12).

The pontine reticulospinal tract originates in the pontine reticular formation, courses ipsilaterally through the medial longitudinal fasciculus and through the anterior funiculus of the SC, and exits ipsilaterally at all spinal levels. Themedullary reticulospinal tract originates in the medullary reticular formation, courses mainly ipsilaterally (although some fibers cross the midline) through the anterior funiculus of the SC, and exits at all spinal levels.

Function. The reticulospinal tracts are a major alternative to the corticospinal tract, by which cortical neurons can control motor function by their inputs onto reticular neurons. These tracts regulate the sensitivity of flexor responses to ensure that only noxious stimuli elicit the responses. Damage to the reticulospinal tract can thus cause harmless stimuli, such as gentle touches, to elicit aflexor reflex. The reticular formation also contains circuitry for many complex actions, such as orienting, stretching, and maintaining a complex posture. Commands that initiate locomotor circuits in the SC are also thought to be transmitted through the medullary reticulospinal tract. Thus, the reticulospinal tracts are involved in many aspects of motor control, including the integration of sensory input to guide motor output.

Tectospinal tract. The tectospinal tract originates in the deep layers of the superior colliculus and crosses the midline immediately. It then courses through the pons and medulla, just anterior to the medial longitudinal fasciculus. It courses through the anterior funiculus of the SC, where the majority of the fibers terminate in the upper cervical levels.

Function. Little is known about the function of the tectospinal tract, but because of the nature of the visual response properties of neurons in the superior colliculus (the optic tectum), it is presumably involved in the reflexive turning of the head to orient to visual stimuli.

Appendix C: Physiological noise

Pulsation of the CSF

SC fMRI is hampered by the fact that the spinal cord moves within the spinal canal together with the flow of CSF. The oscillating CSF pulsation is a response to the transient increase of intracranial blood volume during the cardiac cycle. The arterial inflow of blood has an early systolic peak about 100 ms after the R wave of the ECG, while the venous outflow is almost continuous with only a subtle diastolic flow increase in the internal jugular vein. By considering the brain as the main pump for the circulation of the CSF, an increased systolic intracranial blood volume occurs mainly in the richly vascularized compartments of the brain. This causes the expansion of the grey matter and then the compression of the intracranial subarachnoid space surrounding the cerebral hemispheres. Therefore, a large volume of CSF is initially displaced from the subarachnoid space into the cervical spinal canal immediately after the inflow of systolic blood. The downward flow of CSF in the cervical spinal canal is delayed of about 100–200 ms compared to the arterial inflow [238]. In normal subjects, the caudally directed (systolic) CSF flow in the anterior subarachnoid space reaches its maximum velocity immediately after the beginning of the pulsation. In the literature, CSF velocity in the cervical spine is reported to range from 0.8 to 4.0 cm/s. The diastolic reflux is significantly slower [239, 240]. The velocity decreases as the CSF descends the spinal axis. The maximal velocity in healthy volunteers occurs in the cervical area, at the C4–C5 level, and this is probably due to the fact that at this level, the SC has the maximum section and the subarachnoid space is minimum. In the lumbar area, because the SC extends only to the L2 level, leaving a large subarachnoid space for CSF flux, the velocity is significantly lower. The periodic changes in CSF flow with the cardiac cycle have a frequency of about 1 Hz. In the cervical canal, this cardiac-related CSF pulsation is superimposed upon an additional bulk component with a period of several seconds, identified as related to inspiration and expiration. The respiration-induced modulation of cardiac-related CSF flow is subtle during normal respiration but clearly increases during forced respiration. The respiration-related flux is directed mainly downwards in the anterior subarachnoid space, upwards laterally. In addition, it can be shown that the opposed components of CSF flow are not only anatomically separated, but they alternate with time: caudal CSF flow in the anterior cervical subarachnoid space dominates during inspiration, whereas expiration is accompanied by an increase in cranial flow. The increase of caudal CSF flow in the anterior cervical subarachnoid space can be identified immediately after inspiration begins [239]. The aforementioned knowledge suggests that the better approach to motion artefacts reduction should be the acquisition of functional images at about half of the interval between two consecutive hearth pulsations. In addition motion related artefacts can be minimized by acquiring the fMRI time

series time-locked with the relevant physiological parameters, respiration [11, 12] and cardiac pulsation [26].

Motion of the SC

Pulsatile movement of both the brain and SC is routinely observed during neurosurgical intervention that involves the central nervous system. Data obtained in healthy subjects indicate that the cervical SC moves in a craniocaudal oscillatory damped pattern after cardiac systole. The alternating cranial and caudal SC displacement and velocity decrease to zero in the late cardiac cycle. This pattern of oscillation differs from person to person. Measurements obtained about 100 ms after cardiac systole showed that the SC moves first caudally, at a velocity of about 7 mm/s; this movement is followed (about 160 ms after systole) by a cranial oscillation, with lower velocity (about 3 mm/s), while CSF is still moving in caudal direction. The measurement of caudal displacement of the SC suggests a maximum displacement of approximately 0.5–1 mm. No definite motion is seen in the middle thoracic SC. Transverse velocities may exist within the SC because of CSF pulsatility and systolic inflow within the SC tissue [241].

Susceptibility artifacts

The quality of SC functional maps is affected by local field strong inhomogeneities arising from many different tissues adjacent to the spine, in particular bone [11]. Cooke et al. [242]recently mapped B_0 inside the cervical SC at 2 T, showing local distortions especially in proximity of spinous processes, with spatial periodicity roughly equal to the length of the vertebral bodies. Nonetheless, B_0 is relatively uniform in the center of SC and, as it is easy to guess, the ob- served water linewidth decreased when spectroscopic voxel was shorter in the Inferior/Superior direction, thus symmetrically spanning the minimum number of interspinous spaces. These results strongly suggest to set the imaging slices perpendicular to the bone and to adjust their thickness and spacing so that each slice covers a vertebral body or an intervertebral disc, avoiding the boundary zones between bone and con- nective tissue. SC fMRI was demonstrated in cervical and lumbar segments, but not in correspondence of thoracic segment lower than T2. Below this level, images quality and stability is compromised, probably by lung and larynx motion, blood flow in the carotid artery, air in the trachea[6].

Appendix D: Several approaches to fMRI data analysis can enhance the detection of signals within or across subjects.

The goal of any fMRI experiment is to detect changes in local blood oxygenation—i.e. the BOLD signal—following a task-derived neural stimulation. Through fast MRI techniques, a low resolution functional scan of the entire brain/spinal cord can be acquired every few seconds. Accordingly, a number of volume elements (voxels) can be obtained each constituting a time-series which spans the duration of the experiment. In the simplest possible experiment, periods of stimulation are alternated with periods of *rest*. Conceivably, the signal recording one or more voxel's time-series may exhibit the same temporal pattern of the experimental design. Whether this is the case, the identification of such responding voxels fenced off from the noise level is the ultimate aim of fMRI analysis, which comprises pre-processing and statistical analysis. Pre-processing serves the need to reduce a variety of artefacts in the data, and to prepare the data to achieve an optimal statistical reliability, which in the worst case may be rendered invalid without the pre-processing steps. After the raw k-space data are Fourier transformed to reconstruct the actual images, often a slice-timing correction is carried out to improve the subsequent model fitting procedure. Because each slice is acquired at different time, voxel's time series has to be interpolated so that it appears as if they were scanned at the same time. The time-domain data are Fourier transformed and a phase shift is applied on the frequency-domain representation prior to inverse Fourier transformation. Usually this correction is combined with geometric movement-related distortions correction. For example, uncorrected very small movements of the head (e.g. less than 1 mm) can be a major source of error in data analysis. Each volume is then rotated and translated in order to align different images with one another. Spatial filtering is applied as well in order to increase signal-to-noise ratio as a consequence of local averaging derived by blurring. Commonly each volume is convolved with a Gaussian profile filter. In order for the signal to not be reduced significantly along with the noise, the width of the filter should be chosen not larger than the smaller expected activated region (usually 3-10 mm full width at half maximum). Several non-linear spatial filtering procedures based on neighbourhood information can attain noise reduction without necessarily blurring the signal of interest. Smoothing is also required by some statistical methods to meet certain theoretical assumptions. Further pre-processing concern the overall intensity level of each volume, which is normalized to the same mean intensity to help reducing possible scanner-derived global changes effects during time. The necessity of the normalization step can be questionable because it can induce artificial correlation between different voxel, especially when the mean image intensity is significantly determined by strong activations areas. Clearly, if the overall oxygenation is intentionally altered within the experiment design, intensity normalization should not

be carried out. Finally, voxels are time-filtered by linear and non-linear tools in order to remove low and high frequency components. High-pass filtering removes slowly varying unwanted signals such as aliased heartbeat or breathing as well as scanner-related drifts. Low-pass filtering eliminates the high frequency noise from each voxel's time series, although data treated in this way are more conditioned and may generate false positives due to less independent time points. Of course, it is important that time-filtering does not corrupt the relevant signal by an appropriate choice of cut-off times. Statistical analysis is performed after pre-processing resulting in a statistical map indicating those voxels activated by the stimulus. This outcome, however, is earned on account of the specific statistical approach used. A wealth of procedures for the analysis of fMRI brain response have been developed. Methods based on a model of the expected hemodynamic response (model-based methods) preceded those in which the components of interest do not derive from a comparison with the data, but are extracted from the data on the basis of some specific constraint (model-free methods). Almost in the same way, univariate analysis of each voxel independently from the other ushered in multivariate analysis based on spatial relationships within the data. In the following only the standard general linear model (GLM) for data analysis will be considered.

Appendix E: General linear modelling

General linear modelling is a model-based method which includes an initial univariate analysis followed by a non-univariate final inference stage. The expected response is fitted to a single voxel's time-course to determine to what extent the data might be caused by the stimulation. In the simplest case, given the experimental time-series y(t) the linear modelling can be written as

1) $$y(t) = \beta x(t) + C + \mathcal{E}(t)$$

where C is a constant corresponding to baseline (rest), "(t) is the random error in the model fitting and x(t) is the modelled BOLD response, whose magnitude is accounted for by the parameter β. The response function x(t) can be expressed as the convolution between a function s(t) containing the stimulus paradigm (in terms of 1 s and 0 s) and the so-called hemodynamic response function (HRF) h(t) according to :

2) $$x(t) = \int_0^\infty h(u)s(t-u)du$$

Equations (1) and (2) apply to an individual voxel and a single response. In general, the effect of different responses in all voxels has to be considered, giving rise to a large number of unknown parameters. Several algorithms have been developed to find good estimates for these parameters. An activation threshold has to be applied to the statistical map in order to set the separation between active and non-active voxel states. In a straightforward way, this can be accomplished by a simple significance test over each voxel. Unfortunately, this method needs a very stringent thresholding unless a large number of false positives would be obtained. To increase the sensitivity, it is possible to take into account spatial neighbourhood information through the so-called cluster-based thresholding, which uses an initial significance test to create clusters of voxel for the subsequent thresholding.

Acknowledgments

First, I would like to acknowledge professor Bruno Maraviglia, who welcomed me in his laboratory, and professor M.A. Ricci for the helpfulness she has always shown towards me.

I would like to thank Dr Federico Giove (Fermi Center) for introducing me to the exciting field of fMRI and for scientific discussion related with my research.

I am thankful to Dr.ssa Alessia Cedola (CNR-Nanotec) for introducing me to the exciting field of X-ray Phase contrast Tomography and also for the enthusiasm and constant inspiration to approach solution of the problems related with my research. To Inna Bukreeva (CNR-Nanotec) for fruitful scientific (but not only) collaboration and for sharing with me her expertise.

I also enjoyed fruitful scientific (but not only) discussions and collaboration with, Dr. G. Campi (CNR-IC), Professor Prof. Naurang Lai Saini (University of Rome, Physics department).

I would like to acknowledge experimental help and collaboration in the fMRI work of Professor C. A. Porro and Dr P.E. Summers (University of Modena), in the MRI work of Dr.ssa Silvia Capuani (CNR-ISC), and in the X-ray Tomography work of ID17 beamline staff (ESRF, Grenoble, FR), TOMCAT beamlie (PSI, Villigen, CH) and SYRMEP staff (Elettra, Trieste, IT).

I would like to thank all the members of the MARBILab (Fermi Center), of the IRCCS Santa Lucia Foundation and the NMR group of CNR-ISC at the Sapienza University of Rome for their scientific and human collaboration that have made the work enjoyable.

I am grateful to all my PhD journey companions, of Antonella Iadecola (ESRF) and Laura Maugeri (Roma Tre Univesity) for sharing with me this long experience.

At the end I would like to thank: Marco for his patience and for his important help and Anita for her patience and kindness.